

Time-Domain Protection Scheme for Microgrids with Aggregated Inverter-Based Distributed Renewable Energy Resources

A Dissertation

Presented in Partial Fulfillment of the Requirements for the
Degree of Doctor of Philosophy

with a

Major in Electrical Engineering

in the

College of Graduate Studies

University of Idaho

by

Husam S. Samkari

Major Professor: Brian K. Johnson, Ph.D.

Committee Members: Herbert L. Hess, Ph.D.; Yacine Chakhchoukh, Ph.D.;

Ahmed Abdel-Rahim, Ph.D.

Department Administrator: Joseph D. Law, Ph.D.

August 2021

Authorization to Submit Dissertation

This dissertation of Husam S. Samkari, submitted for the degree of Doctor of Philosophy with a Major in Electrical Engineering and titled "Time-Domain Protection Scheme for Microgrids with Aggregated Inverter-Based Distributed Renewable Energy Resources," has been reviewed in final form. Permission, as indicated by the signatures and dates below, is now granted to submit final copies to the College of Graduate Studies for approval.

Major Professor: _____ Date: _____
Brian K. Johnson, Ph.D.

Committee Members: _____ Date: _____
Herbert L. Hess, Ph.D.

_____ Date: _____
Yacine Chakhchoukh, Ph.D.

_____ Date: _____
Ahmed Abdel-Rahim, Ph.D.

Department
Administrator: _____ Date: _____
Joseph D. Law, Ph.D.

Abstract

This dissertation proposes a time-domain-based protection scheme for radial and loop connected microgrid systems with grid following controlled inverter-based resources (IBRs), such as solar photovoltaic (PV) generation and type-4 wind turbines. The protection scheme is designed to function during grid-interconnected and grid-isolated modes without changing the settings of the protection devices or requiring islanding detection schemes. The proposed scheme provides an ultra-high-speed sub-cycle directional element aided with low bandwidth communication between relays, indicating the fault zone in as little as four milliseconds for fast tripping to retain stability for severe faults. Like directional comparison schemes, relays identify whether faults are in-zone or out-zone in feeders with bidirectional power flow.

The proposed directional element is based on time-domain superimposed quantities and uses the Park's transformation. The superimposed, also known as incremental, quantities are fault-generated instantaneous components of voltages and currents largely dependent on the electric network parameters. The directional element indicates fault direction based on relative polarities of the transient voltages and currents by calculating the transient energy quantities. It is essential to ensure that the element accurately indicates the true direction if the quantities are impacted by IBR nonlinear fault current responses.

Most IBRs generate low fault current magnitudes and high-frequency transients, that are largely dependent on IBRs' fast control and independent of fault location. The fast control response and fault current characteristic of IBR impact current quantities by changing both magnitude and angle. Newer IBRs fault responses are often predominantly positive sequence fault currents with insignificant negative sequence currents. The dissertation shows the response of the superimposed-based element to IBR supplied fault current.

After that, this dissertation proposes a solution to eliminating the impact of IBR on time-domain-based superimposed quantities elements. More specifically, the element calculates the superimposed positive-sequence direct axis component of transient energy during faults. Superimposed voltage and current quantities are calculated using delta filters and decoupled double synchronous reference frame (DDSRF) filters. The proposed filtering method improves the reliability of the superimposed directional element when IBRs are present. The protection scheme is evaluated on a modified IEEE 34-bus distribution system simulated using the electromagnetic transients program (EMTP-RV).

Acknowledgements

I start by thanking the almighty God for the unlimited and continuous blessings in my life.

I express my sincere gratitude to my advisor and major professor, Dr. Brian Johnson, for his guidance and support through this research and my Ph.D. program. His inspirations, suggestions, kindness, and enthusiasm have been invaluable to help me complete my doctoral degree. Dr. Johnson is my mentor, and I will always be thankful to him.

My appreciation is extended to the committee members, Dr. Herbert Hess, Dr. Yacine Chakhchoukh, and Dr. Ahmed Abdel-Rahim, for their valuable time, insightful suggestions, and questions, which motivated me to improve this dissertation.

I am thankful to Dr. Chakhchoukh for selecting me as a Graduate Teaching Assistant. My thanks are extended to Dr. Hess and Dr. Hangtian Lei for the papers' collaboration opportunities.

I appreciate the EMTP-RV simulation software license support from PowerSys Inc., essential software for this doctoral study.

I am grateful to the University of Tabuk and the Ministry of Education for their financial support to complete my doctoral degree. In addition, I am thankful to the Embassy of the Kingdom of Saudi Arabia in the United States of America and the Saudi Arabian Cultural Mission to the United States for their crucial support during my time in the United States.

I am thankful to Idaho National Laboratory and Schweitzer Engineering Laboratories for the engineering internship opportunities. Special thanks to my supervisors, Timothy McJunkin, Jeff Pope, John Hostetler, Ashish Upreti, and Bharath Nayak, for improving my engineering skills and support me to grow personally and professionally.

I appreciate the IEEE Palouse Section for the opportunity to serve as vice-chair and YP chair, assisting me in building a network of contacts in the electrical engineering field with industry and academic professionals. Furthermore, the knowledge I gained from the technical events and the interaction during social events helped me during my doctoral studies.

Last but not least, I am grateful to my fellow students, faculty, and staff of the Department of Electrical and Computer Engineering at the University of Idaho, who have been part of my doctoral degree completion.

Dedication

To my wife, Hala

To my daughter, Laura, and my sons, Hesham and Sahl

To my grandmother, Khadiga

To my parents, family, friends, and nation

Table of Contents

Authorization to Submit Dissertation	ii
Abstract.....	iii
Acknowledgements	iv
Dedication.....	v
Table of Contents.....	vi
List of Tables	x
List of Figures.....	xi
List of Abbreviations	xvii
Chapter 1: Introduction	1
1.1. Problem Definition	1
1.2. Dissertation Contribution	4
1.3. Dissertation Roadmap	5
Chapter 2: Background.....	6
2.1. Microgrid Systems.....	6
2.1.1. Microgrid Concept.....	6
2.1.2. Microgrid Protection Challenges.....	7
2.2. Inverter Based Resources	9
2.2.1. IBR Concept	9
2.2.2. IBR Protection Challenges	12
2.3. Protection Elements.....	14
2.3.1. Voltage Restrained Time Overcurrent Elements.....	14
2.3.2. Time-Domain Superimposed Protection Element	15
Chapter 3: Modeling and Validation	20
3.1. Modified IEEE 34-Bus Model.....	20
3.2. IBR Model	24
3.2.1. Photovoltaic panel model	24

3.2.2.	Voltage source converter model	25
3.3.	Model of the Proposed Protection Scheme	31
3.3.1.	Signal processing	32
3.3.2.	Voltage Restrained Overcurrent Elements	38
3.3.3.	Superimposed Quantities Element	40
Chapter 4: Multi-Agent Protection Scheme for Resilient Microgrid Systems with Aggregated Electronically Coupled Distributed Energy Resources		43
4.1.	Introduction	43
4.2.	Proposed Protection Scheme	45
4.3.	Distributed Energy Resources Model	48
4.4.	Study Case 1: Simple System	49
4.4.1.	Fault Location	49
4.4.2.	Impacts on ΔV	53
4.5.	Study Case 2: IEEE 34-Bus	55
4.5.1.	Tripping Faulted Feeders	56
4.5.2.	Estimating Fault Locations	56
4.6.	Conclusions	57
Chapter 5: Impact of Inverter Based Resources on Superimposed Quantities Based Protection		58
5.1.	Introduction	58
5.2.	Superimposed Quantities	59
5.2.1.	Superimposed Voltage and Current	59
5.2.2.	Superimposed Transient Power	60
5.2.3.	Impact of Inverter-Based Resources	61
5.3.	Study Case and Simulation Results	62
5.3.1.	Study Case	62
5.3.2.	Simulation Results	63

5.3.3.	Additional Case and Discussion	67
5.4.	Conclusion.....	68
Chapter 6: Impact of Distributed Inverter-Based Resources on Incremental Quantities-Based Protection		69
6.1.	Introduction	69
6.2.	Incremental Quantities.....	70
6.2.1.	Incremental Algorithm	70
6.2.2.	Methods of Processing Incremental Quantities	71
6.2.3.	Incremental Transient Power.....	72
6.3.	Simulation Results.....	73
6.3.1.	Study Cases	73
6.3.2.	Fault Current Characteristic.....	74
6.3.3.	Incremental Quantities Results.....	75
6.3.4.	Additional Cases.....	78
6.4.	Conclusions	81
Chapter 7: Time-Domain Protection Scheme for Microgrids with Aggregated Inverter-Based Distributed Energy Resources.....		82
7.1.	Introduction	82
7.2.	Background and Proposed Protection Scheme	83
7.2.1.	Superimposed Quantities.....	84
7.2.2.	Proposed Microgrid Protection Scheme	85
7.2.3.	Proposed Relay	87
7.2.4.	Superimposed Based Directional Element Logic	92
7.2.5.	Phasor-Based Element and Trip Logic.....	94
7.3.	Study Case: Modified IEEE 34-Bus.....	95
7.3.1.	EMTP-RV Simulation Results	96
7.4.	Conclusions	103

Chapter 8: Summary, Conclusions, and Future Work	104
8.1. Summary.....	104
8.2. Conclusions	105
8.3. Future Work.....	106
References.....	108
Appendix A - IBRs Fault Current Characteristics	116
Appendix B - EMTP-RV Model	118
B.1. IEEE 34-Bus Model Validation.....	118
B.2. Synchronous Generator Model Validation	121
B.3. Photovoltaic Model	122
B.4. Voltage Source Converter Model Validation	126
B.5. Relay Model Validation	129
Appendix C - Copyright Permissions.....	137

List of Tables

Table 3.1 IEEE 34-bus system short circuit source data upstream of node 800	20
Table 3.2 The percentage of error of the modified IEEE 34-bus EMTP-RV model when compared to IEEE data in terms of voltage magnitude and the angle at selected nodes	21
Table 3.3 The percentage of error of the modified IEEE 34-bus EMTP-RV model, when compared to IEEE data, in terms of fault currents at node 800.....	22
Table 3.4 Synchronous generator parameters	23
Table 3.5 Generator transformer data	23
Table 3.6 PV model parameters	24
Table 3.7 VSC electrical parameters	29
Table 3.8 VSC control parameters in a per unit based VSC rated voltage and MVA	30
Table 3.9 Relay analog variables	31
Table 3.10 Sine and cosine filters coefficients	37
Table 3.11 Phasor-based sampled analog variables	39
Table 3.12 Time-domain-based analog variables	40
Table 4.1 ΔV in pu calculated at Bus A.....	51
Table 4.2 ΔV in pu calculated at Bus A.....	54
Table 4.3 ΔV in pu calculated at Bus 800.....	57
Table 7. 1 Relay Response Signals Time in Milliseconds	97

List of Figures

Figure 1.1 Summary of the primarily defined problems.....	3
Figure 2.1 A generic microgrid with DERs, loads and PCC	6
Figure 2.2 Fault current change when system topology change: (a) PCC and POI breakers are closed, (b) PCC is open, and POI is closed, and (c) PCC is closed, and POI is open	8
Figure 2.3 Bidirectional power flow in feeders: (a) PCC and POI breakers are closed, allowing the microgrid to import or export power and (b) PCC breaker is closed, and POI breaker is open.....	9
Figure 2.4 PV cell, module, panel and array.....	10
Figure 2.5 An example of a PV system with a voltage source converter, controller, and ac filters	10
Figure 2.6 An example of a volt-var control characteristic	12
Figure 2.7 Three-phase fault currents mainly supplied by: (a) an IBR, (b) zoom in the IBR (c) type-1 wind turbine, and (d) synchronous generator	13
Figure 2.8 An example of a voltage restrained time overcurrent operating characteristic with pickup current varies linearly with voltage	15
Figure 2.9 Delta filter connection defines superimposed quantities method	16
Figure 2.10 An example of using superimposed quantities-based protection in a directional comparison scheme	16
Figure 2.11 Voltage and current delta filters for calculating superimposed quantities.....	17
Figure 2.12 Measuring incremental quantities from waveforms during a single line to ground fault: (a) voltage, (b) current (c) delta voltage, and (d) delta current and replica current.....	17
Figure 2.13 Fundamental operating characteristics of incremental directional elements show that negative-power indicates forward faults, and positive-power indicates reverse faults	18
Figure 3.1 IEEE 34-bus system	20
Figure 3.2 A modified IEEE 34-bus system with IBR and locations for protection studies	22
Figure 3.3 An overall diagram of the IBR model including the PV panels, the VSC, the control, and the ac filters	24
Figure 3.4 Photovoltaic model I-V and P-V characteristics with MPP marked	25
Figure 3.5 A three-phase two-level VSC with insulated-gate bipolar transistors switching devices	26
Figure 3.6 Schematic diagram of a current-controlled real and reactive power controller.....	26
Figure 3.7 PLL block diagram.....	28
Figure 3.8 Inner and outer controller block diagrams with real and reactive power setpoints	29
Figure 3.9 Signal processing for the proposed protective relay	32

Figure 3.10 Frequency response of the low-pass filter with a cutoff frequency at half the sampling frequency	33
Figure 3.11 The designed low-pass filter introduces a delay of less than one millisecond	33
Figure 3.12 An example from the EMTP-RV comparing the low-pass filter model output with the original waveform	34
Figure 3.13 An example of the EMTP-RV sampling at 16 spc	34
Figure 3.14 Frequency response of the mimic filter with a time constant of two power cycles....	35
Figure 3.15 The modeled mimic filter introduces a delay of two milliseconds.....	36
Figure 3.16 The modeled mimic filter in EMTP-RV removed decaying dc offset from the signal	36
Figure 3.17 Calculating the magnitude using DFT filter model	37
Figure 3.18 The designed DFT filter (a) sine filter coefficients and (b) cosine filter coefficients	38
Figure 3.19 An example from the modeled DFT filter in EMTP-RV when current changes from zero to the rated current with a response of one power cycle.....	38
Figure 3.20 Calculating phasor-based superimposed positive-sequence and negative-sequence voltages.....	39
Figure 3.21 An example from the modeled phasor-based superimposed element in EMTP-RV when measured voltage drops	40
Figure 3.22 Calculating DDSRF-based superimposed positive-sequence quantities	40
Figure 3.23 An example of superimposed positive-sequence direct-axis current from the DDSRF compared to time-domain superimposed current during fault.....	41
Figure 3.24 An example of superimposed positive-sequence direct-axis voltage from the DDSRF compared to time-domain superimposed voltage during fault	42
Figure 3.25 Testing the DDSRF-based superimposed quantities with different sampling rates ...	42
Figure 4.1 Test system for the proposed scheme	46
Figure 4.2 Data flow from the CTs and VT to the protective agent	46
Figure 4.3 Per phase protection logic diagram per feeder	48
Figure 4.4 Simplified one line diagram of the EMTP-RV distribution model	50
Figure 4.5 Measured ΔV in pu when SLG fault applied at 75%	50
Figure 4.6 Measured ΔV in pu at Bus A when faults applied at five locations	51
Figure 4.7 Three phase rms voltages in pu when SLG fault is applied at 75%	52
Figure 4.8 Three phase currents at the PV POI when SLG fault applied at 75%	53
Figure 4.9 ΔV in pu calculated at Bus A for the five scenarios.....	54

Figure 4.10 IEEE 34 bus distribution system connected to PV systems and protective agents (faults locations are noted)	56
Figure 5.1 Measuring superimposed quantities from waveforms during an SLG fault: (a) voltage, (b) current, (c) superimposed voltage, and (d) superimposed current and replica current	60
Figure 5.2 An example of superimposed transient and replica power during an SLG fault for a conventional system source	61
Figure 5.3 An example of the impact of IBRs on superimposed quantities during an SLG fault: superimposed (a) voltage, (b) current and replica current, (c) power and replica power	62
Figure 5.4 Single-line diagram for the power system model	63
Figure 5.5 Superimposed power and replica power for SLG faults at 25% of the line from bus R: (a) relay S with $R_f = 0\Omega$, (b) relay S with $R_f = 2\Omega$ (c) relay R with $R_f = 0\Omega$, and (d) relay R with $R_f = 2\Omega$	64
Figure 5.6 Superimposed power and replica power for SLG faults at 50% of the line: (a) relay S with $R_f = 0\Omega$, (b) relay S with $R_f = 2\Omega$ (c) relay R with $R_f = 0\Omega$, and (d) relay R with $R_f = 2\Omega$	65
Figure 5.7 Superimposed power and replica power for SLG faults at 75% of the line from bus R: (a) relay S with $R_f = 0\Omega$, (b) relay S with $R_f = 2\Omega$ (c) relay R with $R_f = 0\Omega$, and (d) relay R with $R_f = 2\Omega$	66
Figure 5.8 Superimposed power and replica power measured at relay R for SLG fault with $R_f = 0\Omega$ at 50% of the line when IBR rated 10 MVA	67
Figure 6.1 Measuring incremental quantities from waveforms: (a) voltage, and (b) current	70
Figure 6.2 Delta filter connection defines incremental quantities method	72
Figure 6.3 Fundamental operating characteristics of incremental directional elements show that negative-power indicates forward faults, and positive-power indicates reverse faults	73
Figure 6.4 Modified IEEE 34-bus system: (a) IBR, (b) WTG-1, and (c) SG	74
Figure 6.5 Primary three phase currents measured at Relay 848 during in-zone 3PH faults: (a) IBR, (b) zoom in IBR (c) WTG-1, and (d) SG	75
Figure 6.6 Relay 846 incremental signals during SLG faults: (a) IBR, (b) WTG-1, and (c) SG; Where (1) delta voltage, (2) delta current and replica current, and (3) delta power and replica power	76
Figure 6.7 Relay 848 incremental signals during SLG faults: (a) IBR, (b) WTG-1, and (c) SG; Where (1) delta voltage, (2) delta current and replica current, and (3) delta power and replica power	77
Figure 6.8 Relay 848 transient power and replica power: (a) IBR, (b) WTG-1, and (c) SG; Where (1) 3PH, (2) DLG, and (3) LL faults	78

Figure 6.9 Incremental signals during SLG faults: (a) $R_f = 10$ ohm, (b) IBR voltage-control, and (c) Relay at 824; Where (1) delta voltage, (2) delta current and replica current, and (3) delta power and replica power	79
Figure 6.10 Relay 848 transient power and replica power during SLG faults with IBR and zero-sequence path: (a) $R_f = 0$ ohm, and (b) $R_f = 10$ ohm	80
Figure 7.1 The condition of the input of the delta filters defines superimposed quantities type ...	85
Figure 7.2 Upstream relays send forward signals to downstream relays, and downstream relays send reverse signals to upstream relays: (a) Radial system, (b) Parallel feeders with a normally open breaker, and (c) Loop system	86
Figure 7.3 Simplified diagram for the proposed relay signal processing, time-domain protection element, phasor-based elements and communication.....	88
Figure 7.4 Calculating superimposed positive-sequence direct quantities: (a) Decoupled double synchronous reference frame (DDSRF), (b) Positive-sequence decoupling, and (c) Per-phase delta filters.....	89
Figure 7.5 Transient superimposed positive-sequence direct Watt and energy	91
Figure 7.6 Comparison of IBRs impacts on superimposed transient Watt, apparent power, and replica power methods: (a) SLG forward fault at a system with no IBRs and (b) SLG reverse fault at a system with IBRs.....	92
Figure 7.7 Time-domain superimposed based directional element: (a) Logic and communication scheme and (b) Operating characteristics.....	93
Figure 7.8 Phasor-based superimposed voltage-restrained overcurrent element and trip logic with fast and slow tripping	94
Figure 7.9 Modified IEEE 34-bus distribution system	96
Figure 7.10 In-zone single line to ground fault at location 1 during grid-isolated mode with FWD/REV, IN-ZONE, and TRIP assert times marked in ms: (a) Relay at node 846 response and (b) Relay at node 848 response	99
Figure 7.11 In-zone double line to ground fault at location 2 during grid-isolated mode with FWD/REV, IN-ZONE, and TRIP assert times marked in ms: (a) Relay at node 816 response and (b) Relay at node 824 response	100
Figure 7.12 In-zone line to line fault at location 3 during grid-interconnected mode with FWD/REV, IN-ZONE, and TRIP assert times marked in ms: (a) Relay at node 858 response and (b) Relay at node 834 response	101
Figure 7.13 FWD/REV, IN-ZONE, and TRIP signals response time statistics.....	102

Figure A.1 PV is rated 2 MW and producing 2 MW during a three-phase fault and with reactive-power mode set to zero reactive power	116
Figure A.2 PV is rated 2 MW but producing 1 MW during a three-phase fault and with reactive-power mode set to zero reactive power	116
Figure A.3 PV is rated 2 MW but producing 0 MW during a three-phase fault and with reactive-power mode set to zero reactive power	117
Figure A.4 PV is rated 2 MW and producing 2 MW during a three-phase fault and volt-reactive-power mode with one per unit voltage set point.....	117
Figure A.5 PV is rated 2 MW and producing 0 MW during a three-phase fault and volt-reactive-power mode with one per unit voltage set point.....	117
Figure B.1 Modified IEEE 34-node voltage validation test which compares between IEEE data and EMTP-RV results at each node (a) phase A magnitude and (b) phase A angle	118
Figure B.2 Modified IEEE 34-node voltage validation test which compares between IEEE data and EMTP-RV results at each node (a) phase B magnitude and (b) phase B angle	118
Figure B.3 Modified IEEE 34-node voltage validation test which compares between IEEE data and EMTP-RV results at each node (a) phase C magnitude and (b) phase C angle	119
Figure B.4 Modified IEEE 34-node voltage validation test which compares between IEEE data and EMTP-RV results at each node (a) percentage of error in magnitude and (b) percentage of error in angle	119
Figure B.5 A screenshot of the IEEE 34-bus model in EMTP-RV	120
Figure B.6 Synchronous generator angular velocity ω in pu when three-phase fault applied at 1 sec and cleared at 1.2 sec.....	121
Figure B.7 Synchronous generator three-phase current when three-phase fault applied at 1 sec and cleared at 1.2 sec.	121
Figure B.8 Synchronous generator three-phase terminal voltage when three-phase fault applied at 1 sec and cleared at 1.2 sec.....	122
Figure B.9 EMTP-RV model of the PV system including the panel model, the VSC, ac filters, and the power transformer	122
Figure B.10 VSC control including the outer and the inner current controls	123
Figure B.11 Switching-based three-phase two-level VSC model.....	123
Figure B.12 ATP-EMTP test bed for validation	126
Figure B.13 EMTP-RV test bed for validation.....	126
Figure B.14 Comparing the change of real power from 50% to 100% between ATP-EMTP and EMTP-RV	127

Figure B.15 Phase A current during a fault on EMTP-RV test bed with averaged model and switched model for validation	128
Figure B.16 EMTP-RV PI control with a feedback.....	128
Figure B.17 Verifying EMTP-RV PI control with feedback by using MATLAB Simulink	129
Figure B.18 An example of the developed EMTP-RV model for the low pass filter	129
Figure B.19 An example of the developed EMTP-RV model for sampling currents (16 spc)....	130
Figure B.20 The developed EMTP-RV model for DFT and sequence calculation	131
Figure B.21 An example of the developed sine and cosine filters for voltage with zoom in magnitude and angle calculation	132
Figure B.22 Zoom in cosine filter.....	133
Figure B.23 Zoom in sine filter.....	134
Figure B.24 The developed EMTP-RV model for calculating positive, negative, and zero sequences voltage after the DFT	135
Figure B.25 An example of the developed EMTP-RV model for calculating superimposed.....	135
Figure B.26 The developed EMTP-RV model for the proposed DDSRF-based superimposed..	136
Figure B.27 An example of the developed EMTP-RV model for the DDSRF scheme.....	136
Figure C.1 IEEE permission for copying a paper as Chapter 4 in this dissertation.....	137

List of Abbreviations

ac	Alternating Current
ANSI	American National Standards Institute
ATP-EMTP	Alternate Transients Program - Electromagnetic Transients Program
BPS	Bulk Power System
CT	Current Transformer
dc	Direct Current
DDSRF	Decoupled Double Synchronous Reference Frame
DERs	Distributed Energy Resources
DFT	Discrete Fourier Transform
DLG	Double Line to Ground
DO	Drop-Out
EMTP	Electromagnetic Transients Program
EPS	Electric Power System
FWD	Forward
GOOSE	Generic Object Oriented Substation Event
IBRs	Inverter-Based Resources
IEC	International Electrotechnical Commission
IEEE	Institute of Electrical and Electronics Engineers
kV	Kilovolt
LL	Line to Line
MPPT	Maximum Power Point Tracking
MVA	Megavolt-Ampere
MVAR	Megavolt-Ampere Reactive

MW	Megawatt
NREL	National Renewable Energy Laboratory
PCC	Point of Common Coupling
PF	Power Factor
PLL	Phase-Locked Loop
POI	Point of Interconnect
PU	Pick-Up
pu	Per Unit
PV	Photovoltaic
REV	Reverse
RTDS	Real-Time Digital Simulation
SLG	Single Line to Ground
spc	Samples Per Cycle
VSC	Voltage Sourced Converter
VT	Voltage Transformer

Chapter 1: Introduction

Each year, more electricity is generated from renewable inverter-based resources (IBRs), such as solar photovoltaic (PV) and type 4 wind turbines. In 2018, PV accounted for 55% of the new global renewable generation capacity, and wind turbines accounted for 28%. Moreover, there is an increasing interest in expanding the percentage of electricity generated by renewable energy globally. For example, nine countries increased their electricity supply from PV and wind resources to 20% in 2018. This growth is due to the rapid decline in the generation costs of PV and wind resources [1]. Another factor is the capability of integrating IBRs into electric power distribution systems.

Bringing IBRs close to consumers can increase electricity delivery system resilience and reliability by reducing the size and duration of power outages [2], [3]. The economic feasibility of residential PV systems and, in general, IBRs' technologies and the improvement on power electronics are tilting the economics of power generation back towards smaller scales [2], [4]. These advantages led to the concept of forming subsystems or "microgrids" to eliminate the need for central dispatch [5], [6]. IBR technologies such as microturbines, PV systems, fuel cells, and type 4 wind turbines are electronically coupled units and considered for the future energy resources of microgrid systems.

As the U.S. Department of Energy explains, a microgrid system is a localized power grid that can be connected and disconnected from the bulk power system. Microgrids can continue operating while the main power system is down, strengthening grid resilience and mitigating grid outages. In addition, microgrids support the use of local sources of energy. Thus, energy losses in power systems are reduced, producing a flexible and efficient electric grid [7], [8]. In other words, microgrid systems operate, control, and protect predefined subsystems while connecting or disconnecting from the bulk power systems.

Integrating high penetration levels of IBRs into microgrid systems creates various challenges [9]. Establishing electricity markets, regulation laws, and policies for interconnections are examples of non-technical challenges. Meanwhile, technical challenges vary from controlling to protecting microgrids [10]–[12].

1.1. Problem Definition

This dissertation focuses on microgrid protection. The problem definition can be divided into two categories:

- Protecting microgrid systems
- Integrating IBRs into microgrid systems

First, microgrid systems pose three protection challenges:

- Wide variation in fault current levels depending on the operation mode of the microgrid
- Dynamic changes in microgrid topology and generation availability
- Bidirectional power flow in feeders

The available fault current may significantly change between grid-isolated mode and grid-interconnected mode. For example, fault currents depend only on the distributed energy resources (DER) within the microgrid during the grid-isolated mode. However, during the grid-interconnected mode, fault currents are supplied from both the bulk power system (BPS), also known as the electric power system (EPS), and the DERs.

The dynamic change in the topology of the microgrid or the change in generation availability can change both the magnitude and direction of fault currents. For example, fault current direction can change in a radial feeder topology if a normally open circuit breaker is closed to form a loop feeder topology. Also, PV systems may be disconnected during the night, changing the magnitude of fault currents on the feeder where the PV is located.

Typical electric power distribution systems have a unidirectional power flow from utility to consumers. However, during the grid-interconnected mode, the power flows bidirectionally in microgrids, which requires faults to be cleared from contributing generation sources and the bulk power system.

Second, integrating IBRs into microgrid systems pose three protection challenges:

- Unique fault current characteristics
- Fast control response
- No inherent inertia

IBRs' fault current characteristics are summarized as:

- Low fault current magnitudes around 1.2-1.5 per unit
- Nonlinear behavior relative to fault location and fault type
- High-frequency transient for the first quarter of a power cycle for up to two cycles
- Primarily dependent on IBRs' control and independent of fault location
- Predominantly positive-sequence fault currents with insignificant negative-sequence currents for most IBR in use at the time of this writing

The fault current contribution from small synchronous and induction generators is typically about four per unit with a decaying dc offset lasting for up to four cycles. Protective devices can be set to detect this current since it is well above the maximum load current. However, IBRs' low fault current makes it difficult to distinguish between overload conditions and fault currents. Also, using sensitive protective devices, such as zero-sequence and negative-sequence protection elements, is not feasible because IBRs predominantly produce positive-sequence fault currents. Finally, coordinating between protective devices is an issue because IBRs' fault currents are largely independent of fault location and instead dependent on IBRs control.

The fast response of the IBRs' controllers provides fast fault current regulation. For example, an IBR controller can regulate the fault current within the first quarter of a power cycle. However, a typical protective device in distribution systems needs significantly more than a cycle to sense the fault and operate.

In addition, unlike synchronous generators, IBRs have no inherent inertia. Thus, the IBRs may not contribute to system inertia in microgrids. Hence, the increasing percentage of IBRs decreases the critical clearing time to retain stability for severe faults.

In summary, microgrid systems changed the traditional electric power distribution system from a static system to a dynamic system. Also, including IBRs in microgrid systems introduced fault currents that depend on IBRs' controllers, not electric grid parameters. Figure 1.1 summarized the identified problems.

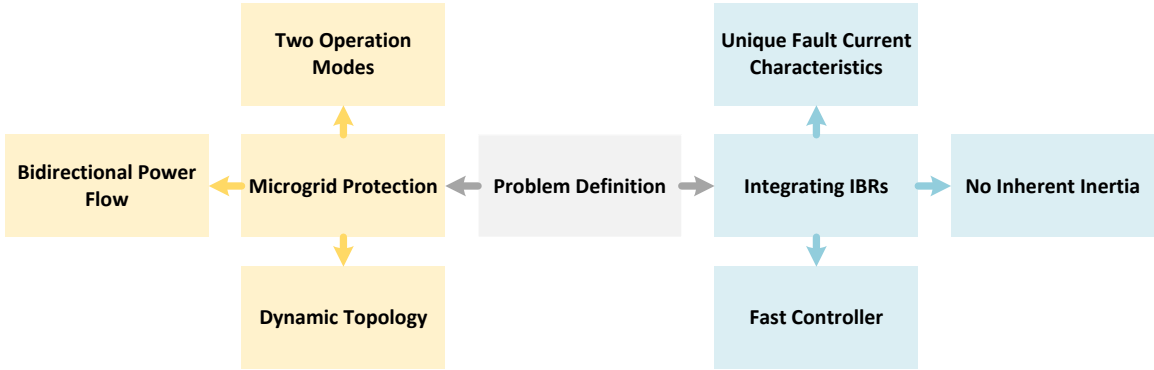


Figure 1.1 Summary of the primarily defined problems

1.2. Dissertation Contribution

This dissertation considers solving the problems defined above and introduces two primary contributions for microgrid systems dominated by IBRs by:

- Proposing a more effective microgrid protection scheme
- Proposing a time-domain-based protective relay with two novel protection elements

First, the proposed microgrid protection scheme:

- Overcomes the two operation modes issue with a protection scheme that eliminates the need to change relay settings or to have an islanding detection scheme, which allows for the same protection strategy for both grid-interconnected and grid-isolated operation modes
- Is applicable for microgrids with dynamic topologies and microgrids with radial and loop topologies
- Can identify the fault zone in a system with unidirectional or bidirectional power flow using only low bandwidth communication between relays

Second, the developed time-domain-based protective relay:

- Has sensitive element to pick up low fault current levels supplied by IBRs, regardless of the high-frequency transient
- Indicates fault zone in as little as seven milliseconds for fast tripping to retain stability for severe faults
- Is based on superimposed quantities, but enhanced with the decoupled double synchronous reference frame (DDSRF) algorithm, which increases the reliability of the directional element with the presence of grid following controlled IBRs
- Operates independently as a multi-agent protective device and is able to continue to protect the system when the communication system is degraded
- Supervised by a phasor-based versatile voltage-restrained overcurrent element

In addition, this study provides an understanding of the impact of IBRs on superimposed quantities-based protection. The impact of IBRs, the proposed protection scheme, and the developed protective relay are evaluated on a modified Institute of Electrical and Electronics Engineers (IEEE) 34-bus distribution system simulated using electromagnetic transients program, revised version (EMTP-RV).

1.3. Dissertation Roadmap

The developed microgrids protection scheme and time-domain protective relay are detailed in this dissertation in eight chapters. A brief introduction, the problem definition, the dissertation contribution, and the dissertation roadmap were presented in this chapter.

Chapter 2 presents a general overview of microgrid systems and their protection challenges, discusses the basic concepts of IBRs and their challenges for system protection, and provides a background and literature review on voltage-restrained time overcurrent and time-domain superimposed protection elements. Chapter 3 explains the modeling information and validation process, including information about the IBR model and the developed protective relay model.

The overall idea of the proposed microgrid protection scheme and the voltage-restrained time overcurrent element are discussed in Chapter 4, a paper presented at the 2018 Conference of the IEEE Industrial Electronics Society (IECON) [13]. Chapter 5 is a paper presented at the 2021 Georgia Tech Protective Relay Conference (PRC), which demonstrates the impact of IBR on superimposed quantities-based protection on a simple transmission line system [14]. Chapter 6 is a paper accepted to be presented at the 2021 IEEE Power and Energy Society General Meeting (PES GM), which demonstrates the impact of IBR on superimposed quantities-based protection on electric distribution systems and microgrids [15].

Chapter 7 is a paper that has been submitted to the IEEE Transactions on Smart Grid, which provides the complete description of the overall protection scheme and the protective relay along with simulation results [16]. Finally, a summary of this dissertation, conclusions, and possible future work are presented in Chapter 8.

Chapter 2: Background

This chapter provides background on microgrid systems and IBR concepts, including protection challenges. A literature review on using time-domain protection in microgrids is also discussed.

2.1. Microgrid Systems

2.1.1. Microgrid Concept

Microgrids are localized power systems that can disconnect from the BPS to operate autonomously, strengthening power grid resilience by operating even while the BPS is down. Microgrids utilize local DER to supply loads, increasing efficiency by reducing energy losses in transmission and distribution. A microgrid can operate as a single standalone controllable entity in both grid-interconnected and grid-isolated modes. A microgrid system has a predefined electrical boundary where DERs are controlled to maintain loads. For example, a microgrid might consist of various DERs, controlled electrical loads, a local controller, and protection and communication systems. Figure 2.1 shows a generic microgrid where loads and four types of DERs are connected: solar (PV), energy storage system (ESS), wind turbine generator (WTG), and synchronous generator (SG). The microgrid is connected to BPS through a point of common coupling (PCC). Each DER is connected to the microgrid through a separate point of interconnect (POI) [3], [7], [8], [17]–[20].

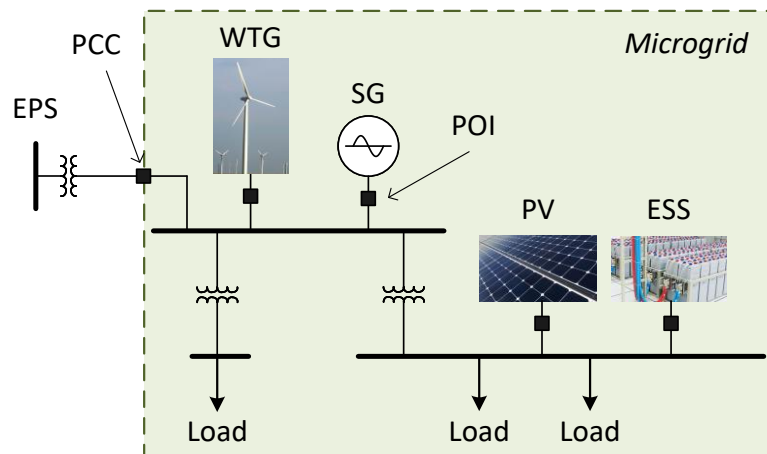


Figure 2.1 A generic microgrid with DERs, loads and PCC

Designing power distribution control systems becomes complex because of the two microgrid operation modes and the presence of DERs. There are two opposing control architectures for microgrids in the literature: centralized and decentralized (or distributed) control systems. The centralized architecture relies on extensive communication within a microgrid. On the other hand, decentralized architecture may require only a minimum level of coordination to function. A hierarchical control

scheme can compromise between fully centralized and fully decentralized control schemes consisting of three control levels: primary, secondary, and tertiary. The primary control has the fastest response and implements the first level in the control hierarchy, such as DER output control and power-sharing control between two or more DERs. The secondary control coordinates different internal primary controllers within the microgrids for energy management. The highest hierarchical control level is tertiary control, with control requirements depending on the BPS host [4], [21], [22].

Protection schemes in microgrids must respond appropriately and rapidly to faults in both grid-interconnected and grid-isolated modes. The two operation modes and the presence of DERs pose protection challenges, which traditional distribution protection schemes may not be able to handle reliably.

2.1.2. Microgrid Protection Challenges

Protecting a microgrid system during grid-interconnected and grid-isolated modes presents unique protection challenges. The available fault current may be significantly less during grid-isolated mode than when grid-interconnected because it depends on the fault current supplied by DERs within the microgrid rather than the strength of the source impedance at the PCC. Moreover, dynamic changes in the microgrid system topology causes changes in fault current paths [23]–[27]. The main protection challenges could be summarized in three points:

- Variable fault current levels depending on the operation mode
- Adapting to topology and generation changes
- Bidirectional power flow in feeders

Figure 2.2 shows an example of three possible cases where fault current varies in a generic microgrid because of the dynamic changes in the system topology. The three cases are:

- During grid-interconnected, the fault current is supplied from both BPS and DER where both the PCC and POI breakers are closed, as shown in Figure 2.2 (a)
- During grid-isolated, the fault current is supplied from only the DER when the PCC breaker is open and the POI breaker is closed, as shown in Figure 2.2 (b)
- During grid-interconnected, the fault current is supplied from the BPS only where the PCC breaker is closed and the POI breaker is open, as shown in Figure 2.2 (c)

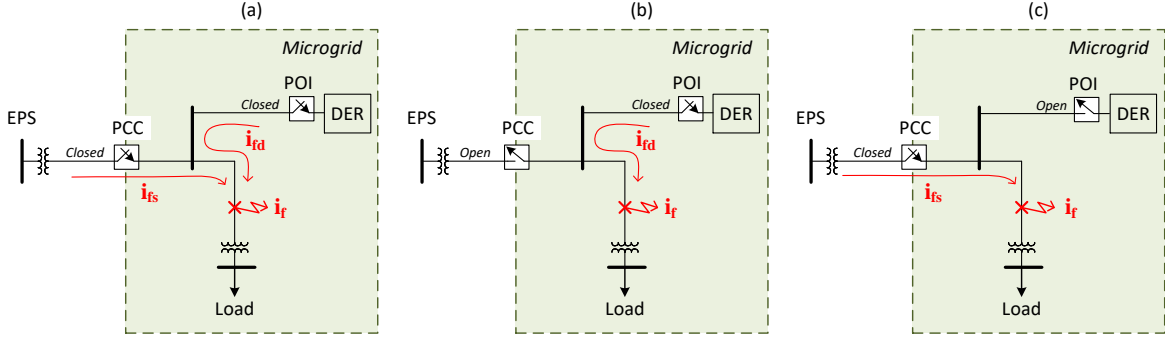


Figure 2.2 Fault current change when system topology change: (a) PCC and POI breakers are closed, (b) PCC is open, and POI is closed, and (c) PCC is closed, and POI is open

The total fault current (i_f) could quite be different in the three cases. In the first case, i_f is high and equal to the sum of the fault current supplied from the BPS (i_{fs}) and the fault current supplied from the DER (i_{fd}). In the second case, i_f is low and equal to i_{fd} . The BPS source typically is a stronger fault current source than the DER ($i_{fs} > i_{fd}$) which is the reason for the reduction in fault current. The last case is the configuration of a conventional power distribution system in which the fault current is supplied from the BPS only ($i_f = i_{fs}$). In all cases, passive loads are assumed, making loads do not contribute to fault currents.

DERs' fault currents levels and characteristics vary based on the rating and type of each DER. For example, fault current contributions from synchronous and induction generators are typically about four per unit with a decaying dc offset lasting for up to four cycles. However, IBR, also known as electronically coupled DERs, typically have low fault currents around 1.2 per unit with a nonlinear characteristic [9], [25], [28]. Therefore, including IBRs in microgrids poses more protection challenges, which are discussed in detail in section (2.2).

DERs allow microgrids to export power to the BPS during the grid-interconnected mode, which means power can flow from downstream nodes to upstream nodes, as shown in Figure 2.3 (a). Faults located between the PCC and the POI are supplied by both the BPS and the DER, which must be cleared from both the BPS and the DER. Feeder protection in a conventional distribution system assumes the direction of the power flow and fault currents are from upstream nodes to downstream nodes, which must be cleared from the BPS only, as shown in Figure 2.3 (b).

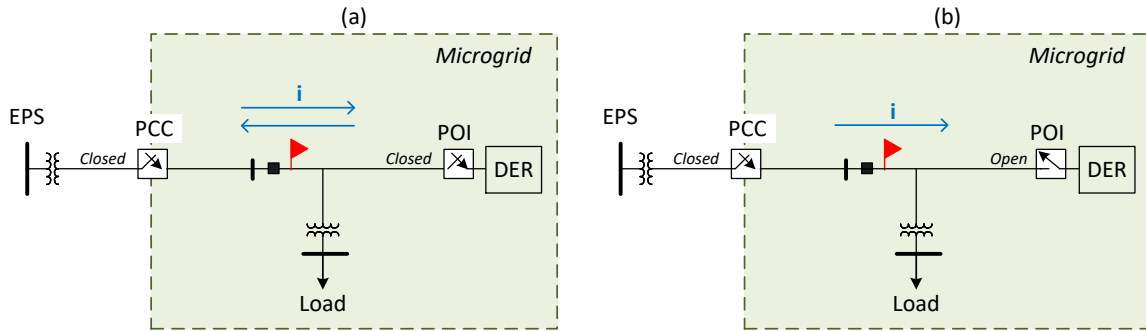


Figure 2.3 Bidirectional power flow in feeders: (a) PCC and POI breakers are closed, allowing the microgrid to import or export power and (b) PCC breaker is closed, and POI breaker is open

2.2. Inverter Based Resources

2.2.1. IBR Concept

Energy resources, such as PV, may have one collector inverter or several inverters for dc to ac conversion to electronically couple the resources to power distribution and microgrid systems. One type of inverter used for this purpose is the voltage source converter (VSC) [29]–[32].

PV systems are environmentally friendly when one ignores fabrication and disposal. The panels are noiseless and produce no carbon dioxide (CO₂) emissions once they are in operation. The systems also have no moving parts, unlike most other generators, and can be installed, quickly, on the ground or the top of buildings. Since the panels generate dc power at a low voltage level, the system can be applied at the power distribution and microgrid systems.

On the other hand, PV systems have a variable output that depends on solar irradiation, generates real power during daylight, and produces zero real power during the night. In addition, PV panels are affected by weather conditions, such as a cloudy day. Also, the output power generated by PV panels depends on the sun's angle during different daylight times and different seasons. For example, in places which the sun angle varies between winter and summer, the panels' position should be changed to face the sun in each season and maybe rotated over a day to maximize the PV output [33]–[35]. Adding a mechanism for solar panels to follow the sun may increase the total output power over a day. However, it adds to the complexity of the PV system, and it is largely a financial decision. Several connected solar cells are considered a module, and several connected modules make a panel, as shown in Figure 2.4. Also, several connected panels are an array. The connection can be in series or parallel, or most likely some combination of both with a goal to increase voltage or current and increase the PV system's power rating.

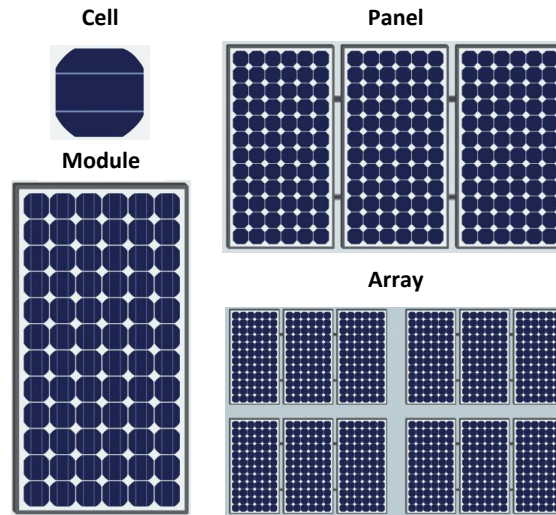


Figure 2.4 PV cell, module, panel and array

Figure 2.5 shows an example of an IBR system that consists of PV panels, a dc bus, ac filters, a VSC, and a control system. The PV panels convert energy from photons, or particles of light, into dc electricity using semiconducting materials. The panels are connected to a dc bus, which typically has a parallel capacitor acting as dc filter, to inject energy to the grid. A boost dc to dc converter might be connected to the PV panels to step up the output voltage in some topologies. A parallel high pass filter and a series low pass filter are connected to the ac terminal to smooth the output voltages and currents [31], [32].

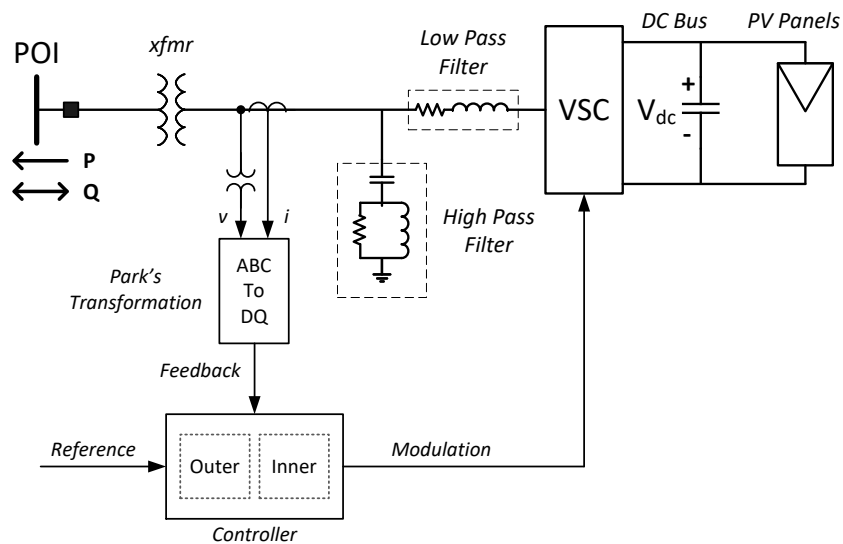


Figure 2.5 An example of a PV system with a voltage source converter, controller, and ac filters

Two-level VSCs are commonly used power-electronic converters for low power applications. Single-phase inverters are used for small systems, while three-phase inverters are used for larger systems. A three-phase two-level inverter consists of six fully controllable and unidirectional switches. The switches are semiconductor devices, such as insulated-gate bipolar transistors (IGBT) or integrated-gate commutated thyristors (IGCT), with anti-parallel diodes. The most commonly applied VSC control uses current-regulated real and reactive power control loops with maximum power point tracking (MPPT) for a PV system. Control loops utilizing the Park's transformation to a synchronous reference frame generate D-axis and Q-axis modulation signals to control the VSC switching. In addition, a phase-locked-loop (PLL) tracks the ac system frequency, provides a reference for the Park's transformation, and synchronizes the converter output with the ac system [31], [32].

The two-axis synchronous reference frame-based controller scheme typically consists of an inner current controller and an outer controller loop. The inner-control provides fast regulation of the output current and protects the IGBT devices from excess currents while limiting and balancing fault currents on the ac side. The controller regulates two independent variables, which are the D-axis current and the Q-axis current. Moreover, the controller could have two DQ current regulators, one for positive sequence and the other for negative sequence. A positive sequence-based control scheme with PLL is typically used to control the IBR, a reliable method during steady-state and symmetrical fault conditions. However, the positive sequence scheme is not accurate during unbalanced power and asymmetrical fault conditions. Some vendors apply a DDSRF or similar scheme to provide a negative sequence current regulator. The use of DDSRF provides accurate grid synchronization under unbalanced grid conditions [31], [32]. In this dissertation, the DDSRF algorithm is modified and used for the proposed protective relay. The algorithm and the relay model are discussed in Chapter 3.

IBRs' outer control can actively participate in regulating the voltage by changing the active and reactive power output according to the 2018 revision to the IEEE 1547 standard [19]. The standard suggests specifications and requirements for interconnection of the DER with the BPS, such as reactive power capabilities and voltage-power control requirements and responses to area BPS abnormal conditions. There are five standard control schemes (or modes) to control IBRs' outputs during normal conditions:

- Constant power factor (PF) mode: maintain a constant power factor, often unity
- Voltage-reactive power (volt-var) mode: the reactive power output is a function of POI ac voltage magnitude, as shown in Figure 2.6
- Active power-reactive power (watt-var) mode: the reactive power output is a function of the active power output

- Constant reactive power (Q) mode: maintain constant reactive power
- Voltage-active power (volt-watt) mode: the active power output is a function of voltage

IBRs may have voltage and frequency ride-through capabilities, which allows the IBRs to stay connected and supply fault currents to the grid for a specified time to meet interconnection requirements [19]. However, the fault currents generated by IBRs are primarily dependent on the controllers and generate regulated low fault current magnitudes, which are limited by the ratings of the semiconductor devices [28].

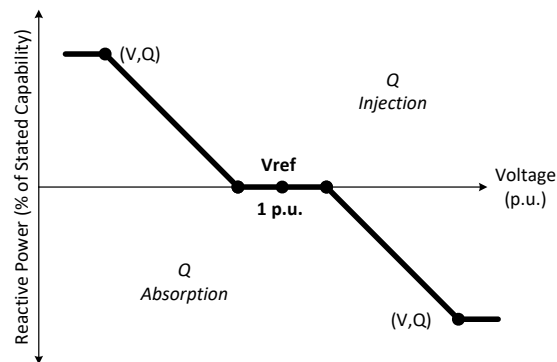


Figure 2.6 An example of a volt-var control characteristic

2.2.2. IBR Protection Challenges

IBRs have different fault current characteristics when compared to the fault current response of synchronous and induction generators. IBRs' unique fault current characteristics pose protection challenges from the grid side protection point of view. The main fault current characteristics of the newly designed IBRs are:

- Low fault current magnitudes around 1.2-1.5 per unit
- Nonlinear behavior relative to fault location and fault type
- High-frequency transient for the first quarter of a power cycle for up to two cycles
- Primarily dependent on IBRs control and independent of fault location
- Predominantly positive-sequence fault currents with insignificant negative-sequence currents [25], [28], [36]–[38]

As noted above, IBRs' controllers are based on the Park's transformation, which generates synchronous reference frame D-axis and Q-axis modulating functions to control the IBR current. This control scheme has a fast response to limit the IBR maximum current, protecting the semiconductor devices. Figure 2.7 compares a simulated IBR fault response to that of a type-1 wind turbine (induction

generator) and synchronous generator during three-phase faults. The IBR regulated the fault current within the first quarter of a cycle providing only the maximum rated current with no dc offset during the fault, as shown in Figure 2.7 (a) and (b). On the other hand, both the induction and the synchronous generators supplied about four per unit fault currents with decaying dc offsets, as shown in Figure 2.7 (c) and (d).

The IBR fault response is similar whether it is operated on constant reactive power or voltage-reactive power since the IBR control aims always to limit the output current. Also, a similar fault current characteristic is observed during different solar irradiation levels, but IBR might have less fault current contribution while operating in constant reactive power with zero real power and zero reactive power (for example a PV system is connected at night). Appendix A shows the IBR fault current during different operating modes and various solar irradiation levels.

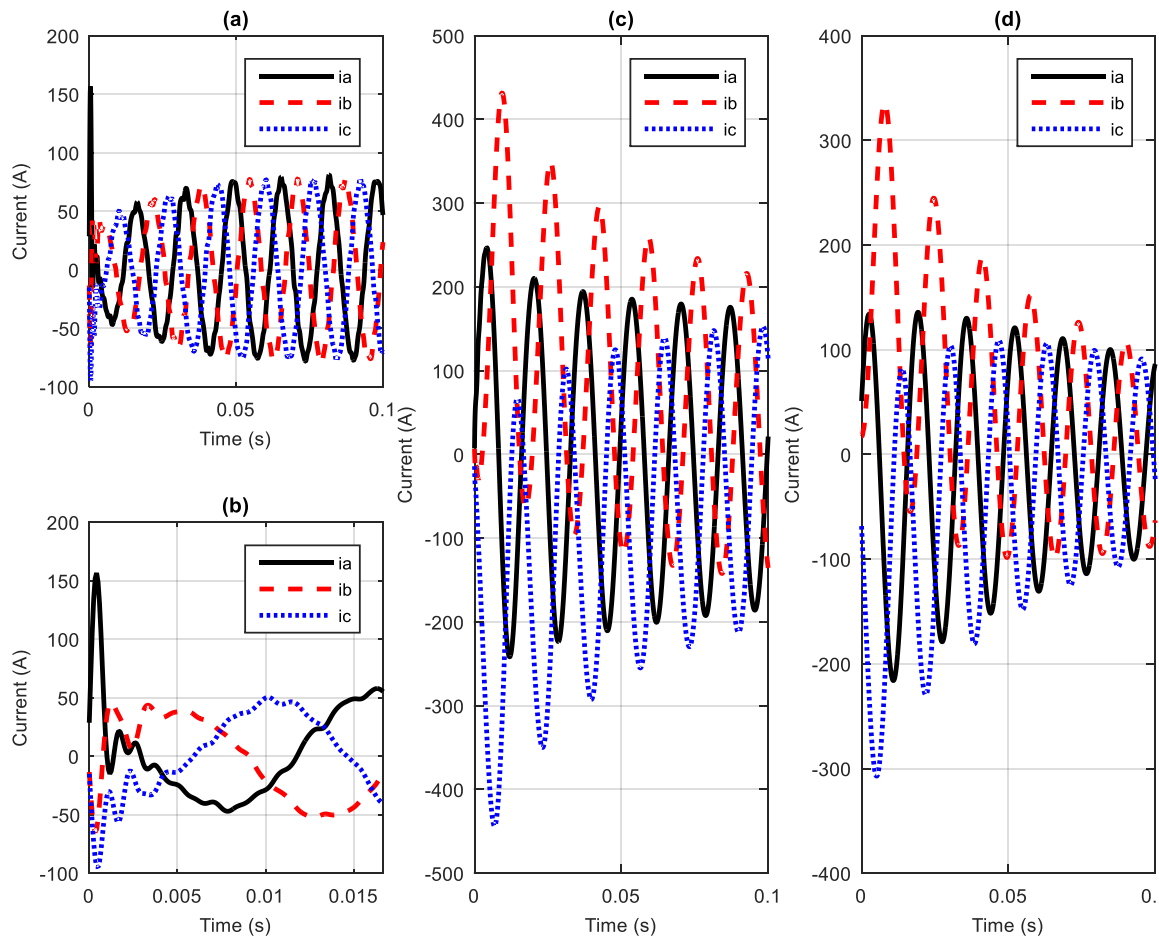


Figure 2.7 Three-phase fault currents mainly supplied by: (a) an IBR, (b) zoom in the IBR (c) type-1 wind turbine, and (d) synchronous generator

Most conventional protection schemes for power distribution systems depend on fault current magnitude using fuses, instantaneous overcurrent (ANSI/IEEE type 50), and ac time overcurrent relays (51) [39], [40]. In some cases, ac directional overcurrent relays (67) are used. The challenge of using the common protection scheme is that there might be no sufficient fault current levels for pick up when IBRs are the main source of fault currents. Therefore, using fault current magnitudes alone can be unreliable for tripping decisions in a distribution system with high IBRs penetration [25], [26].

Moreover, fault clearing time is another factor that should be considered when IBRs are present in microgrids. Unlike synchronous generators, IBRs have no inherent inertia and do not contribute to power system inertia in the large power grid and microgrids. Thus, an increasing percentage of IBRs requires decreasing the critical clearing time to retain stability for severe faults [25], [26].

2.3. Protection Elements

In this dissertation, voltage restrained overcurrent relay (51V) and superimposed quantities-based protection element are modified and used for the proposed protective relay. A voltage restrained overcurrent element can increase the sensitivity and detect faults with low current magnitudes in microgrids, including those from IBRs. Furthermore, superimposed quantities-based protection can be a potential solution to clear faults faster in microgrids to maintain system stability. Finally, superimposed quantities-based protection provides fault direction detection, which is essential for the dynamic changes in the configuration of microgrid systems. The following sections provide background on the two elements.

2.3.1. Voltage Restrained Time Overcurrent Elements

Voltage restrained time overcurrent relays are used for generator backup protection and are also known as ANSI/IEEE type 51V. The voltage restrained time overcurrent element prevents the overcurrent element from operating until the fault reduces the voltage to typically around 80% of the nominal voltage. The pickup current can be a fixed value, or the value can depend upon the voltage magnitude. A typically fixed pickup current is 50% of the rated current. Suppose the pickup current varies linearly with the voltage; the lower the voltage magnitude, the lower the pickup current, as shown in Figure 2.8. The benefit of the 51V element is the ability to operate at currents below the nominal voltage of the maximum load. As a result, fault currents that fall below full load current can be detected [39]–[42].

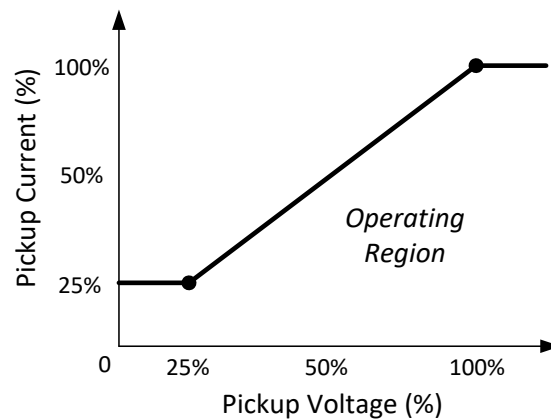


Figure 2.8 An example of a voltage restrained time overcurrent operating characteristic with pickup current varies linearly with voltage

Voltage restrained time overcurrent relays can be used for microgrids with limited fault currents. In addition, voltage restrained time overcurrent relays can have one setting during both grid-interconnected and grid-isolated modes. Since the traditional 51V relay is designed for generator backup protection and is not designed to be connected to multiple feeders, this dissertation develops a more versatile power distribution system and microgrids scheme that allows multiple distribution feeder connections.

2.3.2. Time-Domain Superimposed Protection Element

Unlike phasor-based protection elements, time-domain-based devices do not use discrete Fourier transform (DFT) based filters. The DFT filters cause a maximum delay of a full or a half-power cycle to go from one steady-state level to another. Instead, time-domain-based protection elements are connected after anti-aliasing filters and offer high-speed protection where sub-cycle fault detection is possible. Figure 2.9 shows three common ways to process superimposed current quantities to utilize in protection functions where all three methods use delta filters. A commercial time-domain protection scheme consists of a traveling-wave element and a superimposed, also known as incremental, quantities element. Traveling-wave elements are generated by faults and propagate from the fault location to the line terminals with possible fault detection of one millisecond. The superimposed-quantities elements are fault-generated components of instantaneous voltages and currents, where fault direction can be detected in as little as four milliseconds [43]–[46]. The traveling wave elements are more commonly applied at the transmission level. The proposed element does not require a traveling wave element.

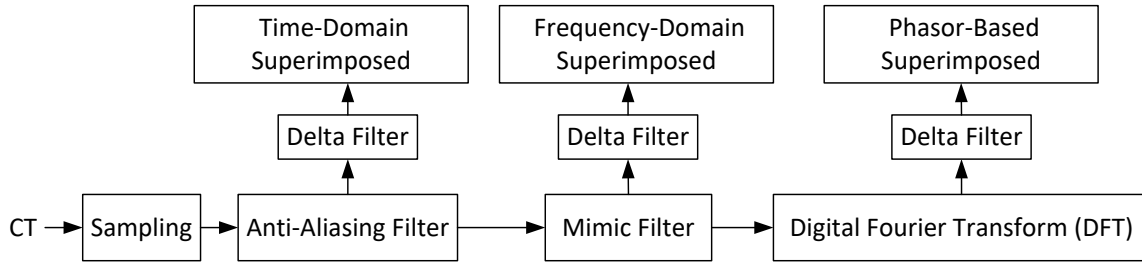


Figure 2.9 Delta filter connection defines superimposed quantities method

An example of implementing superimposed quantities for protection is a high-speed directional element used for line protection. The relays joined together in directional comparison schemes use communications to exchange information on the status of their directional elements and provide fast tripping for in-zone faults, as shown in Figure 2.10.

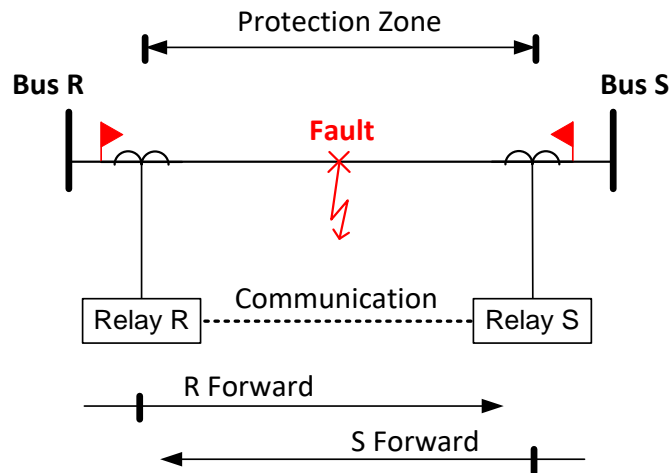


Figure 2.10 An example of using superimposed quantities-based protection in a directional comparison scheme

The superimposed quantities algorithm uses delta filters to subtract delayed memorized quantities from present quantities to find the instantaneous change, or the delta quantities (Δ), of measured data. Figure 2.11 shows voltage and current delta filters with a one-cycle memory buffer for temporarily holding data for one power cycle of samples. Delta filters are applied to the measured voltage and current after anti-aliasing low-pass filters [43]–[46]. During steady-state, the superimposed quantities are zero, ideally. However, during faults, the quantities value equals the fault-imposed component. The difference between the magnitude of each sample represents the incremental change, as shown in Figure 2.12. Also, Figure 2.12 (a) and (b) show the voltage and current waveforms for a single line to ground fault where one-cycle delta quantities are marked.

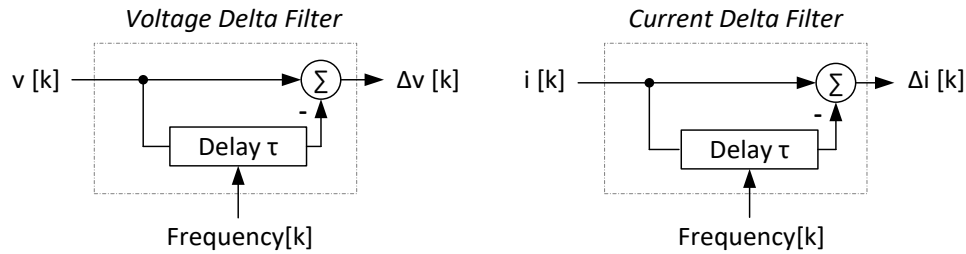


Figure 2.11 Voltage and current delta filters for calculating superimposed quantities

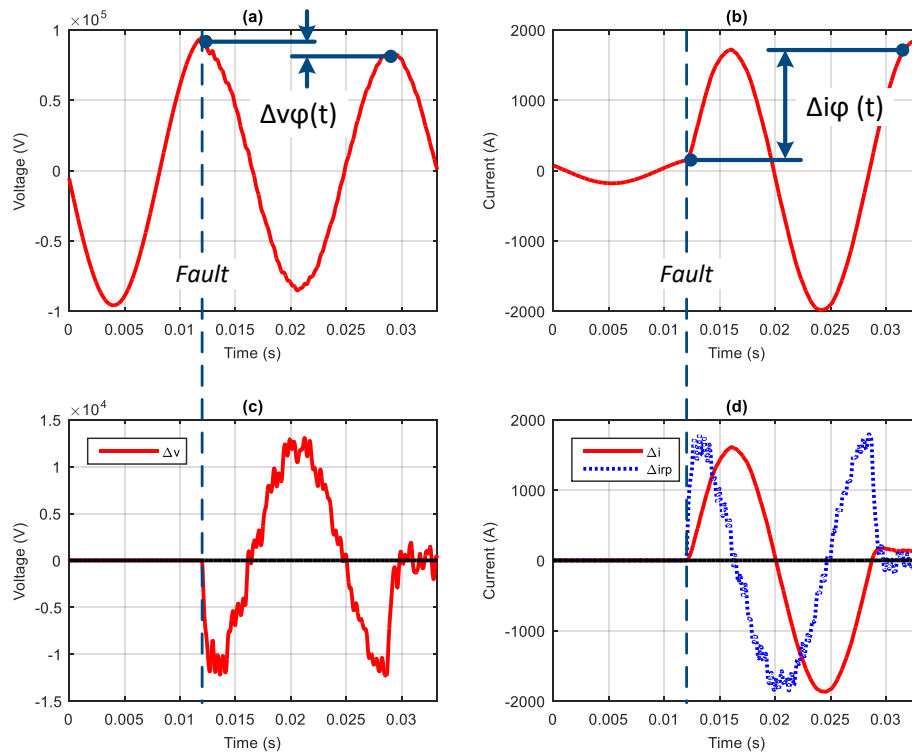


Figure 2.12 Measuring incremental quantities from waveforms during a single line to ground fault: (a) voltage, (b) current (c) delta voltage, and (d) delta current and replica current

Figure 2.12 (c) and (d) show the calculated delta voltage and current during the same single line to ground fault. The superimposed quantities are zero pre-fault and then equal to the incremental change for one power cycle during the fault and then become near zero one cycle later after the transient change has passed. Figure 2.12 (d) also shows delta replica current (Δi_{rp}). The replica current is the delta current compensated by the source's impedance value behind a relay, eliminating the dc offset from propagating to the current quantities and reflecting the actual transient power direction [43]–[46].

The products of per phase delta current and voltage quantities are summed to find the superimposed power quantity. Another option is to use the product of per phase replica current and voltage quantities

to find the replica superimposed power. The polarity of superimposed transient power quantities determines fault direction, where negative power indicates forward faults and positive power indicates reverse faults [43]–[46], as shown in Figure 2.13. The superimposed quantities algorithm as applied in this dissertation, the impact of IBR on the superimposed quantities, and superimposed quantities based on DDSRF are discussed in detail in Chapters 5, 6, and 7.

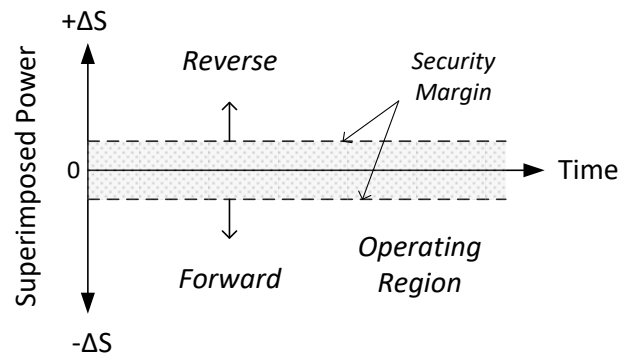


Figure 2.13 Fundamental operating characteristics of incremental directional elements show that negative-power indicates forward faults, and positive-power indicates reverse faults

Commercially available time-domain-based superimposed quantities relays are used for transmission line protection [47]–[50]. In addition, academic researchers investigate the possibility of using superimposed quantities in microgrids with different approaches [51]–[55].

The authors in [51] review several directional elements and highlight the reliability issues of each method. The authors propose a superimposed impedance-based directional element where the positive-sequence impedance is used for symmetrical faults, and the negative-sequence impedance is used for unsymmetrical faults. Although the paper uses superimposed quantities designed like in a commercially available line protection relay, the magnitudes of the quantities are calculated using a half-cycle filter. The filter used on the relay is more likely using a half-cycle window Fourier system combined with a mimic filter. Thus, the scheme is represented on the phasor-domain only, and the half-cycle filter introduces a delay. Also, mimic filters are impacted by the presence of IBR during faults, as will be demonstrated later.

The authors in [52] propose two fault type classification methods that partly use superimposed voltage quantities. The method determines the system imbalance ratio using instantaneous superimposed positive, negative, and zero-sequence quantities to detect faults. In [53], the authors use a Hilbert transform superimposed quantities-based directional element. In [54], the authors use a superimposed energy based directional element. The authors in [55] use phasor positive and negative

current sequence superimposed quantities to find fault direction and use communication between a microgrid control system and protection system.

Although [51]–[55] propose adequate primary and backup microgrid protection schemes that use superimposed quantities, investigating superimposed quantities' effectiveness with IBRs present as the main source of fault current lies outside these papers' scope. This dissertation proposes a time-domain-based superimposed quantities directional element for microgrids with IBRs, and the impact of IBRs on superimposed quantities is investigated. The proposed scheme provides a novel high-speed sub-cycle directional element that functions during grid-interconnected and grid-isolated modes.

Chapter 3: Modeling and Validation

This chapter discusses the EMTP-RV modeling and model validation aspects. First, the EMTP-RV simulation software is used to model the IBR, the power system, and the proposed protective relay [56]. Then, the models are validated using analytical calculations or using ATP-EMTP simulation software. The time-step (Δt) chosen for the EMTP-RV time-domain simulation is 8.3 microseconds.

3.1. Modified IEEE 34-Bus Model

The IEEE 34-bus system was initially created in 1992 and was later approved by the Distribution System Analysis Subcommittee during the 2000 Power and Energy Society Summer Meeting to evaluate and benchmark algorithms developed for unbalanced three-phase radial distribution systems. The IEEE 34-bus system is based on an actual feeder that was in Arizona, with a nominal voltage of 24.9 kV, as shown in Figure 3.1. It is characterized by long and lightly loaded overhead lines, two in-line regulators, an in-line transformer for a short 4.16 kV section, unbalanced loading, and shunt capacitors [57]–[59]. Table 3.1 provides the short circuit data for the system beyond node 800 used in this study.

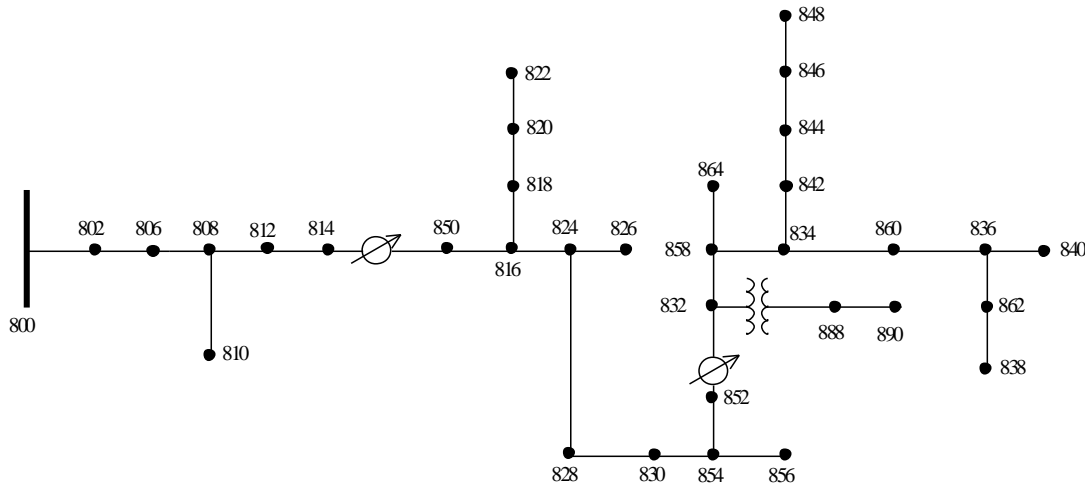


Figure 3.1 IEEE 34-bus system

Table 3.1 IEEE 34-bus system short circuit source data upstream of node 800

Name	Description	Value	Unit
V_{LL}	RMS line to line voltage	69	kV
MVA_3	Three-phase short circuit MVA	$75.558 + j 192.9996$	MVA
MVA_0	Single-phase short circuit MVA	$56.981 + j 139.6973$	MVA

Z_1	Positive sequence impedance	$8.3741 + j 21.3901$	Ω
Z_2	Negative sequence impedance	$8.3741 + j 21.3901$	Ω
Z_0	Zero sequence impedance	$19.0068 + j 44.8784$	Ω

The modified version of the IEEE 34-bus system modeled in EMTP-RV in this dissertation assumes all loads are RL load models and ignores voltage regulation devices. The goal of using the IEEE 34-bus model is to conduct fault analysis and to form a microgrid system. Therefore, the voltage error in validating the model at each node does not exceed five percent, and the fault currents for all fault types do not exceed seven percent. Table 3.2 and Table 3.3 show the percentage of error at some nodes from the voltage validation test, Appendix B provides more validation results. Thus, it was concluded that the model is valid for this study.

Table 3.2 The percentage of error of the modified IEEE 34-bus EMTP-RV model when compared to IEEE data in terms of voltage magnitude and the angle at selected nodes

Node	V_{a_mag}	V_{a_ang}	V_{b_mag}	V_{b_ang}	V_{c_mag}	V_{c_ang}
800	0.0	0.0	0.5	0.1	0.9	0.1
802	0.1	0.0	0.5	0.1	0.9	0.1
806	0.1	0.0	0.5	0.1	1.0	0.1
808	1.0	0.1	0.7	0.3	1.7	0.0
810	0.7	0.1	0.0	0.0	0.0	0.0
812	2.2	0.2	0.8	0.5	2.6	0.1
814	3.1	0.2	1.0	0.6	3.4	0.2
850	0.1	0.2	0.1	0.6	0.5	0.2
816	0.1	0.2	0.1	0.6	0.5	0.2
818	3.7	2.7	0.0	0.0	0.0	0.0
820	3.9	2.7	0.0	0.0	0.0	0.0
822	3.9	2.7	0.0	0.0	0.0	0.0
824	0.3	0.2	0.1	0.6	0.3	0.2
826	0.1	0.3	0.0	0.0	0.0	0.0
828	0.3	0.2	0.1	0.6	0.3	0.2
830	0.7	0.3	0.1	0.7	0.1	0.2

Table 3.3 The percentage of error of the modified IEEE 34-bus EMTP-RV model, when compared to IEEE data, in terms of fault currents at node 800

Node 800	L-G	A-B	A-B-G	A-C	A-C-G	B-C	B-C-G	A-B-C
Ph-A Max	7	7	6	6	7	0	0	7
Ph-A Min	3	4	4	4	4	0	0	3
Ph-B Max	7	7	7	0	0	6	7	7
Ph-B Min	3	4	4	0	0	4	4	3
Ph-C Max	6	0	0	6	6	6	7	6
Ph-C Min	3	0	0	4	4	4	4	3

In addition, the IEEE 34-bus is modified to have a PCC that can connect and disconnect the IEEE 34-bus system from the BPS. Also, two distributed energy resources are added to the system to supply loads during both grid-interconnected and grid-isolated modes. An IBR is connected at node 848 and a synchronous generator is connected at node 800. Finally, the proposed relay and protection scheme is placed in three locations, as shown in Figure 3.2.

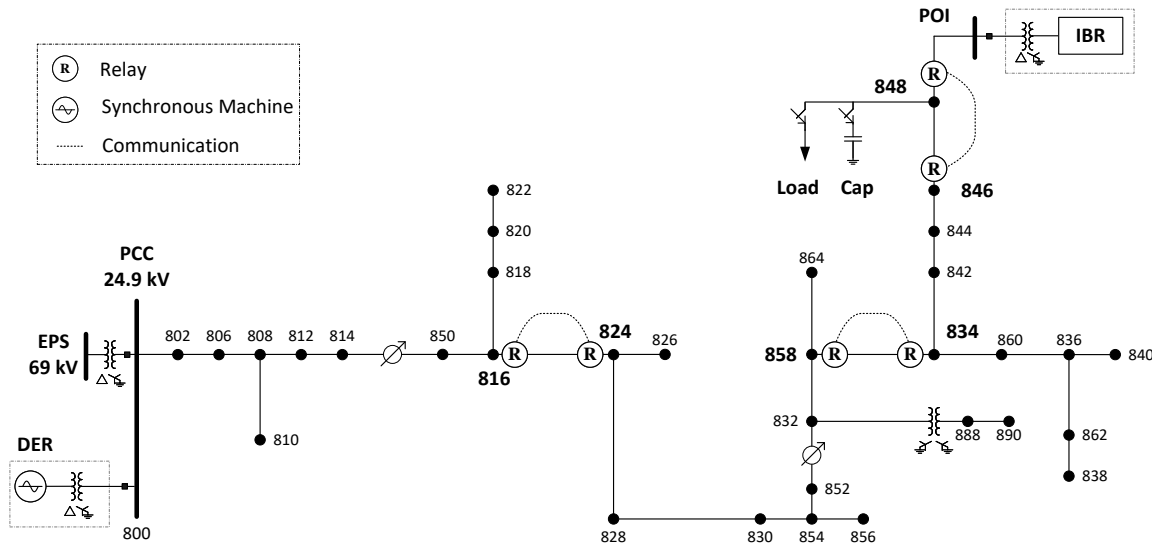


Figure 3.2 A modified IEEE 34-bus system with IBR and locations for protection studies

The synchronous generator used is rated at 2.2 MVA. The governor model is based on Woodward diesel governor DEGOV1, and the exciter model is based on IEEE type ST2A. Table 3.4 shows the mechanical and electrical data of the synchronous generator model, and Table 3.5 shows the step-up transformer model data. Appendix B provides selected validation results for the EMTP-RV generator model. The IBR and the proposed relay are discussed in the next section.

Table 3.4 Synchronous generator parameters

Name	Description	Value	Unit
V_{LL}	Rated RMS line to line voltage (grounded Y)	0.48	kV
MVA	Rated power	2.2	MVA
f	Frequency	60	Hz
p	Number of poles	4	
H	Inertia constant	4	sec
R_a	Armature resistance	0.0184	pu
X_l	Armature leakage reactance	0.189	pu
X_0	Zero-sequence reactance	0.087	pu
X_d	d-axis steady-state reactance	1.5	pu
X_q	q-axis steady-state reactance	1.1278	pu
X_d'	d-axis transient reactance	0.32	pu
X_d''	d-axis subtransient reactance	0.23	pu
X_q'	q-axis transient reactance	1.1277	pu
X_q''	q-axis subtransient reactance	0.23	pu
T_{d0}'	d-axis open circuit transient time constant	3.5	sec
T_{d0}''	d-axis subtransient open circuit time constant	0.05	sec
T_{q0}'	q-axis transient open-circuit time constant	5	sec
T_{q0}''	q-axis sub-transient open-circuit time constant	0.05	sec

Table 3.5 Generator transformer data

Name	Description	Value	Unit
V_P	Primary RMS line to line voltage (Δ)	0.48	kV
V_S	Secondary RMS line to line voltage (grounded Y)	24.9	kV
MVA	Rated apparent power	2.2	MVA
f	Rated frequency	60	Hz
R_{xfmr}	Total winding resistance	0	pu
X_{xfmr}	Total winding leakage reactance	0.06	pu

3.2. IBR Model

The main components of the EMTP-RV IBR model are the PV panels, the VSC, the ac side filters, and the VSC control. Figure 3.3 shows an overall diagram of the IBR model. First, the PV model is connected to the dc bus with a shunt capacitor. Then, the VSC is connected between the ac and dc sides.

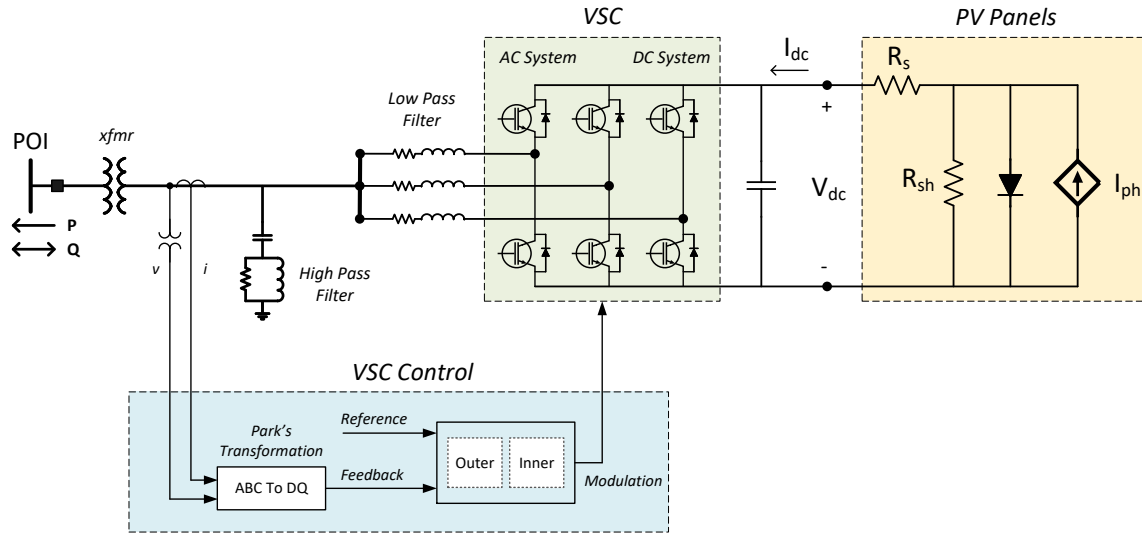


Figure 3.3 An overall diagram of the IBR model including the PV panels, the VSC, the control, and the ac filters

3.2.1. Photovoltaic panel model

The PV cell model is based on the nonlinear current-voltage (I-V) characteristics equation given in equation (3.1)

$$I = I_{ph} - I_0 \left(e^{\left(\frac{V+I R_s}{a k T/q} \right)} - 1 \right) - \left(\frac{V+I R_s}{R_{sh}} \right) \quad (3.1)$$

where I_{ph} represents the photocurrent induced by the solar irradiation, I_0 is the diode reverse saturation current, R_s is the sum of cell resistance, and R_{sh} represents the leakage effect of the cell semiconductor material. Table 3.6 shows the PV model data.

Table 3.6 PV model parameters

Name	Description	Value	Unit
V_{max}	Maximum power voltage	26.3	V
I_{max}	Maximum power current	7.61	A
V_{oc}	Open circuit voltage	32.9	V
I_{sc}	Short circuit current	8.21	A

K_i	Temperature coefficient short circuit	0.00318	A/°C
K_v	Temperature coefficient open circuit	- 0.123	V/°C
N_{cs}	Number of cells in series per module	54	
a	Ideal factor	0.95	
k	Boltzmann constant	$1.3806503 \times 10^{-23}$	J/K
q	The magnitude of an electron charge	1.602176×10^{-19}	C

By using the information from Table 3.6 and equation (3.1), the nonlinear current-voltage (I-V) and power-voltage (P-V) characteristics can be plotted as shown in Figure 3.4, assuming the solar radiation at 1000 W/m^2 . References [60]–[62] discuss PV systems modeling and simulation using this mathematical approach. Moreover, Appendix B provides the EMTP-RV diodes and model code for the PV system.

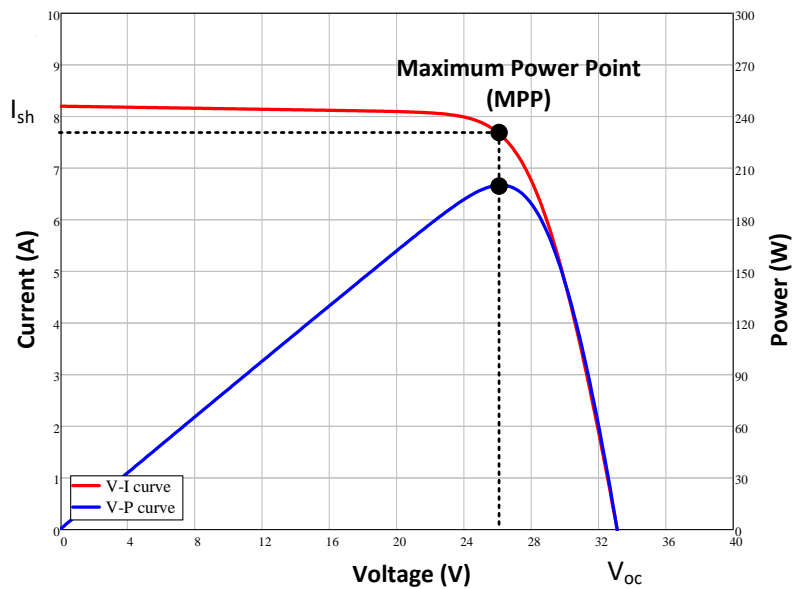


Figure 3.4 Photovoltaic model I-V and P-V characteristics with MPP marked

3.2.2. Voltage source converter model

A switching-based three-phase two-level VSC model is connected between the ac and dc systems, as shown in Figure 3.5. The three-phase switched VSC model consists of fully controllable bidirectional switches with unilateral voltage blocking, including power system dynamic and high-frequency behavior [63]. The VSC control model is based on current-regulated real and reactive power control loops to track the maximum power-point, as shown in Figure 3.6.

The controller uses Park's transformations to generate variables in the two-axis synchronous rotating frame, with a direct axis and a quadrature axis, and a PLL generates the phase angle θ_r for synchronization. In the outer control loops, dc voltage V_{dc_ref} or a real power P_{ref} references are used to generate the D-axis reference current, I_{dref} . Also, an ac voltage V_{ac_ref} or a reactive power Q_{ref} references are used to generate the Q-axis reference current, I_{qref} . The outputs of the outer control are the D-axis and Q-axis reference currents. The inner control loops compare the D-axis and Q-axis measured currents I_d and I_q to the generated I_{dref} and I_{qref} . The D-axis and Q-axis measured voltages V_d and V_q are used for voltage feed-forward compensation [31], [32].

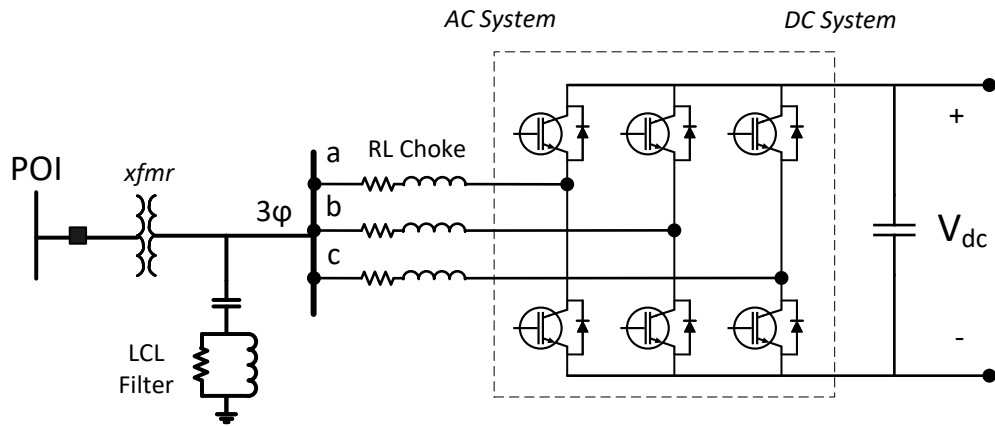


Figure 3.5 A three-phase two-level VSC with insulated-gate bipolar transistors switching devices

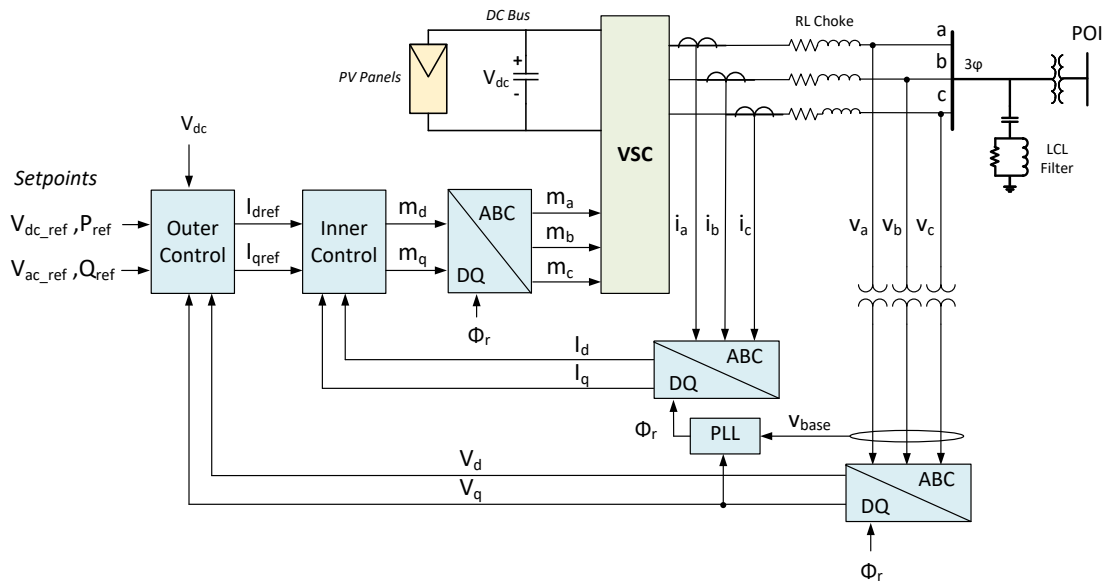


Figure 3.6 Schematic diagram of a current-controlled real and reactive power controller

The Park's transformation converts the stationary reference frame three phase ABC quantities to two-axis synchronously rotating reference frame DQ quantities. The transformation is used for voltages, currents, and the inverse transformation is used for modulation signals. Equation (3.2) shows that Park's transformation equations to convert the measured three-phase ABC voltages to DQ0 voltages. The currents use the same set of equations by substituting the line to ground voltages with the line currents [31], [32]. The 0-axis terms are not needed in the system modeled in this work since the controller uses only DQ components to control the VSC current.

$$\begin{bmatrix} V_d \\ V_q \\ V_0 \end{bmatrix} = \sqrt{\frac{2}{3}} \begin{bmatrix} \cos(\theta_r) & \cos(\theta_r - \frac{2\pi}{3}) & \cos(\theta_r + \frac{2\pi}{3}) \\ -\sin(\theta_r) & -\sin(\theta_r - \frac{2\pi}{3}) & -\sin(\theta_r + \frac{2\pi}{3}) \\ \frac{1}{\sqrt{2}} & \frac{1}{\sqrt{2}} & \frac{1}{\sqrt{2}} \end{bmatrix} \begin{bmatrix} v_a \\ v_b \\ v_c \end{bmatrix} \quad (3.2)$$

Where:

v_a : Phase A, the line to ground voltage

v_b : Phase B, the line to ground voltage

v_c : Phase C, the line to ground voltage

V_d : The direct axis measured voltage

V_q : The quadrature axis measured voltage

V_0 : The zero-axis voltage

θ_r : The phase angle from the PLL

The DQ quantities can be used to calculate the real and reactive power from measured voltages and currents as in equation (3.3) for real power and equation (3.4) for reactive power. In addition, these calculations can be used to check the outputs from the PV model compared to the inputs.

$$P_{0dq} = \frac{3}{2} (V_0 I_0 + V_d I_d + V_q I_q) \quad (3.3)$$

$$Q_{0dq} = \frac{3}{2} (V_d I_d - V_q I_q) \quad (3.4)$$

Where:

I_0 : The zero-sequence current

I_d : The direct axis measured current

I_q : The quadrature axis measured current

P_{0dq} : Real power calculated in the direct axis frame

Q_{0dq} : Reactive power calculated in the direct axis frame

The PLL is essential for tracking the ac frequency and for synchronizing the VSC output with the grid. The PLL model generates θ_r by tracking the voltage at the point of interconnect during all conditions, including transients and oscillations [31], [32]. V_q from the Parks's transformation is the input of the PLL and θ_r is the output, as shown in Figure 3.7. Then, θ_r is connected to the DQ transformation to close the loop. The notations ω_{ref} for the ac system is $2\pi \cdot 60\text{Hz}$. The PLL model has dynamic maximum and minimum limiters based on the measured frequency (fm) at the POI, $\omega_{max} = (1.25 * 2\pi * fm)$ radians per second, and $\omega_{min} = (0.75 * 2\pi * fm)$ radians per second.

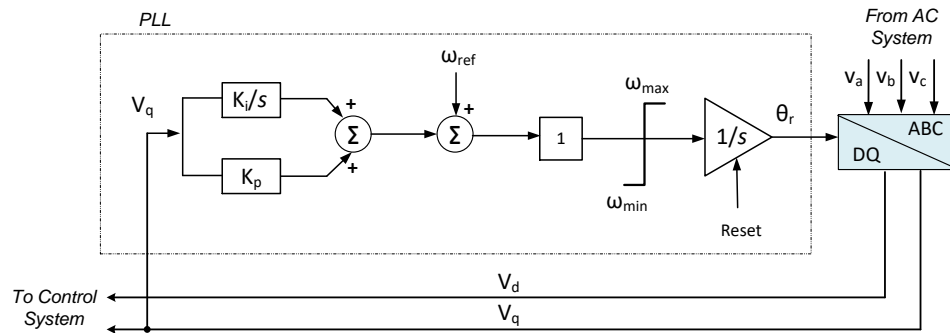


Figure 3.7 PLL block diagram

Figure 3.8 shows both the inner and outer controls for outer controls based on real and reactive power references. First, the outer controllers generate the I_{dref} and I_{qref} according to the real and reactive power reference setpoints, respectively. Then, the inner controller generates the m_d and m_q . In addition, the controller has voltage feed-forward and current decoupling compensators to avoid an undesirable response to transients to large voltage change and to decoupling D and Q axes response of the VSC from the ac system coupling dynamics.

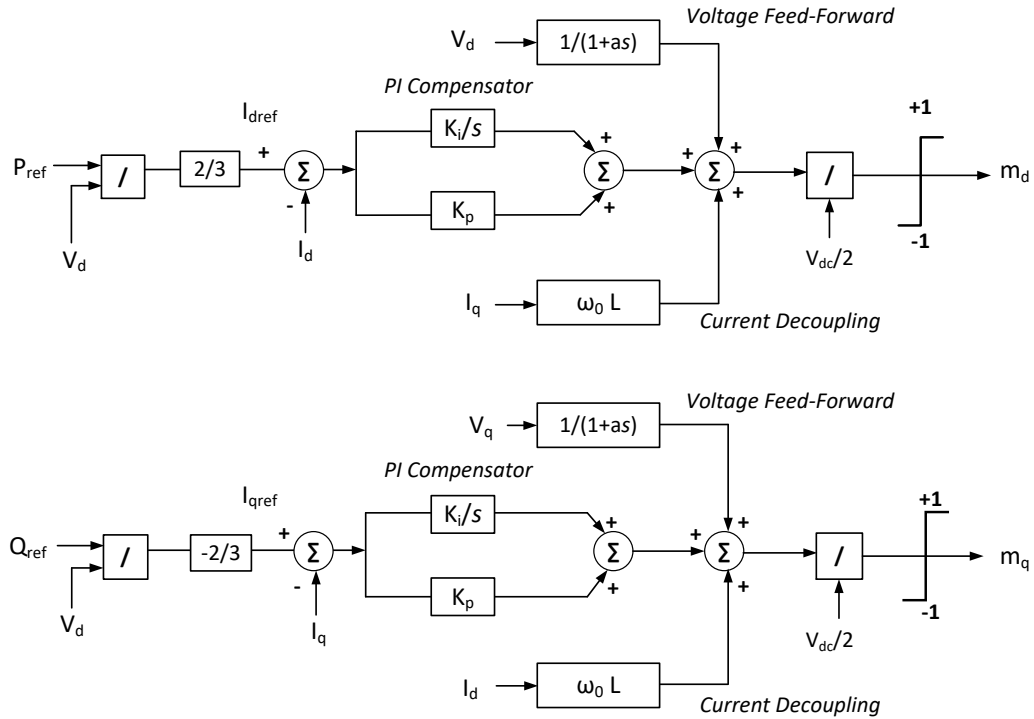


Figure 3.8 Inner and outer controller block diagrams with real and reactive power setpoints

In this PV inverter case, the outer control model has a dc bus voltage regulator to implement MPPT the PV panel, which calculates the maximum real power setpoints; the outer control model is shown in Figure B.10, Appendix B. The model also has the voltage-reactive power (volt-var) mode capability to regulate the VSC terminal ac voltage. References [31], [32] discuss VSC modeling in detail. Additionally, Appendix B provides the EMTP-RV code and control block diagrams for the VSC model. Table 3.7 and Table 3.8 provide the VSC electrical and control parameters.

Table 3.7 VSC electrical parameters

Name	Description	Value	Unit
P_{pv}	Maximum power input from solar arrays	2	MW
S_{vsc}	VSC rating apparent power	2.2	MVA
V_{grid}	Grid nominal RMS line to line voltage	24.9	kV
V_{pv}	VSC nominal RMS line to line ac voltage	0.575	kV
V_{dc}	VSC nominal dc voltage	1.264	kV
f_{sys}	Nominal AC system frequency	60	Hz
X_{xfmr}	Power transformer leakage inductance	0.06	pu
R_{xfmr}	Power transformer winding resistance	0.001	pu

L_{choke}	Choke inductance	0.15	pu
R_{choke}	Choke resistance	0.0015	pu
C_{dc}	DC capacitor	2780	μF
f_{sw}	Pulse width modulation (PWM) carrier signal frequency	3	kHz
R_{snub}	IGBT/diode resistance snubber	3	k Ω
C_{snub}	IGBT/diode capacitor snubber	1	μF

Table 3.8 VSC control parameters in a per unit based VSC rated voltage and MVA

Name	Description	Value	Unit
K_{i_PLL}	Integral gain or the PLL	90000	pu
K_{p_PLL}	Proportional gain for the PLL	80	pu
K_{i_inner}	Integral gain for the inner control	35.8	pu
K_{p_inner}	Proportional gain for the inner control	1.2	pu
K_{i_dc}	Integral gain for the outer dc voltage control	40.8	pu
K_{p_dc}	Proportional gain for the outer dc voltage control	1.3	pu
K_{i_ac}	Integral gain for the outer ac voltage control	102	pu
K_{p_ac}	Proportional gain for the outer ac voltage control	1	pu

To validate the EMTP-RV model, a simple VSC model is built in ATP-EMTP. The ATP model does not have a full PV and control model. Instead, the ATP model has an ideal DC source to represent the PV system with only an inner control system to regulate the output current. Then, the EMTP-RV model is compared to the simplified ATP model. The validation procedures include varying real power to test the controller tracking capability, applying symmetrical and unsymmetrical faults, comparing the switching model to an averaged non-switching model, adding high pass filters, and changing transformer configuration.

The switching model is tested and compared to the averaged model during fault and non-fault events, and impacts of adding an ac high pass filter are simulated. Also, different transformer configurations are tested (Y-grounded/delta and delta/Y-grounded). The results show that changing the transformer configuration does not significantly impact the fault current supplied by the VSC during three-phase faults and line-to-line faults. However, the high pass filter may marginally increase the overshoot during faults. Furthermore, the fault current supplied by the VSC during single-line-to-

ground and double-line-to-ground is different. This is because the transformer provides a zero-sequence current path when the transformer is delta connected on the VSC side and Y-grounded on the grid side.

In general, the results show that the EMTP-RV model is valid for power system studies and shows similar results. Meanwhile, the EMTP-RV provides more accurate results than the simplified ATP model since it has complete control and a PV model. Therefore, the IBR model, including the VSC switching model, is valid for this study. Appendix B provides selected results from the validation tests.

3.3. Model of the Proposed Protection Scheme

This section discusses the modeling aspect of the proposed protective relay only. Whereas chapter 7 provides the complete derivation of the proposed protection scheme along with simulation results evaluating the performance of the scheme. The relay is modeled inside EMTP-RV and verified analytically using a combination of MATLAB and MathCAD. As discussed earlier, the proposed relay has two main elements; the phasor-based versatile voltage restrained overcurrent element and the time domain DDSRF-based superimposed quantities directional element, as shown in Figure 3.9. The relay analog variables are defined in Table 3.9.

Table 3.9 Relay analog variables

Name	Description
$i_{3\phi}(t)$	Three-phase measured currents after low-pass filters (sampled at simulation time step, which is 8.3 microseconds)
$v_{3\phi}(t)$	Three-phase measured voltages after low-pass filters
$i_{3\phi}[k]$	Three-phase measured currents sampled at 64 samples per cycle (spc)
$v_{3\phi}[k]$	Three-phase measured voltages sampled at 64 spc
$i_{3\phi}[n]$	Three-phase measured currents sampled at 16 spc
$v_{3\phi}[n]$	Three-phase measured voltages sampled at 16 spc
$i_{3\phi f}[n]$	Sampled three-phase currents after the full-cycle DFT filter
$v_{3\phi f}[n]$	Sampled three-phase voltages after the full-cycle DFT filter

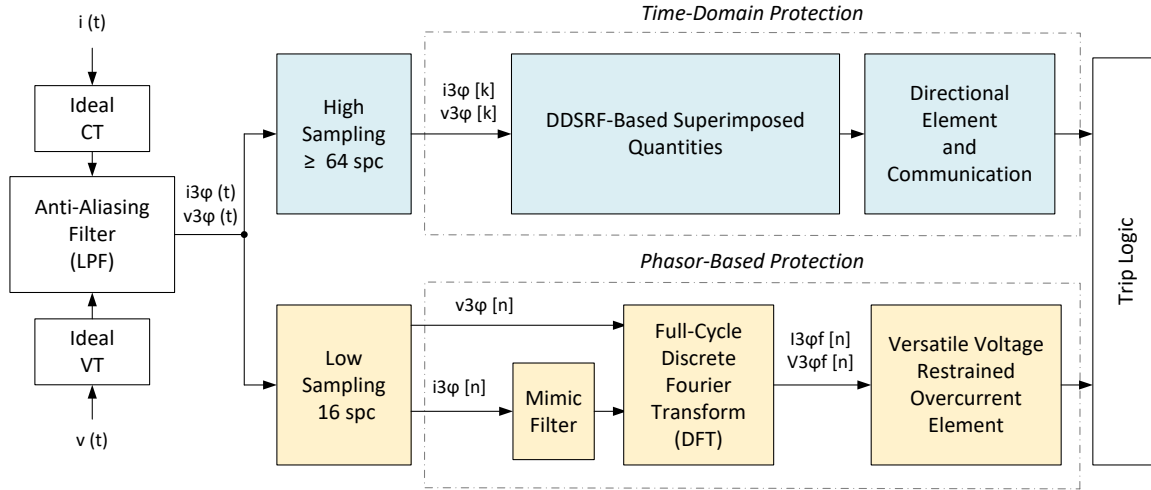


Figure 3.9 Signal processing for the proposed protective relay

3.3.1. Signal processing

The two protection elements have separate signal processing and digital filters. Figure 3.9 shows a simplified block diagram of the EMTP-RV signal processing model. The time-domain superimposed quantities-based protection model requires:

- Anti-aliasing filter with a corner frequency of 480 Hz
- Sampled at the simulation time step

The phasor-based protection model requires:

- Anti-aliasing filter with a corner frequency of 480 Hz
- A digital resampling function at 16 spc or higher
- Mimic filter for current waveforms
- Full-cycle DFT filter

The signals are obtained from the bus or node where a relay is connected. An ideal current transformer (CT) and an ideal voltage transformer (VT) are assumed in this study. A per-phase anti-aliasing filter, simply a second-order low-pass filter, is used for both current and voltage. Equation (3.5) shows the low-pass filter transfer function in Laplace domain for the 16 spc sampling rate.

$$H_{LPF} = \frac{1}{1.099 \times 10^{-7} s^2 + 4.737 \times 10^{-4} s} \quad (3.5)$$

The low-pass filter is modeled with a cutoff frequency at half the sampling frequency for a 60 Hz system, as shown in Figure 3.10. The designed low-pass filter introduces a delay of less than one millisecond, as shown in Figure 3.11. Appendix B provides the MATLAB code for the low-pass filter

design. Finally, an example comparing the low-pass filter result to the original waveform from the EMTP-RV is shown in Figure 3.12.

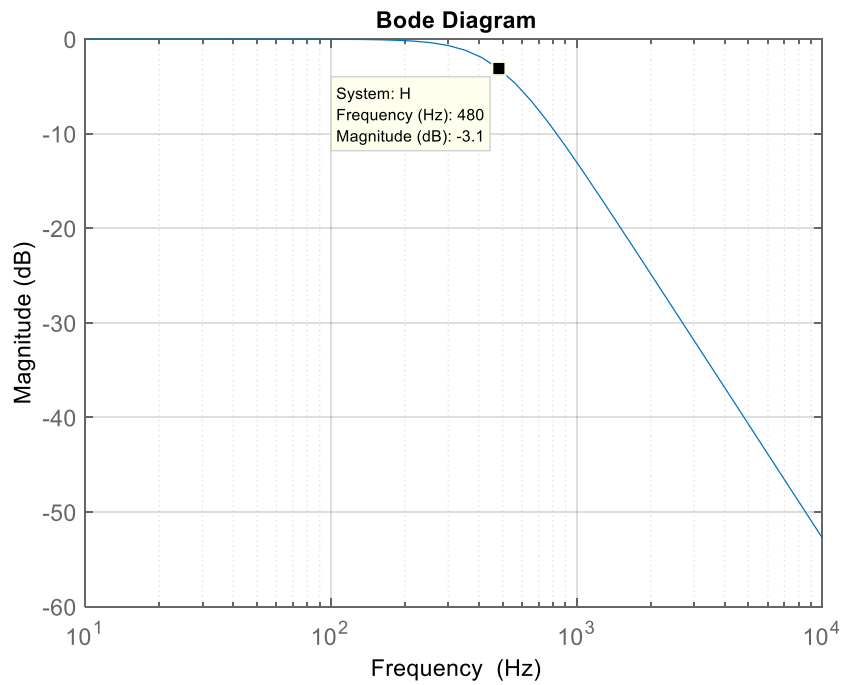


Figure 3.10 Frequency response of the low-pass filter with a cutoff frequency at half the sampling frequency

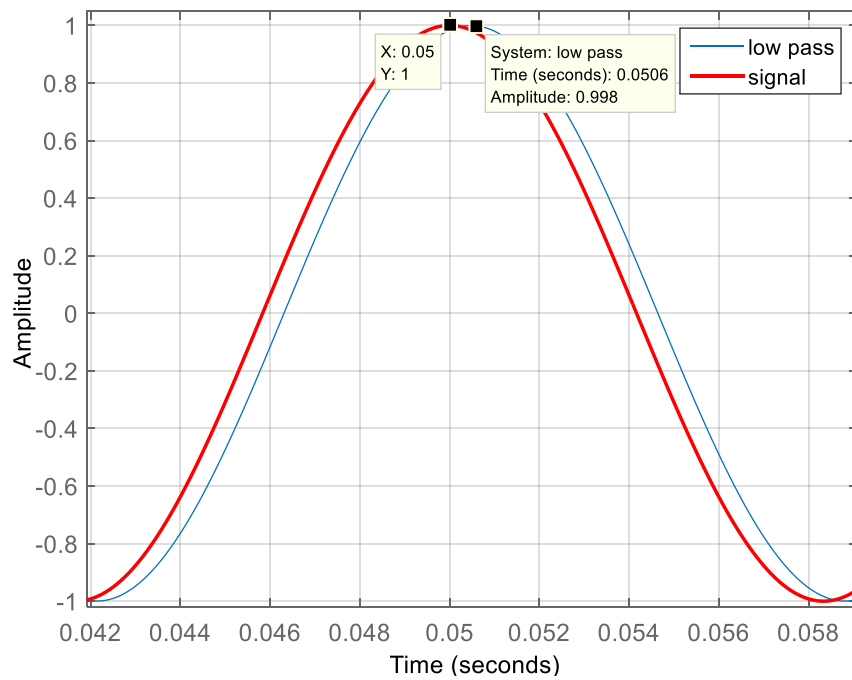


Figure 3.11 The designed low-pass filter introduces a delay of less than one millisecond

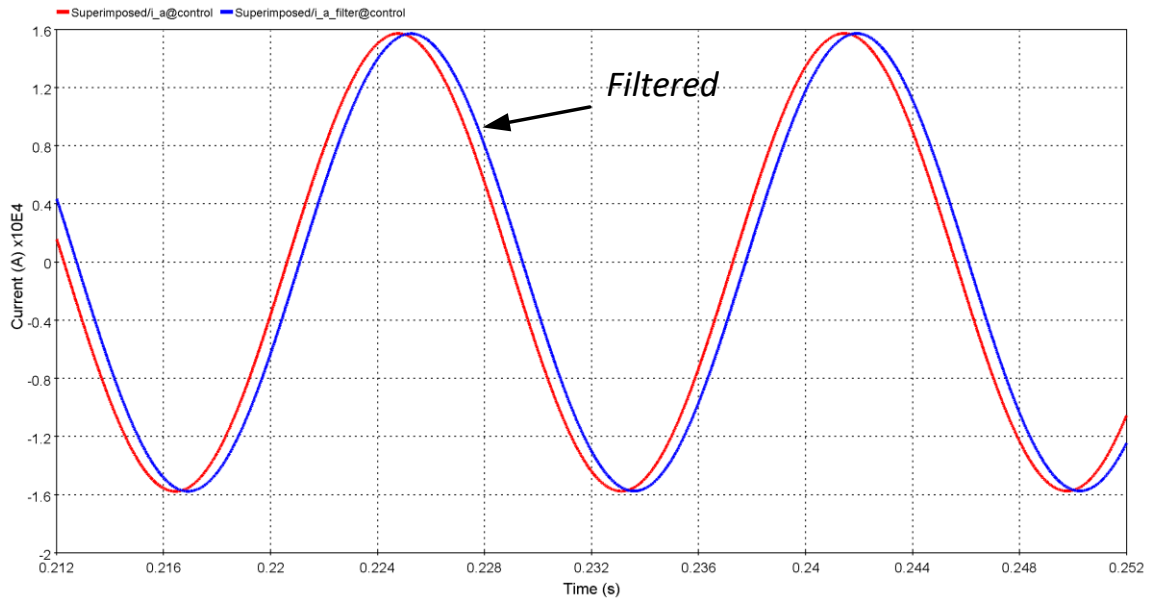


Figure 3.12 An example from the EMTP-RV comparing the low-pass filter model output with the original waveform

The three-phase voltages and currents are sampled at the simulation time step for the time-domain superimposed quantities-based element and 16 spc for the phasor-based element.

On the other hand, the 16 spc sampling is used for the phasor-based element since that is a common sampling rate in commercial distribution relays. Figure 3.13 shows an example of the EMTP-RV model sampling at the 16 spc rate.

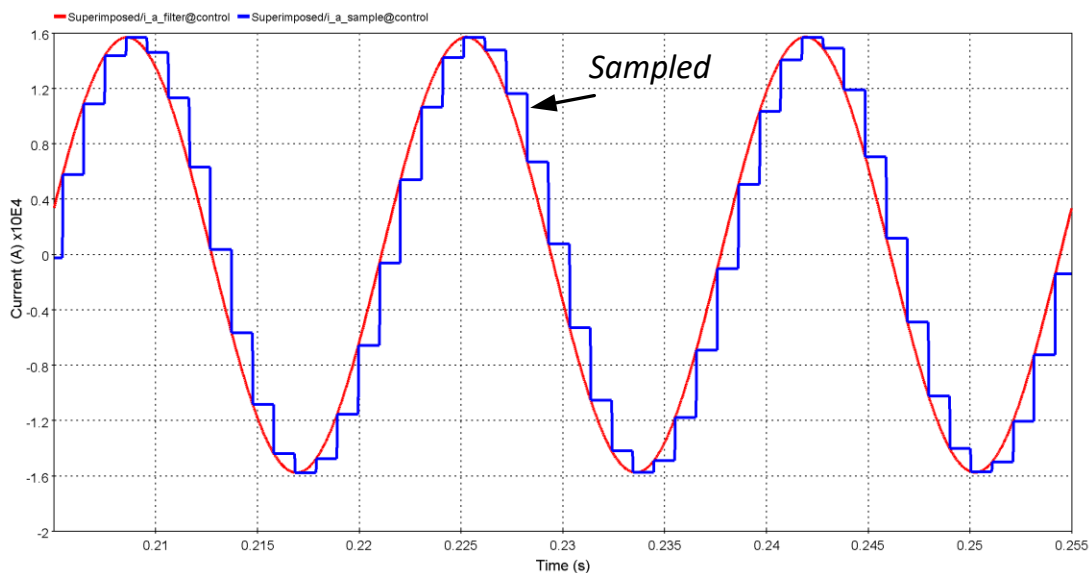


Figure 3.13 An example of the EMTP-RV sampling at 16 spc

Currents in the phasor-based element are filtered using mimic filters to remove decaying dc offset from the signal since the DFT filter is based on full-cycle cosine and sine filters. Equation (3.6) shows the mimic filter transfer function in Z-transform form.

$$H_{mimic} = K (1 + \tau_s) - \tau_s z^{-1} \quad (3.6)$$

where

$$K = \frac{1}{\sqrt{\left[(1+\tau_s) - \tau_s \cos\left(\frac{\omega}{f_s}\right) \right]^2 + \left[\tau_s \sin\left(\frac{\omega}{f_s}\right) \right]^2}} \quad (3.7)$$

τ_s : The number of samples, which is 16 spc in this model

f_s : The sampling frequency

ω : The angular frequency for a 60 Hz power system

The mimic filter is designed as a high-pass filter with a time constant of 2 cycles for the 60 Hz system, as shown in Figure 3.14. The designed mimic filter introduces approximately two milliseconds of delay, as shown in Figure 3.15. Appendix B provides the MATLAB code for the mimic filter design. Finally, an example of the mimic filter result from the EMTP-RV model is shown in Figure 3.16. The mimic filter is applied to both voltage and current signals in the model, so both signals have the same time delay, and the samples are aligned.

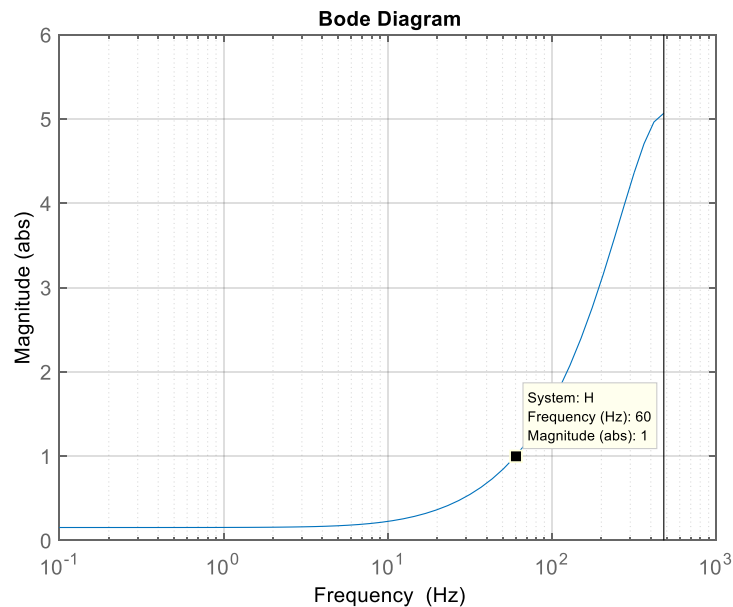


Figure 3.14 Frequency response of the mimic filter with a time constant of two power cycles

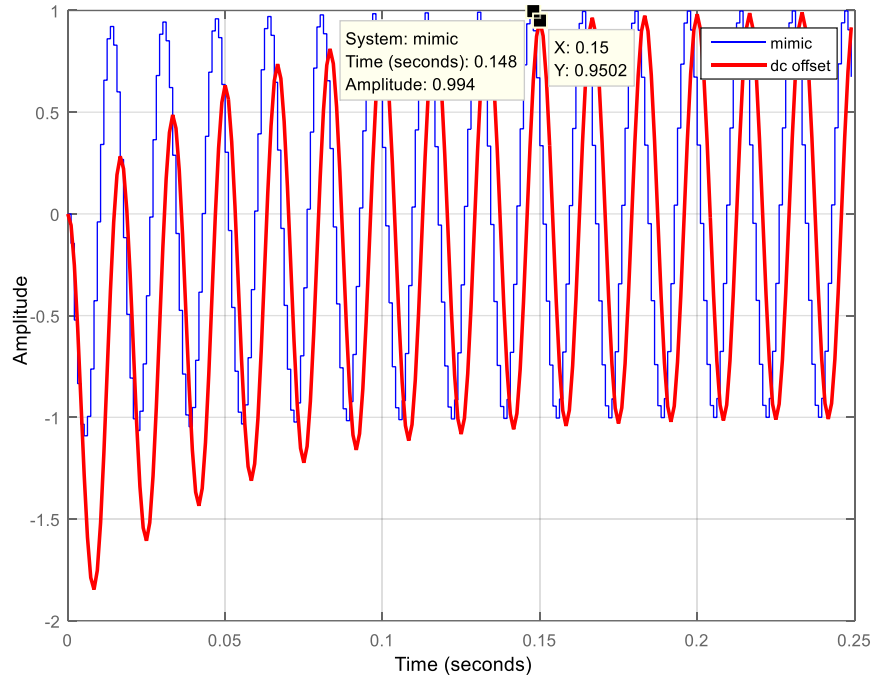


Figure 3.15 The modeled mimic filter introduces a delay of two milliseconds

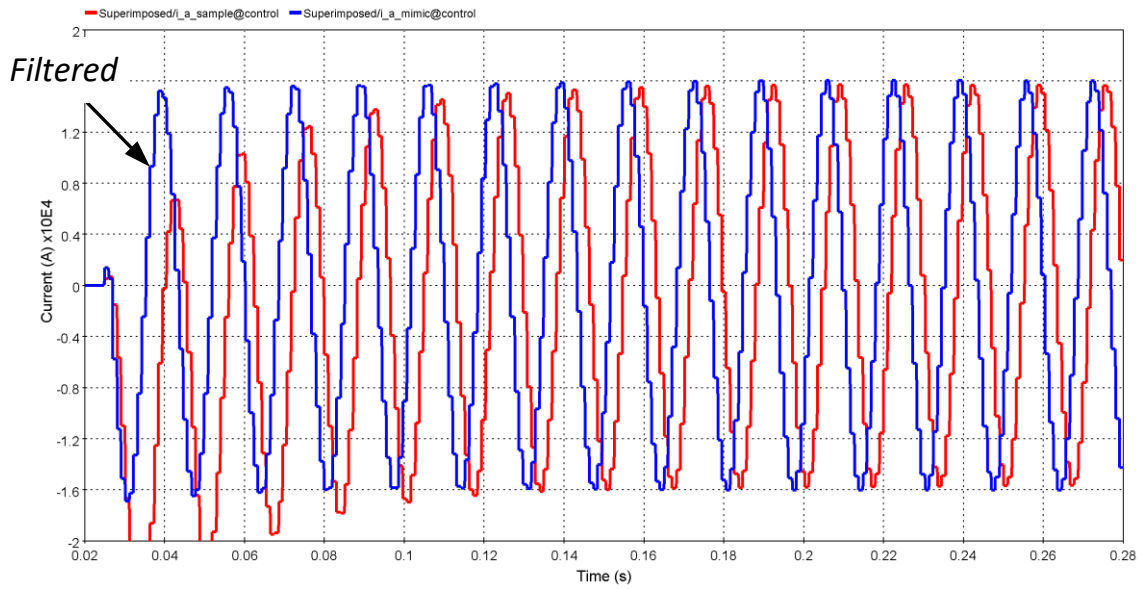


Figure 3.16 The modeled mimic filter in EMTF-RV removed decaying dc offset from the signal

The DFT filter model is divided into two components which are full-cycle sine and cosine filters. The two digital filters are required for the real part and the imaginary part of the phasor. Figure 3.17 shows a block diagram of the implementation for calculating the phasor magnitude using 16 spc sine and cosine filters. Table 3.10 and Figure 3.18 present the coefficients of the sine and cosine filters.

Finally, an example of the DFT filter result from the EMTP-RV model is shown in Figure 3.19. The maximum delay from the DFT filter model to go from steady-state current to another is one power cycle plus one sample.

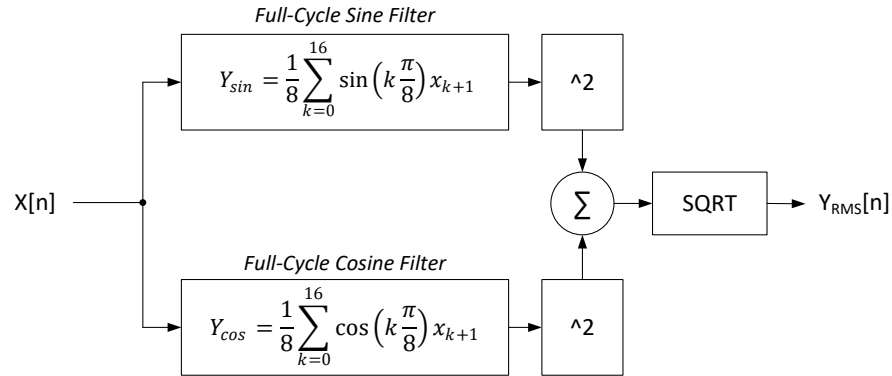


Figure 3.17 Calculating the magnitude using DFT filter model

Table 3.10 Sine and cosine filters coefficients

Sample Number	Sine filter coefficients	Cosine filter coefficients
1	0	1
2	0.383	0.924
3	0.707	0.707
4	0.924	0.383
5	1	0
6	0.924	-0.383
7	0.707	-0.707
8	0.383	-0.924
9	0	-1
10	-0.383	-0.924
11	-0.707	-0.707
12	-0.924	-0.383
13	-1	0
14	-0.924	0.383
15	-0.707	0.707
16	-0.383	0.924

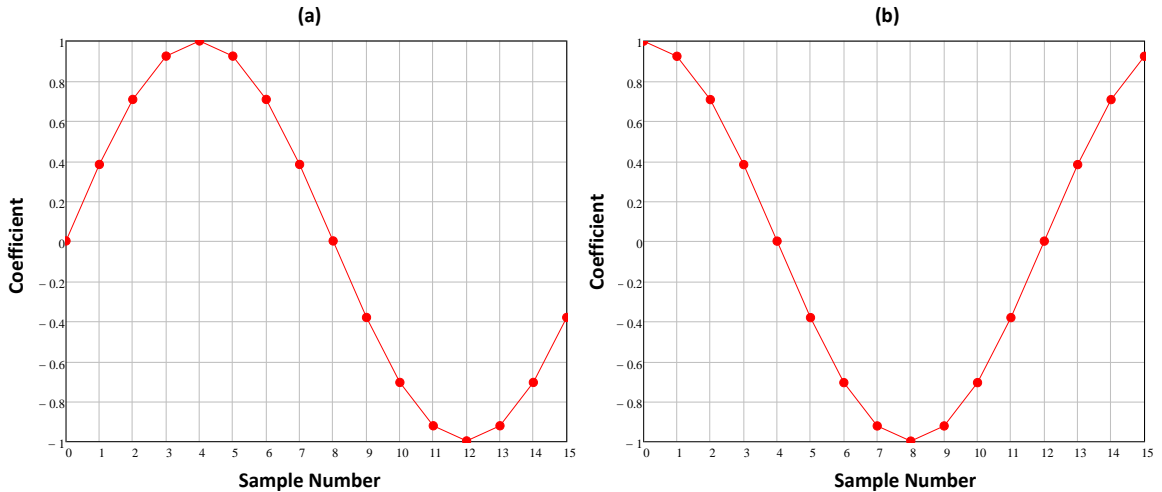


Figure 3.18 The designed DFT filter (a) sine filter coefficients and (b) cosine filter coefficients

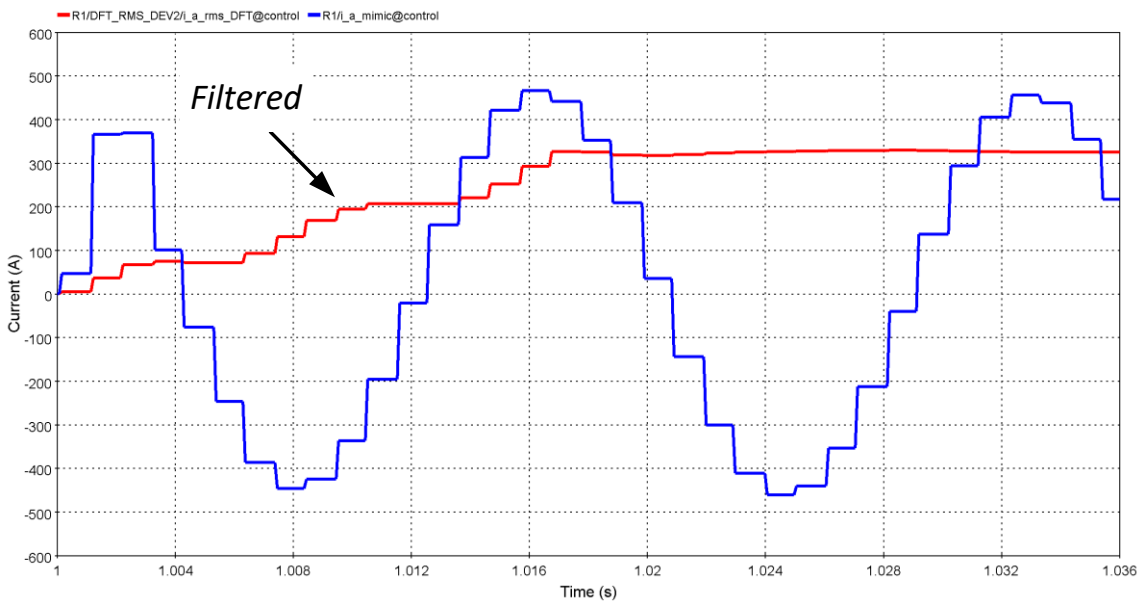


Figure 3.19 An example from the modeled DFT filter in EMTP-RV when current changes from zero to the rated current with a response of one power cycle

3.3.2. Voltage Restrained Overcurrent Elements

The output voltage magnitudes and angles from the DFT filter is used to calculate the phasor-based superimposed positive-sequence and negative-sequence voltages for the voltage restrained overcurrent elements, as shown in Figure 3.20. The phasor-based sampled analog variables are defined in Table 3.11. The set of the three-phase unsymmetrical phasors are converted to a set of three-phase symmetrical phasors using symmetrical components transformation (3.8). The delta filter subtracts

delayed memory quantities from present quantities to find the change, as described in Chapter 2. Figure 3.21 shows an example of the result from the phasor-based superimposed element model when voltage drops due to a fault. Appendix B provides a print screen of the EMTP-RV model. The versatile voltage restrained overcurrent logic is derived and discussed in detail in Chapter 7.

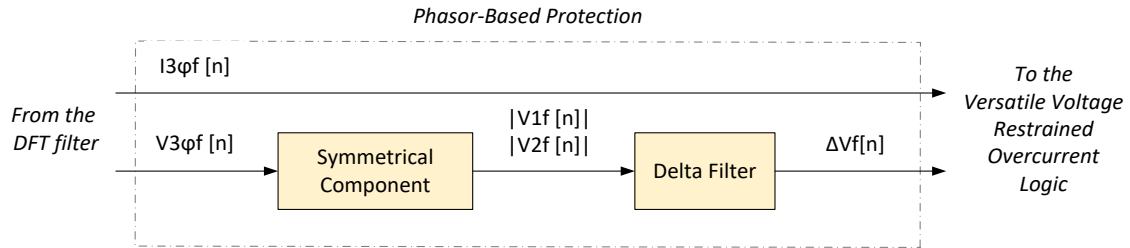


Figure 3.20 Calculating phasor-based superimposed positive-sequence and negative-sequence voltages

Table 3.11 Phasor-based sampled analog variables

Name	Description
V1f[n]	Sampled positive-sequence voltage after the full-cycle DFT filter
V2f[n]	Sampled negative-sequence voltage after the full-cycle DFT filter
ΔVf[n]	Phasor-based superimposed sequence voltage after the full-cycle DFT filter

$$\begin{bmatrix} V_0 \\ V_1 \\ V_2 \end{bmatrix} = \frac{1}{3} \begin{bmatrix} 1 & 1 & 1 \\ 1 & 1\angle 120^\circ & 1\angle -120^\circ \\ 1 & 1\angle -120^\circ & 1\angle 120^\circ \end{bmatrix} \begin{bmatrix} v_a \\ v_b \\ v_c \end{bmatrix} \quad (3.8)$$

where

v_a : Phase A, the line to ground voltage

v_b : Phase B, the line to ground voltage

v_c : Phase C, the line to ground voltage

V_0 : The zero-sequence voltage

V_1 : The positive-sequence voltage

V_2 : The negative-sequence voltage

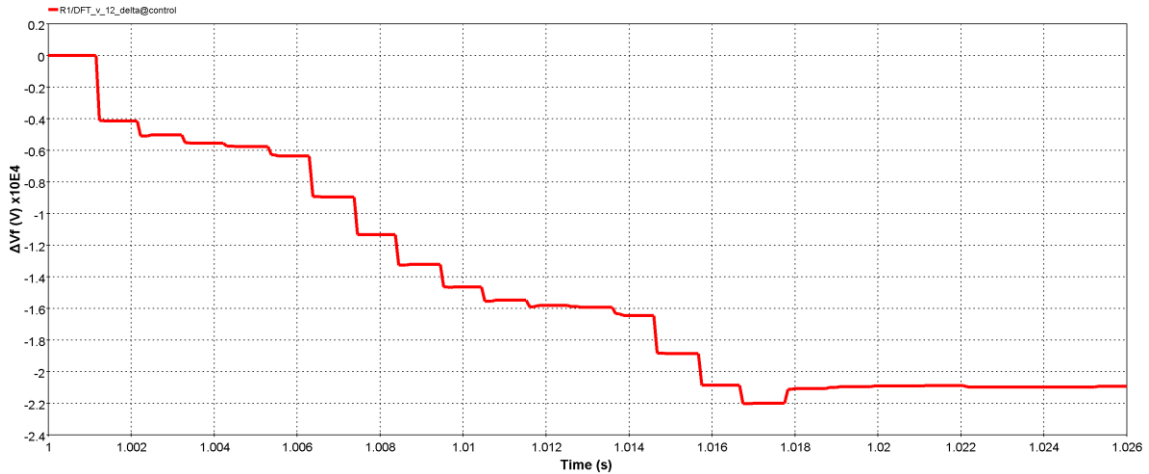


Figure 3.21 An example from the modeled phasor-based superimposed element in EMTP-RV when measured voltage drops

3.3.3. Superimposed Quantities Element

The time-domain-based superimposed quantities model is connected directly after the high digital sampling function, as shown in Figure 3.22. The time-domain-based analog variables are defined in Table 3.12. The delta filter is introduced in chapter 2.

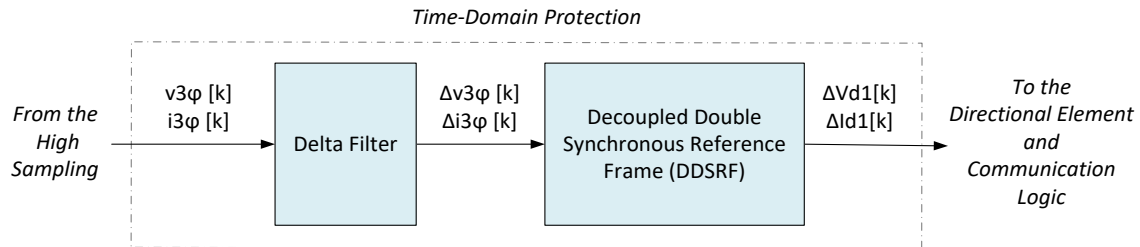


Figure 3.22 Calculating DDSRF-based superimposed positive-sequence quantities

Table 3.12 Time-domain-based analog variables

Name	Description
$\Delta v_{3\phi}$ [k]	Time-domain superimposed voltage
$\Delta i_{3\phi}$ [k]	Time-domain superimposed current
ΔV_{d1} [k]	DDSRF-based superimposed positive-sequence direct axis voltage
ΔI_{d1} [k]	DDSRF-based superimposed positive-sequence direct axis current

After the delta filter, the superimposed quantities are input to a DDSRF algorithm to find the superimposed positive-sequence direct voltage and current amplitudes. The algorithm is used to improve the time-domain superimposed quantities' reliability and calculate instantaneous symmetrical components. DDSRF is based on using two synchronous reference frames rotating with positive and negative directions at the current power system frequency, respectively. Figure 3.23 and Figure 3.24 show the outputs from the time-domain delta filter and amplitudes output from the DDSRF model. The DDSRF algorithm and the directional element logic are discussed in detail in Chapter 7 and in [32].

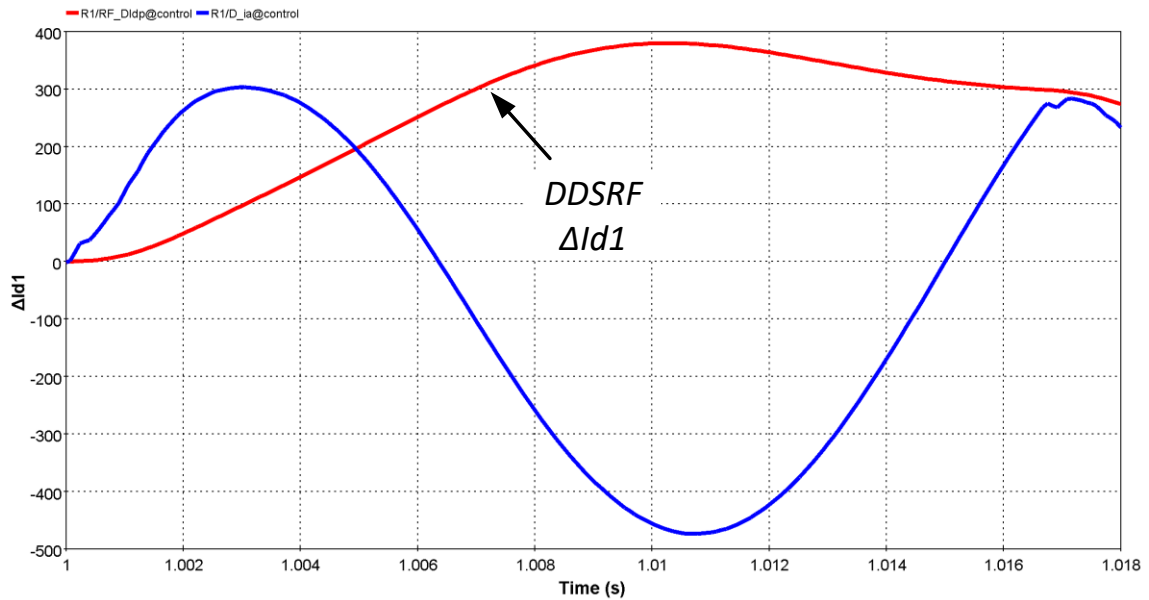


Figure 3.23 An example of superimposed positive-sequence direct-axis current from the DDSRF compared to time-domain superimposed current during fault

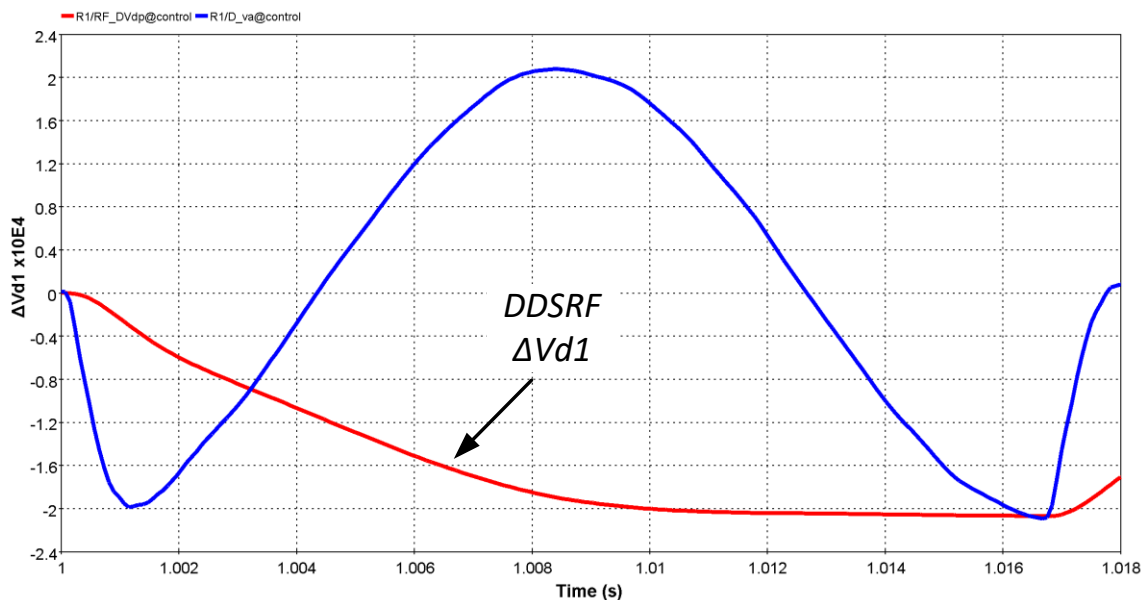


Figure 3.24 An example of superimposed positive-sequence direct-axis voltage from the DDSRF compared to time-domain superimposed voltage during fault

The DDSRF-based superimposed quantities model is tested for different sampling rates, as shown in Figure 3.25. Since the first quarter of the power cycle is the most critical part of for the superimposed quantities, more samples are needed. For example, if eight spc is used, only two samples will fall in the first quarter of the cycle, which is not reliable for the element to make a decision. However, if 64 spc is used, the first quarter has 16 samples, which is enough for this element.

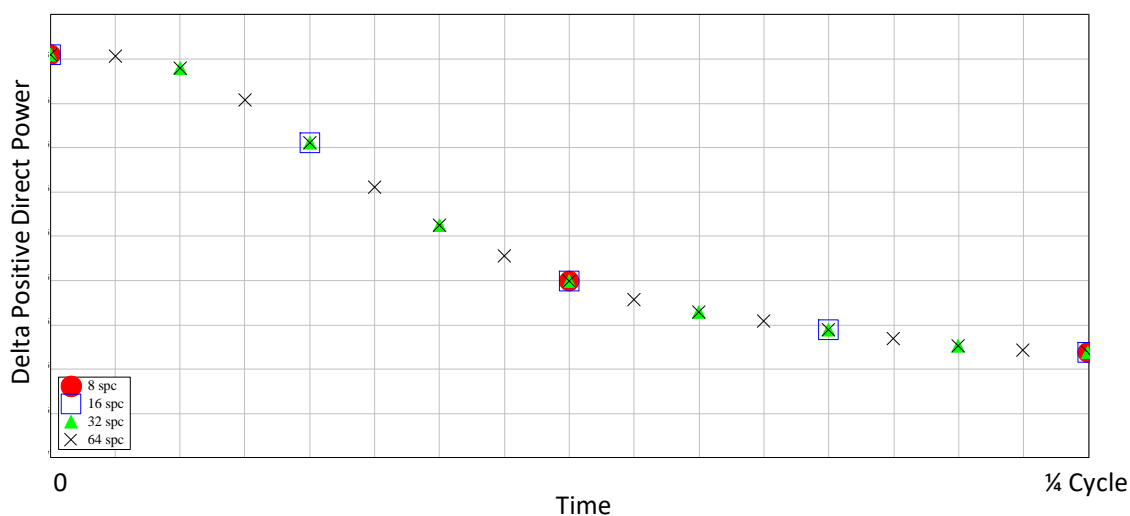


Figure 3.25 Testing the DDSRF-based superimposed quantities with different sampling rates

Chapter 4: Multi-Agent Protection Scheme for Resilient Microgrid Systems with Aggregated Electronically Coupled Distributed Energy Resources

This chapter contains a paper that is published in the Proceedings of the 2018 Annual Conference of the IEEE Industrial Electronics Society [13]. The copyright permission is shown in Appendix C.

4.1. Introduction

In 2016, the world's leading source of new power generating capacity installations was solar photovoltaic (PV). The annual market increased by about 50%, which was equivalent to more than 31,000 solar panels installed every hour [1]. The economic feasibility of residential PV systems and, in general, distributed energy resources (DER) technologies and the improvement on power electronics are tilting the economics of power generation back towards smaller scales [2], [4]. Additionally, the presence of DER units close to consumers can increase the resilience, reliability, and power quality of electricity delivery which has led to the concept of forming power distribution subsystems or "microgrids" to eliminate the need for central dispatch [5], [6].

Microgrid systems utilize a localized power and control system which can be connected and disconnected from the traditional electric power system (EPS). Microgrids can continue work while the main power system is degraded, which can strengthen grid resilience and mitigate grid outages [7], [17]. The development of microgrids will drive the centralized power systems to distributed localized systems, providing resilience in energy management [64].

A resilient system is "one that maintains state awareness and an accepted level of operational normalcy in response to disturbances, including threats of an unexpected and malicious nature" [65]. A microgrid system can meet these conditions because it can isolate a prearranged power subsystem from the EPS smoothly in response to any EPS disturbances and continue to operate in islanded mode. When the EPS is completely restored, the microgrid system can reconnect to the EPS and operate in grid-connected mode [64]. During both islanded and grid-connected modes, the microgrid system must maintain state awareness and an accepted level of operational normalcy to achieve resilience. To further support resilience, intentional islanding is an important feature that allows microgrids to supply power to sensitive loads under system attacks and contingency [66].

DER technologies such as microturbines, PV systems, fuel cells, and type 4 wind turbines are electronically coupled units and considered as the future energy resources of microgrid systems. However, in general, the increase of DER penetration within distribution systems can cause as many

problems as it may solve [6]. Challenges such as protecting microgrid systems while in both grid-connected mode and islanded mode, accounting for bidirectional power flow, and large changes in fault current levels are widely discussed in the literature. Overcoming these challenges is essential to harness the potential benefits of DER units [3], [4].

Protection schemes in microgrids are required to respond properly to faults in both grid-connected and islanded modes. One of the major challenges is that the two operation modes differ in both fault currents levels and paths. Moreover, electronically coupled DER fault currents are limited by the ratings of the silicon devices to around 1.2-1.5 per unit (pu). Thus, traditional distribution overcurrent-based protection schemes may not work sufficiently [23], [67]. There are several proposed protection solutions for microgrids, such as using differential relays, distance relays, adaptive overcurrent relays that change settings during the islanded mode, and communication-based central protection [24], [68], [69].

These solutions might function very well most of the time. However, these schemes are either heavily dependent on communication, such as central protection schemes and differential relays, or not very accurate in islanded microgrid systems such as adaptive overcurrent relays and distance relays. Additionally, decentralized adaptive multi-agent protection is introduced in the literature. Multi-agent protection can have higher speed and reliability when compared to centralized protection [70]. Having “resilient intelligent” protective agents in microgrid systems can improve the overall reliability and resilience of microgrids.

In [71], a resilient, intelligent agent is defined as the “one which maintains a state awareness of its environment and responds to disturbances in order to maintain operational normalcy within this environment.” Resilient multi-agent protection can operate independently and continue to protect the system when the communication system is degraded by either physical or cyber-attacks. The objective of this paper is to improve distribution system resilience by using a minimal communication protection scheme for reducing the size and duration of power outages.

This paper proposes a protection scheme using resilient, intelligent agents. The developed protection scheme is intended specifically for electric power distribution systems and microgrids with aggregated electronically coupled DER. The scheme uses both voltage and current measurements to sense faults and trip faulted feeders only. The scheme can be used to island part of the distribution system in order to form a microgrid or a nanogrid. This method gives a distribution system the ability to reconfigure itself during faults and continue providing power to loads in unfaulted feeders. Protective

devices act as agents and report events to higher control hierarchy levels and adjacent protective devices to improve microgrids' protection and control systems.

This paper is organized as follows. Section 4.2 presents the proposed protection scheme. Section 4.3 briefly explains the DER model. In section 4.4 and section 4.5, two study cases are presented. Section 4.6 concludes the paper.

4.2. Proposed Protection Scheme

Power distribution systems are typically protected by instantaneous/ac inverse time (50/51) overcurrent relays and fuses which depend on fault currents for tripping decisions. The proposed protection scheme uses both voltage and current measurements to sense faults and trip faulted feeders. The main reason for using both voltages and currents instead of using currents only is that electronically coupled DER supply fault current magnitudes and angles that are independent of the source and feeder impedances. Instead, fault currents are dependent on the DER controllers. Most three-phase electronically coupled DER units provide fault currents that have two unique characteristics: 1) largely balance three-phase fault currents during unsymmetrical faults, and 2) low fault current magnitudes largely independent of fault location. Thus, using fault current magnitudes alone can be unreliable for tripping decisions in a distribution system with high electronically coupled DER penetration.

The proposed scheme is comparable to the voltage-restrained time overcurrent relay used for generator backup protection known as ANSI/IEEE type 51V [41]. The voltage-restrained overcurrent relay can distinguish between overload and fault conditions. Thus, the overcurrent relay can be set to pick up for less than or equal to load currents because it will not operate improperly on normal load currents [41], [42]. In other words, the overcurrent relay can be set to be very sensitive and will trip only when voltage is below a certain threshold.

This advantage is important for microgrids because fault currents can be limited during the islanded mode. By using a 51V relay, overcurrent relays can have one setting during both grid-connected and islanded modes which means no need for communication or islanding detection. Since the traditional 51V relay is not designed to be connected to multiple feeders, this paper develops a more versatile scheme for power distribution systems and microgrids.

Figure 4.1 shows a simple microgrid system to demonstrate the basic concepts of the proposed protection scheme. The system consists of three feeders. The microgrid system is connected to the EPS at the point of common coupling (PCC) through Feeder 1. Two loads are connected to Bus A through Feeder 2, and an inverter-based DER is connected to Feeder 3 at the point of interconnect (POI). An intelligent electronic device (IED) is connected to each current transformer (CT) and to the voltage

transformer (VT). Each CT is connected to a feeder, and the VT is connected to Bus A. Subsequently, the IEDs are connected to a single resilient protective agent at that bus.

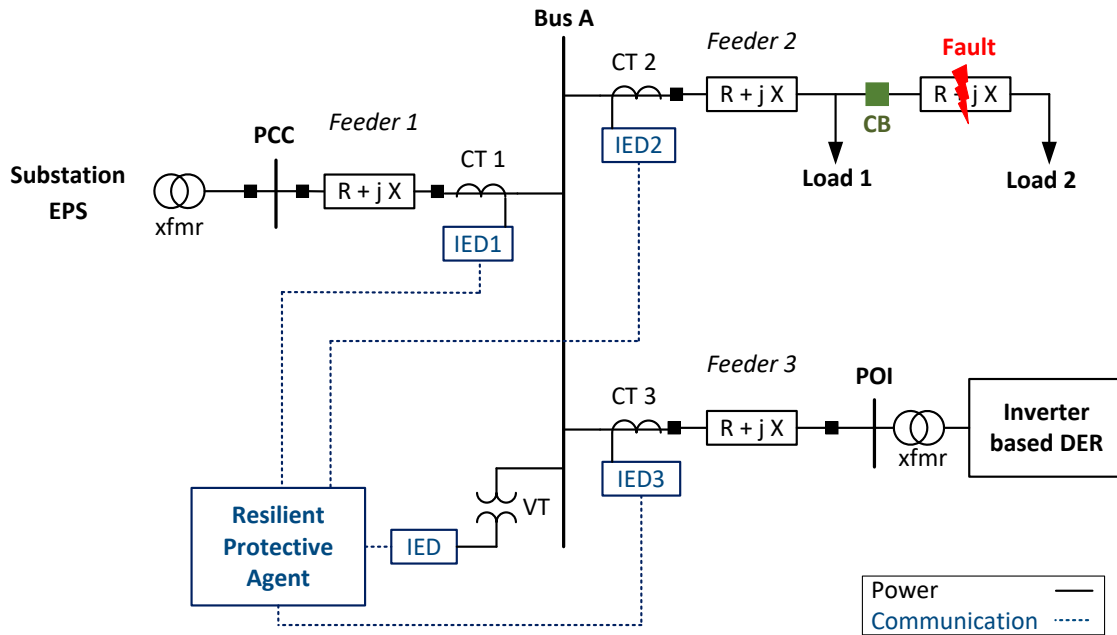


Figure 4.1 Test system for the proposed scheme

The IEDs transmit both magnitude and angle of the measured voltage and currents to the protective agent over the substation communication network using the sampled values (SV) protocol from the IEC 61850 standards. Figure 4.2 shows the data flow from the CTs and the VT to the protective agent. Additionally, the status of each circuit breaker connected to Bus A is reported to the protective agent for breaker failure protection. There are three status conditions for a circuit breaker: on, off, or tripped. IEC 61850 standard Generic Object-Oriented Substation Events (GOOSE) messages communicate indications of the breaker status [72].

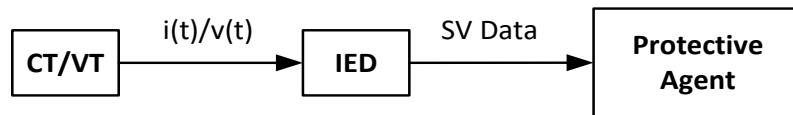


Figure 4.2 Data flow from the CTs and VT to the protective agent

The protective agent has two main capabilities:

- Sense faults based on the measured currents and voltage, and current directions to a) trip circuit breakers that are connected to Bus A, b) send a permissive transfer trip signal to far circuit breakers or c) transfer the microgrid system to islanded mode.
- Broadcast the event to the main microgrid control system, other protective agents, and/or to the EPS operating center.

The measured phase voltages from the VTs are used for fault type detection. The symmetrical components are calculated from the measured three-phase voltages for fault location detection and tripping decisions. More specifically, the difference between positive sequence voltage and negative sequence voltage (ΔV) is used for fault location detection. The calculated ΔV is compared to preset ΔV thresholds to detect faults. The currents from each CT are compared to preset thresholds for each feeder. The measured currents (i) and the direction of the currents (θ_i) are used for faulted feeder detection. In this scheme, the thresholds are set based on pre-fault analysis, and only low-impedance faults are considered.

The direction of the current flow for each feeder is determined. There are several ways to determine current direction, such as using phase-to-phase voltages and the currents of the opposite phase (known as the 90° connection), the angle of a measured positive-sequence impedance, watt-power relay (32), or var-type relay [39], [40]. Investigating current directional determination methods is beyond the scope of this paper, and the directions of the currents are assumed to be successfully determined.

The protective agent sends a trip signal only if three conditions are true: 1) the calculated ΔV is less than one of the preset ΔV thresholds, 2) the measured currents are more than the preset thresholds, and 3) the direction of the currents are flowing out of Bus A. Therefore, a trip signal is sent to the faulted feeder only. In addition, the same logic is duplicated with different voltage thresholds to send a permissive transfer trip signal to further circuit breakers. Time inverse curve or time delay can be used for coordination with other protective devices and to avoid voltage transients' nuisance tripping. Figure 4.3 summarizes the three logic conditions per phase per feeder.

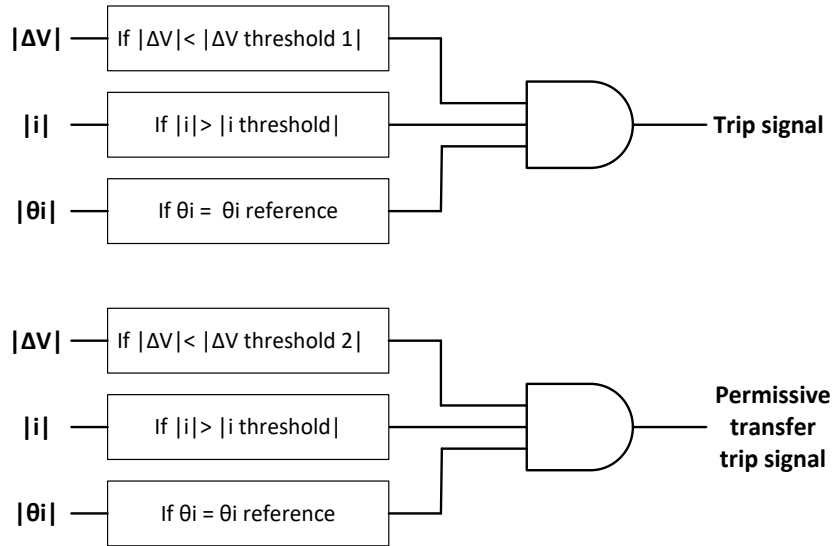


Figure 4.3 Per phase protection logic diagram per feeder

For example, if faults occurred beyond Load 1 at Feeder 2, the protective agent sends a transfer trip signal to CB (the circuit breaker beyond Load 1 noted in Figure 4.1). In this case, Load 1 is online, and only Load 2 is disconnected. The measured change in the voltage (ΔV) is used to estimate the fault location. The ΔV threshold of 2 is preset to consider faults beyond Load 1. Also, the event is broadcast to adjacent protection devices and to the main microgrid controller. The broadcast event can be used by other resilient protective agents. However, this feature is not investigated in detail in this paper and is left for future work.

For demonstration purposes, two study cases are conducted. The EMTP-RV program is used to model the power system and the control systems of a DER unit sourced by PV. EMTP-RV is an electromagnetic transients program [56]. In study case 1, a simple distribution system is chosen to study multiple factors that can impact the proposed scheme. In study case 2, the IEEE 34 bus test system is chosen to connect the DER to a more realistic radial distribution feeder.

4.3. Distributed Energy Resources Model

The DER model will be briefly discussed. The DER model is an inverter-based sourced by a PV system. A three-phase two-level voltage source converter (VSC) with six insulated-gate bipolar transistors (IGBT) switches is modeled in EMTP-RV. The switching frequency is 3 kHz. An EMTP-RV built-in PV model is connected to the dc line across the dc bus capacitor of the VSC. The distribution system/microgrid is connected to the ac side of the VSC. Parallel high pass filters and a series inductive choke are connected to the ac terminal to smooth the voltage and the currents,

respectively. The VSC ac side is connected to a Y-grounded power transformer and then to the distribution system at the POI.

The VSC controller uses current-regulated real and reactive power control loops to track the maximum PV power point to control the PV system output. The controller uses two-axis synchronous reference frame components using direct (d) and quadrature (q) axis terms. The controller generates d-axis and q-axis modulation signals to control the VSC switching. Since the PV control uses a synchronous dq reference frame, a synchronization mechanism is required. It is implemented using an EMTP-RV built-in phase-locked loop (PLL). The PLL tracks the ac system frequency and synchronizes the converter output with the ac system.

4.4. Study Case 1: Simple System

This study case examines two aspects of system performance. First, the change in voltage due to the fault (ΔV) is calculated when symmetrical and unsymmetrical faults are applied at several locations on a feeder. Second, several factors that can impact ΔV are examined. The considered fault types are three-phase (3PH), single line to ground (SLG), double line to ground (DLG), and line to line (LL) fault. Figure 4.4 shows a simplified one-line diagram of the EMTP-RV model, where a 2 MW PV system model, 2.2 MVA diesel generator (DG) with exciter and governor models, and loads of up to 5 MW and 1 MVAR are connected to a 0.48 kV ac distribution system. The system consists of four feeders connected to Bus A. During islanded mode, the protective agent can trip the faulted feeder based on the calculated ΔV and current directions. However, the protective agent cannot send a permissive transfer trip signal since ΔV is very low during the islanded mode. Thus, the microgrid is first studied in grid-connected mode.

4.4.1. Fault Location

The impact of the fault location on voltage measurements at Bus A is studied in this section. Feeder 1 and Feeder 2 are homogeneous, and Feeder 4 is disconnected. The PV system is providing its maximum peak active power and zero reactive power. 3PH, SLG, DLG, and LL faults are applied at 0%, 25%, 50%, 75%, and 100% of Feeder 2 impedance. The protective agent is connected to Bus A, and ΔV is calculated in pu for each fault location and fault type. Figure 4.5 shows the calculated ΔV in pu when SLG fault applied at 75% of Feeder 2 at 0.6 s and cleared at 0.8 s. The same process is conducted for each fault location and fault type, and the simulation results are summarized in Figure 4.6 and Table 4.1.

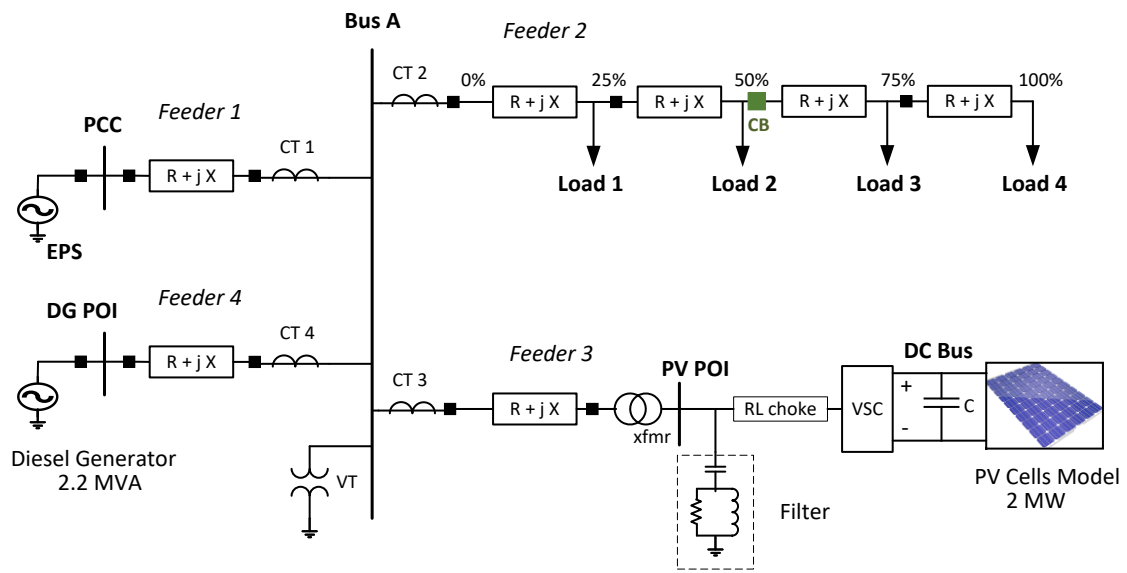


Figure 4.4 Simplified one line diagram of the EMTP-RV distribution model

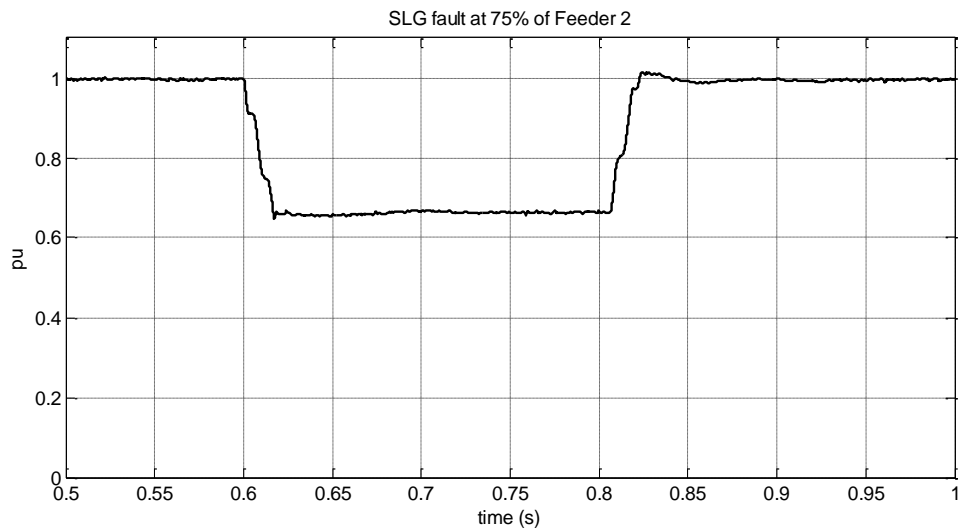


Figure 4.5 Measured ΔV in pu when SLG fault applied at 75%

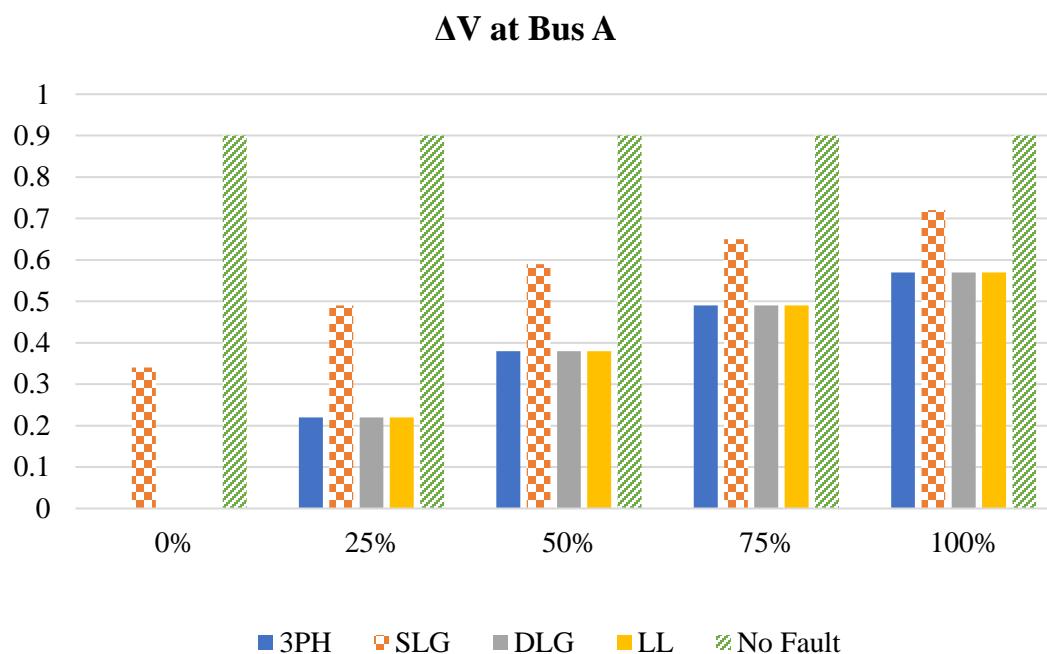


Figure 4.6 Measured ΔV in pu at Bus A when faults applied at five locations

Table 4.1 ΔV in pu calculated at Bus A

Faults Location	ΔV in pu	
	3PH, DLG, and LL	SLG
0%	0	0.34
25%	0.22	0.49
50%	0.38	0.59
75%	0.49	0.65
100%	0.57	0.72

The results in Figure 4.6 and Table 4.1 show that the calculated ΔV at Bus A is positively correlated to the location of faults. The magnitude of ΔV increases for faults farther away and is less for faults closer in. 3PH, DLG, and LL faults show the same ΔV magnitude for faults at the same location. On the other hand, SLG faults show higher ΔV magnitude compared to other faults at the same fault location. The faulted phase is detected from the phase voltage dip. Figure 4.7 shows three-phase RMS voltages in pu measured at Bus A when an SLG fault is applied at 75% of Feeder 2 at 0.6 s and cleared at 0.8 s. Since the SLG fault is applied at phase A, the voltage dip is on phase A only.

Thus, the protective agent should have two thresholds, one for SLG faults and one for other faults. If one phase of the three phases shows a voltage sag, the protective agent considers voltage thresholds for SLG faults; otherwise, the protective agent considers voltage thresholds for other faults.

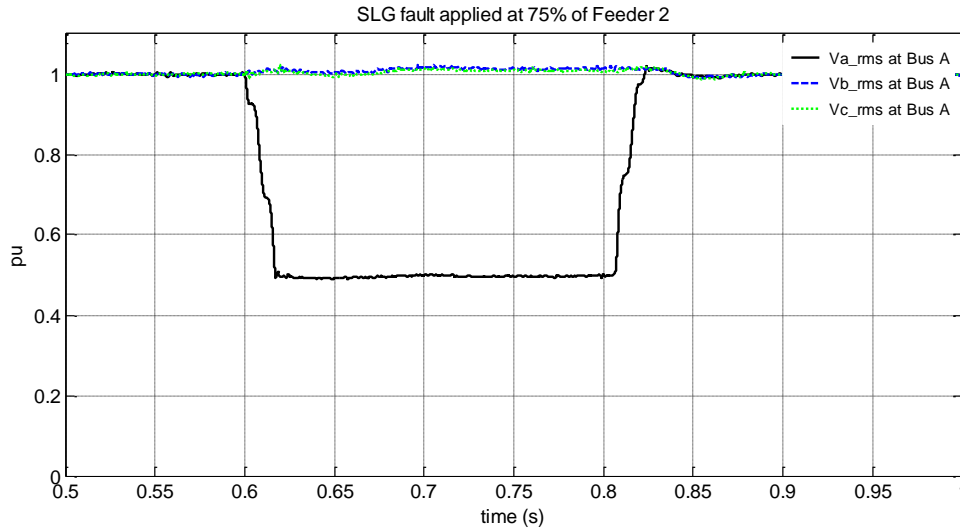


Figure 4.7 Three phase rms voltages in pu when SLG fault is applied at 75%

The protective agent compares the calculated ΔV with preset ΔV thresholds. The thresholds are associated with the number of circuit breakers and their locations in each feeder. In this case, there are four circuit breakers on Feeder 2. For example, when faults occurred at 75% of Feeder 2, the protective agent sends a permissive transfer trip signal to CB (the circuit breaker beyond Load 2 noted in Figure 4.4). Thus, Load 1 and Load 2 do not experience outages.

Another observation is that three-phase currents measured at the PV inverter POI are balanced and limited during all fault events. Figure 4.8 shows the three-phase currents measured at the PV POI when SLG fault applied at 75% of Feeder 2 at 0.6 s. The VSC used in this study case has no voltage ride-through capability nor reactive power supply capability. Thus, the VSC is supplying zero reactive power during faults. Also, the negative and zero sequence currents provided by the PV are under the standard thresholds for tripping.

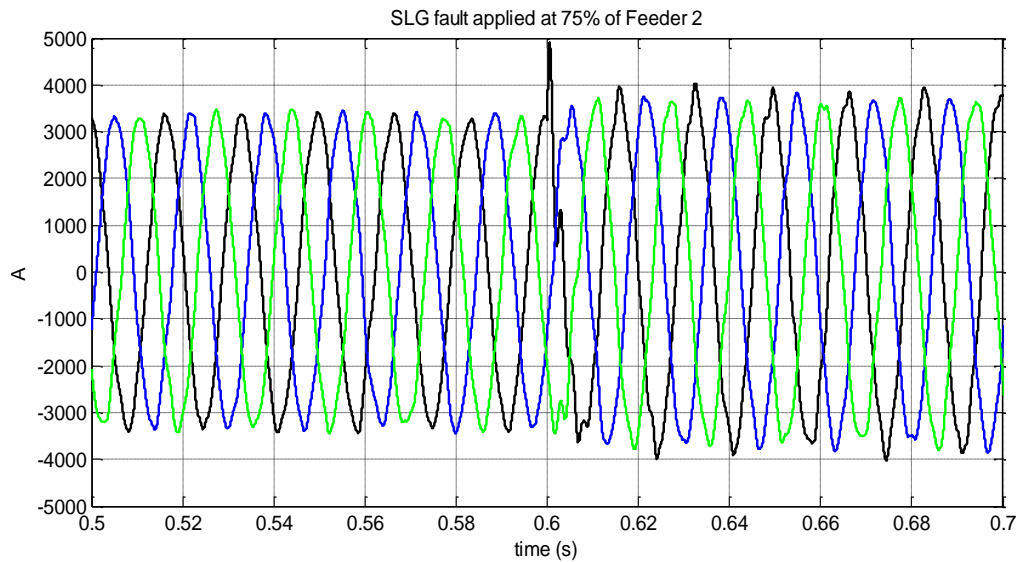


Figure 4.8 Three phase currents at the PV POI when SLG fault applied at 75%

4.4.2. Impacts on ΔV

There are several factors that can impact ΔV magnitude during faults, such as the electric power system characteristics and feeder impedance. In this section, five scenarios are investigated: 1) faults at Feeder 1, 2) Feeder 1 weak, 3) Feeder 1 stiff, 4) Load 1 in the fault loop, and 5) connecting the DG.

In the first scenario, faults are applied at 75% of Feeder 1 impedance. Faults are applied at 75% of Feeder 2 impedance in the following scenarios. In the second and the third scenarios, the source impedance of Feeder 1 is changed to make the feeder weaker or stiffer compared to the original. In these two scenarios, the applied impedance changes are extreme to clarify the impacts. The changes are applied by doubling the source impedance to make the source weaker and by dividing the impedance by two to make the source stiffer. In the fourth scenario, 1.2 MW and 0.15 MVAR Load 1 is connected. In the last scenario, the DG is connected to Feeder 4. The simulation results are summarized in Figure 4.9 and Table 4.2.

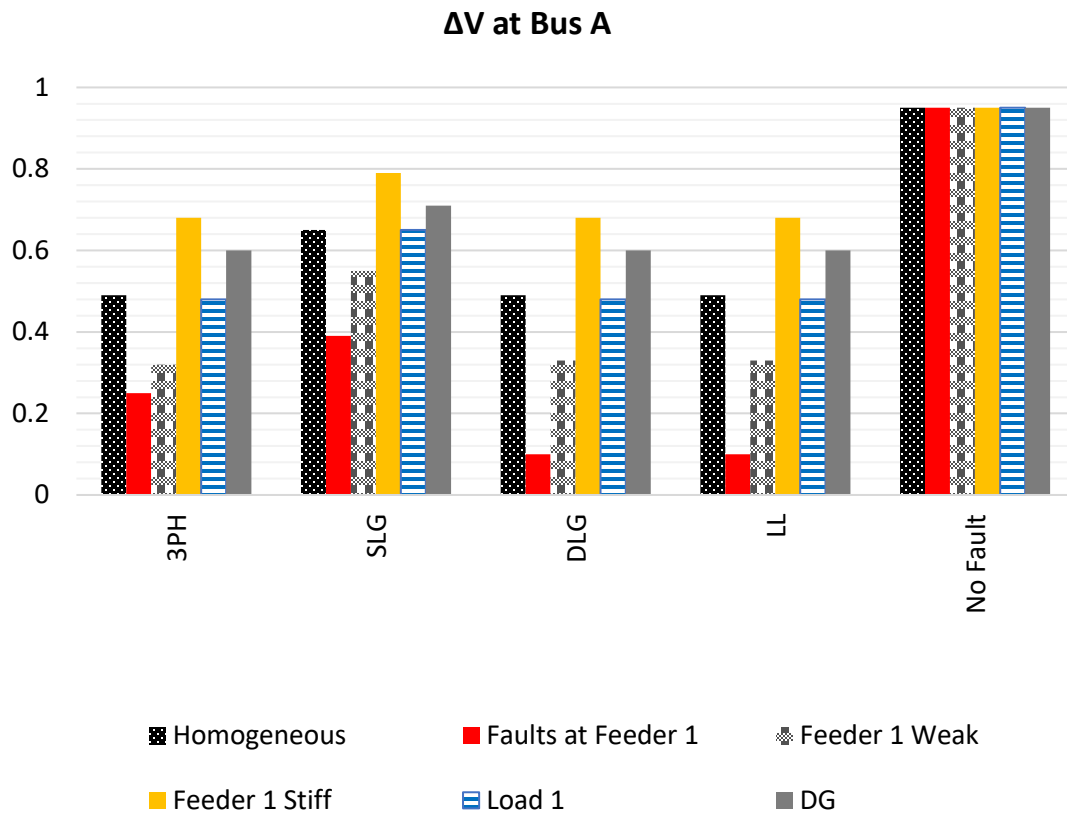


Figure 4.9 ΔV in pu calculated at Bus A for the five scenarios

Table 4.2 ΔV in pu calculated at Bus A

Scenario	ΔV in pu	
	3PH, DLG, and LL	SLG
Homogeneous	0.49	0.65
Faults at Feeder 1	0.25a	0.39
Feeder 1 weak	0.32	0.55
Feeder 1 stiff	0.68	0.79
Load 1	0.48	0.65
DG	0.6	0.71

a. This ΔV is only for 3PH fault. ΔV for DLG and LL faults is 0.1 pu in this case

Figure 4.9 and Table 4.2 show the calculated ΔV at Bus A of the different scenarios compared to the previous homogeneous case. The outcomes are summarized as:

- When faults are applied at 75% of Feeder 1 impedance, the calculated ΔV is very low since Feeder 1 is the only connection to the EPS. In this scenario, the protective agent transfers the microgrid system to islanded mode.
- When Feeder 1 is weak, ΔV is lower. ΔV magnitude is decreased approximately 34%. On the other hand, when Feeder 1 is stiff, ΔV is higher than the homogeneous case since more voltage support is provided from the EPS. ΔV magnitude is increased approximately 38%. Thus, source impedance variation can cause ΔV error.
- Having 1.2 MW and 0.15 MVAR Load 1 connected does not impact the result of ΔV calculated at Bus A.
- The DG supports the voltage at Bus A, so ΔV is higher than the homogeneous case. ΔV magnitude is increased approximately 22%. In general, a DER impact depends on the size, type, and location of the DER.

There are several ways to overcome these issues. One way is to use the magnitude of the currents to set multiple current thresholds. Based on the current thresholds, multiple ΔV thresholds are set. For example, in the second and third scenarios, the currents increase when the source of Feeder 1 is stiff and decrease when the source is weak. Thus, the protective agent should have three current thresholds: normal, stiff, and weak. When the measured currents reach one of the preset thresholds, a ΔV threshold is chosen. Consequently, the current magnitudes are used to adjust ΔV thresholds and to consider the dynamic configuration of the distribution systems.

4.5. Study Case 2: IEEE 34-Bus

In this study case, two brief application examples are presented. First, an example of tripping faulted feeders only. Second, an example case for estimating fault locations is shown. The PV model is connected to the IEEE 34 bus system, as shown in Figure 4.10 [57]. The PV system and two protective agents are connected at bus 800 and bus 834. Bus 834 is connected to four buses through four feeders: bus 842, bus 860, bus 858, and the PV bus. Bus 800 is connected to three buses through three feeders: the EPS, bus 802, and the PV bus.

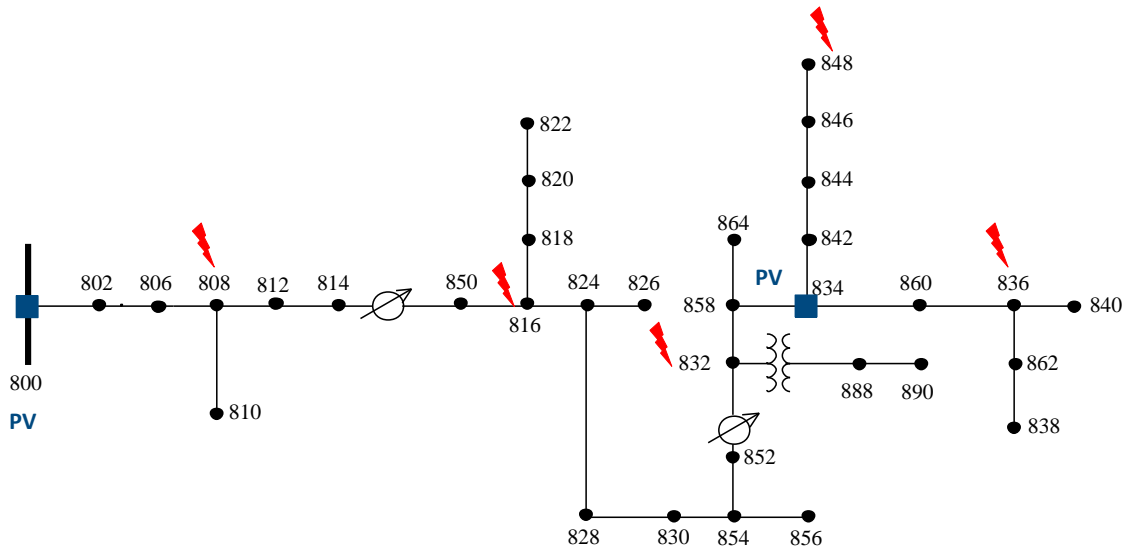


Figure 4.10 IEEE 34 bus distribution system connected to PV systems and protective agents (faults locations are noted)

4.5.1. Tripping Faulted Feeders

Faults are applied at buses 832, 836, and 848 to test the protective agent at bus 834. The calculated ΔV , from simulation, for each location, is approximately 0.5 pu for SLG faults and less than 0.1 pu for 3PH, DLG, and LL faults. When faults are applied at bus 836 and bus 848, the faulted feeders are tripped based on currents directions. The protective agent cannot identify the fault location since the system is very weak on this side. Thus, the faulted feeders are tripped from bus 834. When faults are applied at bus 832, the protective agent can transfer the subsystem to a nanogrid system if it has islanding capability at bus 834; otherwise, the protective agent trips both the faulted feeder from bus 834 side and the PV system. At the same time, the protective agent broadcasts the fault event to adjacent agents and to the protective agent at bus 800.

The reason for tripping the faulted feeder from bus 834 side is to eliminate fault currents provided by any possible DER connected to this side of the system. Also, broadcasting the status can help other agents to estimate fault locations and trip faulted feeders.

4.5.2. Estimating Fault Locations

Faults are applied at bus 808 and bus 816 to test the protective agent at bus 800. The results are summarized in Table 4.3. The calculated ΔV from 3PH, DLG, and LL faults are not equal because the system is imbalanced. However, the difference between the three faults is less than 10%. Thus, the ΔV thresholds can have margins of error to account for imbalance factors and other factors such as fault

resistances. The protective agent can identify the fault location and send a permissive transfer trip signal to trip circuit breakers at bus 806 or bus 850, respectively.

Table 4.3 ΔV in pu calculated at Bus 800

Fault Location	ΔV in pu			
	<i>3PH</i>	<i>DLG</i>	<i>LL</i>	<i>SLG</i>
Bus 808	0.35	0.33	0.32	0.59
Bus 816	0.63	0.61	0.6	0.77

4.6. Conclusions

The paper proposes a multi-agent protection scheme for distribution and microgrid systems with aggregated electronically coupled DER units to improve systems resilience and reduce power outages. A protective agent can sense faults based on calculated ΔV and currents' magnitudes and directions. The protective agent can trip faulted feeders only, send a permissive transfer trip signal to far circuit breakers, and transfer microgrids and nanogrids to islanded mode. Additionally, the protective agent broadcasts fault events to the main microgrid control system, other protective agents, and/or to the EPS operating center to improve microgrids' control and protection.

Currents and ΔV thresholds can be used to account for the dynamic configuration of distribution systems. SLG faults are identified based on phase voltage dip to choose the associated ΔV thresholds. The thresholds should have margins of error to account for imbalance factors and fault resistances. Aspects such as high-impedance faults, coordination, adjacent protective agents' correlations, and backup protection are not investigated in this paper and left for future work. Additionally, using this protection scheme during islanded mode will require more investigation. Also, the updated IEEE standard 1547-2018 discusses recommended requirements for DER response to abnormal voltages and voltage ride-through capabilities [19]. The standard specifies undervoltage thresholds, overvoltage thresholds, and clearing time ranges for DER response to abnormal conditions. These specifications can impact the proposed scheme, and it is a possible next step for this work.

Chapter 5: Impact of Inverter Based Resources on Superimposed Quantities Based Protection

This chapter contains a paper that is published in the Proceedings of the 2021 Annual Georgia Tech Protective Relaying Conference [14].

5.1. Introduction

Unlike conventional synchronous generators, inverter-based resources (IBRs) have no stored kinetic energy as rotational inertia. Increased integration of IBRs such as solar photovoltaic (PV) and type 4 wind turbines into power systems decreases the regional and the overall power system inertia [73]. Faults must be cleared faster than the critical fault clearing time in such systems to maintain power system stability. Fast fault tripping can be achieved using time-domain-based protection elements, often using traveling-waves or superimposed quantities, where faults can be detected in as little as one millisecond and four milliseconds, respectively [74].

An example of an implementation of superimposed quantities for protection is a high-speed directional element used with line protection. The superimposed quantities-based directional element indicates fault direction based on relative polarities of the transient voltages and currents. The quantities are based on fault-generated components of instantaneous voltages and currents, which primarily depend on the electric network parameters [43], [44].

However, IBRs fault current characteristic and fast control responses impact superimposed current quantities by changing both magnitude and angle fault current response. IBRs fault currents are mainly dependent on IBRs control action and are independent of fault locations. The fault current characteristic of most IBRs is low magnitudes around 1.2 per unit with high-frequency transients for up to two cycles [38], [75].

It is important to ensure IBRs' nonlinear fault current responses do not cause the superimposed quantities-based element to fail to indicate the correct direction. This paper is motivated by the increasing interest in using superimposed-based directional protection, where few researchers focus on evaluating the impact of IBRs on the quantities. This paper presents the impact of IBRs on time-domain-based current and voltage quantities. The impact of IBRs is simulated using an electromagnetic transients program (EMTP-RV) [56].

5.2. Superimposed Quantities

5.2.1. Superimposed Voltage and Current

Ideally, superimposed voltage and current quantities are equal to the fault-generated components during faults and zero during no faults. The calculation of superimposed voltage $\Delta v\varphi(t)$ and current $\Delta i\varphi(t)$ quantities measured at a relay terminal is based on subtracting the present voltage $v\varphi(t)$ and current $i\varphi(t)$ samples from the corresponding stored voltage $v\varphi(t - \tau)$ and current $i\varphi(t - \tau)$ samples. Superimposed relays typically use one power cycle memory buffers called delta filters to hold samples [3], [4]. Delta filters are applied to the measured voltage and current after anti-aliasing low-pass filters. Superimposed voltage and current quantities $\Delta v\varphi(t)$ and $\Delta i\varphi(t)$ are calculated, as in (5.1) and (5.2).

$$\Delta v\varphi(t) = v\varphi(t) - v\varphi(t - \tau) \quad (5.1)$$

$$\Delta i\varphi(t) = i\varphi(t) - i\varphi(t - \tau) \quad (5.2)$$

Figure 5.1 (a) and (b) show the faulted phase voltage and current waveforms during a simulated single line to ground (SLG) fault, with the example, one-cycle delta quantities marked. Figure 5.1 (c) and (d) show the calculated instantaneous superimposed quantities. Applying replica impedance filters to current quantities suppresses the dc offset, which increases element reliability. The reason is that replica filters provide compensated current and eliminate the dc offset from propagating to the current quantities, reflecting the true transient power direction. The replica impedance filter is a high pass filter that functions as a mimic filter [43]. Figure 5.1 (d) shows both superimposed current and superimposed quantity replica current. The replica current $\Delta i\varphi_{rp}(t)$ is scaled by the source impedance ($Z_s = R_s + j\omega L_s$) behind a relay as in (5.3).

$$\Delta i\varphi_{rp}(t) = \frac{R_s}{|Z_s|} * \Delta i\varphi(t) + \frac{L_s}{|Z_s|} * \frac{d}{dt} \Delta i\varphi(t) \quad (5.3)$$

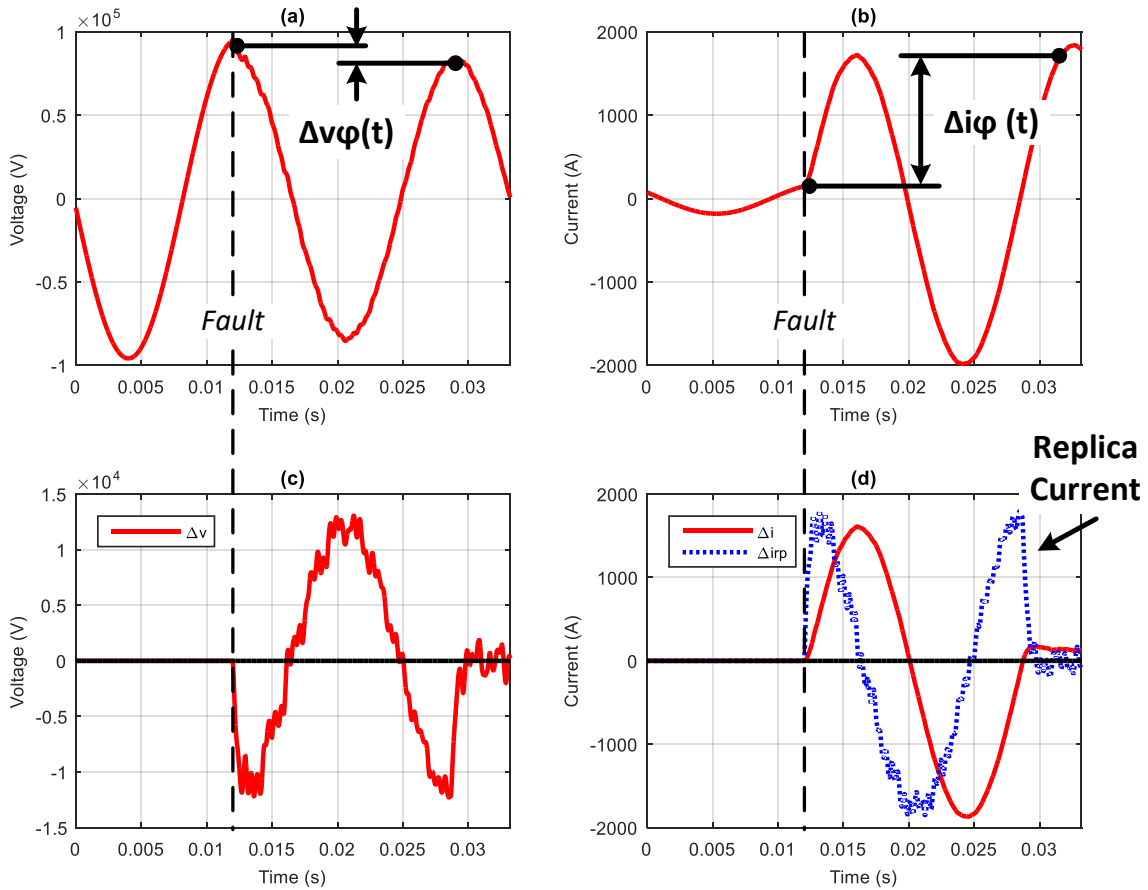


Figure 5.1 Measuring superimposed quantities from waveforms during an SLG fault: (a) voltage, (b) current, (c) superimposed voltage, and (d) superimposed current and replica current

5.2.2. Superimposed Transient Power

Superimposed transient power quantities can be used to indicate the fault direction [43], [44]. The products of per phase delta current and voltage quantities are summed to find the superimposed power $\Delta S(t)$ as in (5.4). Another option is to use replica current quantities to find the superimposed replica power $\Delta Srp(t)$ as in (5.5).

$$\Delta S(t) = \Delta va(t) \Delta ia(t) + \Delta vb(t) \Delta ib(t) + \Delta vc(t) \Delta ic(t) \quad (5.4)$$

$$\Delta Srp(t) = \Delta va(t) \Delta iar(t) + \Delta vb(t) \Delta ibrp(t) + \Delta vc(t) \Delta icrp(t) \quad (5.5)$$

A negative polarity of superimposed transient power quantities indicates forward faults, and a positive polarity indicates reverse faults. Also, superimposed power and replica power quantities can be integrated over one power cycle to increase security [43], [44]. Figure 5.2 shows an example of superimposed power and replica power quantities during a forward SLG fault from Figure 5.1, where a voltage behind an impedance model is used behind the relay. Figure 5.2 shows that superimposed and

superimposed replica power quantities indicate forward faults with negative power in the first quarter cycle. The plots show that the replica power signal is more clearly negative and is more reliable. This behavior is because of the elimination of the dc offset [49].

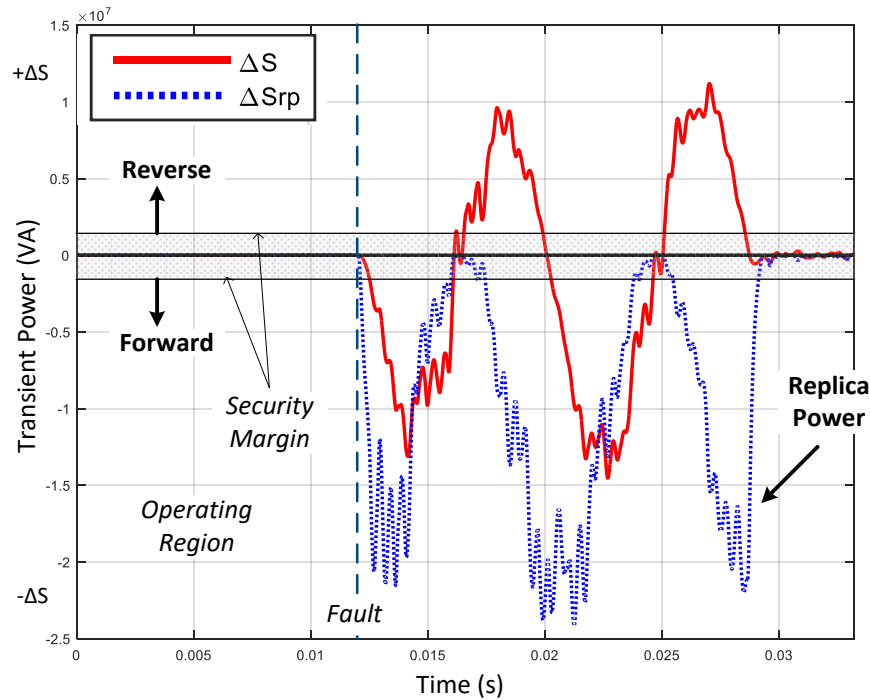


Figure 5.2 An example of superimposed transient and replica power during an SLG fault for a conventional system source

5.2.3. Impact of Inverter-Based Resources

Figure 5.3. (a) and (b) shows an example of superimposed voltage and current replica power quantities during a forward SLG fault at the same location as the results shown in Figure 5.1, where an IBR source is connected behind the relay. The fault current, as seen by the relay, is supplied by the IBR. Figure 5.3 (a) shows that the IBR does not have much impact on the superimposed voltage. However, Figure 5.3 (b) shows a significant change in the superimposed current response since the IBR control regulates the output current. The superimposed current shows an oscillation due to the controller response that also appears in the superimposed replica current.

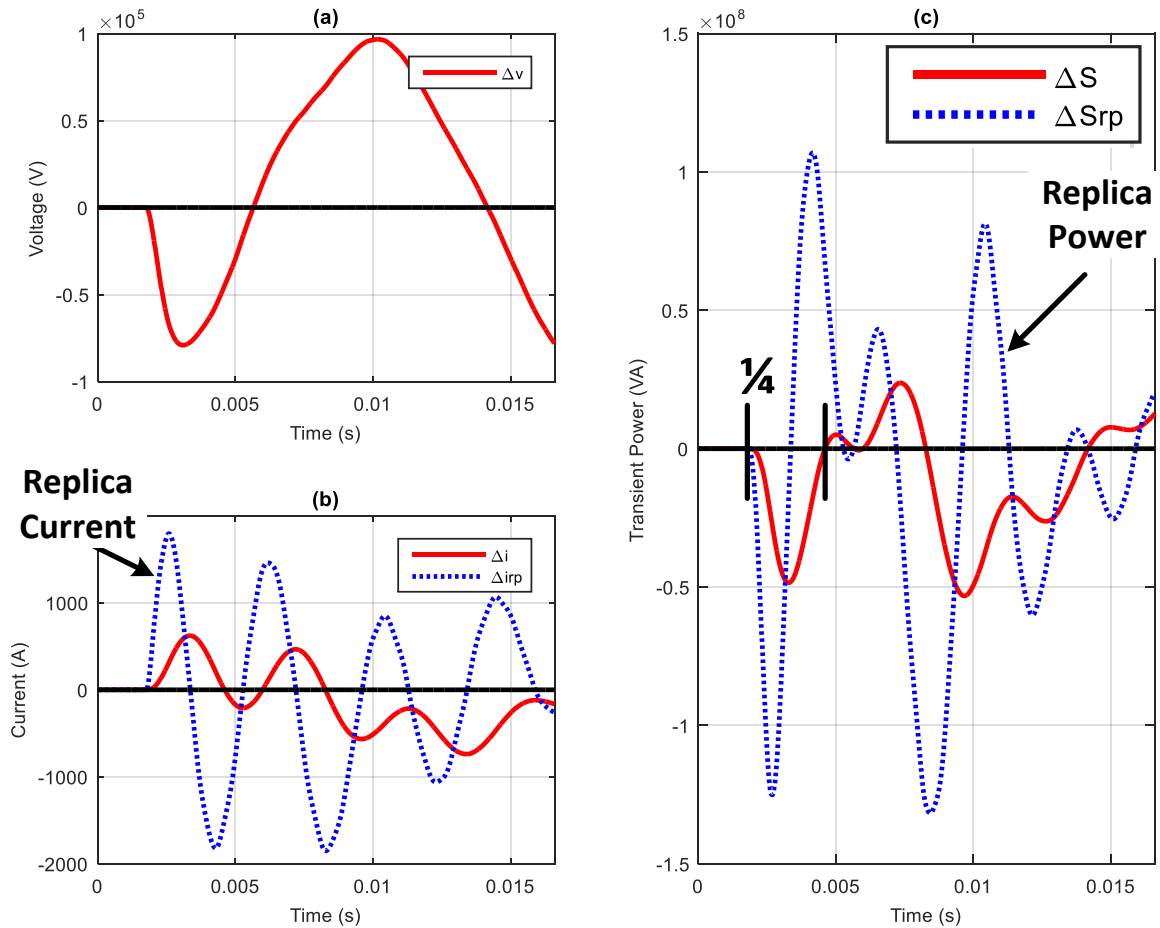


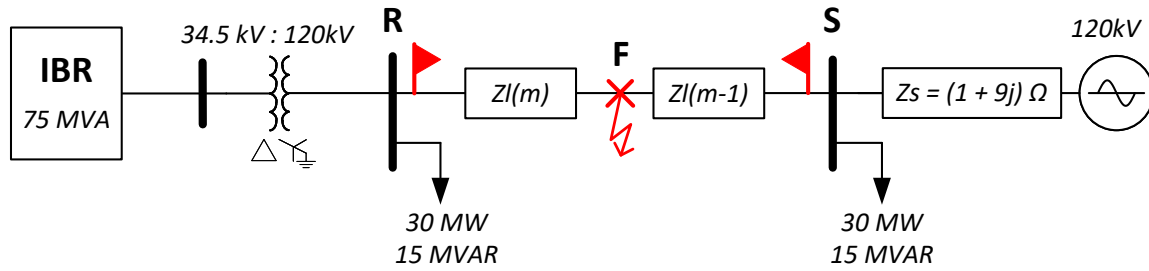
Figure 5.3 An example of the impact of IBRs on superimposed quantities during an SLG fault: superimposed (a) voltage, (b) current and replica current, (c) power and replica power

Moreover, Figure 5.3 (c) shows that superimposed replica power quantities do not indicate the correct fault direction. However, the superimposed power signal seems more stable than the replica power signal because the IBR control effectively varies the source impedance behind the relay and the replica impedance filter amplifies the higher frequency components. Both superimposed power and replica power quantities show nonlinear behavior impacted by the IBR fault current control response.

5.3. Study Case and Simulation Results

5.3.1. Study Case

EMTP-RV is used to model and simulate the power system components. The modeled system includes an ideal source behind an impedance Z_s at bus S, a 100 km frequency-independent transposed transmission line model, and an aggregated inverter model of a 75 MVA PV installation connected at bus R, as shown in Figure 5.4. The superimposed quantities-based relay is connected on the line side of bus R.



Line Parameters (Zl):

Zero-Mode	Positive-Mode
$L' = 1.6621 \Omega/\text{km}$	$L' = 0.1270 \Omega/\text{km}$
$R' = 0.3125 \Omega/\text{km}$	$R' = 0.4794 \Omega/\text{km}$
$C' = 1.8166 \mu\text{S}/\text{km}$	$C' = 3.4788 \mu\text{S}/\text{km}$

Figure 5.4 Single-line diagram for the power system model

The aggregated IBR is connected to bus R through a power transformer with a delta configuration on the IBR side and wye-grounded on the grid side to provide a zero-sequence current path for transmission protection. The IBR model has a three-phase two-level voltage source converter (VSC) with six insulated-gate bipolar transistors switched at a 3 kHz switching frequency. The VSC control uses current-regulated real and reactive power control loops with maximum power point tracking. The Park's transformation to a synchronous reference frame generates D-axis and Q-axis modulation signals to control the VSC switching [31]. The IBR current is limited to 1.2 per unit through fast inverter current controller response.

Relay S and relay R are placed at bus S and R forward-looking to the transmission line. In-zone SLG faults are applied at 25%, 50%, and 75% of the line from bus R. For in-zone faults, the two relays should indicate forward. The system is simulated with two fault resistance (R_f) values 0Ω and 2Ω on the primary 120 kV system. Relay S and relay R calculates superimposed power $\Delta S(t)$ and replica power $\Delta Srp(t)$ using equations (5.4) and (5.5), respectively.

Through all figures below, the figures titled (a) and (b) are signals obtained from relay S when $R_f = 0 \Omega$ and $R_f = 2 \Omega$, respectively, and figures titled (c) and (d) are signals obtained from relay R when $R_f = 0 \Omega$ and $R_f = 2 \Omega$, respectively. Also, both superimposed power $\Delta S(t)$ and replica power $\Delta Srp(t)$ are shown in the figures to demonstrate the impact of the IBR.

5.3.2. Simulation Results

This section demonstrates the impact of IBR on the superimposed-based relay when SLG faults are applied at different locations with two fault resistance values. In this case, the IBR is rated 75 MVA

and connected to bus R. Figures 5.5, 6, and 7 show the relay responses to SLG faults applied at 25%, 50%, and 75% of the line from bus R, respectively. The main source of fault current measured at relay S is the equivalent system source, whereas the IBR is the main source of fault current measured at relay R.

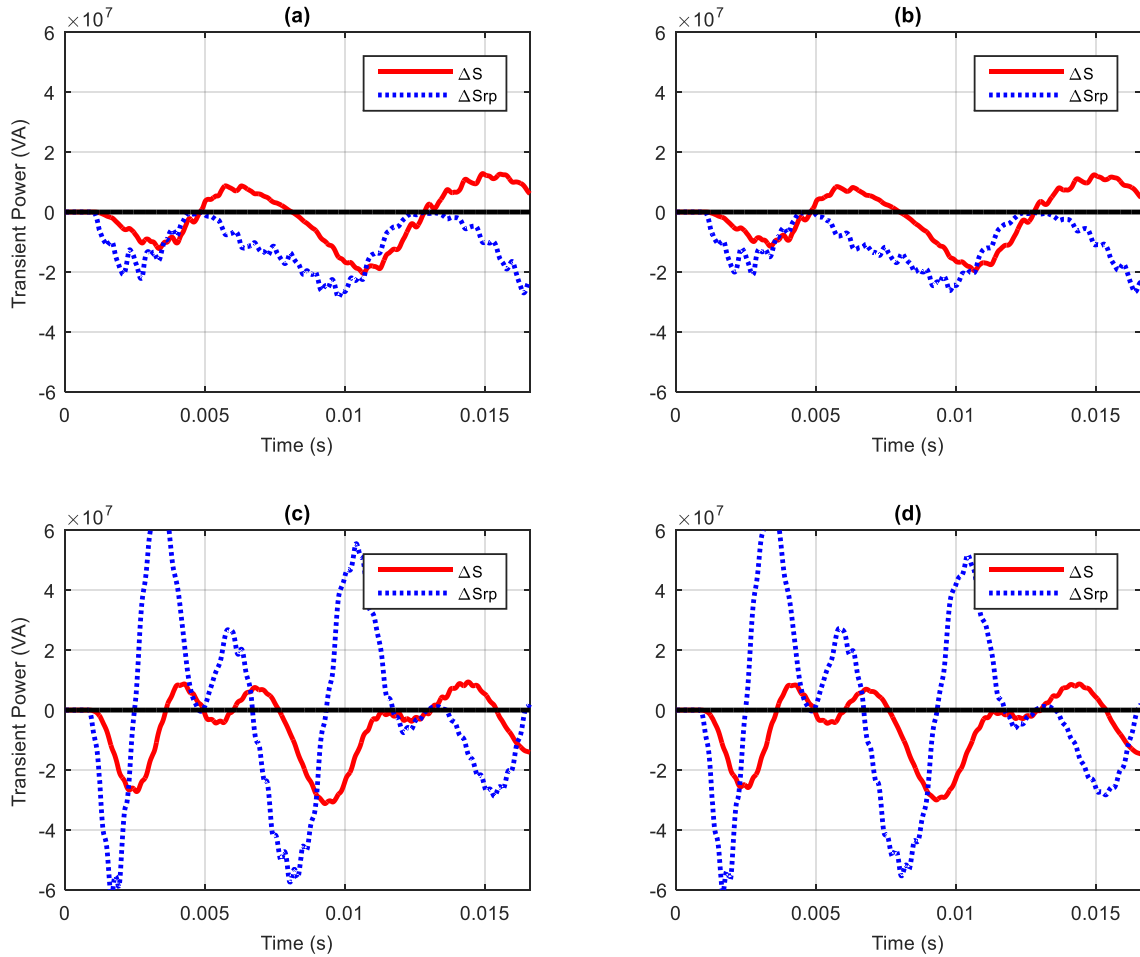


Figure 5.5 Superimposed power and replica power for SLG faults at 25% of the line from bus R: (a) relay S with $R_f = 0\Omega$, (b) relay S with $R_f = 2\Omega$ (c) relay R with $R_f = 0\Omega$, and (d) relay R with $R_f = 2\Omega$

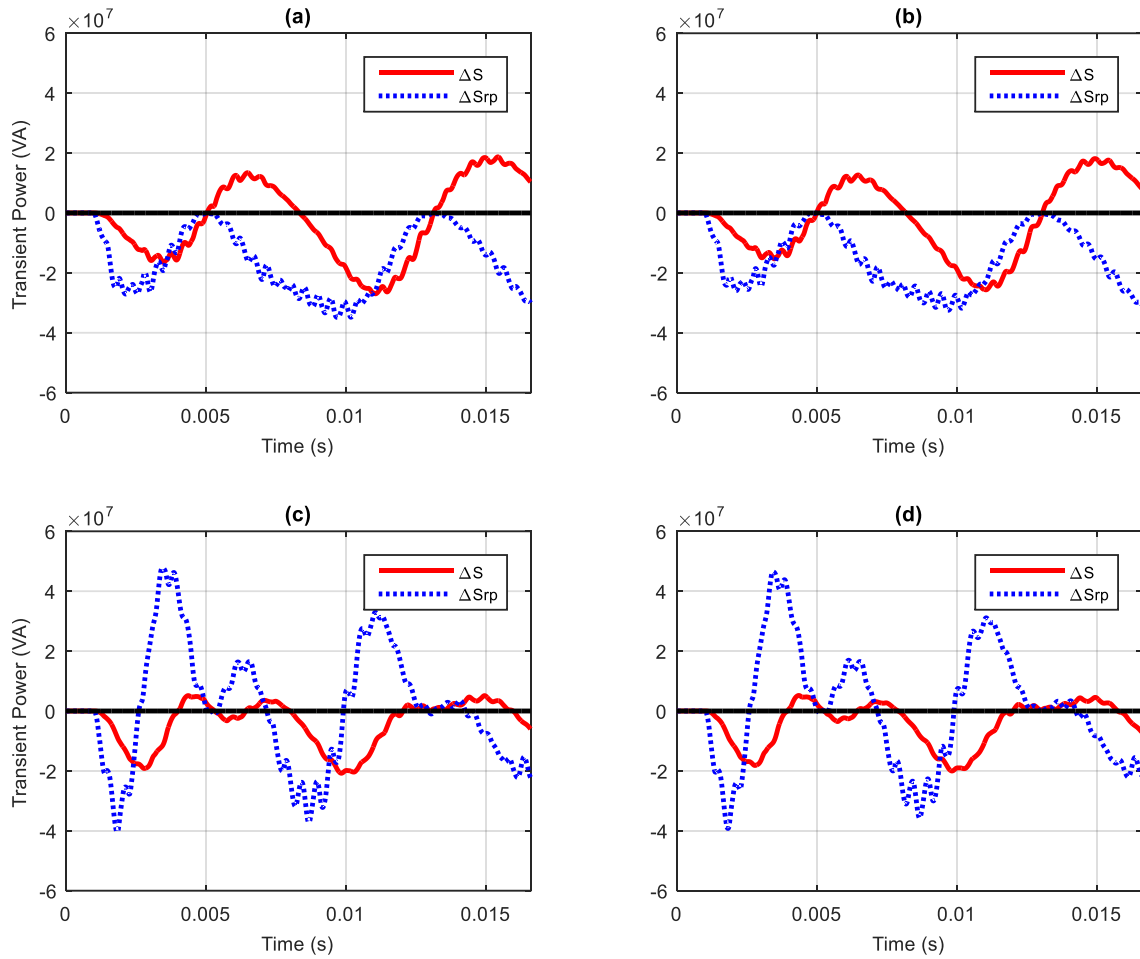


Figure 5.6 Superimposed power and replica power for SLG faults at 50% of the line: (a) relay S with $R_f = 0\Omega$, (b) relay S with $R_f = 2\Omega$ (c) relay R with $R_f = 0\Omega$, and (d) relay R with $R_f = 2\Omega$

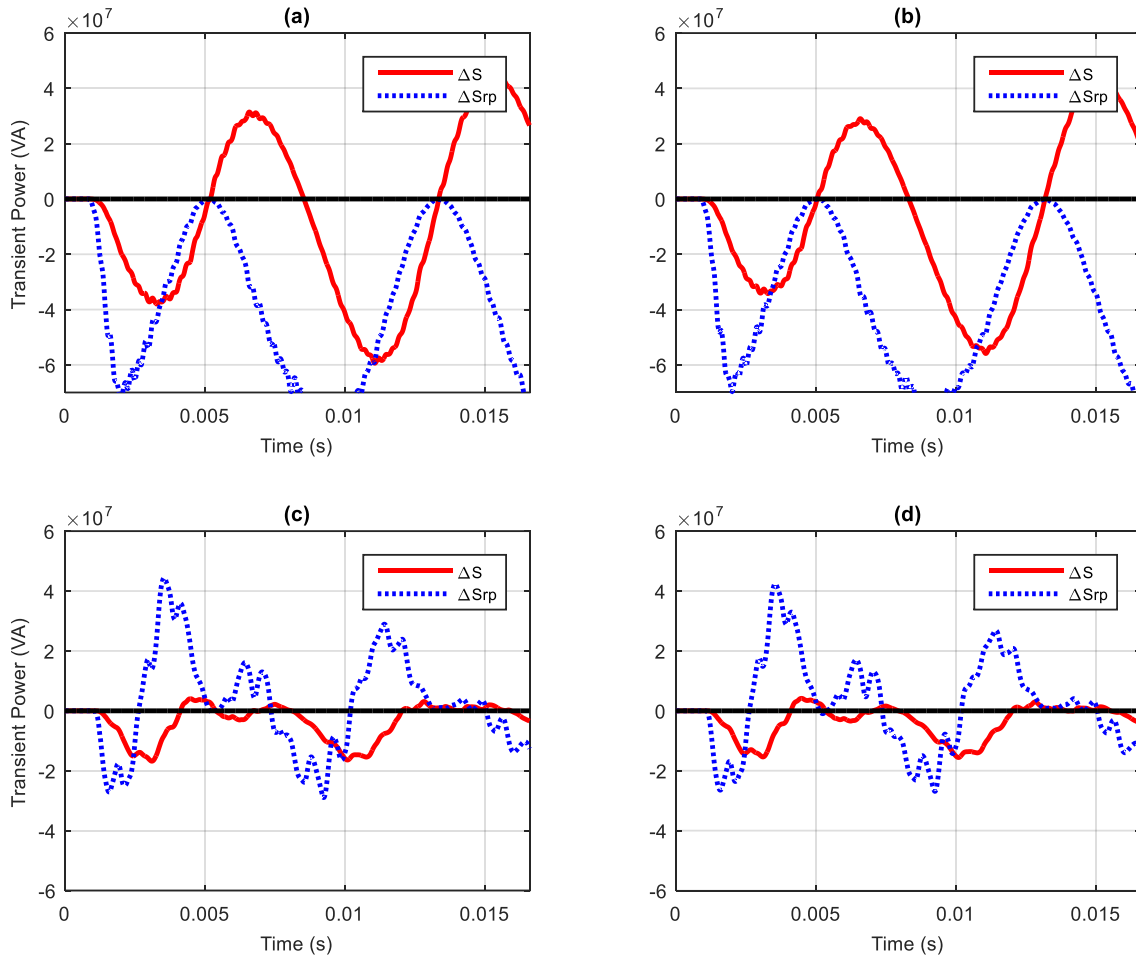


Figure 5.7 Superimposed power and replica power for SLG faults at 75% of the line from bus R: (a) relay S with $R_f = 0\Omega$, (b) relay S with $R_f = 2\Omega$ (c) relay R with $R_f = 0\Omega$, and (d) relay R with $R_f = 2\Omega$

Through all of the simulation cases of the three fault locations and the two fault resistance values, relay S superimposed replica power indicates the correct fault direction by providing negative power, as shown on (a) and (b) in Figures 5.5, 6, and 7. As discussed earlier, the replica power provided a more reliable signal because the dc offset is eliminated. However, superimposed power provides negative power in the first quarter cycle but then changes polarity to positive, which may lead to failure to indicate the correct direction.

On the other hand, relay R does not provide reliable replica power signals that would allow the directional element to indicate the correct fault direction, as shown in (c) and (d) in Figures 5.5, 6, and 7. As discussed earlier, the leading cause of this issue is the IBR controller's response to the fault since the IBR is the main source of fault current measured by relay R. However, superimposed power provides a more reliable signal that is mostly negative power in the first quarter cycle.

5.3.3. Additional Case and Discussion

The same issue of not indicating the correct fault direction is observed when IBR only rated 10 MVA, further limiting the maximum fault current that the PV installation can provide. Figure 5.8 shows the relays' response to SLG faults applied at the midpoint of the line.

The same issue observed for the IBR in the early cases appears for three-phase, line to line, and double line to ground fault types when the IBR is connected, either with the 74 MVA rating or the 10 MVA rating.

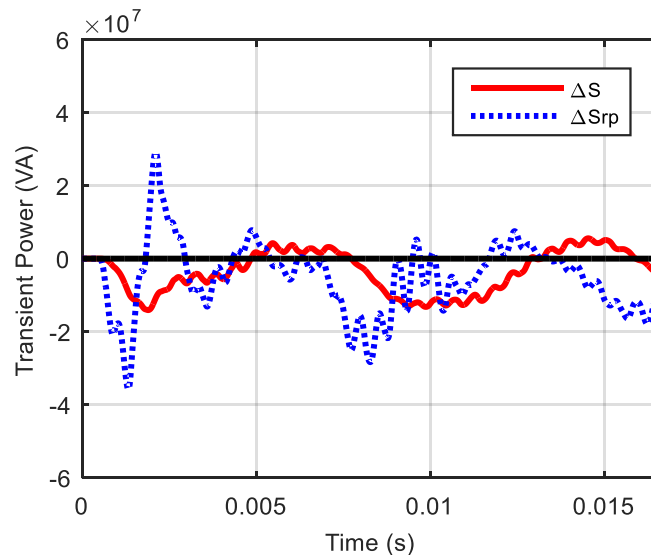


Figure 5.8 Superimposed power and replica power measured at relay R for SLG fault with $R_f = 0\Omega$ at 50% of the line when IBR rated 10 MVA

If the results in Figure 5.8. are compared to Figure 5.6 (c), it can be seen that the severity of the IBRs' impact on superimposed quantities-based protection is linked to the IBR rating. The reason is that the amplitude of the nonlinear behavior seen in the superimposed current signal is less because of the limited fault current supplied by the lower-rated IBR. Another observation is that different fault locations change the superimposed power and replica power magnitudes, as shown in (c) and (d) in Figures 5.5, 6, and 7. In all simulated cases where the IBR is connected to bus R as the main source of fault current, the superimposed replica power fails to indicate the correct fault direction. However, the superimposed power method provides more reliable signals when the IBR is the primary source of fault current, which may indicate the correct fault direction if the superimposed element's threshold is set accordingly.

5.4. Conclusion

The impact of IBRs on superimposed-based protection is discussed and demonstrated using EMTP-RV simulations. The superimposed replica power method indicates the correct fault direction when a conventional system source is the main source of fault current. On the other hand, the simulation results show that IBR negatively impacts superimposed replica power quantities. Superimposed replica power does not indicate the correct fault direction when the IBR is the main source of fault current, particularly with a high IBR MVA rating. The primary cause of the fault direction detection issue is the impact of the IBR's fast inverter current controller response on the superimposed current quantities. However, the superimposed power quantities method appears more reliable when the IBR is the source of fault current but less reliable for the conventional system source. Testing the dynamic behavior of multiple IBRs is left for future work.

Chapter 6: Impact of Distributed Inverter-Based Resources on Incremental Quantities-Based Protection

This chapter contains a paper scheduled to be published in the Proceedings of the 2021 IEEE Power Energy Society General Meeting [15].

6.1. Introduction

Inverter-based resources (IBRs) such as solar photovoltaic (PV) generation and type 4 wind turbines are increasingly integrated into power systems. Unlike synchronous generators (SG), IBRs have no inherent inertia. Thus, the overall power system inertia in the large power grid and microgrids may decrease with the increasing percentage of IBRs, decreasing the critical clearing time to retain stability for severe faults [76]. Time-domain-based protection offers high-speed protection where sub-cycle fault detection is possible. Time-domain protection consists of traveling-wave and incremental-quantities elements. Traveling-waves are generated by faults and propagate from the fault location to the line terminals with possible fault detection of one millisecond [74].

Incremental quantities are instantaneous voltage and current components that become non-zero after a fault occurs. High-speed directional elements use the incremental algorithm to indicate fault direction based on the relative polarities of the transient voltages and currents. The quantities mostly dependent on the electric network parameters, whereas power system load flow has minimum impacts. The directional element can give a fault direction indication in as little as four milliseconds [43], [44], [77].

Integrating IBRs on distribution systems creates protection challenges where traditional protection schemes might fail to detect faults. Published research proposed and evaluated protection schemes, including using differential, undervoltage, adaptive overcurrent, and time-domain schemes, to name a few [13], [51], [68]. Time-domain protection can be a potential solution to clear faults faster in microgrids to maintain system stability. However, the fast control response of IBRs and their fault current characteristics impact incremental current quantities by changing both magnitude and angle. IBRs fault currents are primarily dependent on IBRs control and independent of fault locations. Most IBRs are designed to provide low fault current magnitudes around 1.2 per unit. During fault events, IBRs generate high-frequency transients for up to a cycle and typically behave as nonlinear sources [25], [28].

It is crucial to ensure that the incremental quantities-based directional element indicates the correct fault direction if IBR nonlinear fault current impacts the quantities. The motivation for investigating

the incremental quantities is the increasing interest in using incremental quantities as a protection solution for microgrids and power distribution systems with IBRs. Most research papers focus on phasor-domain-based protection and do not necessarily focus explicitly on evaluating the impact of IBRs on time-domain-based protection. This paper discusses the impact of IBRs on time-domain incremental current and voltage quantities and examines the effects on high-speed directional elements. The impact of IBRs is demonstrated on a modified version IEEE 34-bus distribution system that incorporates IBR and simulates it using the electromagnetic transients program (EMTP-RV) [56], [57].

6.2. Incremental Quantities

6.2.1. Incremental Algorithm

The incremental quantities are calculated based on finding the difference between the present values for a signal and those from a previous cycle. In the case of a fault, relays sample instantaneous currents and voltages at their terminals and compare those with memorized currents and voltages, which act as pre-fault signals. Typically, a one-cycle memory buffer temporarily holds measured currents and voltages for one power cycle of samples [43], [44], [74], [77]. The difference between the magnitude of each sample represents the incremental change, as shown in Figure 6.1.

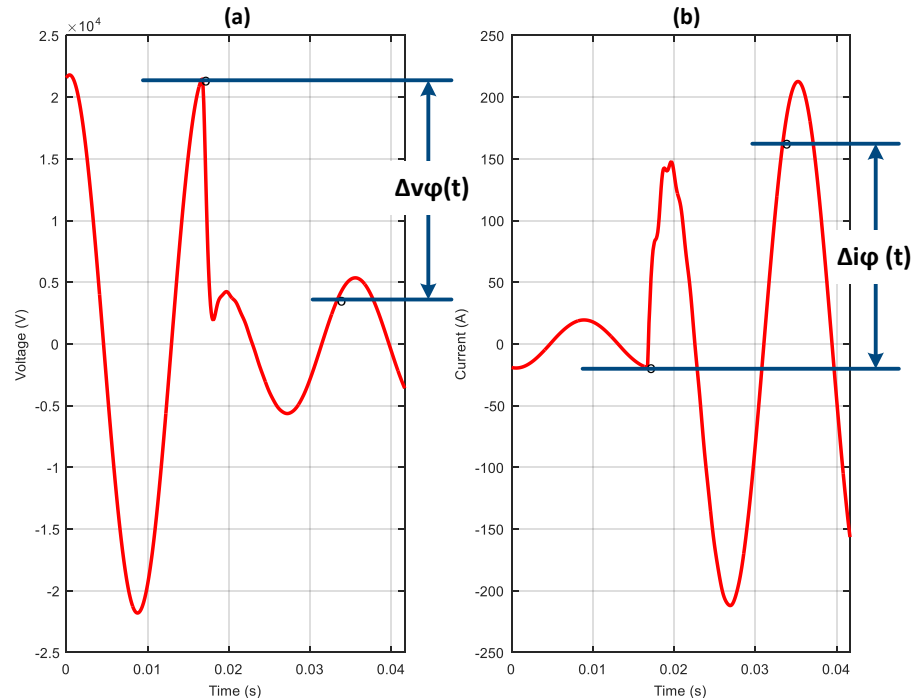


Figure 6.1 Measuring incremental quantities from waveforms: (a) voltage, and (b) current

Relays use delta filters to calculate incremental voltage and current quantities. Incremental voltage quantities $\Delta v\varphi(t)$ are calculated using the difference between instantaneous measured voltage sample $v\varphi(t)$ and memorized voltage sample $v\varphi(t - \tau)$ as in (6.1), where τ is often the period for one power system cycle. The power system frequency is used to calculate the instantaneous time delay τ for the delta filters. Similarly, current quantities $\Delta i\varphi(t)$ are calculated, as in (6.2).

$$\Delta v\varphi(t) = v\varphi(t) - v\varphi(t - \tau) \quad (6.1)$$

$$\Delta i\varphi(t) = i\varphi(t) - i\varphi(t - \tau) \quad (6.2)$$

During steady-state, $\Delta v\varphi(t)$ and $\Delta i\varphi(t)$ are zero assuming no change in the system. During faults, both quantities are equal to the fault-generated components.

6.2.2. *Methods of Processing Incremental Quantities*

Measured voltage and current signals are first sampled and then processed through anti-aliasing filters. Following this step, there are commonly used three ways to process incremental quantities to utilize in protection functions. All three methods use delta filters to calculate both voltage and current components using the approach shown for current in Figure 6.2. However, the approach applied after the delta filter differentiates each method. The first method uses time-domain incremental quantities, where delta filters come after anti-aliasing filters, and the instantaneous delta quantities are used [44]. This type has a minimum delay, but the DC offset in current waveforms may reduce the method's reliability.

The frequency-domain incremental quantities apply a replica impedance filter to the measured current before delta filters to suppress the DC offset, making this method more reliable. The replica impedance filter is a high pass filter that functions as a mimic filter [43], [49]. The last method creates phasor-domain incremental quantities where the delta filter is connected after a half-cycle or full-cycle discrete Fourier transform (DFT) filter. This method may not be considered a high-speed scheme because of the DFT.

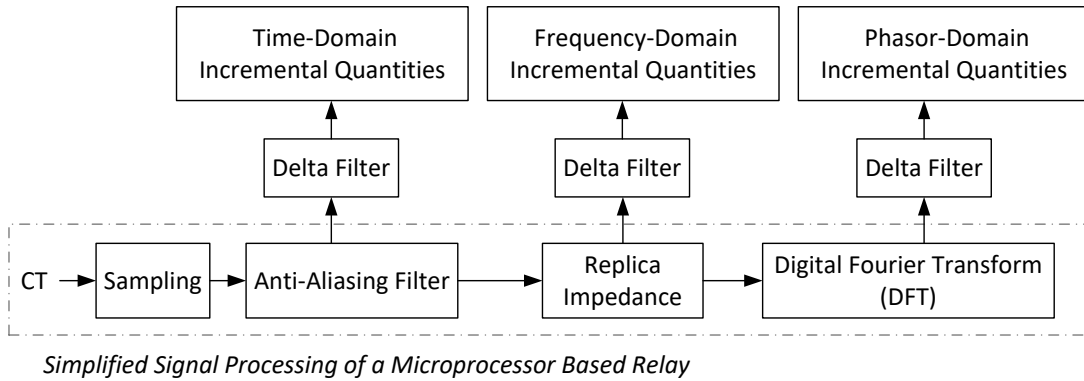


Figure 6.2 Delta filter connection defines incremental quantities method

6.2.3. Incremental Transient Power

Incremental power quantities are calculated to indicate the fault direction. In the time-domain method, the products of per phase delta current and voltage quantities are summed to find the incremental power $\Delta S(t)$ as in (6.3). Another option is to use delta replica current quantities from the frequency-domain method to find the replica incremental power $\Delta S_r(t)$ as in (6.4).

$$\Delta S(t) = \Delta va(t) \Delta ia(t) + \Delta vb(t) \Delta ib(t) + \Delta vc(t) \Delta ic(t) \quad (6.3)$$

$$\Delta S_r(t) = \Delta va(t) \Delta iar(t) + \Delta vb(t) \Delta ibr(t) + \Delta vc(t) \Delta icr(t) \quad (6.4)$$

The replica current $\Delta i\phi_r(t)$ is scaled by the source impedance ($Z_s = R_s + j\omega L_s$) behind a relay as in (6.5).

$$\Delta i\phi_r(t) = \frac{R_s}{|Z_s|} * \Delta i\phi(t) + \frac{L_s}{|Z_s|} * \frac{d}{dt} \Delta i\phi(t) \quad (6.5)$$

The incremental transient power quantities' polarity determines fault direction where negative power indicates forward faults, and positive power indicates reverse faults, as shown in Figure 6.3. In directional comparison schemes, relays use communications to exchange information on the status of their directional elements. For in-zone faults, both relays should indicate forward faults [77].

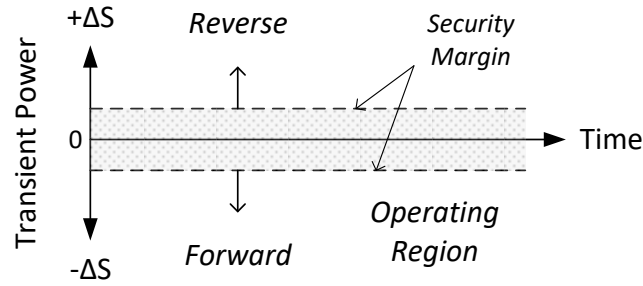


Figure 6.3 Fundamental operating characteristics of incremental directional elements show that negative-power indicates forward faults, and positive-power indicates reverse faults

Transient power quantities from (6.3) or (6.4) are integrated ($\Delta E(t) = \int \Delta S dt$) to calculate transient energy quantities to increase the directional element's security [50].

In this paper, incremental power and replica power quantities are calculated for several cases to simulate IBR's impact on the incremental directional element.

6.3. Simulation Results

EMTP-RV is used to model the power system components and the incremental quantities-based protection scheme. The model includes an inverter coupled PV system (IBRs), type-1 wind turbine generator (WTG-1), and synchronous generation (SG) with governor and exciter models. Additionally, an incremental quantities-based directional element model is developed with a directional comparison scheme.

The IBR model has a three-phase two-level voltage source converter (VSC) with six insulated-gate bipolar transistors switched at a 3 kHz switching frequency. Parallel high pass filters and a series inductive choke are connected to the AC terminal. The VSC controller uses current-regulated real and reactive power control loops with maximum power point tracking. The DQ synchronous reference frame generates D-axis and Q-axis modulation signals to control the VSC switching [31]. The IBR current is limited to 1.2 per unit through fast inverter current controller response.

6.3.1. Study Cases

A modified IEEE 34-bus distribution system is used for demonstration, as shown in Figure 6.4. Three cases are simulated to study the impact of three energy resources on incremental quantities when connected to node 848. In each case, one energy resource is connected for testing. The resources are (a) IBR, (b) WTG-1, and (c) SG, as described above. The energy resources integrate into the IEEE 34-bus system through power transformers with the wye-grounded configuration on the resources side and

delta on the grid side. Thus, no zero-sequence is provided from the integrated resources. The power ratings are 2 MW, 2.2 MVA, and 0.75 MVA for the IBR, WTG-1, and SG, respectively.

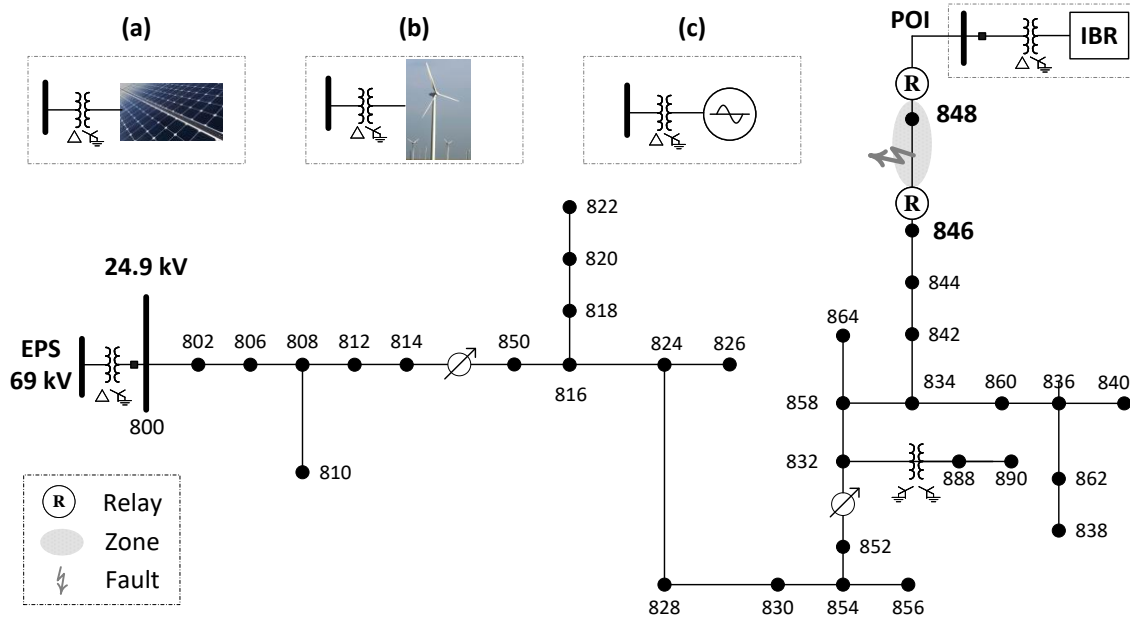


Figure 6.4 Modified IEEE 34-bus system: (a) IBR, (b) WTG-1, and (c) SG

Relay 846 and Relay 848 are placed at nodes 846 and 848, respectively, to protect the feeder between the two nodes. For in-zone faults, the two relays indicate forward. In-zone three-phase (3PH), double line to ground (DLG), line to line (LL), and single line to ground (SLG) faults are applied between 846 and 848. Fault resistance (R_f) is zero ohms in all cases. Each relay has an incremental quantities-based directional element. The incremental power and replica power are calculated using equations (6.3) and (6.4), respectively. The two incremental methods are tested for each resource case and fault type.

6.3.2. Fault Current Characteristic

Figure 6.5 shows the responses of the three resources to in-zone 3PH faults. The currents are measured at Relay 848 terminal. The IBR response in Figure 6.5 (a) and (b) shows a high-frequency transient for the first one-quarter-cycle, where the control acted fast to regulate the IBR current. Figure 6.5 (b) shows a zoomed-in view of the first part of Figure 6.5 (a). The IBR controller then gradually increases the current to support the system voltage. IBR behavior is different from the other two resources. Figure 6.5 (c) and (d) show the WTG-1 and SG responses, respectively. Both resources provided high magnitude currents during the 3PH faults.

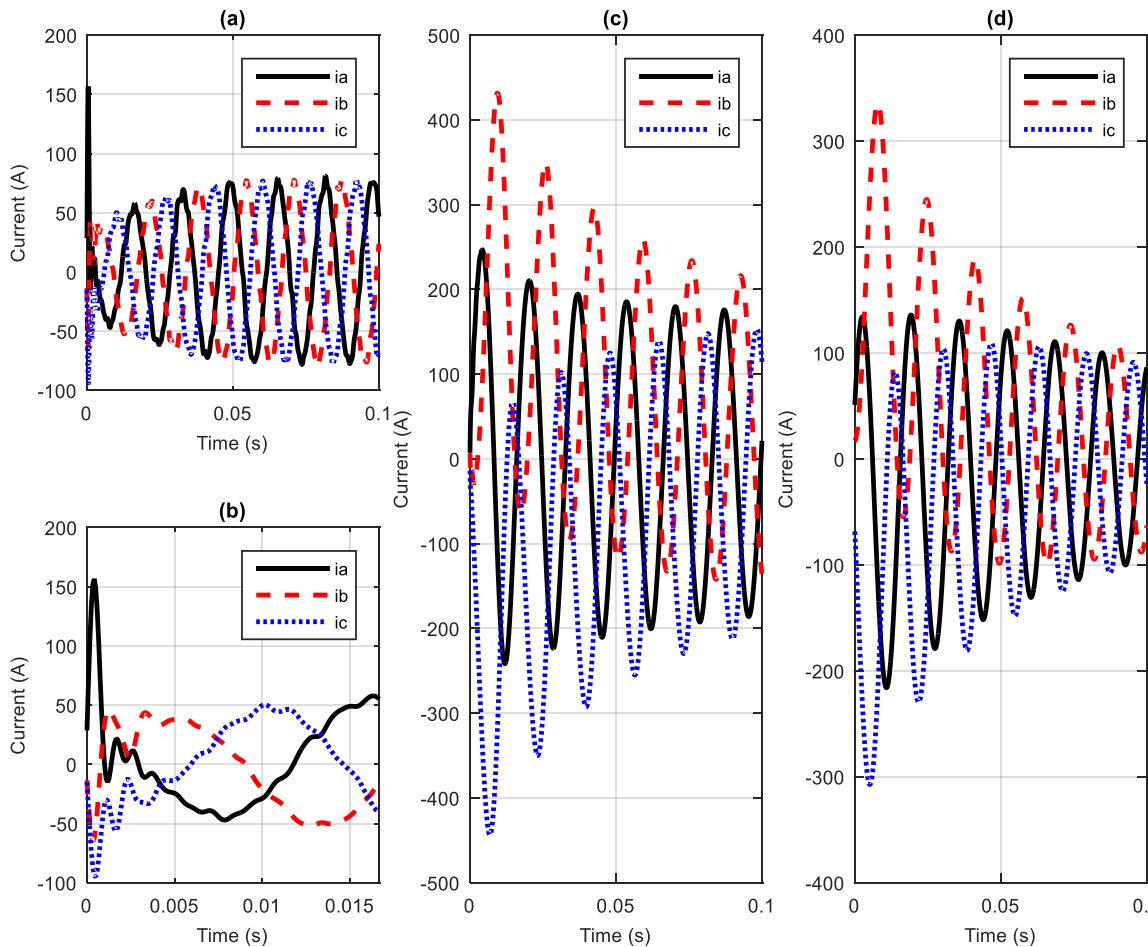


Figure 6.5 Primary three phase currents measured at Relay 848 during in-zone 3PH faults: (a) IBR, (b) zoom in IBR (c) WTG-1, and (d) SG

6.3.3. Incremental Quantities Results

The relay 846 directional element response to the SLG faults for the three resources are shown in Figure 6.6 (a) IBR, (b) WTG-1, and (c) SG. The figure shows incremental quantities (1) delta voltage, (2) delta current and replica delta current, and (3) delta power and replica delta power reading down the column. The directional element detects the correct direction, which is forward since the power is negative. The resources do not impact relay 846 because the fault current is provided from the grid side source.

The relay 848 directional element response to the SLG faults for the three resources is shown in Figure 6.7 with column (a) IBR, (b) WTG-1, and (c) SG. The figure shows incremental quantities (1) delta voltage, (2) delta current and replica delta current, and (3) delta power and replica delta power reading down the column. The Relay 848 directional element does not indicate the correct SLG fault

direction when the IBR is connected, as shown in Figure 6.7 (a-3). Neither the delta power nor the replica power provides reliable signals that would allow the directional element to indicate the correct fault direction. In this case, the fault current is mainly supplied from the IBR. As stated earlier, incremental quantities primarily depend on electric network parameters, but IBRs' fault currents primarily depend on the control system. Thus, the issue comes from the delta current, as shown in Figure 6.7 (a-2).

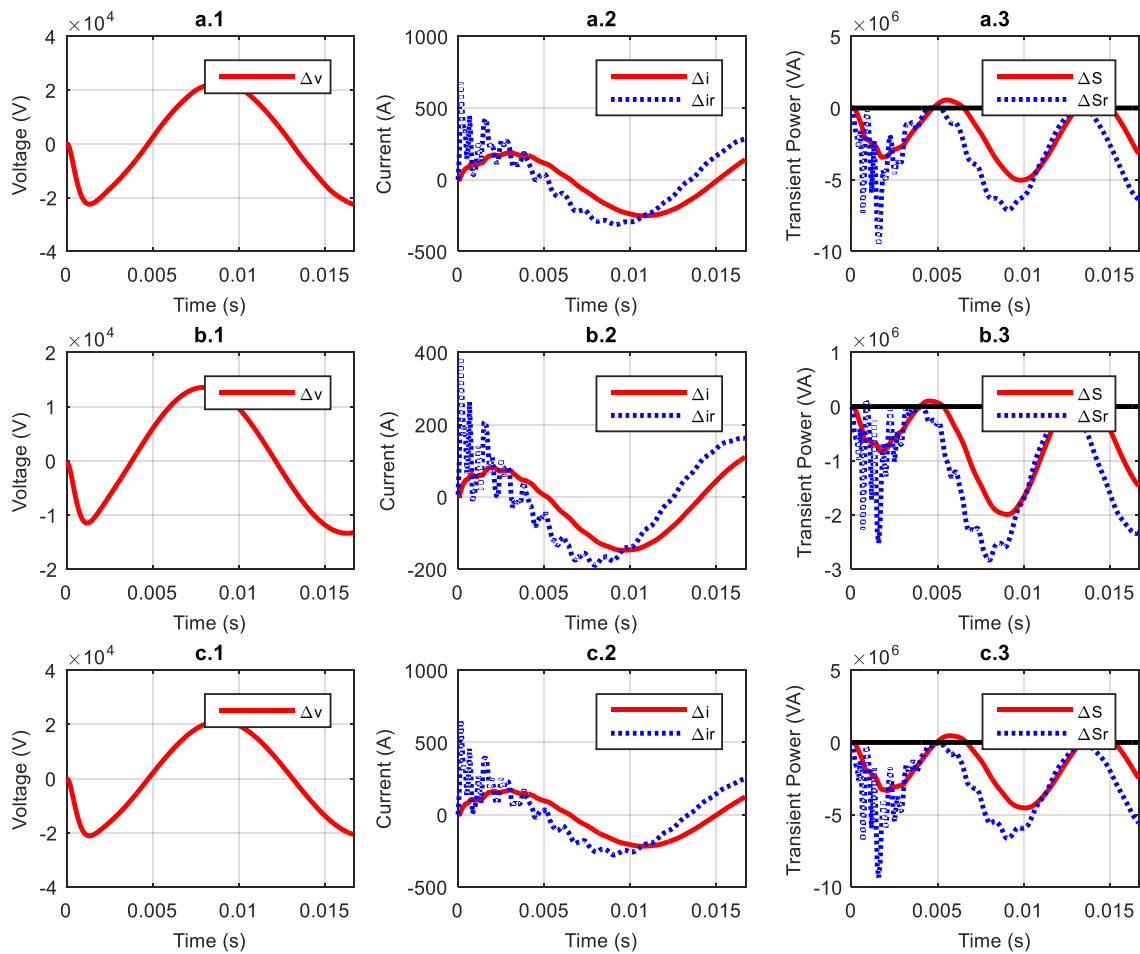


Figure 6.6 Relay 846 incremental signals during SLG faults: (a) IBR, (b) WTG-1, and (c) SG; Where (1) delta voltage, (2) delta current and replica current, and (3) delta power and replica power

The directional element indicates the correct direction when WTG-1 and SG are connected, as shown in Figure 6.7 (b) and (c), respectively. During the SLG fault, the two generators provided fault currents with DC offsets reflected in the delta current components. However, replica power provided a more reliable signal because the replica impedance filter suppressed the DC offset in current waveforms, as shown in Figure 6.7 (b-3) and (c-3). The replica delta current components are shifted if

compared with the delta current to correct for the DC offset from WTG-1 and SG, as shown in Figure 6.7 (b-2) and (c-2), respectively.

The IBR does not impact the delta voltage quantities because the IBR's control system regulates the current. Figure 6.7 (a-1) shows the delta voltage quantities during the SLG fault. Since the IBR voltage support during the fault is limited, high delta voltage quantities are expected. The WTG-1 and SG resources also provided similar delta voltage quantities, as shown in Figure 6.7 (b-1) and (c-1), respectively.

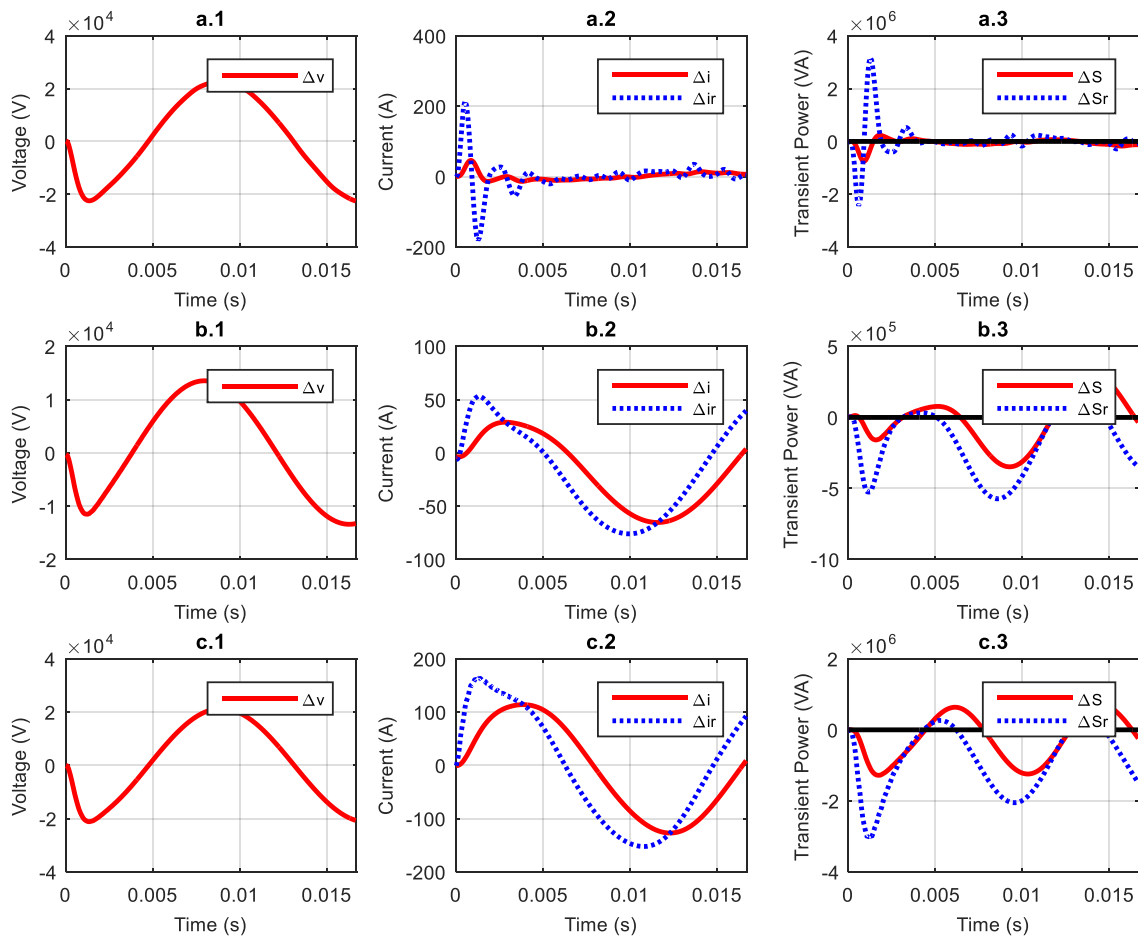


Figure 6.7 Relay 848 incremental signals during SLG faults: (a) IBR, (b) WTG-1, and (c) SG; Where (1) delta voltage, (2) delta current and replica current, and (3) delta power and replica power

Similarly, Figure 6.8 shows Relay 848 responses to different fault types with columns showing (1) 3PH, (2) DLG, (3) LL faults, and rows (a), (b), and (c) indicating IBR, WTG-1, and SG respectively. The same issue observed for the IBR in the early cases appears for the three fault types when the IBR

is connected, as shown in Figure 6.8 (a-1), (a-2), and (a-3). The directional element does not indicate the correct fault direction when the IBR is the source of fault current. On the other hand, Relay 848 indicates the correct fault direction when WTG-1 and SG are connected, as shown in Figure 6.8 (b) and (c), respectively. Similar to the results SLG case, the replica delta power signals are more reliable than the delta power for these fault types with decaying dc offsets.

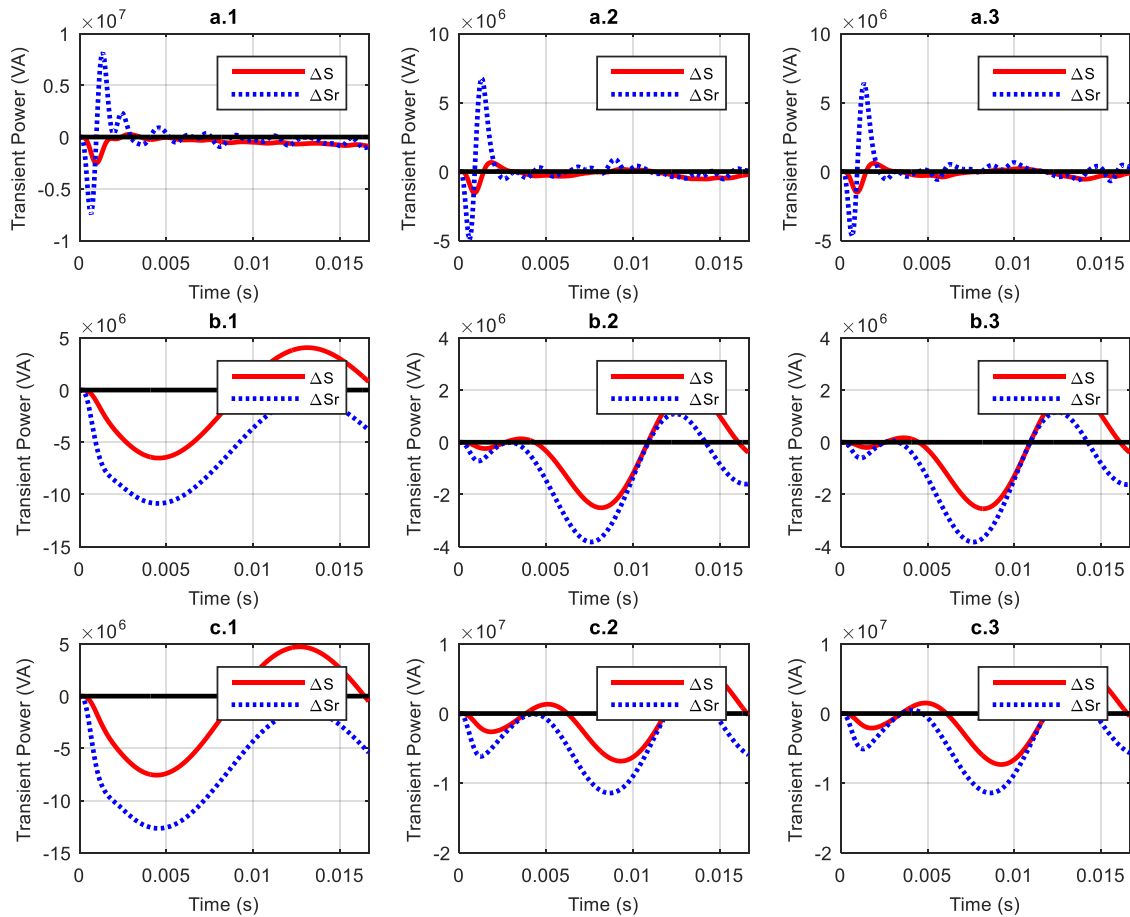


Figure 6.8 Relay 848 transient power and replica power: (a) IBR, (b) WTG-1, and (c) SG; Where (1) 3PH, (2) DLG, and (3) LL faults

6.3.4. Additional Cases

The same set of tests was conducted with the IBR source present, with different conditions: (a) non-zero fault resistance, (b) IBR controlled to vary reactive power to regulate node voltage, and (c) move fault location to branch between nodes 816 and 824 and move measurement points to those nodes. The additional cases demonstrate that the impact of IBRs on the incremental directional element is still present in these different scenarios.

In the first case, several fault resistance values were tested. The SLG fault results with $R_f = 10$ ohms on the primary 24.9 kV system are shown in Figure 6.9 (a), where (1) delta voltage, (2) delta current, and replica current, and (3) delta power and delta replica power. The results were similar with other fault resistance values. The incremental quantities directional response is not reliable. The delta power and replica power quantities do not indicate the correct fault direction, as shown in Figure 6.9 (a-3).

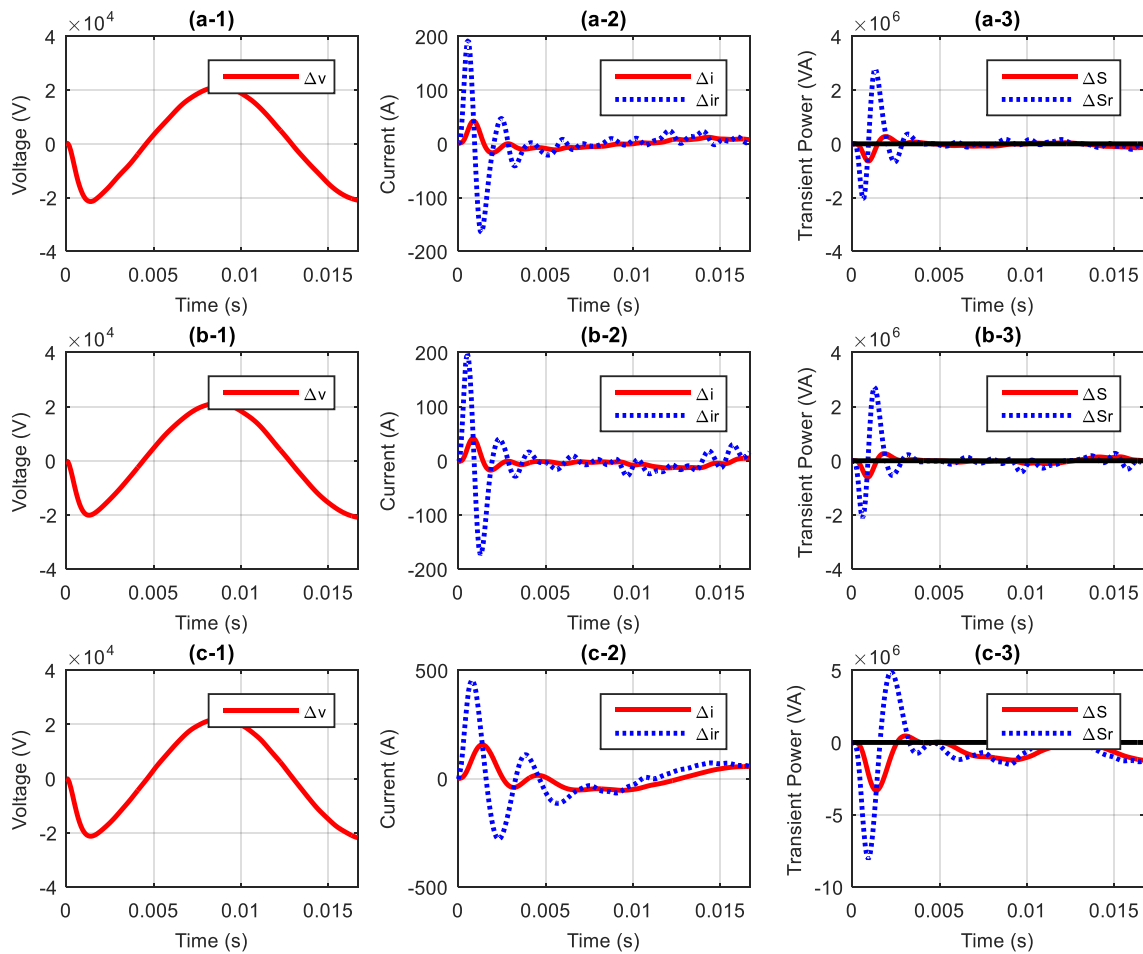


Figure 6.9 Incremental signals during SLG faults: (a) $R_f = 10$ ohm, (b) IBR voltage-control, and (c) Relay at 824; Where (1) delta voltage, (2) delta current and replica current, and (3) delta power and replica power

The second case examines changing the IBR inverter from reactive power control to voltage regulation mode, where the incremental quantities response for SLG fault is shown in Figure 6.9 (b). The delta power and replica power quantities in Figure 6.9 (b-3) show the same issue of not indicating

the correct fault direction. The IBR voltage regulation control mode provides more reactive power and voltage support during the fault, but it does not change the fault currents characteristic.

The last case tests the directional element but in a different location while the IBR is still connected to node 848. Two relays are placed at nodes 816 and 824, and faults are applied on the feeder between the two nodes. Figure 6.9 (c) shows the SLG fault results when the location is changed. The delta power signal in Figure 6.9 (c-3) might be less impacted because the relay at 824 is far from the IBR bus. However, the directional element still does not indicate the correct fault direction.

In a final set of cases, the IBR transformer configuration is changed to wye-grounded on the grid side and delta on the IBR side. Figure 6.10 shows Relay 848 delta power and replica power when SLG faults are applied with (a) $R_f = 0$ ohms and (b) $R_f = 10$ ohms. Having a zero-sequence path might reduce the IBR's impact on the incremental directional element, but it does not eliminate the misoperation.

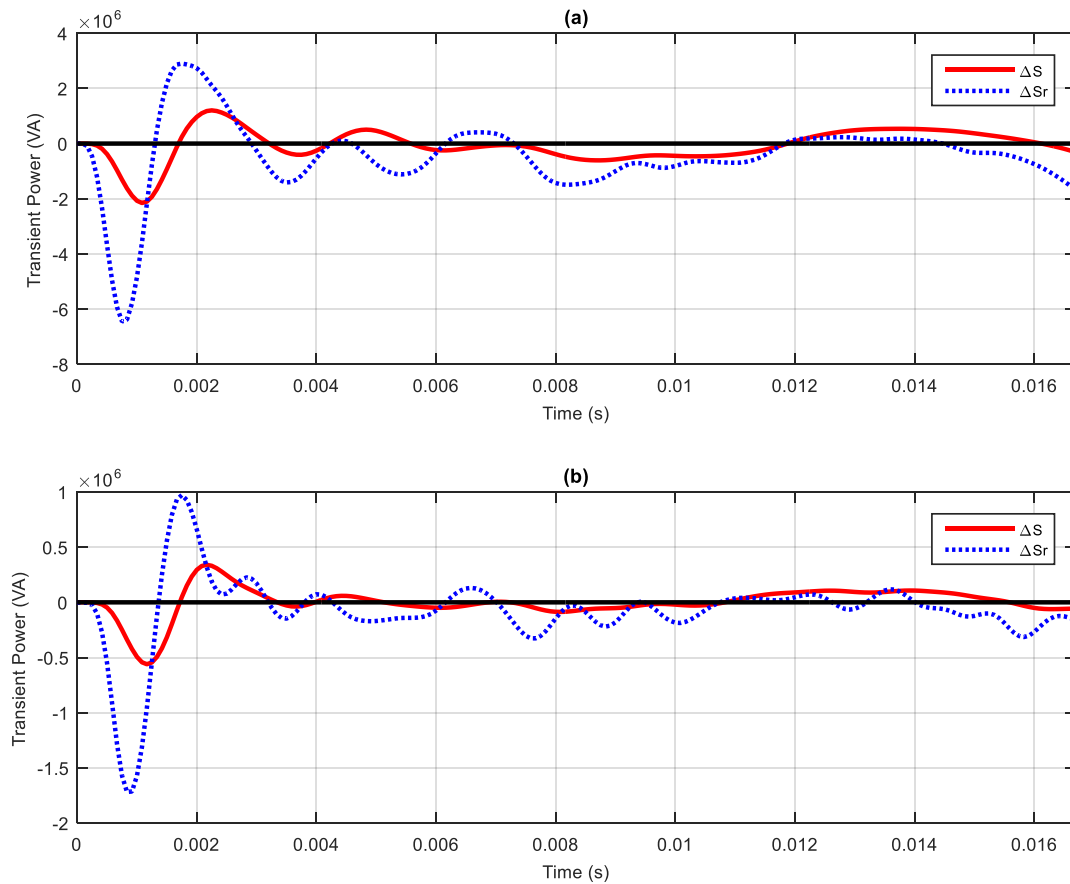


Figure 6.10 Relay 848 transient power and replica power during SLG faults with IBR and zero-sequence path: (a) $R_f = 0$ ohm, and (b) $R_f = 10$ ohm

Having the IBR as a source negatively impacts the incremental quantities-based directional element's decision. Applying a directional comparison scheme or using the quantities to detect the fault direction is not reliable, with the IBR present as the main source of fault current. The primary cause of the fault direction detection issue is the impact of the IBR control response on the incremental current quantities. The severity of the IBRs' impact depends on how close the IBR location relative to the incremental quantities-based relays.

6.4. Conclusions

The impact of IBRs on incremental quantities-based directional elements is demonstrated on a modified IEEE 34-bus distribution system with distributed energy resources simulated using EMTP-RV. The simulation results show that IBRs negatively impact incremental current quantities compared to the responses of synchronous generators or type-1 wind turbine generators. This negative impact caused the incremental quantities-based directional element to fail to detect the correct fault direction since it is based on the current and voltage quantities. However, the presence of IBRs does not impact the voltage quantities. Thus, the only reliable signal is the voltage quantities, which can only detect the presence of faults but cannot identify the direction of faults without reliable current direction. Testing microgrid systems during different operation modes and variable percentages of IBRs penetration levels are left for future work.

Chapter 7: Time-Domain Protection Scheme for Microgrids with Aggregated Inverter-Based Distributed Energy Resources

This chapter contains a paper that is submitted to the IEEE Transactions on Smart Grid [16].

7.1. Introduction

Each year, more electricity is generated from renewable inverter-based resources (IBRs), such as solar photovoltaic (PV) and type 4 wind turbines. In 2018, PV accounted for 55% of new global renewable capacity, and wind turbines accounted for 28%. Nine countries supplied 20% of their electricity from these resources. This growth is due to the rapid decline in the generation costs of PV and wind resources [1]. Another factor is the impact of integrating IBRs into power systems as distributed energy resources (DERs). Bringing IBRs close to consumers can increase electricity delivery's resilience and reliability by reducing the size and duration of power outages for most end-users [2], [3].

This idea led to the concept of forming subsystems or "microgrids" to eliminate the need for central dispatch and with the ability to operate in grid-isolated mode [5], [6]. Microgrid systems operate, control, and protect predefined subsystems while connecting or disconnecting from the electric power systems (EPS) through the point of common couplings (PCC). The two operation modes available are known as grid-interconnected mode and grid-isolated mode, respectively [19].

Integrating high penetration levels of IBRs into microgrids creates various challenges [9]. Establishing electricity markets, regulation laws, and policies for interconnections are examples of non-technical challenges. Meanwhile, technical challenges arise from controlling and protecting microgrids [10]–[12]. Researchers identified microgrid protection issues such as variable fault current levels, bidirectional power flow, dynamic topology, and IBRs fault current contribution [27].

The dynamic behaviors of fault currents from IBRs are different from synchronous machines. Fault currents are primarily dependent on IBRs controllers and are largely independent of fault locations. Most IBRs provide low fault current magnitudes, around 1.2 pu, with less than a cycle of decaying envelopes. During the initial response, IBRs typically behave as nonlinear sources along with high-frequency transients. Most three-phase IBRs are designed to produce mostly positive-sequence currents, as a result, during symmetrical and unsymmetrical faults. IBRs inject insignificant negative-sequence currents depending upon the switching controller. IBRs only provide detectable zero-sequence currents if wye-grounded transformers connected on the grid side and delta or wye-ungrounded on the inverter side [25], [28], [36]–[38], [76].

A practical philosophy for microgrid protection is to have the same protection strategy for both grid-interconnected and grid-isolated operation modes [23]. The published research on microgrid protection has not led to a commercially available microgrid relay, according to [24]. Nevertheless, several microgrid protection schemes have been proposed, such as differential, central, undervoltage, distance, adaptive overcurrent, and time-domain protection schemes, to name a few [13], [68], [70], [78], [79]. Depending on the microgrid type, topology, and type of DER, these protection schemes might function competently. For example, [68] provides a review of a few implemented protection schemes in North American microgrid projects.

However, schemes like line current differential and central protection systems are nearly dependent on communication and probably not economically feasible to implement in residential microgrids. Undervoltage protection is difficult to coordinate and may fail to detect high-impedance faults. Distance and adaptive overcurrent protection have less accuracy during grid-isolated mode [70], [78], [79]. A common disadvantage is the relatively slow fault-clearing time, whereas having a high-speed element is critical for microgrids with high penetration levels of IBRs [76].

This paper proposes a time-domain-based protection scheme for microgrids with IBRs, which functions during grid-interconnected and grid-isolated modes. The scheme provides an ultra-high-speed sub-cycle directional element aided with low bandwidth communication channels. The time-domain directional element is based on superimposed quantities and a decoupled double synchronous reference frame (DDSRF) transformation algorithm to improve the reliability of the directional element when IBRs are present. The proposed scheme is evaluated on a modified IEEE 34-bus distribution system simulated using an electromagnetic transients program.

This paper is organized as follows. Background and the proposed scheme are discussed in Section 7.2. A study case is presented in Sections 7.3. Section 7.4 concludes the paper.

7.2. Background and Proposed Protection Scheme

Time-domain protection provides an ultra-high-speed fault directional detection [77], [80], [81]. Commercially available time-domain-based relays used for transmission line protection have functioned reliably [47]–[50]. Time-domain protection uses of traveling-wave or/and superimposed quantities. This paper focuses on the superimposed quantities element, also known as incremental quantities. Academic researchers investigate the possibility of using superimposed quantities in microgrids with different approaches [51]–[55].

The authors in [51] review several directional elements and highlight the reliability issues of each method. The authors propose a superimposed impedance-based directional element where the positive-sequence impedance is used for symmetrical faults, and a negative-sequence impedance is used for unsymmetrical faults. The authors in [52] find a system imbalance ratio using instantaneous superimposed positive, negative, and zero-sequence quantities to detect faults. In [53], the authors use a Hilbert transform and superimposed quantities-based directional element. In [54], the authors use communication-assisted energy superimposed based directional element. The authors in [55] use phasor positive and negative current sequence superimposed quantities to find faults direction and use communication between a microgrid control system and protection system.

Although [51]–[55] propose adequate primary and or backup microgrid protection schemes, investigating time-domain superimposed quantities' schemes in detail with IBRs present as the main source of fault current lies outside these papers' scope.

7.2.1. Superimposed Quantities

The calculation of superimposed quantity $\Delta x(t)$ measured at a relay terminal is based on subtracting the present $x(t)$ samples from the corresponding stored $x(t - \tau)$ samples, as in (7.1).

$$\Delta x(t) = x(t) - x(t - \tau) \quad (7.1)$$

The notation $x(t)$ in (7.1) is the input of a delta filter and can be measured voltage or current data. The $\Delta x(t)$ is the superimposed quantity for x , which is the output of the delta filter. The τ is a delay in power cycles. Commonly a one-cycle memory buffer is used to temporarily hold one power cycle of sampled data. During steady-state, $\Delta x(t)$ is zero assuming no change in the system from one cycle to the next. However, during faults, $\Delta x(t)$ value is equal to the fault-imposed component. In other words, the superimposed algorithm is based on the fault-generated components and is only influenced by the network impedance parameters. Therefore, power system load flow has minimum impact on the superimposed algorithm [43], [44], [46].

There are three common ways to calculate and utilize superimposed quantities in protection: time-domain, frequency-domain, and phasor-based. All three types use delta filters to calculate superimposed quantities [43]. However, the condition of the input of the delta filters defines each type, as shown in Figure 7.1. Delta filters for the time-domain-based approach are connected to anti-aliasing filters for minimum delay [44].

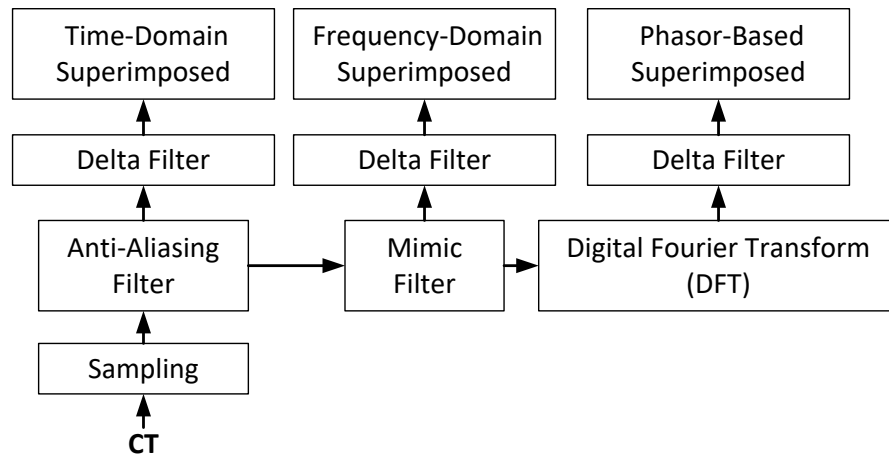


Figure 7.1 The condition of the input of the delta filters defines superimposed quantities type

In the frequency-domain approach, measured currents pass through a mimic filter to eliminate the exponentially decaying dc component [46]. The mimic filter's design criteria for superimposed quantities may differ from mimic filters used for phasor-based elements and are often referred to as a replica impedance filter. The replica impedance filter is tuned to consider the source impedance value behind a relay [50]. On the other hand, mimic filters for phasor-based elements are designed to suppress dc offset based on the time constant in cycles [82]. However, both replica and mimic filters are high pass filters and have similar behavior and impacts, such as amplifying the higher-frequency components.

The third type of superimposed quantities is the phasor-based, where the delta filter is applied after a half-cycle or full-cycle discrete Fourier transform (DFT) filter [45]. The phasor quantities are calculated after half-cycle or full-cycle depending on the DFT filter [83]. Latter, this type may not be considered as an ultra-high-speed scheme.

The following section proposes the microgrid protection scheme and an improved time-domain superimposed directional element.

7.2.2. Proposed Microgrid Protection Scheme

The proposed scheme uses time-domain directional elements and only low bandwidth communication between relays. In directional comparison schemes, relays use communications to exchange information on their directional elements' status and provide fast tripping for in-zone faults [84]. The proposed scheme is modified to allow relays to communicate within a microgrid. One relay

at a border of a zone declares forward (FWD), and one relay declares reverse (REV) for in-zone faults. For out-zone faults, both relays declare FWD or REV.

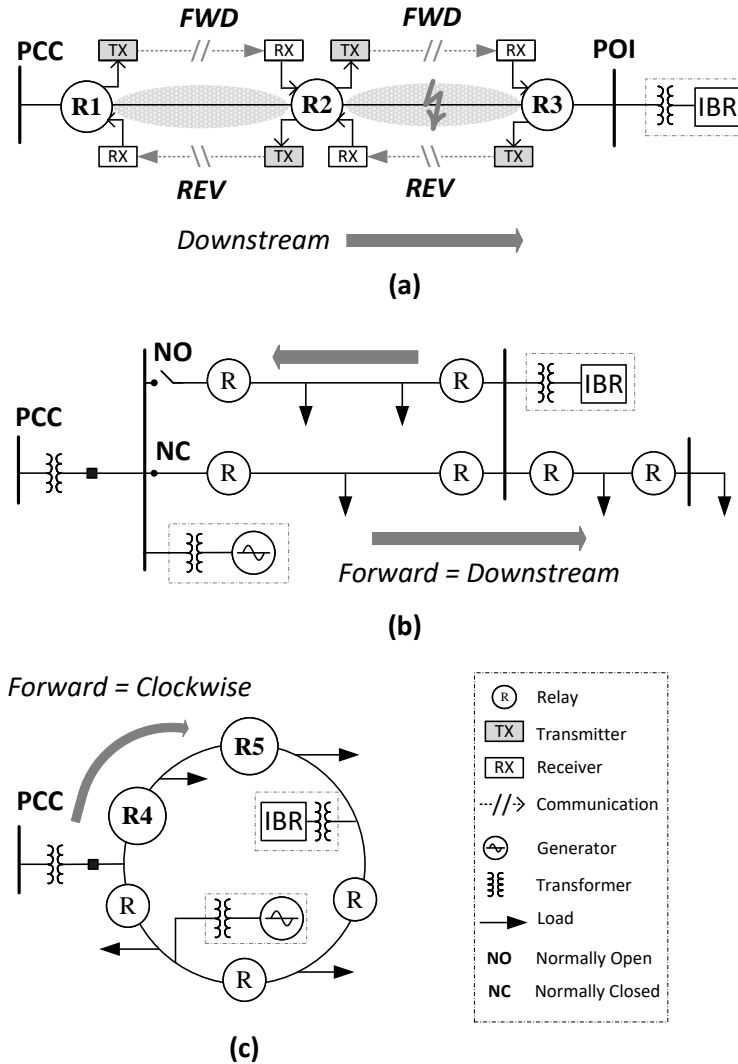


Figure 7.2 Upstream relays send forward signals to downstream relays, and downstream relays send reverse signals to upstream relays: (a) Radial system, (b) Parallel feeders with a normally open breaker, and (c) Loop system

The microgrid's PCC is chosen as a reference to define upstream and downstream. In radial systems, downstream is looking to the end of the feeder, and upstream is looking back towards the PCC. Relays assume downstream faults as FWD faults and upstream faults as REV faults. In Figure 7.2 (a), relay R2 sends FWD signals to downstream relay R3 and sends REV signals to upstream relay R1. Also, relay R2 receives FWD signals from relay R1 and receives REV signals from relay R3. For example,

if a fault is applied between relay R2 and relay R3, both relay R2 and relay R3 see in-zone fault and trip.

The scheme can be applied to dynamic microgrid topologies. For example, Figure 7.2 (b) shows two parallel feeders with normally open (NO) and normally closed (NC) breakers. This setup is just to choose a direction reference for relays, but breakers' status does not impact the protection scheme. Once the reference is chosen, a relay trips in-zone faults when it declares FWD and receives REV from the other relay.

Similarly, Figure 7.2 (c) shows a loop system where relays assume clockwise faults as FWD and anticlockwise faults as REV. For example, for in-zone fault applied between relay R4 and relay R5, as marked in Figure 7.2 (c), relay R4 sees a clockwise fault and declares forward fault, and relay R5 sees an anticlockwise fault and declares reverse fault. As a result, relay R4 sends FWD signals to relay R5, receives REV signals from relay R5, and relays trip.

7.2.3. Proposed Relay

The proposed relay includes a combination of time-domain and phasor-based protection, as shown in Figure 7.3. The time-domain protection has the directional element and the communication capability, where the phasor-based protection consists of a voltage-restrained overcurrent element and the backup elements.

The time-domain protection uses high sampling rates to calculate superimposed voltage and current quantities. First, analog voltage and current measurements are digitized after anti-aliasing filters. The digital quantities are then processed through per phase delta filters [43], [44], [46], where θ is phase-a, b, or c, as shown in Figure 7.4 (c). Delta filters use one power cycle memory buffers to hold the samples.

After the delta filters, a DDSRF is connected to improve the time-domain superimposed quantities element's reliability and calculate instantaneous symmetrical components. The DDSRF is based on using two synchronous reference frames rotating with positive and negative synchronous speed, respectively. The purpose is to decouple the effect of the negative-sequence component on the direct axis, and quadrature axis (DQ) signals detected by the synchronous reference frame rotating with positive-angular speed and vice versa [32], [85], [86].

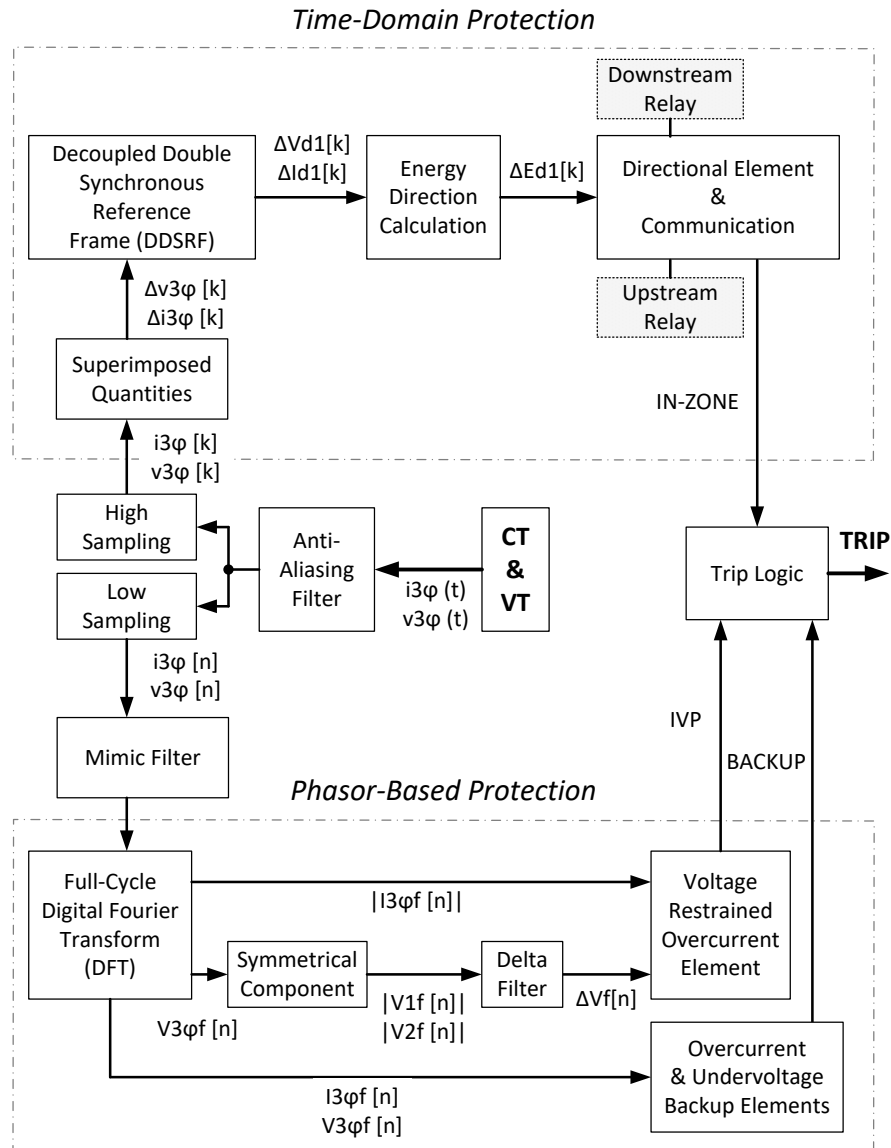


Figure 7.3 Simplified diagram for the proposed relay signal processing, time-domain protection element, phasor-based elements and communication

The overall DDSRF block diagram is shown in Figure 7.4 (a), converting three-phase voltage components to positive and negative sequence DQ components. The positive sequence decoupling algorithm is shown in Figure 7.4 (b). The DDSRF algorithm is described below in detail.

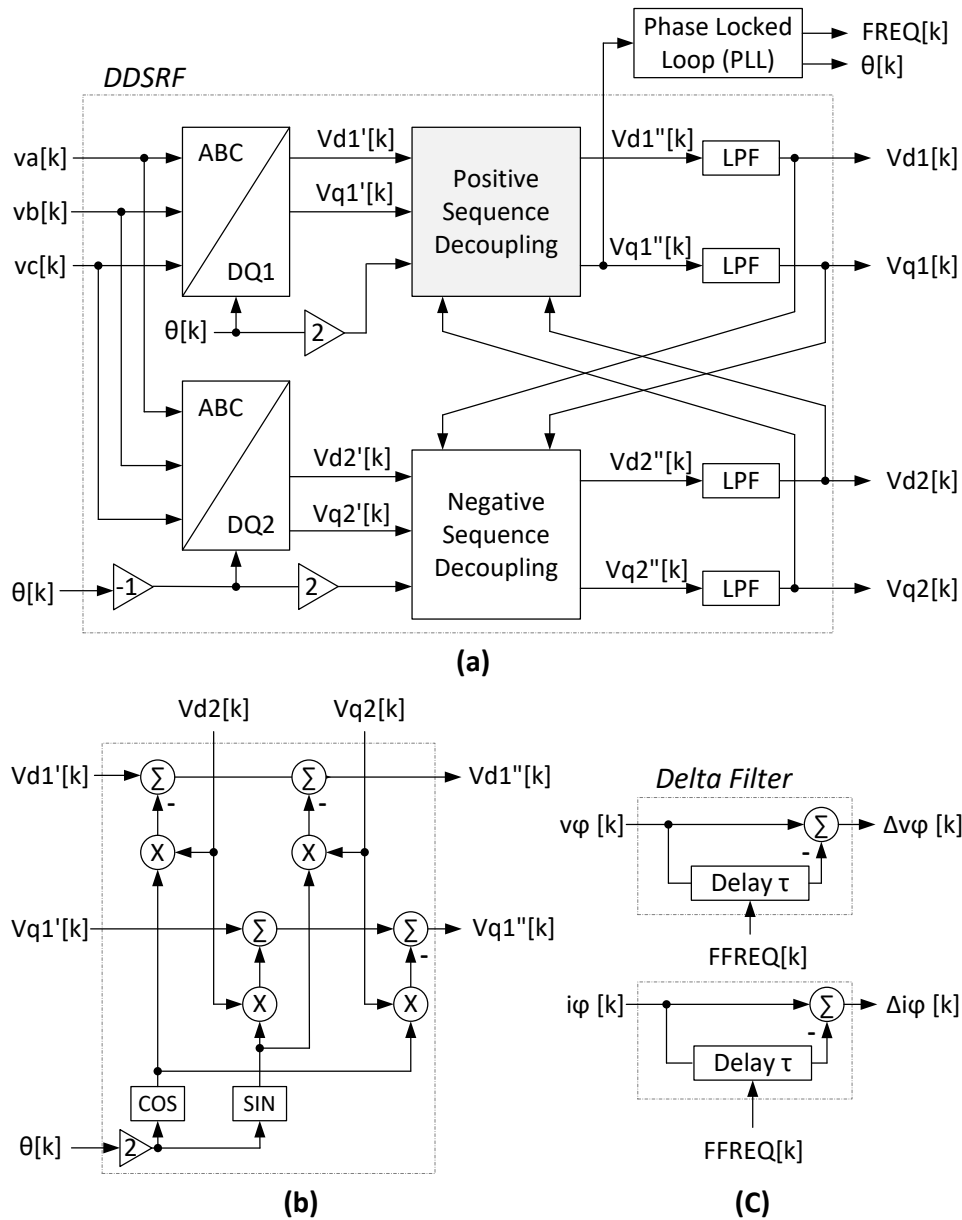


Figure 7.4 Calculating superimposed positive-sequence direct quantities: (a) Decoupled double synchronous reference frame (DDSRF), (b) Positive-sequence decoupling, and (c) Per-phase delta filters

The first step converts the three-phase voltage components to DQ components using Park's transformation [87]. The DQ signals are denoted as $Vd1'$ and $Vq1'$ for positive-sequence, where the positive DQ1 transformation is driven by positive synchronous angle θ as in (7.4).

$$\begin{pmatrix} Vd1' \\ Vq1' \end{pmatrix} = \sqrt{\frac{2}{3}} \begin{pmatrix} \cos \theta & \cos(\theta - \frac{2\pi}{3}) & \cos(\theta + \frac{2\pi}{3}) \\ -\sin \theta & -\sin(\theta - \frac{2\pi}{3}) & -\sin(\theta + \frac{2\pi}{3}) \end{pmatrix} \begin{pmatrix} Va \\ Vb \\ Vc \end{pmatrix} \quad (7.4)$$

$Vd2'$ and $Vq2'$ are the negative-sequence DQ voltage, respectively. The negative DQ2 transformation is driven by negative synchronous angle $-\theta$, respectively.

The second step decouples the double frequency negative-sequence component from the positive-sequence component as in (7.5) and, as shown in Figure 7.4 (b). Similarly, the negative-sequence components are decoupled from the double frequency positive-sequence as in (7.6).

$$\begin{pmatrix} Vd1'' \\ Vq1'' \end{pmatrix} = \begin{pmatrix} Vd1' \\ Vq1' \end{pmatrix} + \begin{pmatrix} \cos 2\theta & \sin 2\theta \\ -\sin 2\theta & \cos 2\theta \end{pmatrix} \begin{pmatrix} Vd2' \\ Vq2' \end{pmatrix} \quad (7.5)$$

$$\begin{pmatrix} Vd2'' \\ Vq2'' \end{pmatrix} = \begin{pmatrix} Vd2' \\ Vq2' \end{pmatrix} + \begin{pmatrix} \cos 2\theta & -\sin 2\theta \\ \sin 2\theta & \cos 2\theta \end{pmatrix} \begin{pmatrix} Vd1' \\ Vq1' \end{pmatrix} \quad (7.6)$$

First-order low-pass filters (LPF) with cut-off frequency $\left(\frac{\omega}{\sqrt{2}}\right)$ are applied to DQ components [32], [85]. The output quantities from the DDSRF are DQ positive-sequence components $Vd1$ and $Vq1$, respectively, and DQ negative-sequence components $Vd2$ and $Vq2$, respectively. References [32], [85] provide more analysis and explanation of the DDSRF algorithm.

The DDSRF algorithm is then used to convert per phase superimposed voltage and current quantities to DQ positive and negative sequences, as shown in Figure 7.5. However, only the superimposed positive-sequence direct voltage $\Delta Vd1$ and current $\Delta Id1$ components are multiplied to calculate the transient superimposed positive-sequence direct "power" or Watt component $\Delta Wd1$.

This Watt component is comparable to the wattmetric ground-fault detection method used in Petersen coil compensated distribution systems. A wattmetric relay can detect the correct fault direction because it depends on the "real" component of the voltage and current, which are independent of the coil and phase-to-earth capacitance currents [88], [89].

As discussed earlier, IBRs behave as nonlinear sources and produce unreliable negative-sequence currents with high-frequency transients. Using the $\Delta Wd1$ component can be more reliable in microgrids with IBRs because it depends on the direct positive-sequence components. Figure 7.6 compares three transient superimposed power methods during a single line to ground (SLG) fault where ΔS is apparent power, ΔSr is replica-apparent power, and $\Delta Wd1$ is the proposed method.

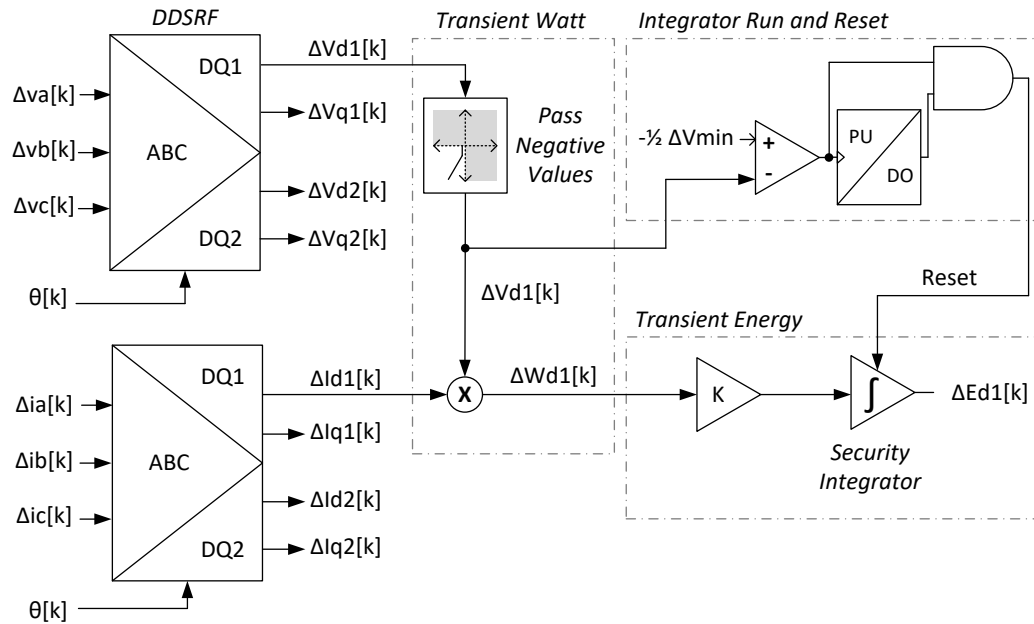


Figure 7.5 Transient superimposed positive-sequence direct Watt and energy

In general, the superimposed based directional element indicates FWD faults for negative power and REV fault for positive power [38]. In Figure 7.6 (a), the SLG fault is applied to be an FWD fault in a system with no IBRs. The ΔS method detected FWD's fault, but the sine wave crossed to the positive plane because of the current angle of dc offset. The ΔS_r overcomes this issue using the equivalent source-impedance behind the relay terminal to account for the phase angle mismatch [43], [46]. The proposed ΔW_{d1} method provided a more secure result but introduced a one-millisecond delay caused by the DDSRF filter.

The SLG fault is then applied as a REV fault in a system with an IBR, as in Figure 7.6 (b). The IBR negatively impacts both ΔS and ΔS_r because the IBR current controller responds to the fault and causes the superimposed currents to have a mixture of both inductive and capacitive currents. Thus, both methods fail to provide reliable fault direction indications.

The impact of IBRs on time-domain superimposed quantities elements is presented in [14], [15]. IBRs' fast control response impacts the current quantities by changing both magnitude and angle. Thus, using time-domain superimposed quantities to detect the fault direction is unreliable, with IBRs present as the main source of fault currents [14], [15].

On the other hand, the proposed method is more reliable since the direct positive-sequence component reduces the IBRs impact. The $\Delta Wd1$ indicates the correct fault direction with the IBR present as the main source of fault current, as in Figure 7.6.

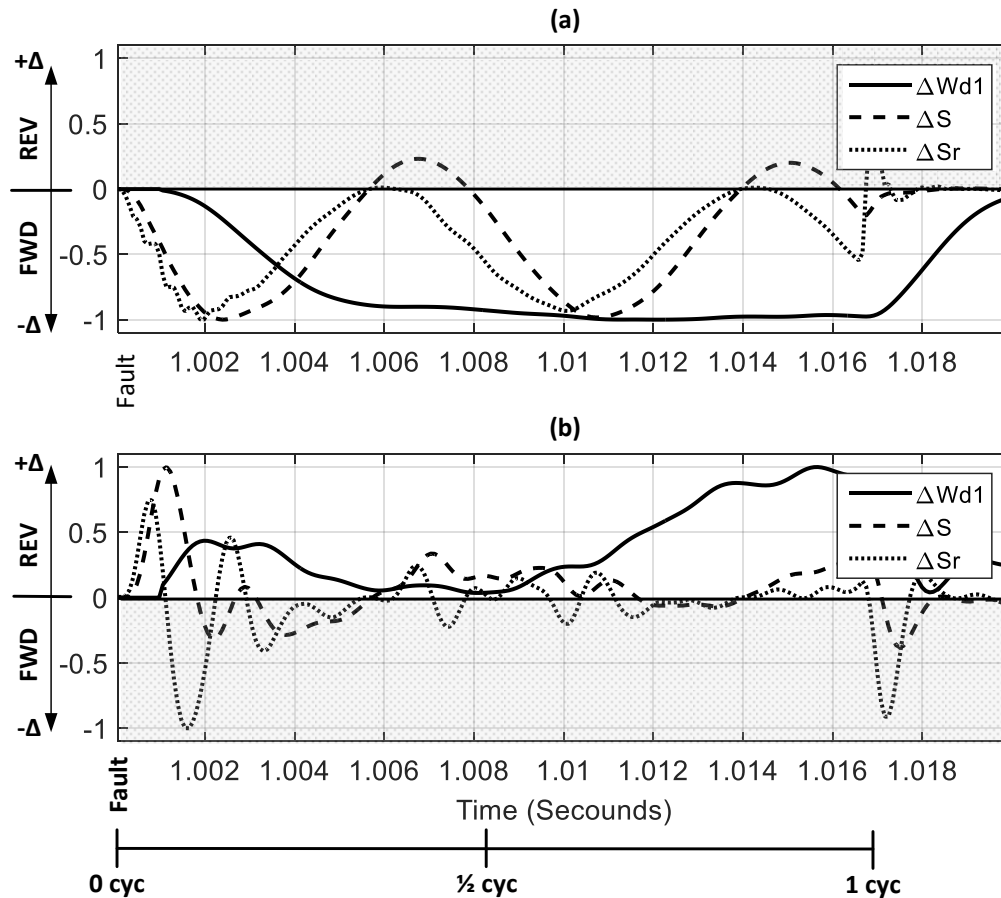


Figure 7.6 Comparison of IBRs impacts on superimposed transient Watt, apparent power, and replica power methods: (a) SLG forward fault at a system with no IBRs and (b) SLG reverse fault at a system with IBRs

Practically, transient energy is calculated instead of using transient power to increase the superimposed directional element's security [50]. Then, $\Delta Wd1$ is integrated using a run-reset integrator to calculate the superimposed positive-sequence direct energy $\Delta Ed1$, as shown in Figure 7.5. The proposed directional element depends on $\Delta Ed1$ to confirm the fault direction and uses $\Delta Vd1$ to run the security integrator.

7.2.4. Superimposed Based Directional Element Logic

The superimposed based directional element logic diagram is shown in Figure 7.7 (a). The forward and reverse logic circuits compare $\Delta Ed1$ to negative and positive security thresholds $\pm \Delta Emin$,

respectively. The thresholds are small values to create a dead-band zone. Then $\Delta E_{d1} < -\Delta E_{min}$ indicates an FWD fault, and $\Delta E_{d1} > \Delta E_{min}$ indicates a REV fault as in Figure 7.7 (b). The voltage control logic compares ΔV_{d1} to a threshold $-\Delta V_{min}$ as a fault indicator. The voltage threshold could be set as low as 5% of the system's peak line-to-neutral nominal voltage since the phasor-based protection supervises the element as described below.

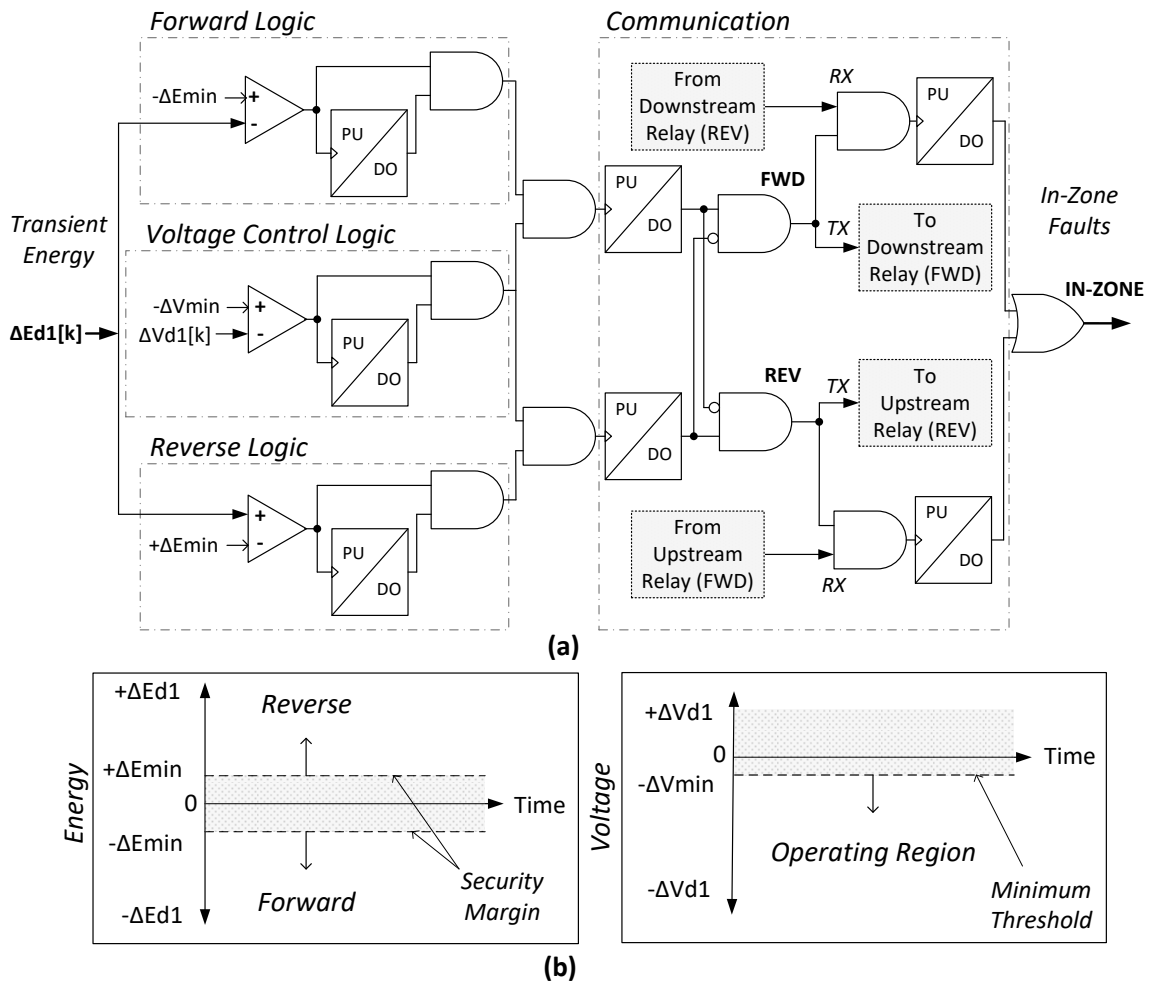


Figure 7.7 Time-domain superimposed based directional element: (a) Logic and communication scheme and (b) Operating characteristics

There are several confirmation timers to ensure the security and reliability of the element. The timers allow the element to indicate direction within the first half-cycle, which is the most reliable period in superimposed schemes. Also, timers are used to freeze the asserted FWD/REV for enough cycles to allow the element to communicate and confirm in-zone faults.

After a fault direction is confirmed, the signal is sent to a downstream relay for FWD faults or an upstream relay for REV faults. The local relay receives a signal: from a downstream relay for REV faults or an upstream relay for FWD faults. The local relay confirms IN-ZONE faults only if it: (1) asserts FWD and receives REV from downstream, or (2) asserts REV and receives FWD from upstream.

The element only needs low bandwidth communication to send and receive signals. There are several choices for distribution communications, such as direct pilot wire, multiplexed fiber-optic, and spread-spectrum radio. Communication systems vary in speed, cost, and reliability [90]. For demonstration purposes, an average communication speed of four milliseconds is assumed.

7.2.5. Phasor-Based Element and Trip Logic

The directional element is supervised by a phasor-based [versatile] voltage-restrained overcurrent element, as shown in Figure 7.8. The three-phase currents are filtered by the mimic filter and the DFT filter, as shown in Figure 7.3. The overcurrent element compares three-phase currents I_{af} , I_{bf} , and I_{cf} to a current threshold ϵ_i , which can be set to a sensitivity level that is less than load currents, as shown in Figure 7.8.

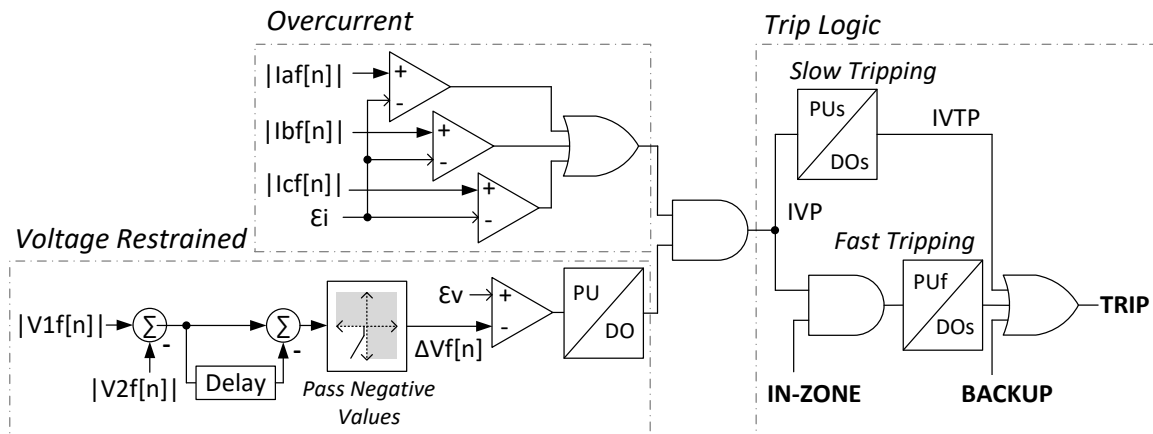


Figure 7.8 Phasor-based superimposed voltage-restrained overcurrent element and trip logic with fast and slow tripping

The unsymmetrical voltage phasors from the DFT filter are converted to symmetrical phasors using symmetrical components transformation to calculate the phasor-based positive-sequence and negative-sequence voltages for the voltage-restrained overcurrent element, as shown in Figure 7.3. Then, the difference between positive-sequence voltage V_{1f} and negative-sequence voltage V_{2f} is calculated, as shown in Figure 7.8.

After that, the phasor-based superimposed voltage quantity ΔV_f is calculated using a delta filter that functions as the time-domain-based delta filter discussed earlier. Finally, the overcurrent is restrained by the delta voltage ΔV_f where the threshold ε_v determines the element sensitivity, as shown in Figure 7.8. A typical setting is 20% of the nominal system voltage. Details about using the phasor-based voltage-restrained overcurrent elements in microgrids are presented in [13].

The voltage-restrained overcurrent element asserts IVP if both overcurrent and voltage-restrained comparators are satisfied. The relay then uses fast tripping logic if both IVP signal from Figure 7.8 and IN-ZONE signal from Figure 7.7 (a) assert where the timer pickup P_{UF} can be set to zero for maximum speed. In case of communication failures, the relay uses IVP only for slow tripping logic where timer pickup P_U s should be coordinated with other relays, which is not discussed in this paper. The backup scheme uses traditional overcurrent elements (ANSI/IEEE type 50/51), which is useful during the grid-interconnected mode, and an undervoltage element (27), which is useful during the grid-isolated mode. Investigating the backup scheme are beyond the scope of this paper.

7.3. Study Case: Modified IEEE 34-Bus

A modified version of the IEEE 34-bus distribution system is chosen as a study case [57]. An IBR is connected at node 848, a synchronous DER is connected at Bus 800, and six relays are added to the system, as shown in Figure 7.9. The system forms a microgrid by disconnecting from the EPS at Bus 800, which is the PCC. The system is modeled using an electromagnetic transients program, including a 2 MW IBR with a switching voltage source converter (VSC) model, a 2.2 MVA synchronous DER with governor and exciter models, and a digital relay model [56]. The relay model includes filters, time-domain, and phasor-based protection elements, and communications between relays.

Three locations on the IEEE 34-bus system are chosen to test the protection scheme, location 1 is close to the IBR, location 2 is in the stiff part of the system, and location 3 is in the weak part of the system. Location 1 includes relays at node 846 and node 848, location 2 includes relays at node 816 and node 824, and location 3 includes relays at node 858 and node 834. Each location is tested during both grid-isolated and grid-interconnected modes with ten possibilities of in-zone fault types. In addition, faults with high (H) and low (L) fault resistances (R_f) are tested for each fault type where 80 Ω is for high R_f and 0 Ω for low R_f on the primary 24.9 kV system.

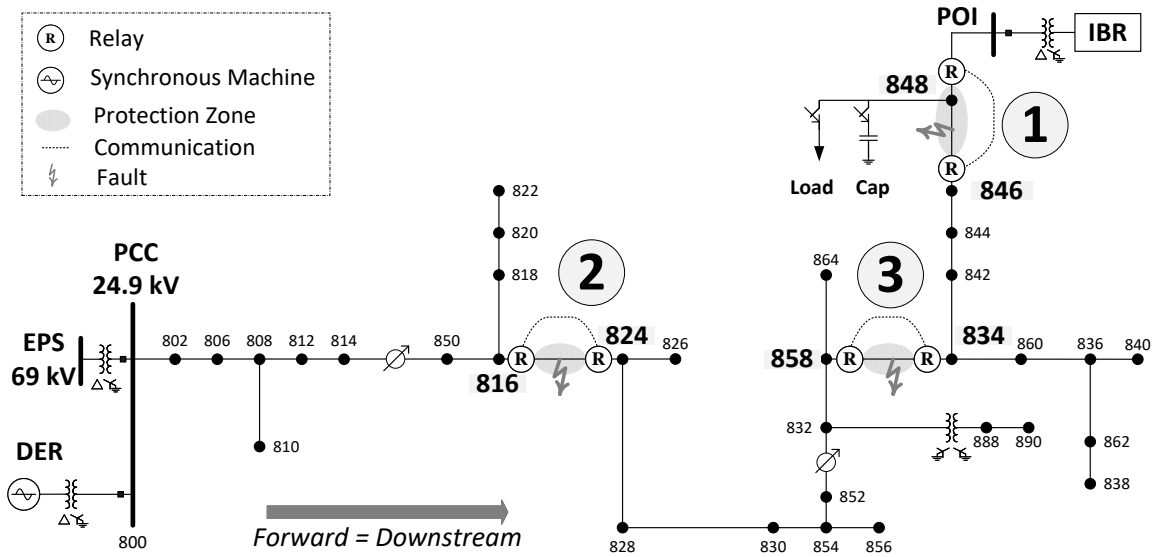


Figure 7.9 Modified IEEE 34-bus distribution system

7.3.1. EMTF-RV Simulation Results

The relay signals and response time is recorded for each scenario in milliseconds, in Table 7.1. The recorded signals are FWD/REV, IN-ZONE, and TRIP. The system phases are denoted as A, B, and C, and the ground is denoted as G. The relays successfully identify fault direction and zone during both microgrid modes for different fault types and fault resistances.

For example, during the grid-isolated mode, the relay at node 846 correctly indicates an FWD fault with a response time of 2.6 ms, and the relay at node 848 indicates a REV fault with a response time of 2.6 ms for an SLG fault between node 846 and node 848, as shown in the timing diagrams in the lower part of Figure 7.10. The relay at node 846 sends an FWD signal to the relay at node 848 and receives a REV signal from the relay at node 848. Then, the relay at node 846 asserts IN-ZONE and TRIP with a response time of 6.6 ms and 7.7 ms, respectively, as shown in Figure 7.10 (a). Similarly, the relay at node 848 asserts IN-ZONE and TRIP with a 6.6 ms and 7.7 ms response time, respectively, as in Figure 7.10 (b).

Figure 7.11 and Figure 7.12 show the responses to a double line to ground fault at location 2 during the grid-isolated mode and line to line fault at location 3 during the grid-interconnected mode, respectively.

In addition to the logic signals, the figures show two analog signals, the Watt component $\Delta Wd1$, and the superimposed positive-sequence direct energy $\Delta Ed1$. FWD and REV assert if both $\Delta Ed1$ and

ΔV_{d1} satisfy the thresholds where $\pm\Delta E_{min}$ is a small value and $-\Delta V_{min}$ is 5% of the peak line to neutral voltage of the system, as discussed earlier. Figures 7.10, 7.11, and 7.12 (b) show reliable analog signals when the IBR is the main source of fault current measured by relays at nodes 848, 824, and 834, respectively. The improved superimposed-based directional element at each relay successfully indicate the direction of faults supplied by the IBR.

Table 7.1 lists the response of FWD/REV, IN-ZONE, and TRIP times in milliseconds for ten possibilities of in-zone fault types with high and low fault resistances at the three locations and during both grid-interconnected and grid-isolated modes.

Table 7. 1 Relay Response Signals Time in Milliseconds

Location: 1		Fault	R_f	Relay at node 846 response time (ms)			Relay at node 848 response time (ms)			Relay at node 846 response time (ms)			Relay at node 848 response time (ms)			
				FWD	IN-ZONE	TRIP	REV	IN-ZONE	TRIP	FWD	IN-ZONE	TRIP	REV	IN-ZONE	TRIP	
																Grid-Interconnected Mode
ABC	L	2.24	6.22	6.22	2.24	6.22	6.22	2.24	6.22	6.22	2.24	6.22	6.22	2.24	6.22	6.22
	H	2.57	6.56	7.30	2.57	6.56	7.30	2.49	6.47	7.30	2.49	6.47	7.30	2.49	6.47	7.30
AG	L	2.40	6.39	7.72	2.40	6.39	7.72	2.57	6.56	7.72	2.57	6.56	7.72	2.82	6.80	10.5
	H	2.90	6.97	14.7	2.90	6.97	14.7	2.82	6.80	10.5	2.82	6.80	10.5	3.74	7.88	7.88
BG	L	5.15	9.46	10.9	5.48	9.13	10.9	2.99	6.97	9.55	2.99	6.97	9.55	2.99	6.97	9.55
	H	5.81	9.79	14.8	5.81	9.79	14.8	2.74	6.72	6.72	2.74	6.72	6.72	2.74	6.72	6.72
CG	L	2.90	6.97	7.88	2.90	6.97	7.88	2.82	6.80	9.63	2.82	6.80	9.63	2.74	6.72	6.72
	H	3.57	7.55	14.9	3.57	7.55	14.9	2.74	6.72	6.72	2.74	6.72	6.72	2.90	6.97	6.97
AB	L	2.40	6.39	6.72	2.40	6.39	6.72	4.48	8.47	8.47	4.48	8.47	8.47	4.48	8.47	8.47
	H	2.74	6.72	7.47	2.74	6.72	7.47	3.07	7.06	7.06	3.07	7.06	7.06	2.90	6.97	6.97
AC	L	2.32	6.30	6.30	2.32	6.30	6.30	4.48	8.47	8.47	4.48	8.47	8.47	4.48	8.47	8.47
	H	2.49	6.47	7.55	2.49	6.47	7.55	3.07	7.06	7.06	3.07	7.06	7.06	2.90	6.97	6.97
BC	L	3.65	7.64	7.64	3.65	7.64	7.64	2.57	6.56	6.56	2.57	6.56	6.56	2.57	6.56	6.56
	H	3.90	7.88	8.88	3.90	7.88	8.88	3.82	7.80	7.80	3.82	7.80	7.80	3.82	7.80	7.80
ABG	L	2.32	6.30	6.30	2.32	6.30	6.30	2.74	6.72	6.72	2.66	6.72	6.72	2.74	6.72	6.72
	H	2.57	6.64	6.89	2.57	6.64	6.89	2.57	6.56	6.89	2.57	6.56	6.89	2.57	6.56	6.89
ACG	L	2.32	6.30	6.30	2.32	6.30	6.30	2.24	6.30	6.30	2.24	6.30	6.30	2.24	6.30	6.30
	H	2.40	6.47	6.89	2.40	6.47	6.89	2.82	6.80	6.80	2.82	6.80	6.80	2.82	6.80	6.80
BCG	L	2.74	6.72	6.72	2.74	6.72	6.72	2.24	6.23	6.23	2.24	6.23	6.23	2.24	6.23	6.23
	H	2.99	7.06	9.05	2.99	7.06	9.05	2.40	6.39	6.39	2.40	6.39	6.39	2.40	6.39	6.39

Location: 2		Fault	R_f	Relay at node 816 response time (ms)			Relay at node 824 response time (ms)			Relay at node 816 response time (ms)			Relay at node 824 response time (ms)			
				FWD	IN-ZONE	TRIP	REV	IN-ZONE	TRIP	FWD	IN-ZONE	TRIP	REV	IN-ZONE	TRIP	
																Grid-Interconnected
ABC	L	2.24	6.22	6.22	2.24	6.22	6.22	2.40	6.39	6.56	2.40	6.39	6.56	2.24	6.23	6.23
	H	2.40	6.47	8.38	2.40	6.39	8.38	2.24	6.23	6.23	2.24	6.23	6.23	2.24	6.23	6.23

AG	L	2.49	6.47	8.55	2.49	6.47	7.72	2.40	6.39	7.72	2.40	6.39	7.72
	H	2.90	6.89	15.7	2.90	6.89	15.7	3.40	7.47	12.6	3.40	7.47	12.6
BG	L	5.15	9.13	10.9	5.15	9.21	10.9	2.74	6.64	6.64	2.66	6.72	6.72
	H	5.98	9.96	18.9	5.89	9.96	18.9	2.74	6.81	9.38	2.74	6.81	9.38
CG	L	2.90	6.89	7.88	2.90	6.89	7.88	5.06	8.88	8.88	4.89	9.05	9.05
	H	3.57	7.55	16.9	3.49	7.72	15.9	2.74	6.72	9.46	2.74	6.72	9.46
AB	L	2.49	6.47	6.72	2.49	6.47	6.72	2.74	6.72	6.72	2.74	6.72	6.72
	H	2.74	6.72	7.64	2.74	6.72	7.64	2.57	6.56	7.47	2.57	6.56	7.47
AC	L	2.32	6.31	6.31	2.32	6.31	6.31	2.24	6.23	6.23	2.24	6.23	6.23
	H	2.40	6.47	7.55	2.40	6.39	7.55	3.82	7.89	8.79	3.82	7.89	8.79
BC	L	3.49	7.47	7.47	3.49	7.47	7.47	4.48	8.47	8.47	4.48	8.47	8.47
	H	3.90	7.89	8.88	3.90	7.89	8.88	3.49	7.39	7.39	3.49	7.39	7.39
ABG	L	2.41	6.39	6.97	2.41	6.39	6.39	2.16	6.14	6.89	2.16	6.14	6.89
	H	2.57	6.64	6.89	2.57	6.64	6.89	2.66	6.72	6.72	2.66	6.72	6.72
ACG	L	2.24	6.23	6.23	2.24	6.23	6.23	2.82	6.81	6.81	2.82	6.81	6.81
	H	2.32	6.39	7.72	2.32	6.39	6.89	2.49	6.47	6.97	2.49	6.47	6.97
BCG	L	2.82	6.81	6.81	2.82	6.81	6.81	2.24	6.31	6.31	2.24	6.31	6.31
	H	3.07	7.06	9.05	3.07	7.06	9.05	2.49	6.39	6.81	2.49	6.39	6.81

Fault	R _f	Relay at node 858 response time (ms)			Relay at node 834 response time (ms)			Relay at node 858 response time (ms)			Relay at node 834 response time (ms)			
		FWD	IN-ZONE	TRIP	REV	IN-ZONE	TRIP	FWD	IN-ZONE	TRIP	REV	IN-ZONE	TRIP	
Location: 3 Grid-Interconnected Mode	ABC	L	2.24	6.22	6.22	2.24	6.22	6.22	2.74	6.14	6.14	2.16	6.23	6.23
		H	2.49	6.47	7.30	2.49	6.47	7.30	2.57	6.56	7.22	2.57	6.56	7.22
	AG	L	2.41	6.39	7.72	2.41	6.39	7.72	2.49	6.47	7.72	2.49	6.47	7.72
		H	2.74	6.72	13.7	2.82	6.80	13.6	3.07	7.06	7.06	3.07	7.06	7.06
	BG	L	5.06	9.13	10.9	5.06	9.13	10.9	2.57	6.64	7.55	2.57	6.64	7.55
		H	5.64	9.63	12.7	5.64	9.63	12.7	2.74	6.81	8.55	2.82	6.81	8.55
	CG	L	2.82	6.89	7.89	2.82	6.89	7.89	2.66	6.64	7.64	2.66	6.64	7.64
		H	3.24	7.22	10.7	3.24	7.22	10.7	5.64	9.63	12.5	5.64	9.63	12.5
	AB	L	2.41	6.39	6.72	2.41	6.39	6.72	2.24	6.23	6.72	2.24	6.23	6.72
		H	2.66	6.64	6.64	2.66	6.64	6.64	2.40	6.39	7.47	2.40	6.39	7.47
	AC	L	2.32	6.31	6.31	2.32	6.31	6.31	2.40	6.39	6.39	2.40	6.39	6.36
		H	2.49	6.47	6.72	2.49	6.47	6.72	2.40	6.39	6.72	2.40	6.39	6.72
BC	L	3.57	7.55	7.55	3.49	7.55	7.55	2.49	6.47	6.47	2.41	6.56	6.56	
	H	3.74	7.80	7.80	3.74	7.80	7.80	3.15	7.22	7.22	3.15	7.14	7.14	
ABG	L	2.32	6.31	6.31	2.32	6.31	6.31	2.49	6.47	6.47	2.49	6.47	6.47	
	H	2.57	6.56	6.89	2.57	6.56	6.89	2.40	6.47	6.89	2.40	6.47	6.89	
ACG	L	2.24	6.23	6.23	2.24	6.23	6.23	2.82	6.81	6.81	2.82	6.81	6.81	
	H	2.49	6.47	6.97	2.49	6.47	6.97	3.15	7.22	7.22	3.15	7.22	7.22	
BCG	L	2.74	6.72	6.72	2.74	6.72	6.72	2.16	6.14	6.14	2.16	6.14	6.14	
	H	3.07	7.06	8.05	3.07	7.06	7.06	2.82	6.81	6.81	2.82	6.81	6.81	

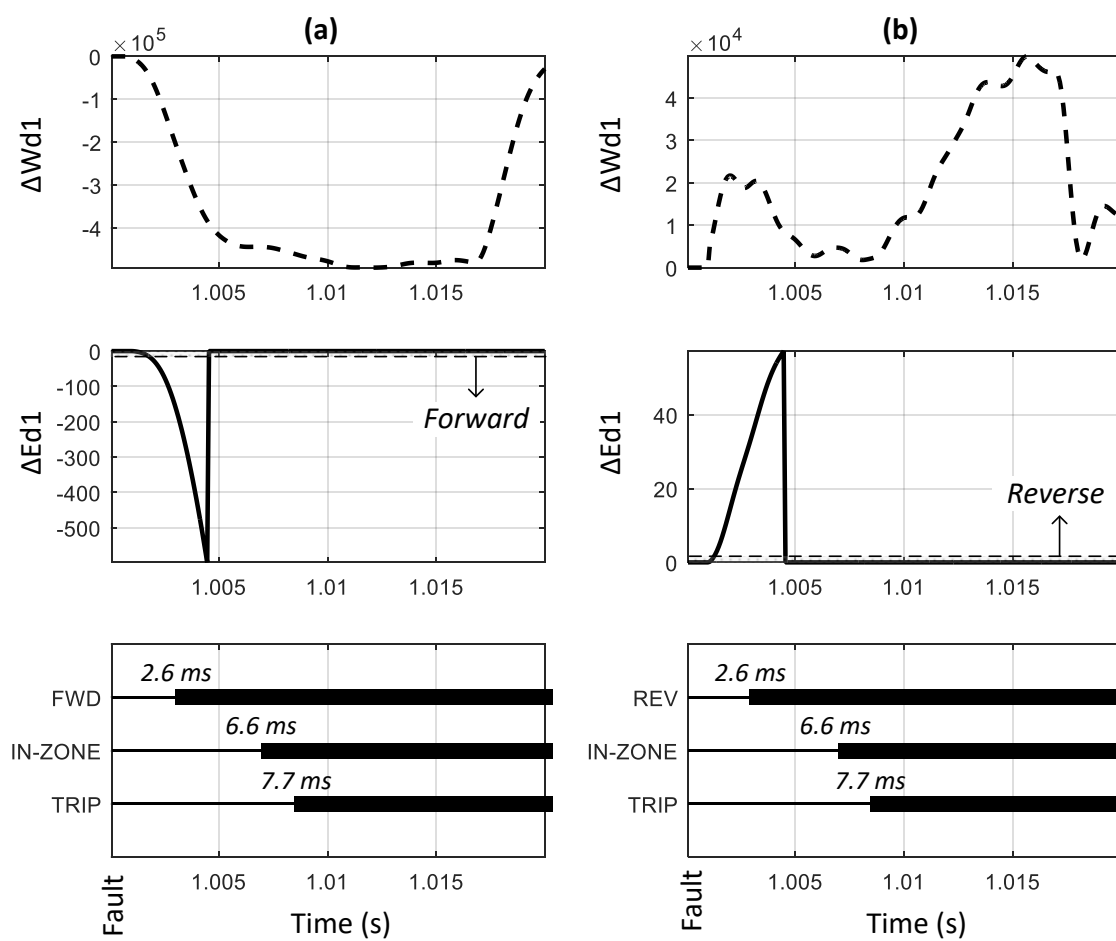


Figure 7.10 In-zone single line to ground fault at location 1 during grid-isolated mode with FWD/REV, IN-ZONE, and TRIP assert times marked in ms: (a) Relay at node 846 response and (b) Relay at node 848 response

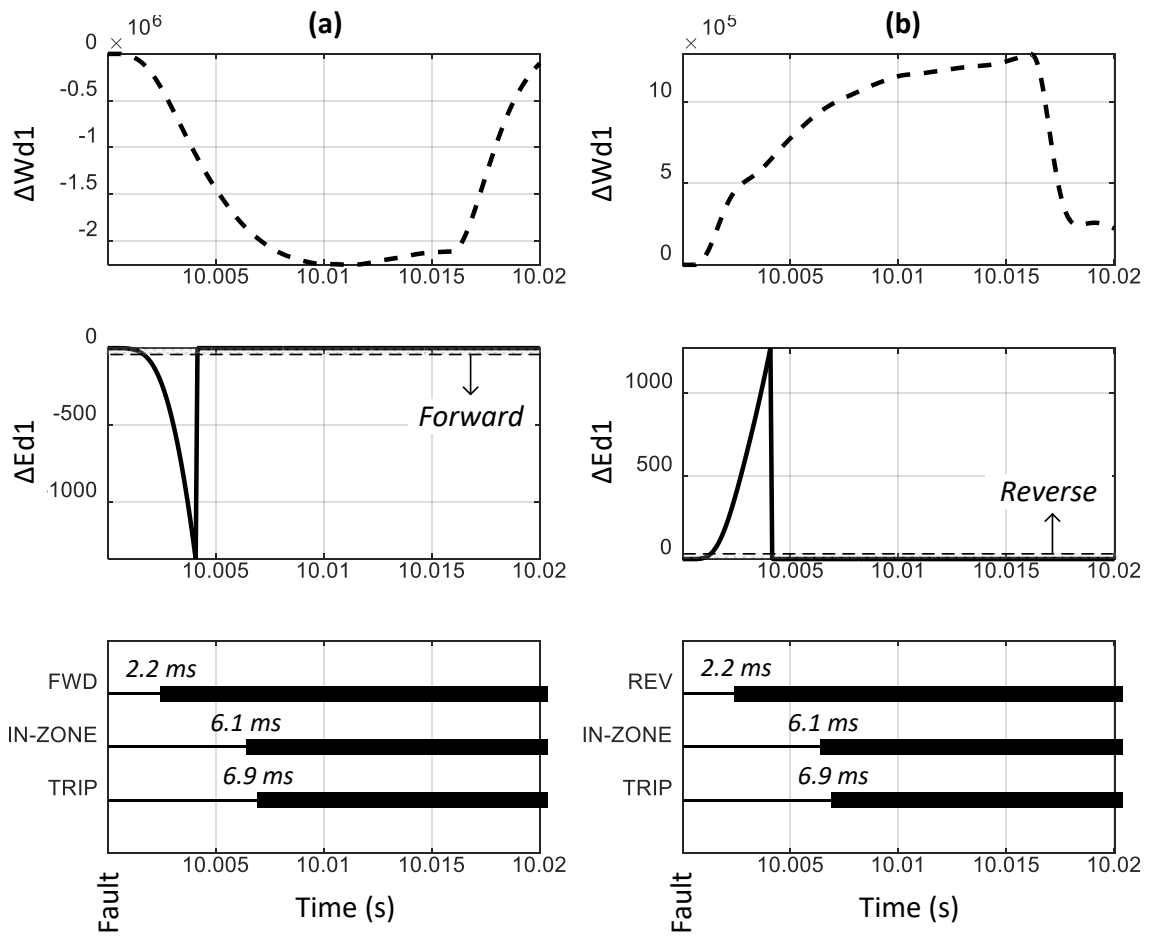


Figure 7.11 In-zone double line to ground fault at location 2 during grid-isolated mode with FWD/REV, IN-ZONE, and TRIP assert times marked in ms: (a) Relay at node 816 response and (b) Relay at node 824 response

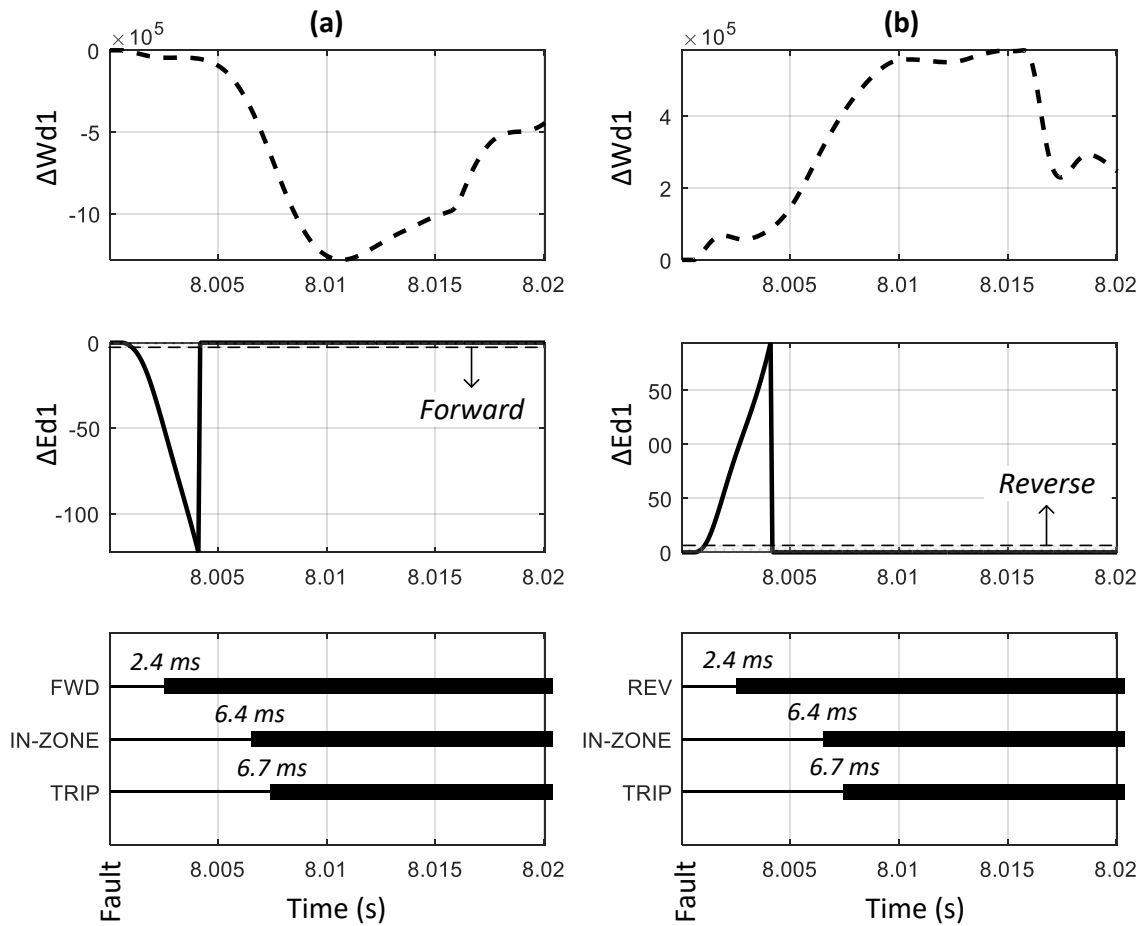


Figure 7.12 In-zone line to line fault at location 3 during grid-interconnected mode with FWD/REV, IN-ZONE, and TRIP assert times marked in ms: (a) Relay at node 858 response and (b) Relay at node 834 response

Figure 7.13 presents the response statistics of FWD/REV, IN-ZONE, and TRIP times. The average and mode response times of FWD/REV are less than one-quarter-cycle, and the maximum response time is less than half-cycle. The signal processing delay comes from the response of the anti-aliasing filter, delta filter, and the DDSRF.

The IN-ZONE detection has an additional fixed four milliseconds delay added for communications delay. This delay could be increased or decreased depending on the communication scheme. IN-ZONE average and mode response time are less than half-cycle, and the maximum is less than one cycle. The average and mode TRIP response times are about half-cycle, and the maximum is slightly above one-cycle. The main delay for TRIP comes from the full-cycle DFT filter. Using a half-cycle DFT filter could improve the delay, but it might reduce signal stability.

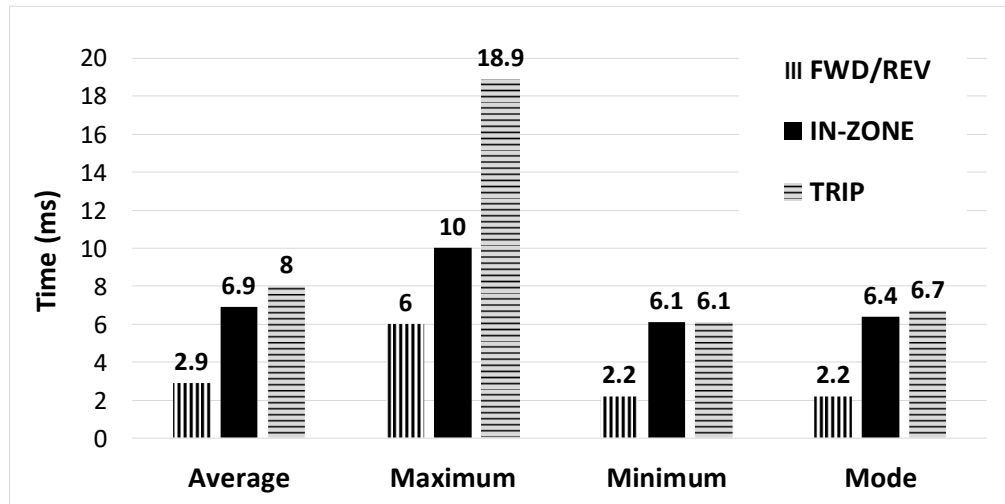


Figure 7.13 FWD/REV, IN-ZONE, and TRIP signals response time statistics

Furthermore, different response times are observed with different scenarios. For instance, during grid-isolated cases, relays assert FWD/REV 5% faster and assert TRIP 10% faster on average than when grid-interconnected. SLG faults tend to be 15% slower than the average response time of 2.9 ms. Also, for the high fault resistance condition, the relays assert FWD/REV 9% slower and assert TRIP 24% slower than the low fault resistance case. The possible reasons for this variation are most likely due: the voltage drop rate of change that controls the elements and the initial torque angle for the current, which is part of the $\Delta Wd1$ equation.

The scheme's sensitivity is determined by phasor-based superimposed voltage ΔV_f where the threshold is set based on the pre-fault analysis. Thus, high fault resistance conditions in stiff systems are challenging because fault resistance coverage depends on the voltage threshold. However, using the proposed superimposed-based voltage-restrained element is an advantage. The proposed element is more reliable than typical voltage-restrained elements because the threshold of the superimposed voltage quantity is based on the voltage change in the system.

Additional cases are also conducted to test the security of the element. A 750 kVAR capacitor bank and a (60+48i) kVA load are switched into the system between relay 846 and 848 in separate cases. The relays did not trip in either case. Several out-zone faults are applied to the system in different locations; the directional element did not assert an IN-ZONE signal in any of the cases. The scheme was also tested in a loop configuration microgrid system and in a system with two parallel feeders with normally open and normally closed breakers. The protection scheme responded correctly in all cases.

7.4. Conclusions

The proposed microgrid superimposed-based protection scheme provides an ultra-high-speed sub-cycle directional element aided with only low bandwidth communications. The directional element's average response time to indicate fault direction is three milliseconds, and to identify the fault zone is seven milliseconds. The two relays trip for an in-zone fault within a half-cycle during both grid-interconnected and grid-isolated modes. The scheme can be applied to dynamic microgrid topologies and microgrids with radial or loop configurations. Additionally, the improved time-domain superimposed directional element, which uses the DDSRF algorithm, successfully indicates the direction of faults when the IBR is the main source of fault current. The superimposed positive-sequence direct energy component reduces the negative impact of the IBR control response during faults. The element also was secure against load and capacitor switching as well as out-of-zone faults.

Chapter 8: Summary, Conclusions, and Future Work

8.1. Summary

This dissertation defines two problems, protecting microgrid systems and protecting microgrids with IBRs integrated.

First, microgrid systems have two operation modes, grid-isolated mode and grid-interconnected mode, which may cause a significant change in the available fault current. Moreover, dynamic changes in the topology of microgrids and variations in generation availability change both the magnitude and direction of fault currents. The direction of the power flow also changes due to the two modes of operation and the dynamic change in the topology.

Second, including IBRs in microgrid systems pose more protection challenges because of IBRs' fast control response, lack of inherent inertia, and regulated fault current characteristics. Fault currents supplied by IBRs have low fault current magnitudes, are primarily positive sequence, at a unity power factor and exhibit nonlinear behavior relative to fault location and fault type.

This dissertation studies the response of a superimposed quantities-based protection element to IBRs supplied fault current. The fast control response and nonlinear fault current characteristic of IBRs impact the superimposed current quantities by changing both magnitude and angle. This dissertation shows how the negative impact of the IBR fault current response of commonly applied grid following inverter control schemes causes the conventional time-domain superimposed quantities-based directional element to fail to detect the correct fault direction since it is based on the current and voltage quantities.

After that, this dissertation proposes an improved time-domain-based protection scheme for microgrid systems and a solution eliminating the negative impact of IBRs' response on the superimposed quantities' protection elements. The proposed protection scheme is a high-speed sub-cycle directional element aided with low bandwidth communication and supervised by a phasor-based versatile voltage-restrained overcurrent element. More specifically, the element calculates the superimposed positive-sequence direct-axis component of transient energy during faults to serve as a directional indication. Superimposed voltage and current quantities are calculated using a combination of delta filters and DDSRF filters.

The microgrid protection scheme and the proposed relay are evaluated on a generic microgrid system built from a modified version of the IEEE 34-bus distribution system simulated using an electromagnetic transients program.

8.2. Conclusions

This dissertation shows that the proposed microgrid protection scheme overcomes challenges posed by the two operation modes, the dynamic topologies and the bidirectional power flow. Furthermore, simulating the proposed time-domain superimposed-based relay shows the advantage of the proposed element in terms of sensitivity to pick up low fault currents supplied by IBRs, indicating fault zone in as little as seven milliseconds to retain stability for severe faults.

First, the simulation results show that IBRs negatively impact superimposed current quantities compared to the fault currents from synchronous generators or type-1 wind turbine generators. This negative impact caused the superimposed quantities-based directional element to fail to detect the correct fault direction since it is based on the current and voltage quantities. However, the presence of IBRs does not impact the voltage quantities. The voltage quantities can only detect the presence of faults but cannot identify the direction of faults without the reliable current direction indication.

Then, this dissertation shows that the proposed directional element overcomes the negative impact of IBRs. The proposed element is based on superimposed quantities but enhanced with the DDSRF algorithm, which improves the superimposed current quantity signal when IBRs are the main source of fault currents. The DDSRF-based superimposed element trips symmetrical and unsymmetrical fault types within a microgrid, including IBRs. Using superimposed positive-sequence direct energy components reduces the negative impact of the IBRs' controller during faults.

Typically for distribution feeder protection, phasor-based overcurrent relays are coordinated by current and/or time, where the upstream relays wait for the downstream relays. The time response of this typical scheme varies from a few cycles to a few seconds. On the other hand, the proposed DDSRF-based superimposed relays trip an in-zone fault in only a half-cycle, requiring only low bandwidth communication during grid-interconnected and grid-isolated modes. The average response time to indicate fault direction is three milliseconds, while identifying the fault zone is seven milliseconds. This fast response of the proposed relay helps to retain stability for severe faults within a microgrid system.

Relays with communication capabilities can improve protection schemes in microgrids. However, using communication-based protection schemes such as the current differential, central protection, and adaptive overcurrent that change settings based on operation mode increases cyber vulnerabilities in microgrid systems. The reason for this vulnerability is that these schemes are nearly dependent on communication systems to operate and trip faults. The proposed DDSRF-based superimposed relay operates independently as a multi-agent protective device where limited communication enhances

performance. It continues to protect the system when the communication system is degraded because it is supervised by a phasor-based versatile voltage-restrained overcurrent element that does not need communication to operate. In other words, the proposed protection scheme is not entirely dependent on the availability of the communication system.

On the other hand, there are a few drawbacks and limitations to the proposed scheme. The DDSRF-based superimposed quantities element introduces a maximum of one millisecond of delay, and the overall speed of the protection scheme depends on communication. The voltage-restrained overcurrent element depends on voltage dip, which may fail with very high-impedance faults. Potential backup protection is not investigated in detail in this dissertation. The Park's transformation, PLL, and DDSRF are not commonly used in commercially available relays, however, they are used in commercial power electronic converters such as those used in IBRs. More studies are required to research the applicability and computational resource requirements of these algorithms in microprocessor-based protection devices.

8.3. Future Work

This dissertation proposed DDSRF-based superimposed protection scheme for microgrid systems, including IBRs, with many simulations and study cases. However, to put this scheme to practical use, more testing is required, including evaluation for different types and sizes of microgrid systems. Moreover, implementing the DDSRF-based superimposed element in a relay and testing it using hardware-in-the-loop simulation and physical test environments is essential to move the developed protection method in this dissertation to application.

Some potential avenues of possible future work comprise testing the proposed DDSRF-based superimposed protection scheme in transmission applications with IBRs and investigating the challenges of DC line systems, including IBRs. Moreover, modeling systems with large numbers of IBRs, instead of the aggregated IBR models at one location and simulating the response and impact on the proposed protection, could be considered. More sensitivity analysis on the proposed scheme should be conducted, including relay settings, system impedance, high impedance faults, different generation types, and load contribution to fault current. This study should also consider cases where the IBR controller uses grid forming controls which have fault current responses that differ from those of IBRs with grid following controls. Furthermore, microgrid systems could be studied with power electronic-based power transformers connected at the PCC.

Additionally, backup protection for the proposed DDSRF-based superimposed protection scheme is not discussed in this dissertation. One possible option for backup protection is to combine a central protection system with a central control system in microgrids during grid-isolated operating mode. Since the proposed protection scheme can operate within one power cycle, the central backup protection can be slower than the main protection and less dependent on the availability of the high-speed communication system.

Finally, investigating cyber vulnerabilities in terms of the application software and the communication network of the proposed protection is an important next step. One scenario that could be considered is testing the impact of false data injection of the communicated directional indication on the proposed DDSRF-based superimposed protection scheme during a cyber-attack. Another vulnerability in the proposed protection scheme is if sampled values protocol (IEC 61850) is used to transmit streams of data between Merging Units and the proposed relays over the Ethernet using a publisher/subscriber model. The rationale is that the integrity of data is crucial to the proposed scheme.

References

- [1] Renewable Energy Policy Network for the 21st Century, *Renewables 2017 Global Status Report*, REN21 2017.
- [2] C. Marnay, F. J. Rubio, and A. S. Siddiqui, "Shape of the microgrid," *Proc. IEEE Power Eng. Soc. Transm. Distrib. Conf.*, vol. 1, no. Winter Meeting, pp. 150–153, 2001.
- [3] S. Parhizi, H. Lotfi, A. Khodaei, and S. Bahramirad, "State of the art in research on microgrids: A review," *IEEE Access*, vol. 3, pp. 890–925, 2015.
- [4] D. E. Olivares *et al.*, "Trends in microgrid control," *IEEE Trans. Smart Grid*, vol. 5, no. 4, pp. 1905–1919, 2014.
- [5] N. Hatziargyriou, H. Asano, R. Iravani, and C. Marnay, "Microgrids," *IEEE Power & Energy Mag.*, vol. 5, no. 4, pp. 78–94, 2007.
- [6] R. H. Lasseter and P. Paigi, "Microgrid: A conceptual solution," in *PESC Record - IEEE Annual Power Electronics Specialists Conference*, 2004, vol. 6, pp. 4285–4290.
- [7] *The Role of Microgrids in Helping to Advance the Nation's Energy System*. U.S. Department of Energy, 2018. [Online]. Available: <https://www.energy.gov/oe/activities/technology-development/grid-modernization-and-smart-grid/role-microgrids-helping>. [Accessed: 05-Apr-2018].
- [8] H. S. Samkari, H. L. Hess, and B. K. Johnson, "Renewable Energy Planning for a Microgrid in a Pacific Northwest City," in *North American Power Symposium, NAPS*, 2018.
- [9] S. Achilles *et al.*, "Integrating Inverter-Based Resources into Low Short Circuit Strength Systems," NERC Reliability Guideline, 2017.
- [10] B. Kroposki *et al.*, "Achieving a 100% Renewable Grid: Operating Electric Power Systems with Extremely High Levels of Variable Renewable Energy," *IEEE Power & Energy Mag.*, vol. 15, no. 2, pp. 61–73, 2017.
- [11] E. Ela *et al.*, "Future Electricity Markets: Designing for Massive Amounts of Zero-Variable-Cost Renewable Resources," *IEEE Power & Energy Mag.*, vol. 17, no. 6, pp. 58–66, 2019.
- [12] W. Feng *et al.*, "A review of microgrid development in the United States – A decade of progress on policies, demonstrations, controls, and software tools," *Appl. Energy*, vol. 228, no. October,

- pp. 1656–1668, 2018.
- [13] H. S. Samkari and B. K. Johnson, “Multi-Agent Protection Scheme for Resilient Microgrid Systems with Aggregated Electronically Coupled Distributed Energy Resources,” in *IECON 2018*, 2018, pp. 752–757.
 - [14] H. S. Samkari and B. K. Johnson, “Impact of Inverter Based Resources on Superimposed Quantities-Based Protection,” in *PRC 2021 - 74th Annual Georgia Tech Protective Relaying Conference*, 2021.
 - [15] H. S. Samkari and B. K. Johnson, “Impact of Distributed Inverter-Based Resources on Incremental Quantities-Based Protection,” in To be presented at the *2021 IEEE Power and Energy Society General Meeting*. July 2021.
 - [16] H. S. Samkari and B. K. Johnson, “Time-Domain Protection Scheme for Microgrids with Aggregated Inverter-Based Distributed Energy Resources,” Submitted to *IEE Trans. Smart Grid*.
 - [17] R. H. Lasseter, “MicroGrids,” in *2002 IEEE Power Engineering Society Winter Meeting. Conference Proceedings (Cat. No.02CH37309)*, 2002, vol. 1, pp. 305–308 vol.1.
 - [18] B. Kroposki, R. Lasseter, T. Ise, S. Morozumi, S. Papathanassiou, and N. Hatziargyriou, “Making microgrids work,” *IEEE Power & Energy Mag.*, vol. 6, no. 3, pp. 40–53, 2008.
 - [19] IEEE Std. 1547-2018. *Standard for Interconnection and Interoperability of Distributed Energy Resources with Associated Electric Power Systems Interfaces*. IEEE Standard Association, 2018.
 - [20] P. Penkey, H. Samkari, B. K. Johnson, and H. L. Hess, “Voltage control by using capacitor banks and tap changing transformers in a renewable microgrid,” in *IEEE Power and Energy Society Innovative Smart Grid Technologies Conference, ISGT*, 2017.
 - [21] F. Katiraei, R. Iravani, N. Hatziargyriou, and A. Dimeas, “Microgrid Management,” *IEEE Power & Energy Magazine*, vol. 6, no. June, pp. 54–65, 2008.
 - [22] A. Bidram and A. Davoudi, “Hierarchical structure of microgrids control system,” *IEEE Trans. on Smart Grid*, vol. 3, no. 4, pp. 1963–1976, 2012.
 - [23] H. Nikkhajoei and R. H. Lasseter, “Microgrid protection,” *2007 IEEE Power Eng. Soc. Gen.*

Meet. PES, pp. 1–6, 2007.

- [24] A. Hooshyar and R. Iravani, “Microgrid Protection,” *Proc. IEEE*, vol. 105, no. 7, pp. 1332–1353, 2017.
- [25] K. Jones *et al.*, *Impact of Inverter Based Generation on Bulk Power System Dynamics and Short-Circuit Performance*. IEEE Power and Energy Society Technical report PES-TR68, 2018.
- [26] B. Bak-Jensen *et al.*, “Protection of Distribution Systems with Distributed Energy Resources,” CIGRE Group B5/C6.26/CIREN, 2015.
- [27] M. Higginson *et al.*, “Microgrid Protection Systems,” IEEE Power and Energy Society Technical Report PES-TR71, 2019.
- [28] N. Nimpitiwan, S. Member, G. T. Heydt, and R. Ayyanar, “Fault Current Contribution From Synchronous Machine and Inverter Based Distributed Generators,” *IEEE Trans. on Power Deliv.*, vol. 22, no. 1, pp. 634–641, 2007.
- [29] J. M. Carrasco *et al.*, “Power-electronic systems for the grid integration of renewable energy sources: A survey,” *IEEE Transactions on Industrial Electronics*, vol. 53, no. 4, pp. 1002-1016, June 2006.
- [30] F. Blaabjerg, R. Teodorescu, M. Liserre, and A. V. Timbus, “Overview of control and grid synchronization for distributed power generation systems,” *IEEE Transactions on Industrial Electronics*, vol. 53, no. 5, pp. 1398-1409, Oct. 2006, doi: 10.1109/TIE.2006.881997.
- [31] A. Yazdani and R. Iravani, *Voltage-Sourced Converters in Power Systems: Modeling, Control, and Applications*. IEEE, 2010.
- [32] R. Teodorescu, M. Liserre, and P. Rodriguez, *Grid converters for photovoltaic and wind power systems*, vol. 29. John Wiley & Sons, 2011.
- [33] “Solar Energy Resources | Department of Energy.” [Online]. Available: <https://www.energy.gov/eere/solar/solar-energy-resources>. [Accessed: 31-May-2021].
- [34] H. Samkari, *Modeling and Simulation the Impacts of STATCOMs on Distance Protection and Developing a Microgrid Energy Management Scheme for a Pacific Northwest City*. Master's Thesis, University of Idaho, 2016.
- [35] “Solar Photovoltaic Technology Basics | NREL.” [Online]. Available:

- <https://www.nrel.gov/research/re-photovoltaics.html>. [Accessed: 31-May-2021].
- [36] L. R. Tuladhar and K. Banerjee, “Impact of the Penetration of Inverter-Based Systems on Grid Protection,” in *2019 Grid of the Future Symposium*, CIGRE 2019.
- [37] M. Brucoli and T. C. Green, “Fault Behavior in Islanded Microgrid,” *19 th Int. Conf. Electr. Distrib.*, no. 0548, pp. 21–24, 2007.
- [38] N. Fischer, “Protection of Inverter-Based Resources - ESIG.” [Online]. Available: <https://www.esig.energy/protection-of-inverter-based-resources/>. [Accessed: 31-May-2021].
- [39] H. J. A. Ferrer and E. O. Schweitzer, *Modern solutions for protection, control, and monitoring of electric power systems*. Schweitzer Engineering Laboratories Pullman, 2010.
- [40] J. L. Blackburn and T. J. Domin, *Protective relaying: Principles and applications*, Fourth edi. New York: Taylor & Francis Group, 2015.
- [41] J. S. Dudor and L. K. Padden, “Protective Relay Applications for Generators and Transformers,” *IEEE Industry Applications Magazine*, 1997.
- [42] D. Ventruella and P. Steciuk, “A second look at generator 51-V relays,” *IEEE Trans. on Ind. Appl.*, vol. 33, no. 3, pp. 848–856, 1997.
- [43] G. Benmouyal and J. Roberts, “Superimposed Quantities: Their True Nature and Application in Relays,” *26th Annu. West. Prot. Relay Conference*, 1999.
- [44] A. P. Apostolov, “Implementation of a Transient Energy Method for Directional Detection in Numerical Distance Relays,” *1999 IEEE Transmission and Distribution Conference (Cat. No. 99CH36333)*, 1999.
- [45] SELINC, “SEL-411L Advanced Line Differential Protection, Automation, and Control System,” p. SEL; Pullman; WA; USA, 2018.
- [46] K. S. Prakash, O. P. Malik, G. S. Hope, G. C. Hancock, and K. K. Wong, “Laboratory investigation of an amplitude comparator based directional comparison digital protection scheme,” *IEEE Trans. Power Deliv.*, vol. 5, no. 4, pp. 1687–1694, 1990.
- [47] A. Guzmán, M. V Mynam, V. Skendzic, J. L. Eternod, and R. M. Morales, “Traveling-wave and incremental quantity directional elements speed up directional comparison protection schemes,” *14th Int. Conf. on Developments in Power System Protection*, UK, 2018.

- [48] M. Kockott, Sinisa Zubic, Zhiying Liu, Hans Jernberg, Tom Roseburg, and Warren Rees, "A POTT scheme , using transient directional elements , for a complex 525kV transmission corridor comprising long , heavily loaded and heavily series compensated parallel lines," 46th WPRC, 2019.
- [49] E. Leite, F. Lopes, and K. Silva, "Using incremental replica current in phase comparison transmission line protection schemes: Advantages and limitations," *SBSE 2018 - 7th Brazilian Electr. Syst. Symp.*, pp. 1–6, 2018.
- [50] T. L. Relay, T. F. Locator, and H. Event, "SEL T400L Ultra-High-Speed Transmission Line Relay, Traveling-Wave Fault Locator, Instruction Manual," 2017.
- [51] A. Hooshyar and R. Iravani, "A New Directional Element for Microgrid Protection," *IEEE Trans. Smart Grid*, vol. 9, no.6, November 2018, pp.6862-6876.
- [52] A. Hooshyar, E. F. El-saadany, and M. Sanaye-pasand, "Fault Type Classification in Microgrids Including Photovoltaic DGs," *IEEE Trans. Smart Grid*, vol. 7, no. 5, pp. 2218–2229, 2016.
- [53] S. B. A. Bukhari, M. Saeed Uz Zaman, R. Haider, Y. S. Oh, and C. H. Kim, "A protection scheme for microgrid with multiple distributed generations using superimposed reactive energy," *Int. J. Electr. Power Energy Syst.*, vol. 92, pp. 156–166, 2017.
- [54] Zamani, M. A., Yazdani, A., Sidhu, T., "A Communication-Assisted Protection Strategy for Inverter-Based Medium-Voltage Microgrids," *IEEE Trans. Smart Grid*, vol. 3, no. 4, pp. 2088–2099, 2012.
- [55] H. Muda, S. Member, and P. Jena, "Superimposed Adaptive Sequence Current Based Microgrid Protection : A New Technique," *IEEE Transactions on Power Delivery*, vol. 32, no. 2, pp. 757–767, 2017.
- [56] "EMTP-RV." [Online]. Available: <https://www.emtp.com/>. [Accessed: 07-Feb-2021].
- [57] "PES Test Feeder." [Online]. Available: <https://site.ieee.org/pes-testfeeders/resources/>. [Accessed: 07-Feb-2021].
- [58] K. P. Schneider *et al.*, "Analytic Considerations and Design Basis for the IEEE Distribution Test Feeders Report Prepared by the Test Feeder Working Group of the Distribution System Analysis Subcommittee," *IEEE Transactions on Power Systems*, vol. 33, no. 3, pp. 3181–3188, 2018.

- [59] W. H. Kersting and G. Shirek, "Short circuit analysis of IEEE test feeders," *Proc. IEEE Power Eng. Soc. Transm. Distrib. Conf.*, no. 1, pp. 1–9, 2012.
- [60] O. Nzimako and R. Wierckx, "Modeling and simulation of a grid-integrated photovoltaic system using a real-time digital simulator," *IEEE Trans. Ind. Appl.*, vol. 53, no. 2, pp. 1326–1336, 2017.
- [61] S. M. Yeo, H. I. Cho, C. H. Kim, T. Funabashi, and T. Senjyu, "Modeling and analysis of photovoltaic system using EMTP," *Transm. Distrib. Conf. Expo. Asia Pacific, TD Asia 2009*, 2009.
- [62] A. Yazdani *et al.*, "Modeling guidelines and a benchmark for power system simulation studies of three-phase single-stage photovoltaic systems," *IEEE Trans. Power Deliv.*, vol. 26, no. 2, pp. 1247–1264, 2011.
- [63] B. Johnson, H. Hess and J. A. Martinez, "Parameter determination for modeling system transients - Part VII: Semiconductors," *IEEE Trans. Power Deliv.*, vol. 20, no. 3, pp. 2086-2094, 2005.
- [64] Z. Li and M. Shahidehpour, "Role of microgrids in enhancing power system resilience," *2017 IEEE Power & Energy Society General Meeting*, 2017.
- [65] C. G. Rieger, D. I. Gertman, and M. A. McQueen, "Resilient Control Systems: Next Generation Design Research," *Proc. from 2nd Conf. Hum. Syst. Interact.*, pp. 632–636, 2009.
- [66] H. Qi *et al.*, "A resilient real-time system design for a secure and reconfigurable power grid," *IEEE Trans. Smart Grid*, vol. 2, no. 4, pp. 770-781, 2011.
- [67] S. N. Bhaskara and B. H. Chowdhury, "Microgrids — A review of modeling, control, protection, simulation and future potential," *2012 IEEE Power and Energy Society General Meeting*, 2012.
- [68] J. Shiles *et al.*, "Microgrid protection: An overview of protection strategies in North American microgrid projects," *2017 IEEE Power & Energy Society General Meeting*, 2017.
- [69] T. S. Ustun, C. Ozansoy, and A. Zayegh, "Modeling of a centralized microgrid protection system and distributed energy resources according to IEC 61850-7-420," *IEEE Trans. Power Syst.*, vol. 27, no. 3, pp. 1560–1567, 2012.
- [70] S. A. Hosseini, H. A. Abyaneh, S. H. H. Sadeghi, F. Razavi, and A. Nasiri, "An overview of microgrid protection methods and the factors involved," *Renew. Sustain. Energy Rev.*, vol. 64, pp. 174–186, 2016.

- [71] K. Eshghi, B. K. Johnson, and C. G. Rieger, "Power system protection and resilient metrics," *Proc. - 2015 Resil. Week, RSW 2015*, pp. 212–219, 2015.
- [72] M. S. Thomas and J. D. McDonald, *Power system SCADA and Smart Grids*, CRC press, 2017.
- [73] J. Jensen, K. Bolton, and D. Simons, *Changes to System Inertia with High Renewable Implementation*, WECC Tech. Report, 2020..
- [74] E. O. Schweitzer, B. Kasztenny, A. Guzmán, V. Skendzic, and M. V. Mynam, "Speed of line protection - Can we break free of phasor limitations?," *2015 68th Annu. Conf. Prot. Relay Eng. CPRE 2015*, pp. 448–461, 2015.
- [75] A. Bapary et al., "Protection Challenges and Practices for Interconnecting Inverter Based Resources to Utility Transmission Systems," IEEE PES-TR81 Tech. Report, 2020.
- [76] R. Zhang, B. Ellison, J. Holbach, and S. Ward, "Assessment of Protection Functionality and Performance with Respect to Declining System Fault Levels and Inertia due to a Significant Increase of Inverter Based Generation on National Grid ' s Transmission System in the United Kingdom," *46th WPRC*, 2019.
- [77] A. T. Johns, "New Ultra-High-Speed Directional Comparison Technique for the Protection of E. H. V. Transmission Lines.," *IEE Proc. C Gener. Transm. Distrib.*, vol. 127, no. 4, pp. 228–239, 1980.
- [78] A. A. Memon and K. Kauhaniemi, "A critical review of AC Microgrid protection issues and available solutions," *Electr. Power Syst. Res.*, vol. 129, pp. 23–31, 2015.
- [79] S. Beheshtaein, R. Cuzner, M. Savaghebi, and J. M. Guerrero, "Review on microgrids protection," *IET Gener. Transm. Distrib.*, vol. 13, no. 6, pp. 743–759, 2019.
- [80] M. Vitins, "A fundamental concept for high speed relaying," *IEEE Trans. Power Appar. Syst.*, vol. PAS-100, no. 1, pp. 163–173, 1981.
- [81] E. O. Schweitzer, B. Kasztenny, and M. V. Mynam, "Performance of time-domain line protection elements on real-world faults," *69th Annu. Conf. Prot. Relay Eng. (CPRE)*, 2016.
- [82] G. Benmouyal, "Removal of DC-offset in current waveforms using digital mimic filtering," *IEEE Transactions on Power Delivery*, vol. 10, no. 2, pp. 621–630, 1995.
- [83] R. W. Wall, "Cosine Filter Theory," ECE 525 course material, University of Idaho, 2019.

- [84] S. Sánchez *et al.*, “Directional comparison protection over radio channels for subtransmission lines: Field experience in Mexico,” *2008 61st Annu. Conf. Prot. Relay Eng.*, 2008.
- [85] P. Rodriguez, J. Pou, J. Bergas, J. I. Candela, R. P. Burgos, and D. Boroyevich, “Decoupled Double Synchronous Reference Frame PLL for Power Converters Control,” *IEEE Trans. Power Electron.*, vol. 22, no. 2, pp. 584–592, 2007.
- [86] G. C. Paap, “Symmetrical components in the time domain and their application to power network calculations,” *IEEE Trans. Power Syst.*, vol. 15, no. 2, pp. 522–528, 2000.
- [87] R. H. PARK, “Two-Reaction Theory of Synchronous Machines: Generalized Method of Analysis-Part I,” *Trans. Am. Inst. Electr. Eng.*, vol. 48, no. 3, pp. 716–727, 1929.
- [88] F. Pitot and N. Vassilevsky, “WATTMETRIC EARTH FAULT PROTECTION – INNOVATION FOR COMPENSATED DISTRIBUTION NETWORKS,” *23rd International Conference on Electricity Distribution*, 2015.
- [89] J. Roberts, H. J. Altuve, and D. Hou, “Review of ground fault protection methods for grounded, ungrounded, and compensated distribution systems,” *27th Annu. West. Prot. Relay Conf.*, 2001.
- [90] R. Moxley and F. Becker, “Adaptive protection - What does it mean and what can it do?,” *2006 Power Systems Conference: Advanced Metering, Protection, Control, Communication, and Distributed Resources*, 2006.

Appendix A - IBRs Fault Current Characteristics

Results from simulating the modeled PV system during different operating conditions are shown in Figure A.1, Figure A.2, Figure A.3, Figure A.4, and Figure A.5. The three-phase fault current supplied has similar behavior regardless of the converter control mode, when three-phase faults are applied at the same location. However, Figure A.3 shows less fault current when the controller is set to provide zero active and reactive power from the PV system.

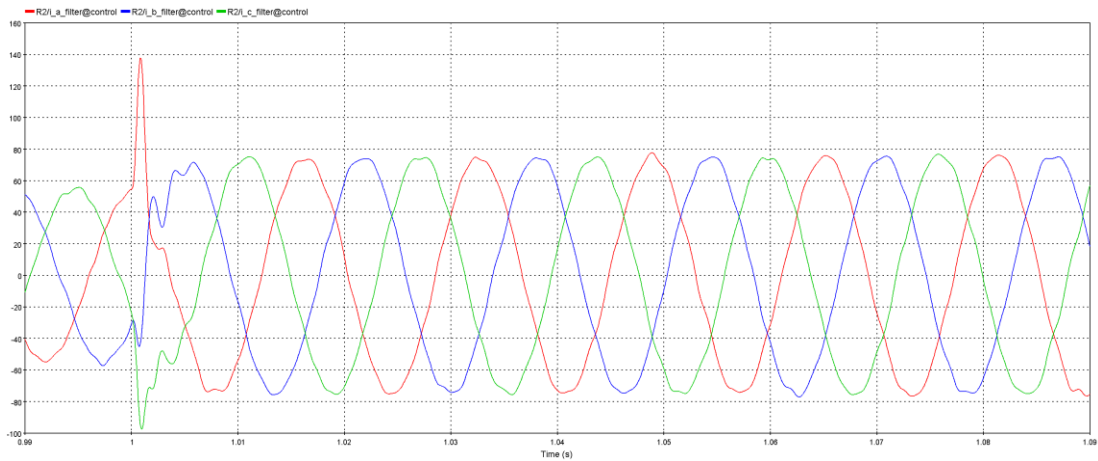


Figure A.1 PV is rated 2 MW and producing 2 MW during a three-phase fault and with reactive-power mode set to zero reactive power

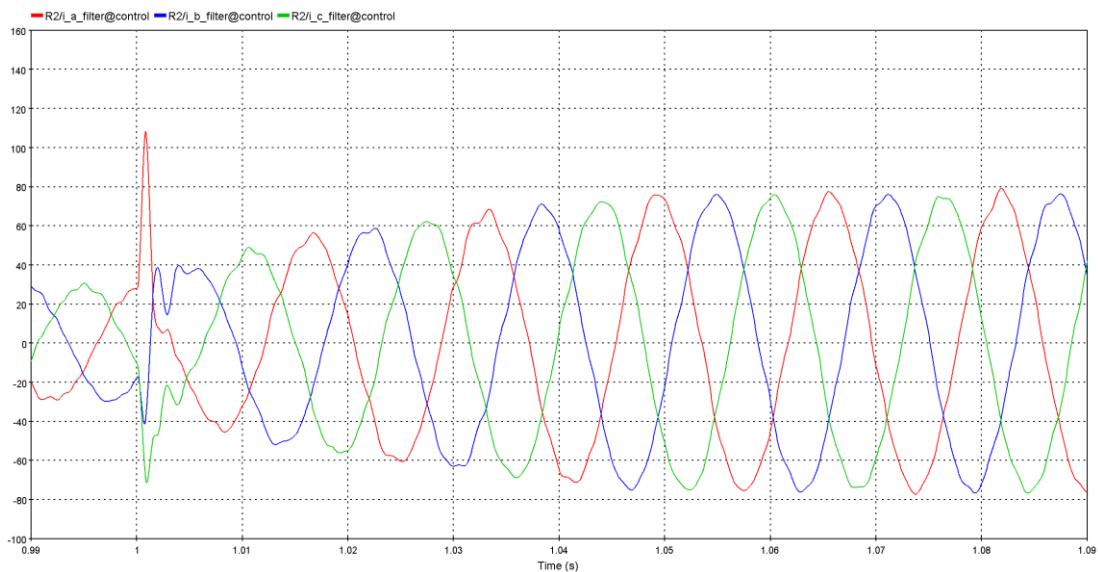


Figure A.2 PV is rated 2 MW but producing 1 MW during a three-phase fault and with reactive-power mode set to zero reactive power

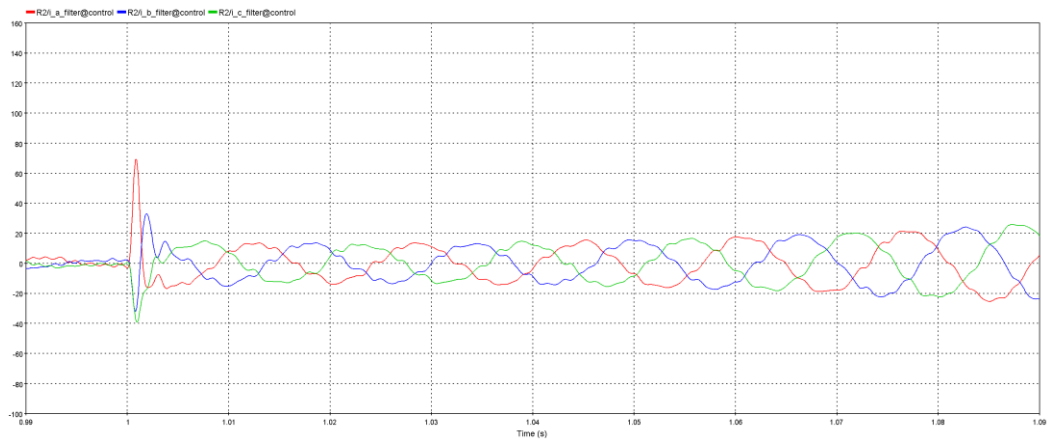


Figure A.3 PV is rated 2 MW but producing 0 MW during a three-phase fault and with reactive-power mode set to zero reactive power

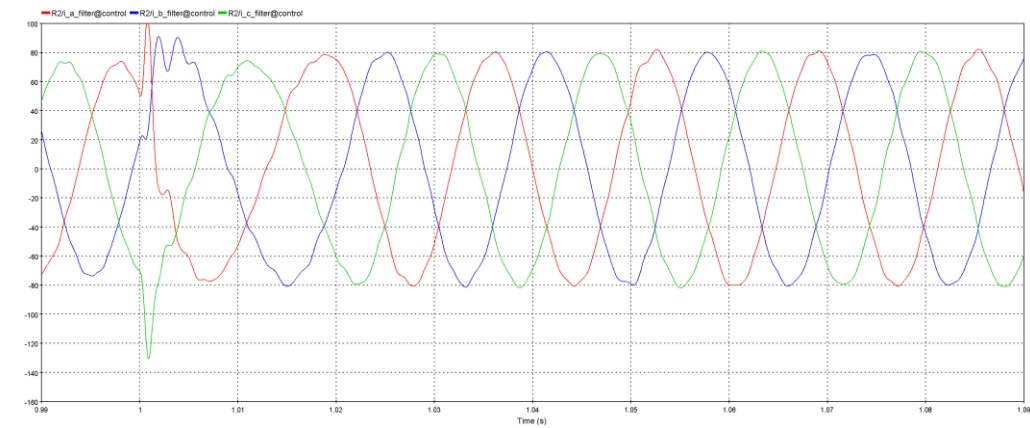


Figure A.4 PV is rated 2 MW and producing 2 MW during a three-phase fault and volt-reactive-power mode with one per unit voltage set point

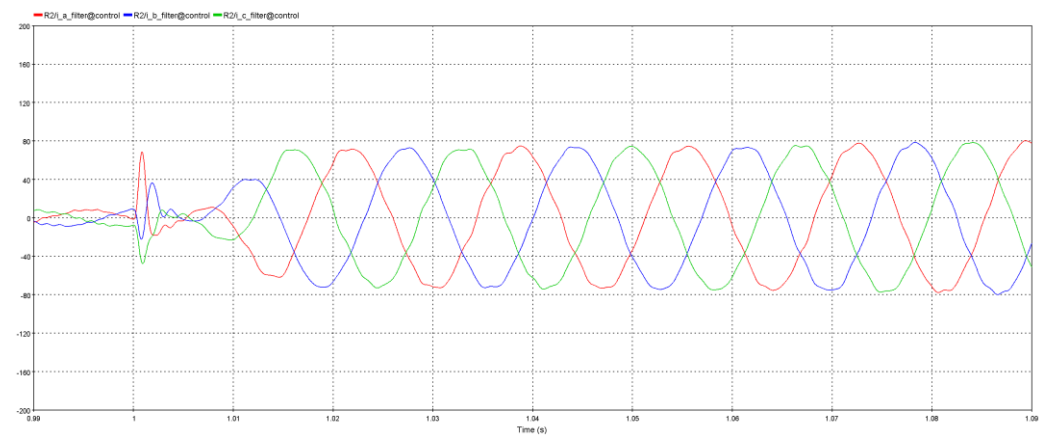


Figure A.5 PV is rated 2 MW and producing 0 MW during a three-phase fault and volt-reactive-power mode with one per unit voltage set point

Appendix B - EMTP-RV Model

B.1. IEEE 34-Bus Model Validation

The figures below show results from the EMTP-RV and compare them with the IEEE data. The figures show the voltage validation tests, and Listing B.1 shows the results from the fault validation tests.

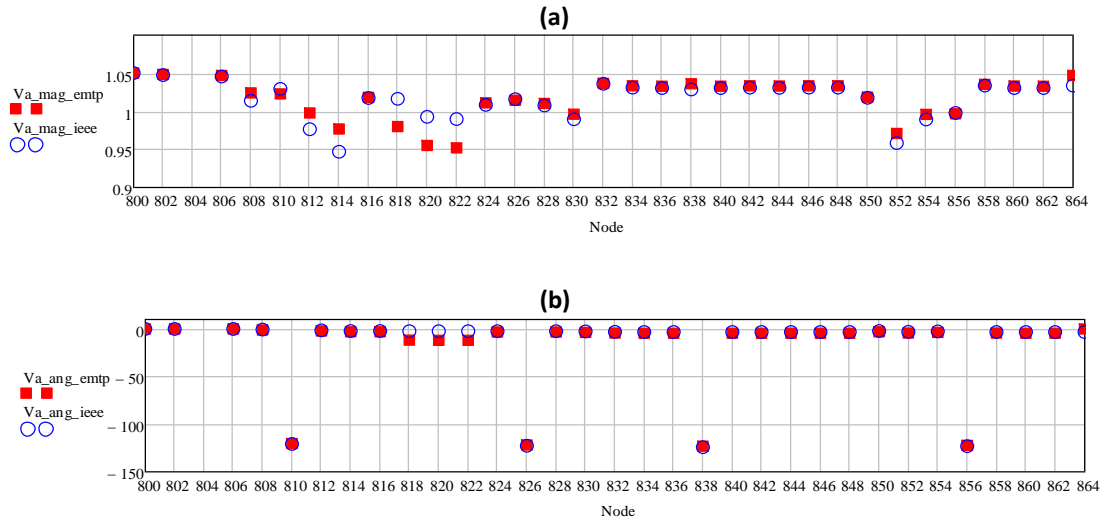


Figure B.1 Modified IEEE 34-node voltage validation test which compares between IEEE data and EMTP-RV results at each node (a) phase A magnitude and (b) phase A angle

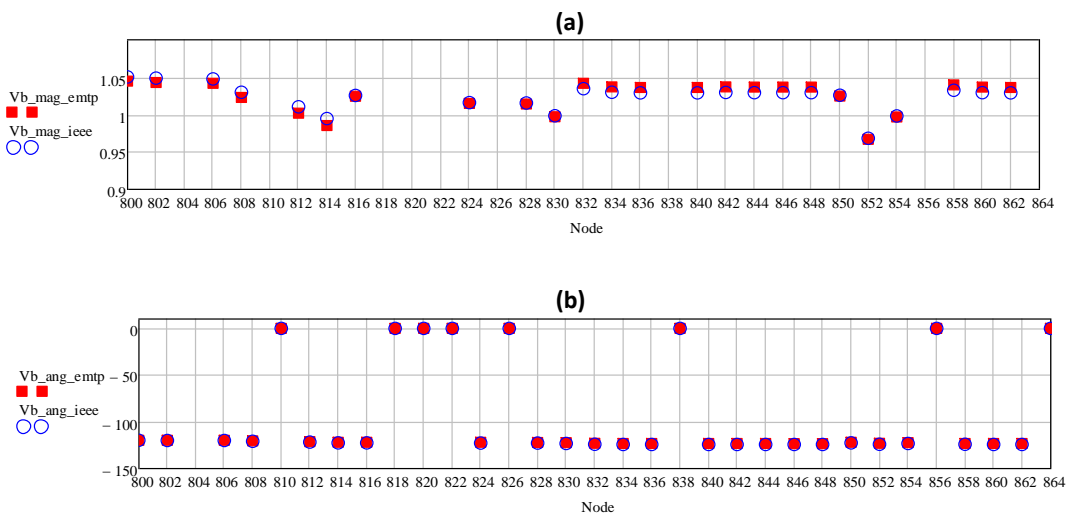


Figure B.2 Modified IEEE 34-node voltage validation test which compares between IEEE data and EMTP-RV results at each node (a) phase B magnitude and (b) phase B angle

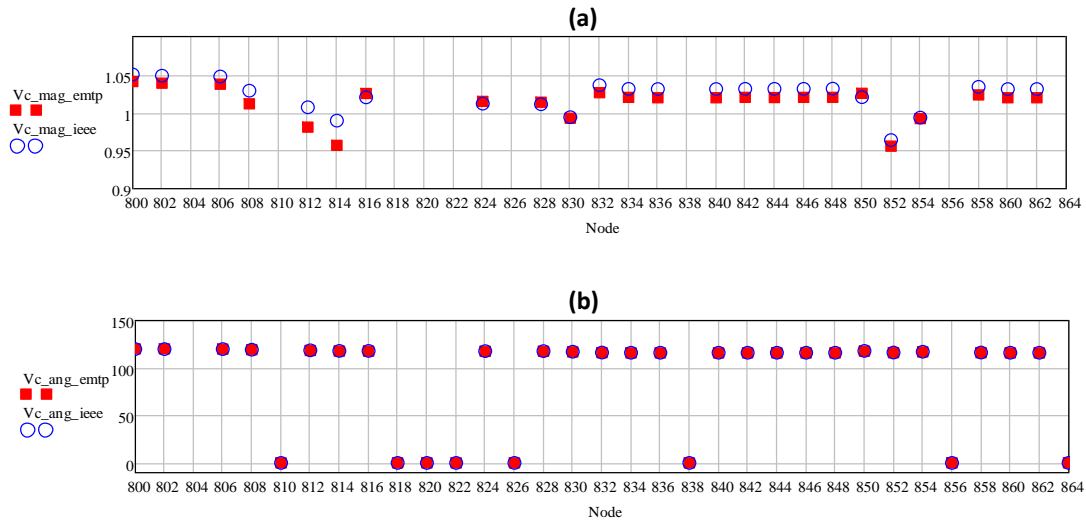


Figure B.3 Modified IEEE 34-node voltage validation test which compares between IEEE data and EMTP-RV results at each node (a) phase C magnitude and (b) phase C angle

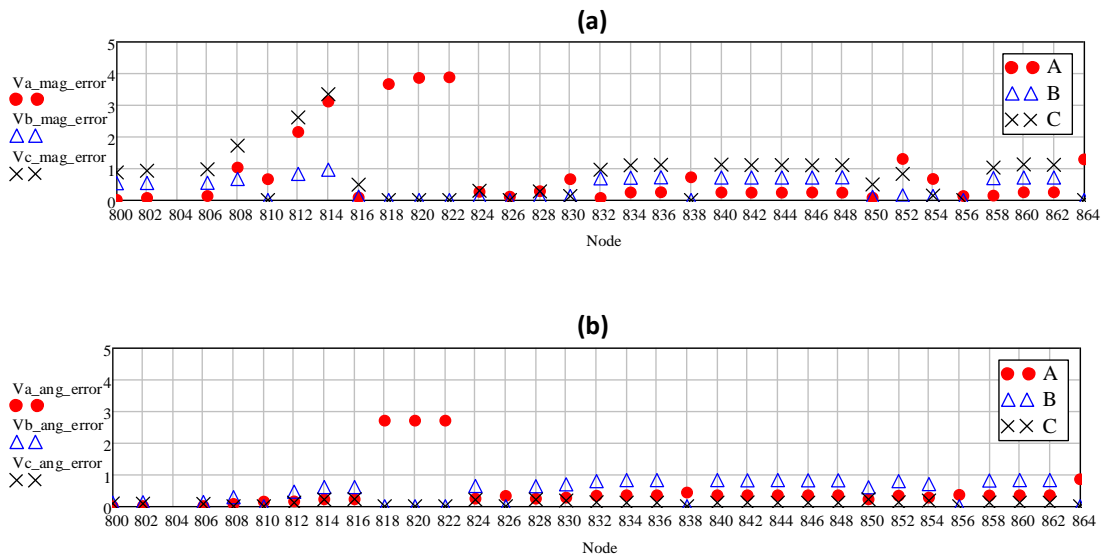


Figure B.4 Modified IEEE 34-node voltage validation test which compares between IEEE data and EMTP-RV results at each node (a) percentage of error in magnitude and (b) percentage of error in angle

IEEE TEST FEEDERS FROM WHK 12/3/2002
 SUBSTATION: IEEE 34; FEEDER: IEEE 34
 SHORT CIRCUIT STUDIES DATE: 8-24-2011
 20. Ohm resistance used for minimum fault calculation and zero Ohm resistance used for maximum fault calculation
 Bus Name followed by fault values in Amperes

Node 800	L-G	A-B	A-B-G	A-C	A-C-G	B-C	B-C-G	A-B-C	A-B-C-G
Ph-A Max ,	655.2,	543.3,	636.4,	543.3,	648.3,	0.0,	0.0,	627.3,	627.3
Ph-A Min ,	452.4,	471.7,	559.4,	471.7,	552.6,	0.0,	0.0,	439.9,	439.9
Ph-B Max ,	655.2,	543.3,	648.3,	0.0,	0.0,	543.3,	636.4,	627.3,	627.3
Ph-B Min ,	452.4,	471.7,	552.6,	0.0,	0.0,	471.7,	559.4,	439.9,	439.9
Ph-C Max ,	655.2,	0.0,	0.0,	543.3,	636.4,	543.3,	648.3,	627.3,	627.3
Ph-C Min ,	452.4,	0.0,	0.0,	471.7,	559.4,	471.7,	552.6,	439.9,	439.9

EMTP-RV Results

Node 800	L-G	A-B	A-B-G	A-C	A-C-G	B-C	B-C-G
Ph-A Max	699.078	579.951	675.585	577.72	695.359	0	0
Ph-A Min	465.136	489.334	579.791	489.428	576.422	0	0
Ph-B Max	701.318	579.951	695.88	0	0	578.216	678.468
Ph-B Min	464.796	489.334	575.997	0	0	489.767	580.072
Ph-C Max	696.157	0	0	577.72	674.167	578.216	692.882
Ph-C Min	463.964	0	0	489.428	578.988	489.767	576.333

Listing B.1 An example of fault currents during faults at node 800 from IEEE data and EMTP-RV

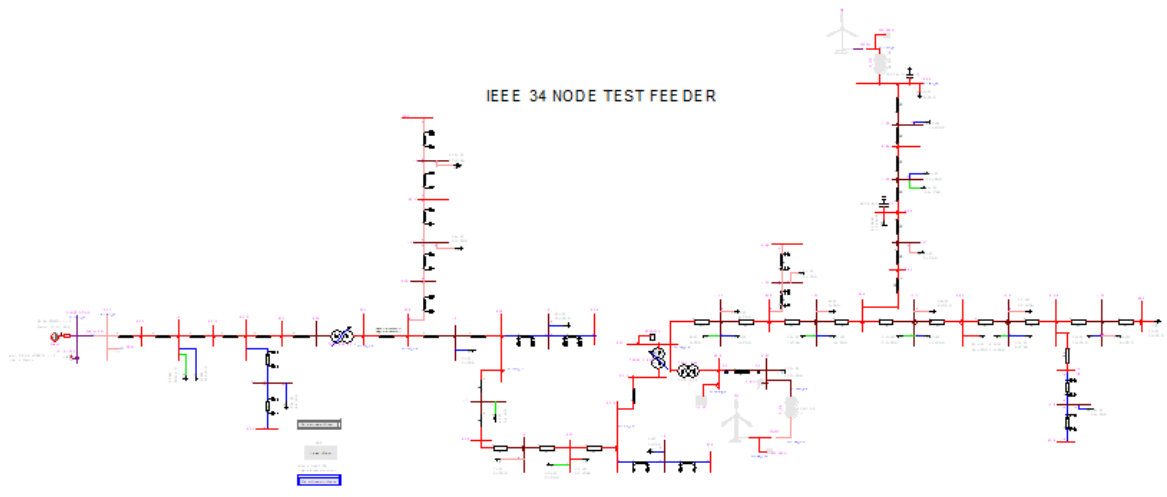


Figure B.5 A screenshot of the IEEE 34-bus model in EMTP-RV

B.2. Synchronous Generator Model Validation

The figures below show results from the EMTP-RV model of the synchronous generator during a three-phase fault.

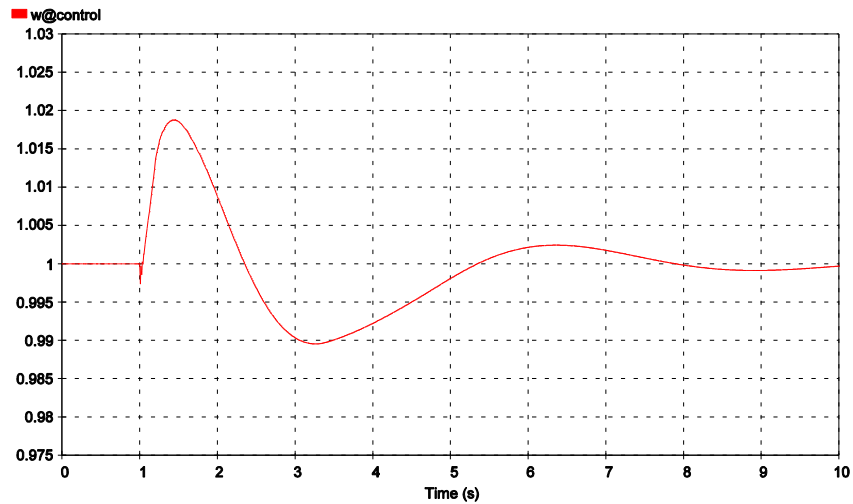


Figure B.6 Synchronous generator angular velocity ω in pu when three-phase fault applied at 1 sec and cleared at 1.2 sec.

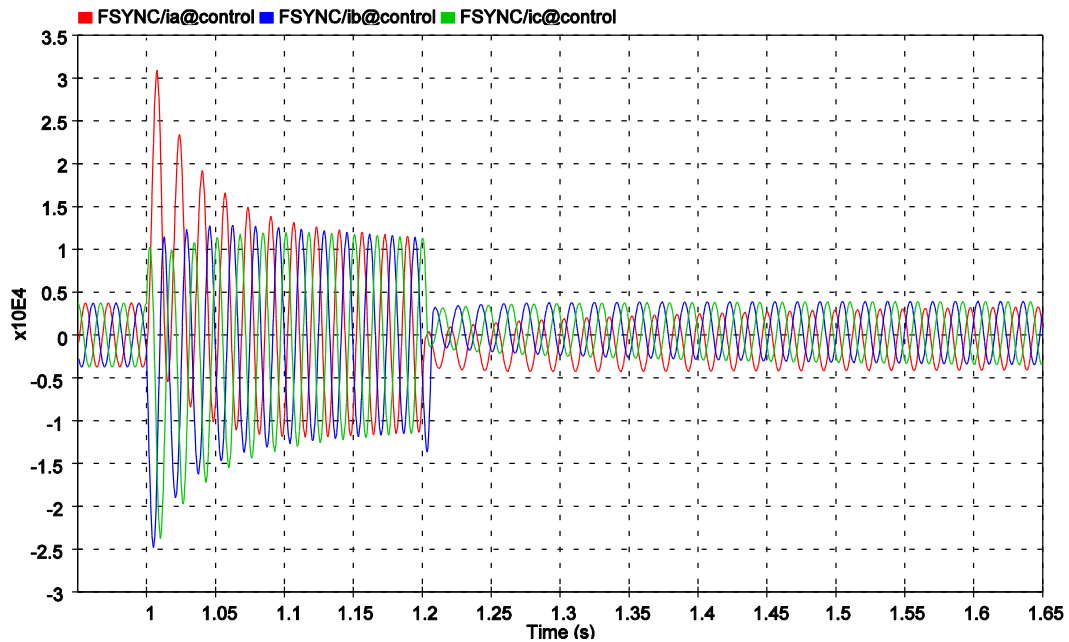


Figure B.7 Synchronous generator three-phase current when three-phase fault applied at 1 sec and cleared at 1.2 sec.

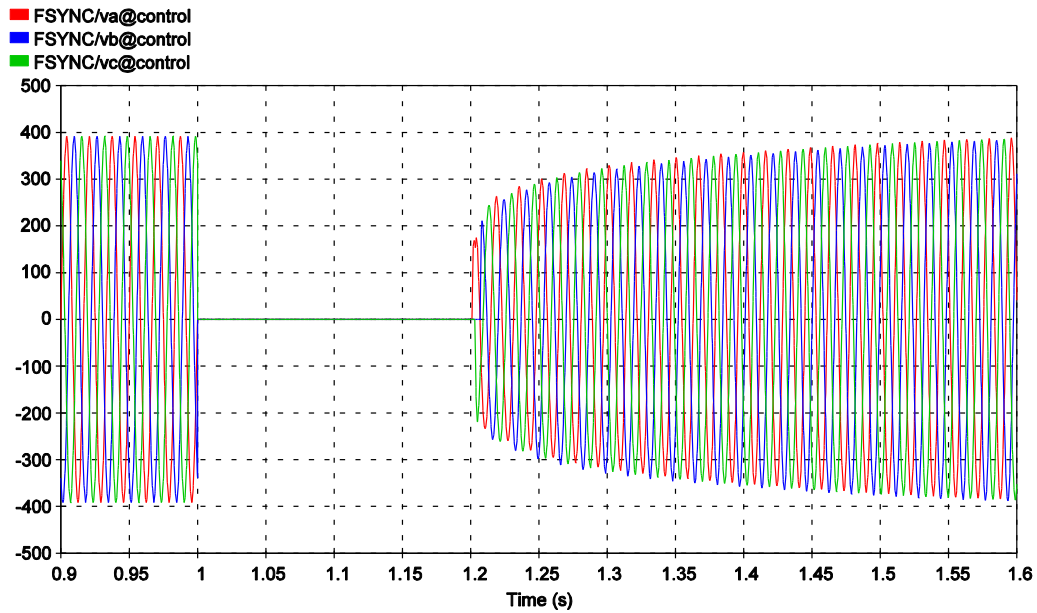


Figure B.8 Synchronous generator three-phase terminal voltage when three-phase fault applied at 1 sec and cleared at 1.2 sec.

B.3. Photovoltaic Model

The figures below show screenshots of the PV model, and Listing B.2 shows the EMTP-RV code for part of the PV model.

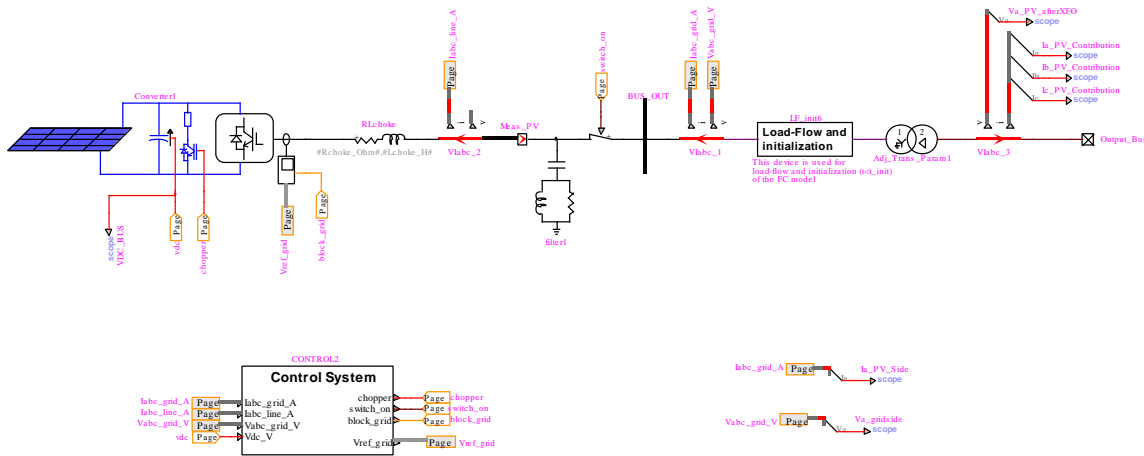


Figure B.9 EMTP-RV model of the PV system including the panel model, the VSC, ac filters, and the power transformer

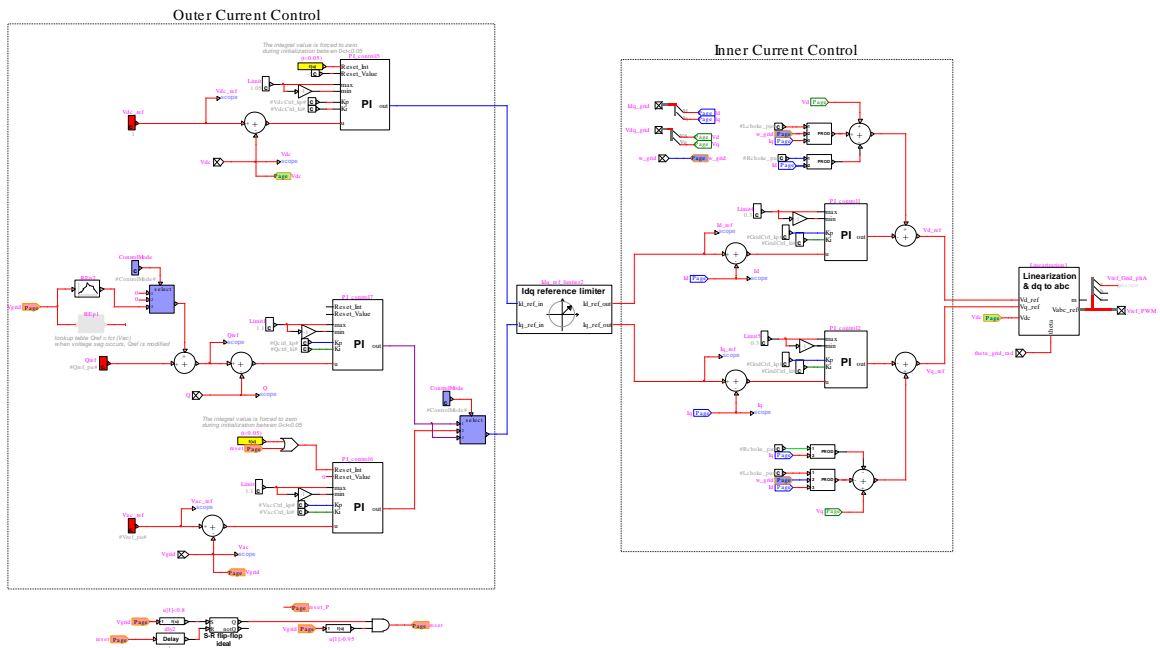


Figure B.10 VSC control including the outer and the inner current controls

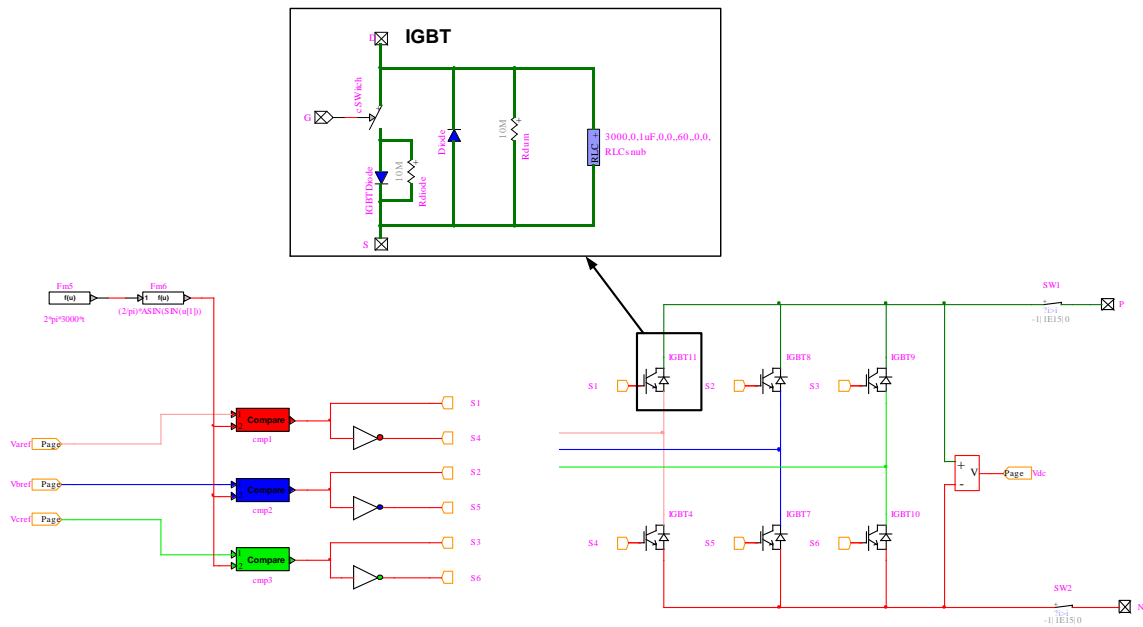


Figure B.11 Switching-based three-phase two-level VSC model

```

//BASIC CALCULATIONS
Period = 1 / Freq; // Period in s
period = Period;
w = 2 * PI * Freq;
/* Total solar panel S and P
Sgen_MVA = Pgen_MW * 1.11; // Rated apparent power of solar generator
(MVA). Note that 11% of reserve power is added
Pgen_W = Pgen_MW * 1e6; // Rated active power of solar generator (W)
Sgen_VA = Sgen_MVA * 1e6; // Rated apparent power of solar generator
(VA). Note that 11% of reserve power is added.
Spark_VA = Ngen * Sgen_VA; // Total aggregated solar plant S (VA)
Spark_MVA = Ngen * Sgen_VA / 1e6; // Total aggregated solar plant S (MVA),
Ppark_W = Ngen * Pgen_W; // Total aggregated solar plant P (W) (used
for the load-flow device)
Qpark_Var = Qref_pu * Spark_VA; // Total aggregated solar plant Q (Var) (used
for the load-flow device when Q or Q+Vac control is selected)
Vdc_V = Vdc_kV * 1e3; // DC voltage (V)
/* base calculations
Vbase_VRMSLL = Vgen_kVRMSLL * 1e3; // Rated generator voltage (VRMSLL)
Vbase_V = Vbase_VRMSLL * sqrt(2 / 3); // Peak generator voltage (V)
Ibase_A = Spark_VA / Vbase_VRMSLL * sqrt(2 / 3); // Peak generator current (A)
Zbase_Ohm = (Vgen_kVRMSLL * Vgen_kVRMSLL) / Spark_MVA; // Base impedance (Ohm)
// Control Settling time to within 5% relative error in s
TimeConstant_Q = 100e-3; // Q control of the converter
TimeConstant_Vac = 100e-3; // Vac control of the converter
TimeConstant_P = 100e-3; // P control of the converter
TimeConstant_Vdc = 100e-3; // Vdc control of the Grid side converter
TimeConstant_PLL = 75e-3; // PLL control
TimeConstant_i_grid = 10e-3; // Inner control of the Grid side converter
// DC/AC CONVERTER PARAMETERS
Rchoke_pu = 1.5e-3; // in pu
Rchoke_Ohm = Rchoke_pu * Zbase_Ohm; // in Ohm
Lchoke_pu = 0.15; // in pu
Lchoke_H = Lchoke_pu * Zbase_Ohm / w; // in H
/* DC/AC Converter parameters
E_Cdc = 10; // in KJ/MVA
Cdc_F = E_Cdc * 1e-3 / (1 / 2 * pow(Vdc_V, 2) / Sgen_VA); // DC capacitor (F)
CdcPark_F = Cdc_F * Ngen; // Aggregated DC capacitor (F)
CarrierSignal_Freq = 3e3; // PWM Carrier signal
frequency (Hz) (used only for Detailed Converter Model)
CarrierSignal_ratio = CarrierSignal_Freq / Freq; // PWM carrier signal ratio
Rsnubber_Ohm = 3000; // IGBT/diode resistance snubber (Ohm)
Csnubber_F = 1e-6; // IGBT/diode capacitor
snubber (F) (used only for Detailed Converter Model)
Rchopper_Ohm = 0.2; // Chopper resistance in Ohm
RchopperPark_Ohm = Rchopper_Ohm / Ngen; // Aggregation of the chopper resistance
/* High pass filter parameters
Qfilter_Var = 150e3 * Ngen // Reactive power generated by each filter
n1 = CarrierSignal_ratio // First tuning harmonic
n2 = CarrierSignal_ratio * 2 // Second tuning harmonic
QF = 5 // Quality factor
Cfilter1_F = Qfilter_Var / (Vbase_VRMSLL * Vbase_VRMSLL * 2*PI*Freq); // capacitor in F
Lfilter1_H = 1 / (Cfilter1_F * pow((n1 * Freq * 2 * PI), 2)); // inductance in H
Rfilter1_Ohm = QF * 2 * PI * n1 * Freq * Lfilter1_H; // resistance in Ohm
Cfilter2_F = Cfilter1_F; // capacitor in F
Lfilter2_H = 1 / (Cfilter2_F * pow((n2 * Freq * 2 * PI), 2)); // inductance in H
Rfilter2_Ohm = QF * 2 * PI * n2 * Freq * Lfilter2_H; // resistance in Ohm
//CONTROL SYSTEM PARAMETERS
//+Grid Inner current control
eps = 1; // Damping ratio
w_i = 3 / (eps * TimeConstant_i_grid); // Impulse of the closed loop control
GridCtrl_ki = (Lchoke_pu / w) * w_i * w_i; // Integral Gain of the Inner Current control
GridCtrl_kp = 5 * 2 * eps * w_i * (Lchoke_pu / w); // Proportional gain of the Inner
Current control
//+Vdc control
E_Cdc_J = 0.5 * CdcPark_F * Vdc_V * Vdc_V; // Energy stored in the DC capacitor (Joule)
H_Cdc = E_Cdc_J / (1 * Ppark_W); // Static moment of inertia (S)
eps = 0.7; // Damping ratio
w_Vdc = 3 / (eps * TimeConstant_Vdc); // Time response for 5% (sec)

```

```

VdcCtrl_ki = 2 * H_Cdc * w_Vdc * w_Vdc;           // Proportional Gain of Vdc control
VdcCtrl_kp = 2 * 2 * eps * w_Vdc * H_Cdc;        // Integral Gain of Vdc control
//+ Idq limit (see CONTROL/Grid_Control/Idq_ref_limiter1 )
Q_priority = 1;                                   // 1 = priority is given for reactive power (should be set
for FRT capability). 0 = priority is given to active power
I_lim_Grid_pu = 1.1;                             // Maximum Grid Converter Idq limit
Id_lim_Grid_pu = 1;                              // Maximum Grid Converter Id limit, if Q_priority = 1
Iq_lim_Grid_pu = 1;                              // Maximum Grid Converter Iq limit, if Q_priority = 0
//+Q control and Q+Vac control
Qctrl_kp = 0;                                     // Proportional Gain of Q control (Only Integral part of the PI)
Qctrl_ki = 3 / TimeConstant_Q;                   // Integral Gain of Q control
//+Vac control
X_tot = X_PCC_pu + Xtransfo_pu; // Total impedance in pu at solar connection point
VacCtrl_kp = 1;                                  // Proportional Gain of Vac control (Only Integral part of the PI)
VacCtrl_ki = 3 / (X_tot * TimeConstant_Vac);     // Integral Gain of Vac control
//* PLL
PLL_lim_low = 12
PLL_lim_up = 12
PLL_max_delay = 0.0223
eps = 1;                                          // Damping ratio
w_i = 3 / (eps * TimeConstant_PLL);
PLL_ki = 1 * w_i * w_i;                          // Integral Gain (rad/V)
PLL_kp = 2 * eps * w_i * 1;                      // Proportional Gain (rad/s/V)
//SOLAR PANEL PARAMETERS
// ~75 W per module // input // Calcul
//dVmpp=16.2; // maximum power voltage (V) under STC
//dnNbPVCellsSeries=Vdc_V / dVmpp; //PoweratVmpp=73.9273; // new model diode
//dnNbPVCellsParallel=Pgen W/dnNbPVCellsSeries/PoweratVmpp;
Nmod_series = Vdc_V / VmaxP; // number of PV modules in series
Nmod_parallel = Ppark_W / (Vdc_V * ImaxP); // number of PV modules in parallel
//Nmod_parallel = Spark_VA / (Vdc_V * ImaxP); // number of PV modules in parallel
//SOLAR PANEL PARAMETER CALCULATION from DATASHEET
Vth = (Temp_ref + 273) * 1.38065e-23 / 1.6022e-19; // diode threshold voltage
Ns = Ncell_series;
Io = Isc / (-1 + exp(Voc / (IdealFactor * Ns * Vth))); // diode reversed saturation current
Rs_max = Ns * ((Voc - VmaxP) / (Ns * ImaxP) - exp(-
Voc / (Vth * Ns * IdealFactor)) * Vth * IdealFactor / Io);
x1 = 10 * Rs_max; // to initialize the while loop
x2 = Rs_max;
ite = 0;
while ((x1 - x2) > num_tolerance) {
x1 = x2;
Rp_x1 = 1 / (1 / (VmaxP / ImaxP - x1) - Io / (IdealFactor * Ns * Vth) * exp((VmaxP +
ImaxP * x1) / (IdealFactor * Ns * Vth)));
Iph_x1 = Isc * (VmaxP / (VmaxP - x1 * ImaxP) - Io * x1 * exp((VmaxP +
ImaxP * x1) / (IdealFactor * Ns * Vth)) / IdealFactor / Ns / Vth);
// Newton Method
fx1 = Iph_x1 - ImaxP - (VmaxP + ImaxP * x1) / Rp_x1 - Io * (exp((VmaxP +
ImaxP * x1) / (IdealFactor * Ns * Vth)) - 1);
df_x1 = ImaxP * VmaxP * (Isc - 2 * ImaxP) / pow(VmaxP - x1 * ImaxP, 2) + Io * exp((VmaxP +
ImaxP * x1) / (IdealFactor * Ns * Vth)) * (ImaxP * VmaxP - Isc * IdealFactor * Ns * Vth + x1 * ImaxP * (ImaxP -
Isc)) / pow(IdealFactor * Ns * Vth, 2);
x2 = x1 - fx1 / df_x1;
ite = ite + 1;
}
Rs = x2;
Rp = 1 / (1 / (VmaxP / ImaxP - x2) - Io / (IdealFactor * Ns * Vth) * exp((VmaxP +
ImaxP * x2) / (IdealFactor * Ns * Vth)));
Iph = Isc * (Rs + Rp) / Rp;
Rseries_PV = Rs * (Nmod_series / Nmod_parallel);
Rparallel_PV = Rp * (Nmod_series / Nmod_parallel);
Vth_diode = (Temp + 273) * 1.38065e-23 / 1.6022e-19;
IO_diode = Nmod_parallel * (Isc + Ki_pv * (Temp - Temp_ref)) / (-1 + exp((Voc + Kv_pv * (Temp
- Temp_ref)) / (IdealFactor * Ns * Vth)));
Iph_T = Nmod_parallel * (Iph + Ki_pv * (Temp - Temp_ref));
Nseries = Ns * Nmod_series // total number of cell in series (value transmitted)
}

```

Listing B.2 The PV model code from the EMTP-RV model

B.4. Voltage Source Converter Model Validation

Figure B.12 and Figure B.13 show the EMTP-RV and the ATP VSC model used for validation. Figure B.14 shows the results from the two models. Figure B.15 compares the VSC switching model to the VSC averaged model. Figure B.16 shows the PI controller model in EMTP-RV with feedback. Finally, Figure B.17 compares the PI controller with feedback to a PI without feedback using MATLAB. The feedback improves the PI controller by reducing the overshoot.

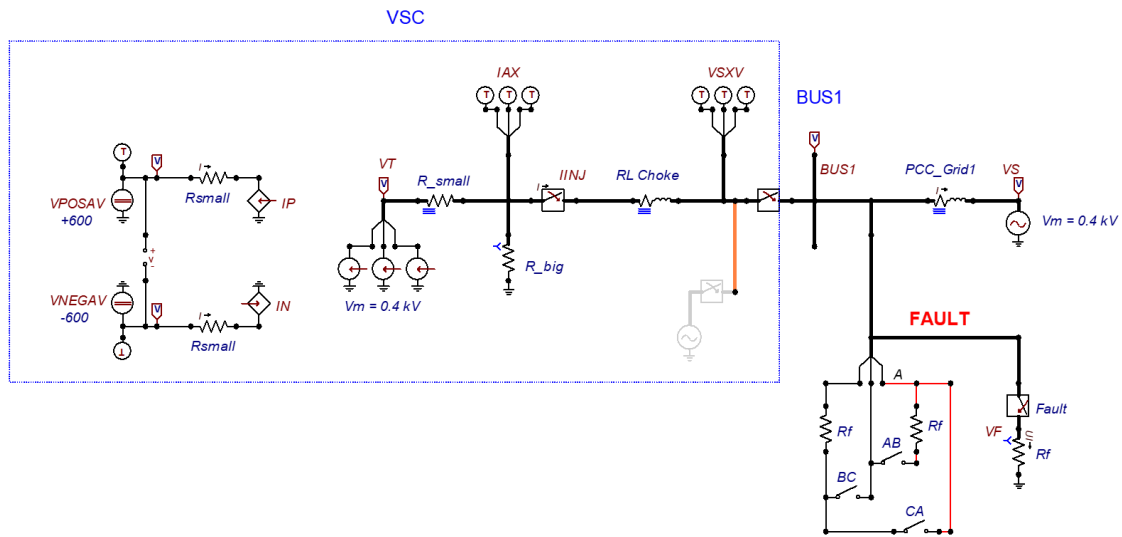


Figure B.12 ATP-EMTP test bed for validation

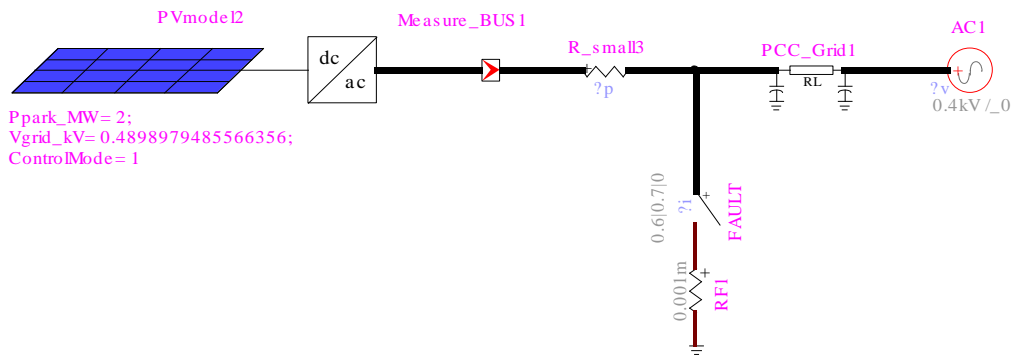


Figure B.13 EMTP-RV test bed for validation

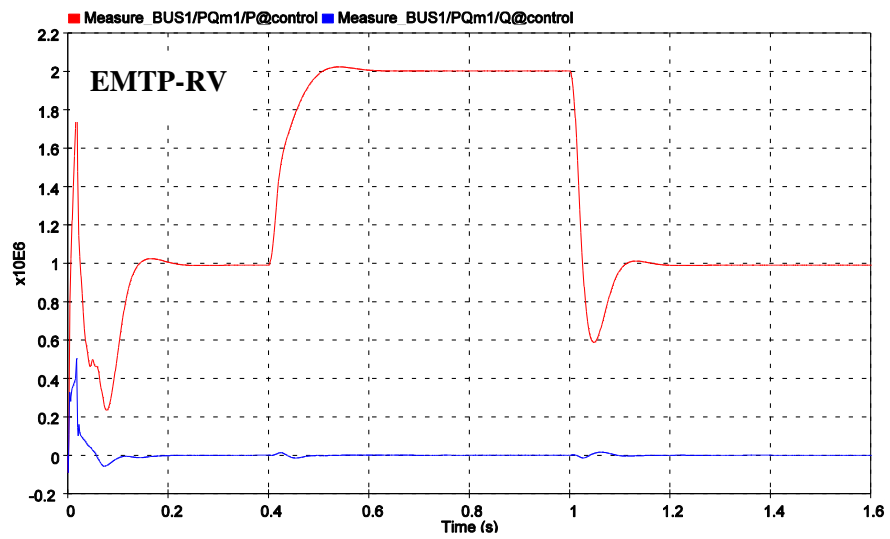
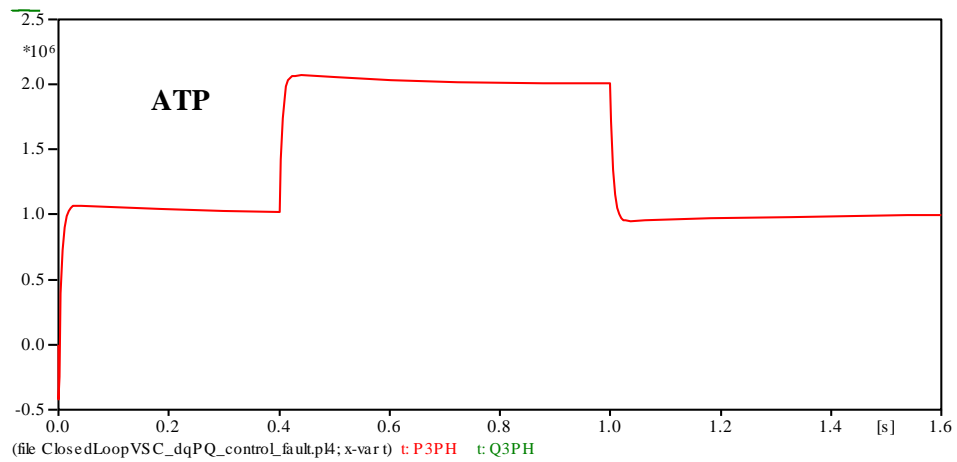


Figure B.14 Comparing the change of real power from 50% to 100% between ATP-EMTP and EMTP-RV

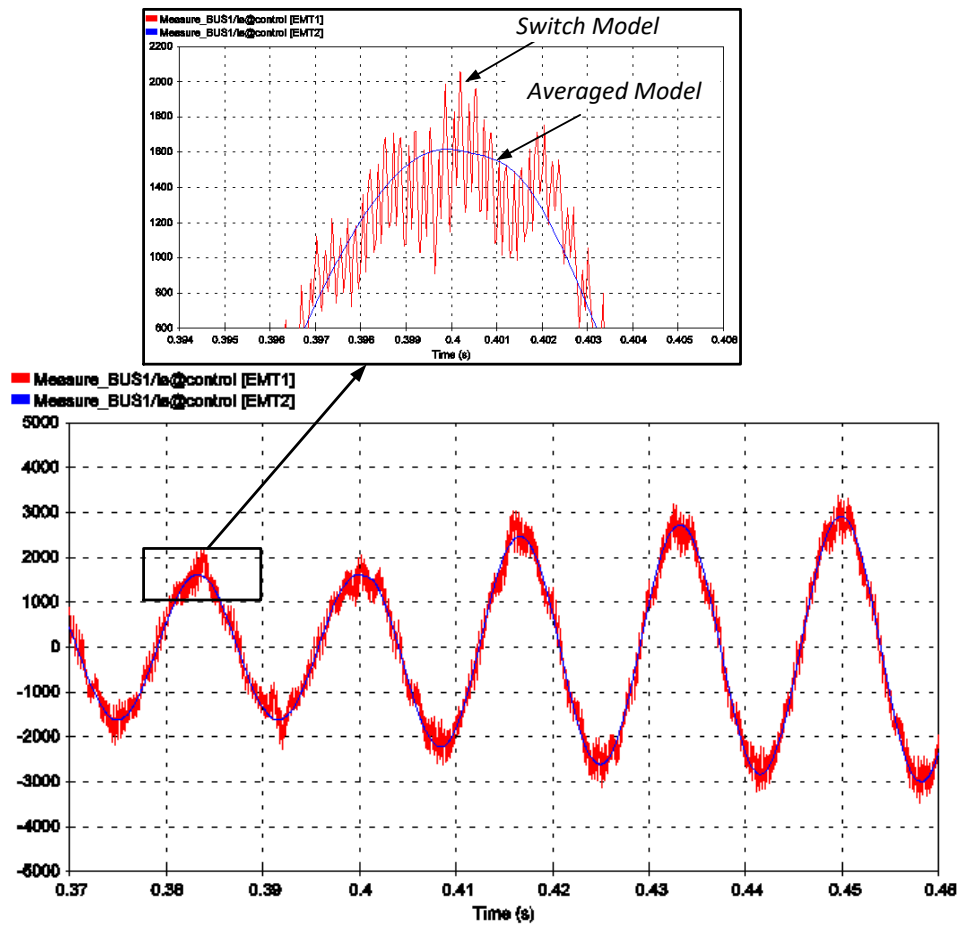


Figure B.15 Phase A current during a fault on EMTP-RV test bed with averaged model and switched model

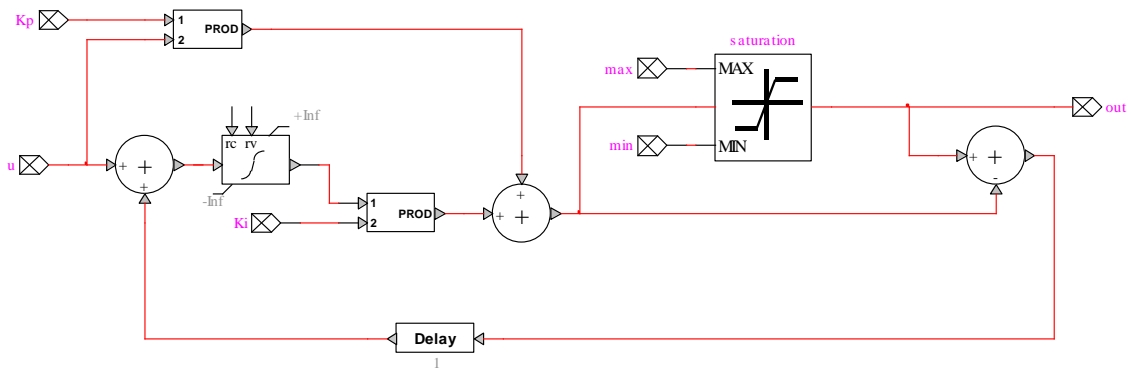


Figure B.16 EMTP-RV PI control with a feedback

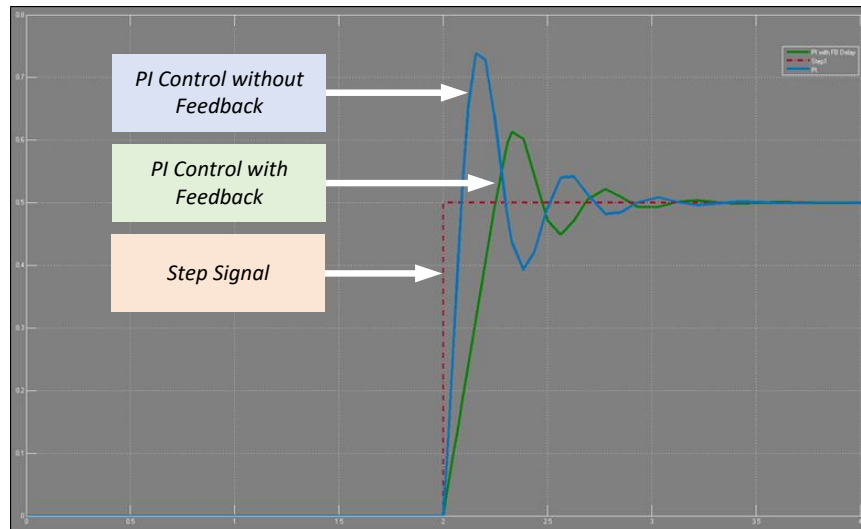


Figure B.17 Verifying EMTP-RV PI control with feedback by using MATLAB Simulink

B.5. Relay Model Validation

The figures below show the signal processing model such as low pass filters, sampling, DFT with cosine and sine filters, sequence calculation, delta filters, DDS RF algorithm. Listing B.3 and B.4 show the MATLAB code for the digital low pass and mimic filters.

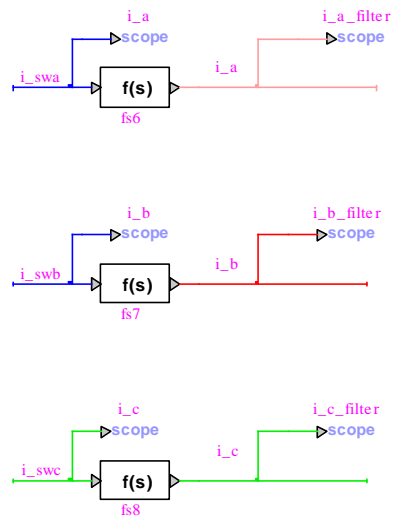


Figure B.18 An example of the developed EMTP-RV model for the low pass filter

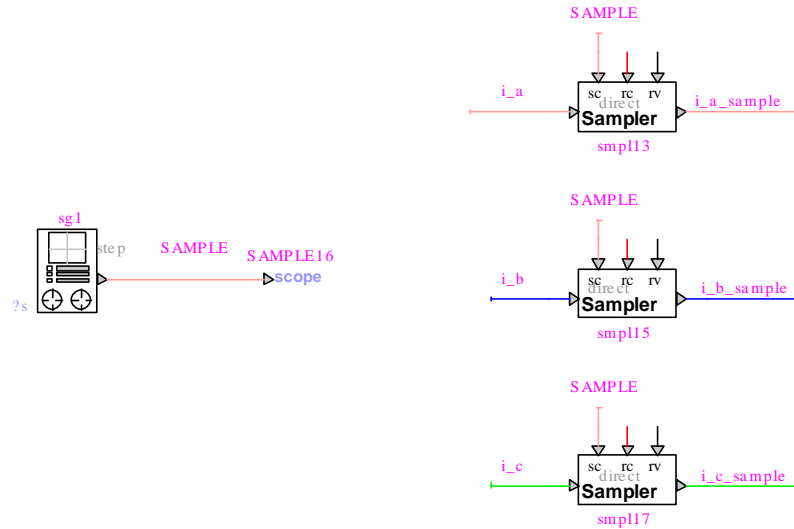


Figure B.19 An example of the developed EMTP-RV model for sampling currents (16 spc)

```
% A DIGITAL LOW PASS FILTER (16 spc)
% TIME CONSTANT T2 (T2 in number of samples)
s = tf('s');
H = 1/(1.0994052044524501e-7*s^2 + 0.0004736754258687362*s + 1)
Fs = 12000; % samples per second
H =
```

$$\frac{1}{1.099e-07 s^2 + 0.0004737 s + 1}$$

Listing B.3 Testing the developed low pass filter model in MATLAB for sampling rate of 16 spc

```

% A DIGITAL MIMIC
% TIME CONSTANT T2 (T2 in number of samples)
SAMFREQ=16*60;
T2=2*16;
gain3=((T2+1)-T2*cos(2*pi*60/SAMFREQ))^2+(T2*sin(2*pi*60/SAMFREQ))^2)^0.5;
b2=[(T2+1) -T2];
b2=b2/gain3;
Ts1 = 16;           % number of samples
Fsamp = 16*60;     % sampling frequency
% Gain (at 60Hz)
K = 1/(((1+Ts1)-Ts1*cos(2*pi*60/Fsamp))^2 + (Ts1*sin(2*pi*60/Fsamp))^2)^0.5;
% Transfer Function
z = tf('z', 1/Fsamp);
H = K*((1+Ts1) - (Ts1*z^-1))

```

H =

$2.61 z^{-1} - 2.457$

z

Listing B.4 Testing the developed mimic filter model in MATLAB for sampling rate of 16 spc

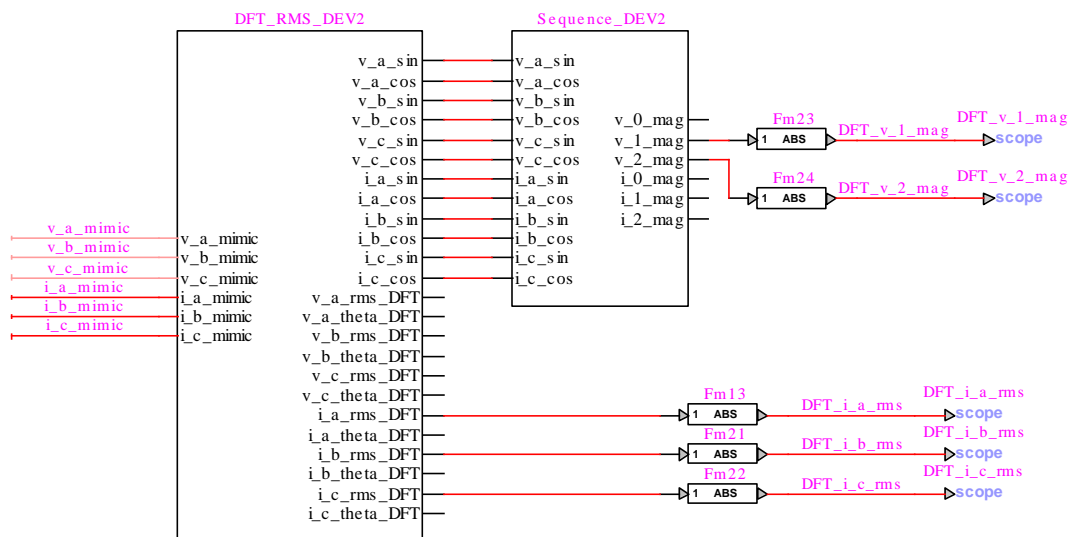


Figure B.20 The developed EMTP-RV model for DFT and sequence calculation

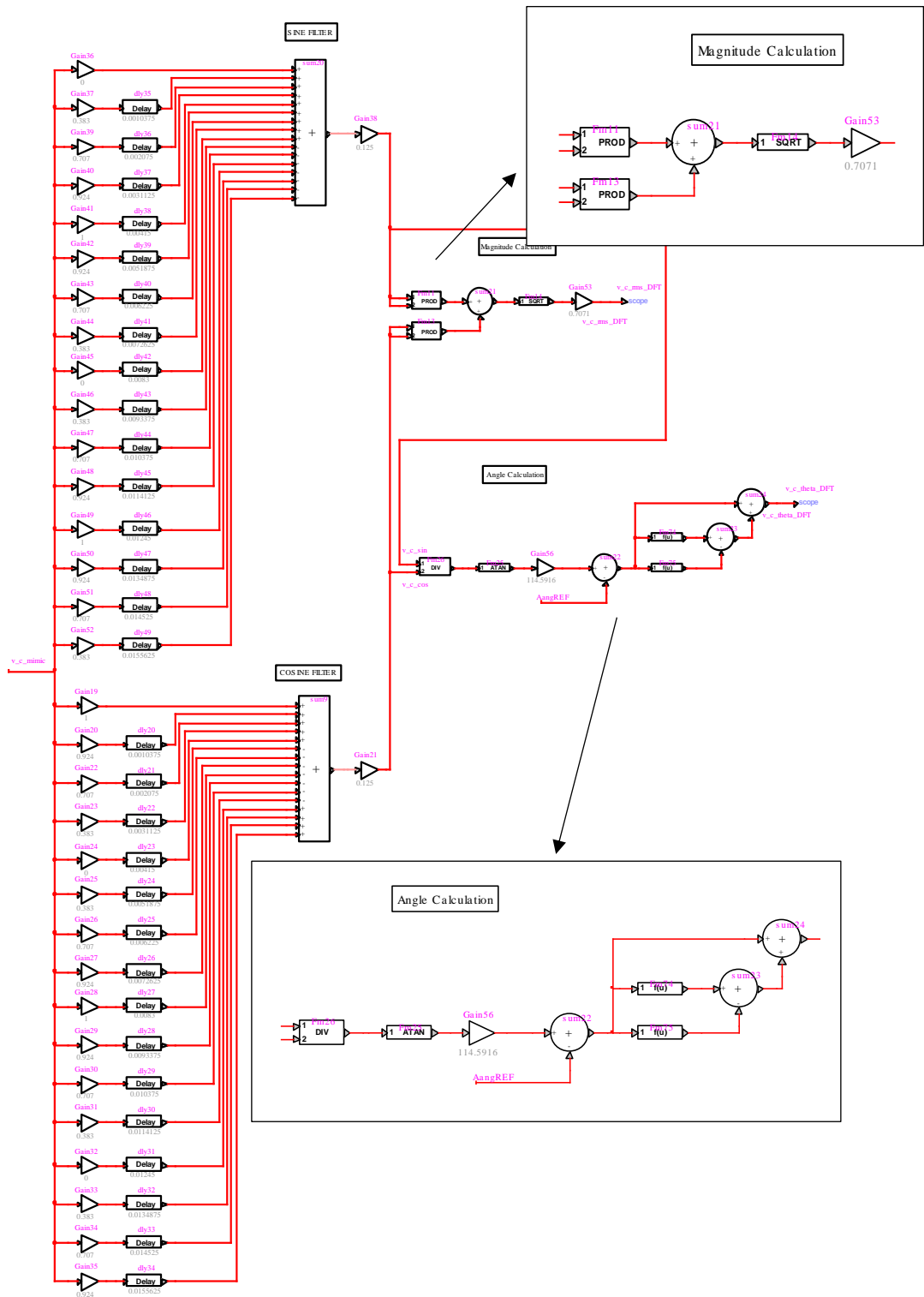


Figure B.21 An example of the developed sine and cosine filters for voltage with zoom in magnitude and angle calculation

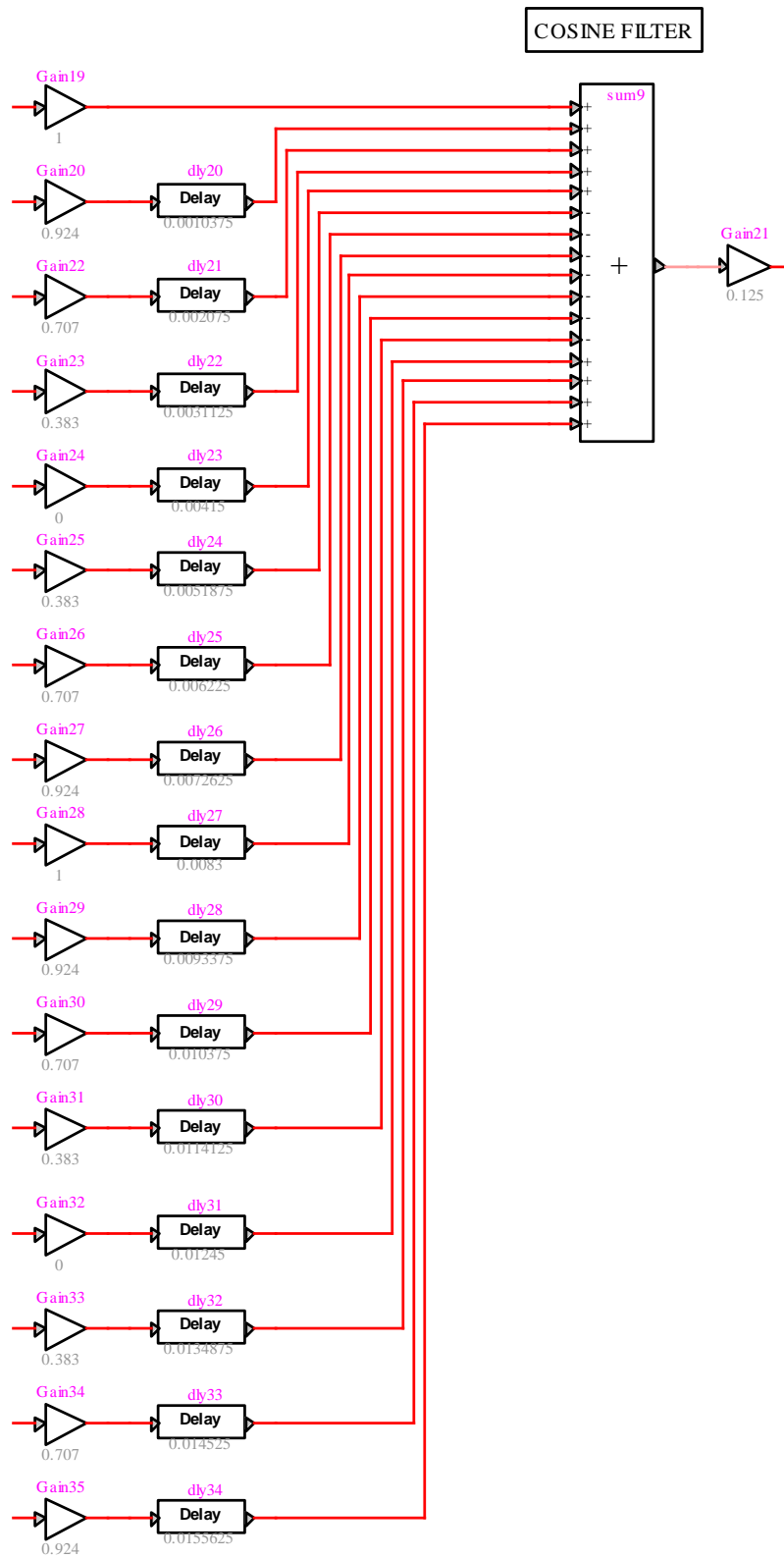


Figure B.22 Zoom in cosine filter

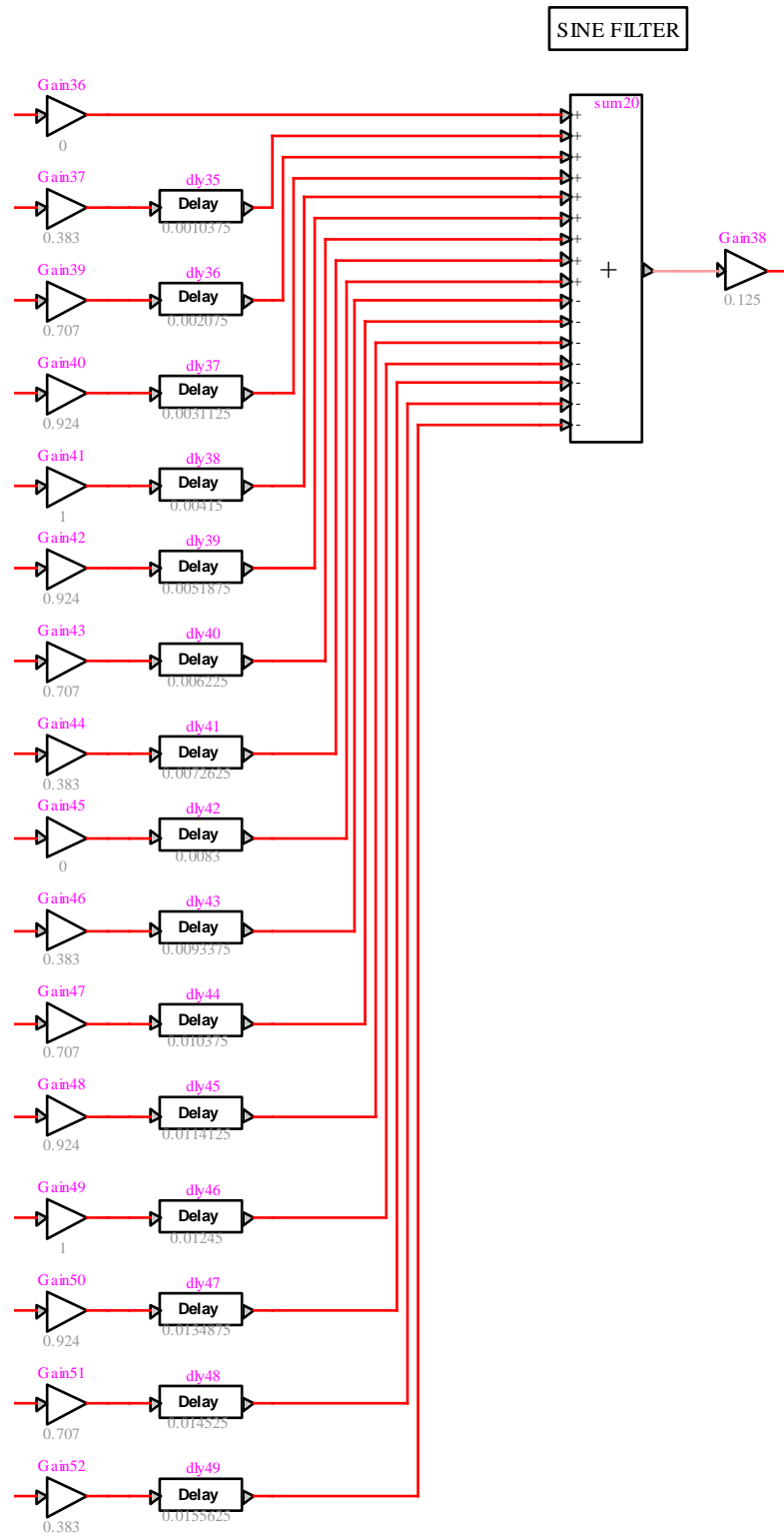


Figure B.23 Zoom in sine filter

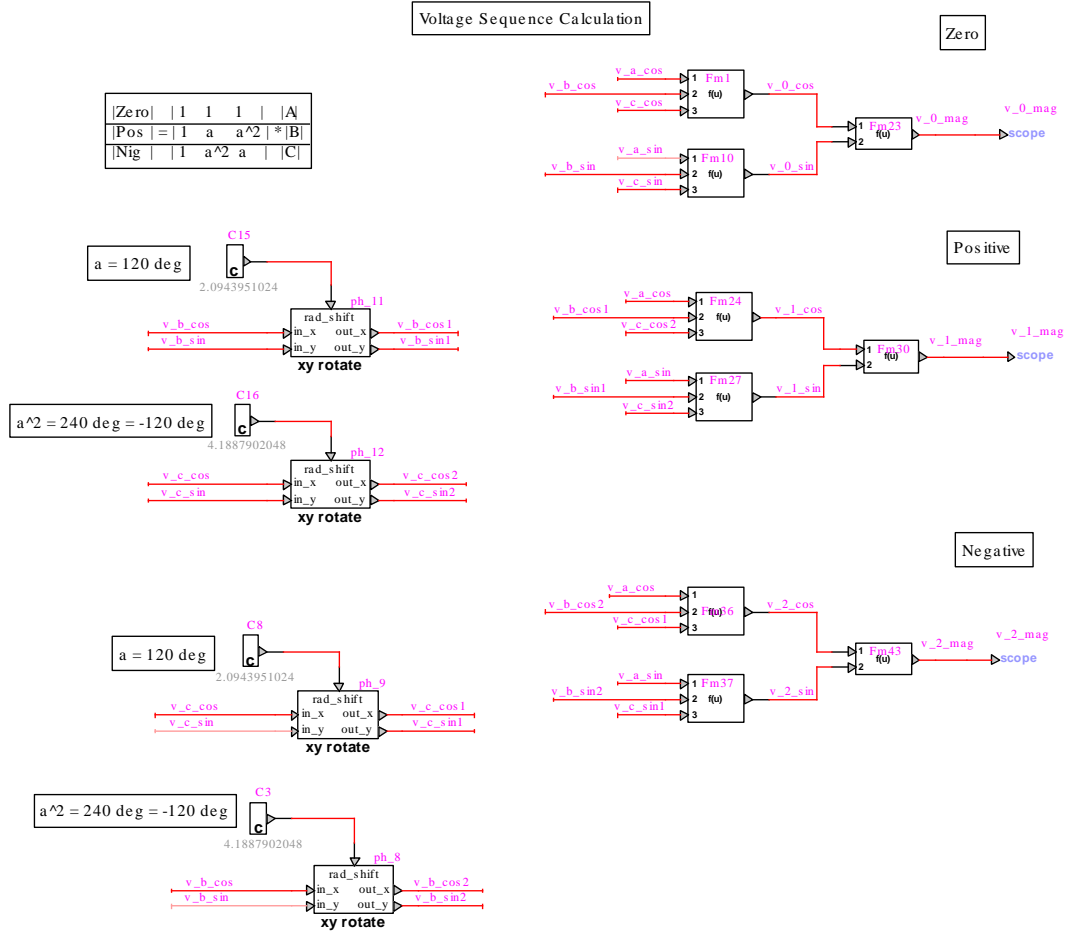


Figure B.24 The developed EMTP-RV model for calculating positive, negative, and zero sequences voltage after the DFT

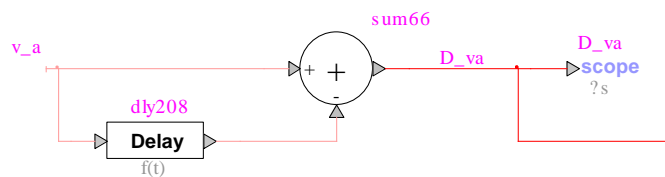


Figure B.25 An example of the developed EMTP-RV model for calculating superimposed

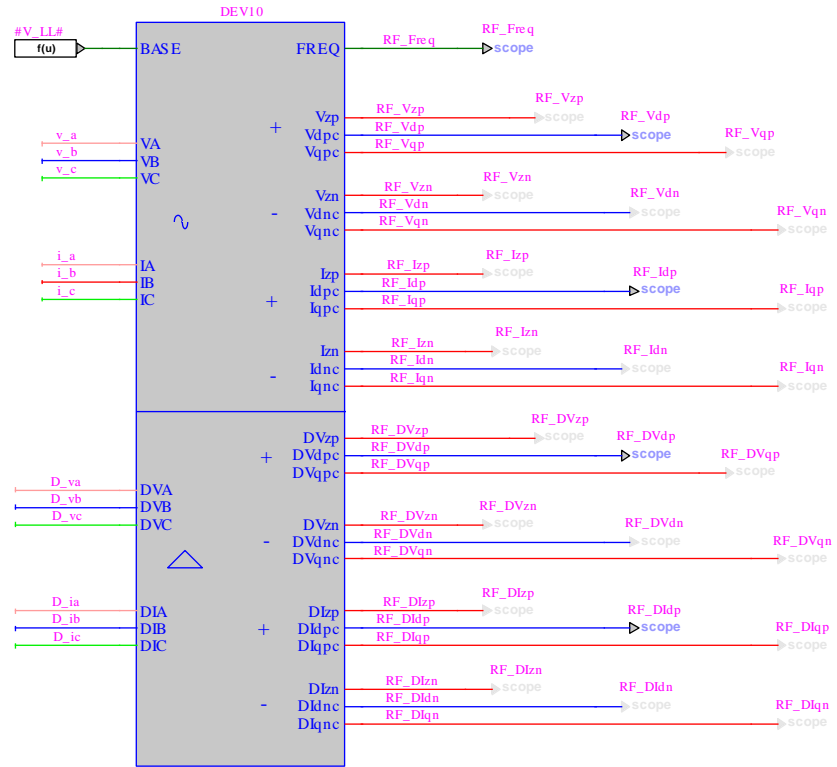


Figure B.26 The developed EMTP-RV model for the proposed DDSRF-based superimposed

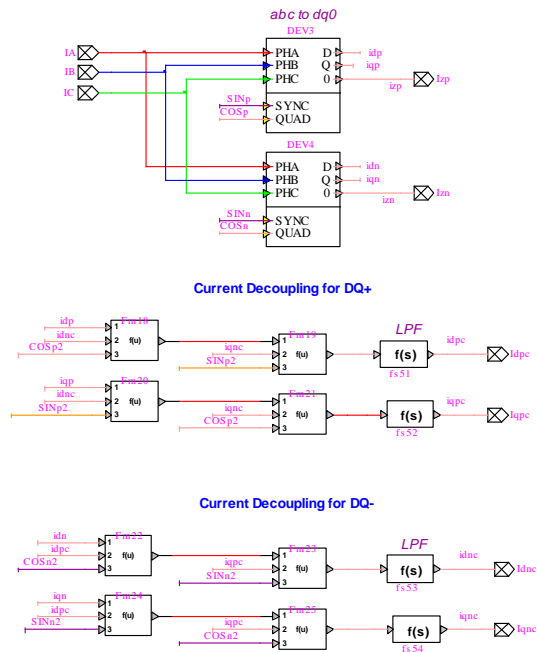
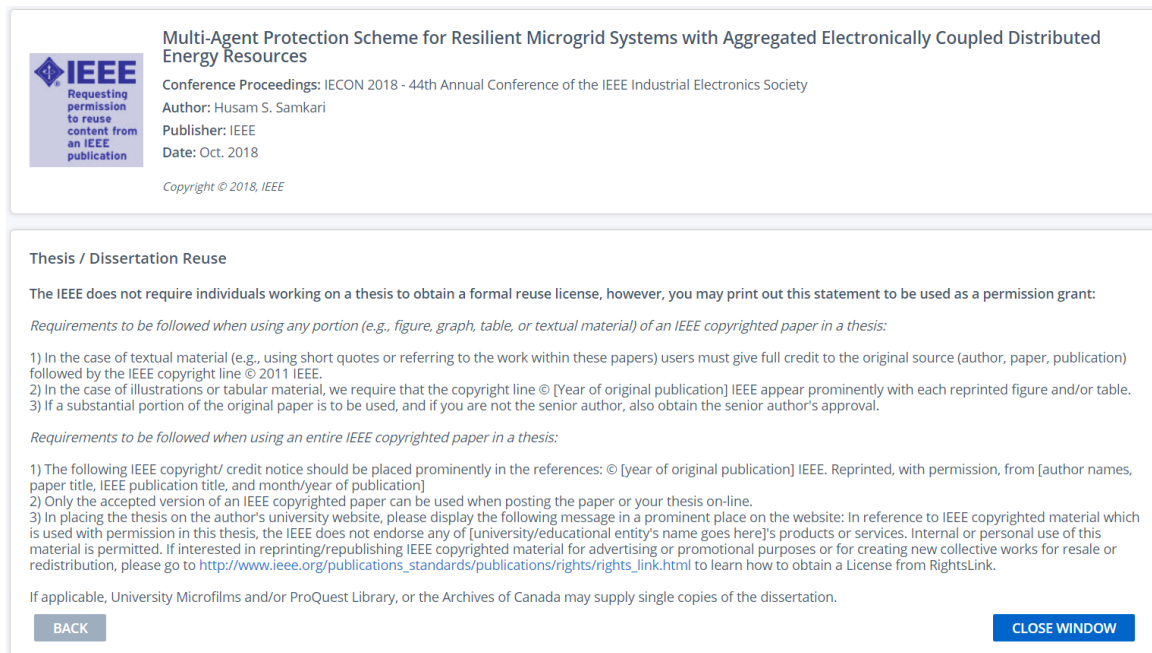


Figure B.27 An example of the developed EMTP-RV model for the DDSRF scheme

Appendix C - Copyright Permissions

Part of this dissertation is copyrighted by the Institute of Electrical and Electronics Engineers Inc. (IEEE). The IEEE has issued permission for copying papers in this dissertation. The format of these papers has been changed to match the format of this dissertation. The changes include the numbering of the tables and figures, but their captions did not change. Figure C.1 shows the proof of copyright permissions for Chapter 4.



The screenshot shows a permission form from IEEE. At the top left is the IEEE logo with the text "Requesting permission to reuse content from an IEEE publication". To the right of the logo, the title of the paper is "Multi-Agent Protection Scheme for Resilient Microgrid Systems with Aggregated Electronically Coupled Distributed Energy Resources". Below the title, it lists "Conference Proceedings: IECON 2018 - 44th Annual Conference of the IEEE Industrial Electronics Society", "Author: Husam S. Samkari", "Publisher: IEEE", and "Date: Oct. 2018". At the bottom of this section is "Copyright © 2018, IEEE".

The main body of the form is titled "Thesis / Dissertation Reuse". It states: "The IEEE does not require individuals working on a thesis to obtain a formal reuse license, however, you may print out this statement to be used as a permission grant: Requirements to be followed when using any portion (e.g., figure, graph, table, or textual material) of an IEEE copyrighted paper in a thesis:"

- 1) In the case of textual material (e.g., using short quotes or referring to the work within these papers) users must give full credit to the original source (author, paper, publication) followed by the IEEE copyright line © 2011 IEEE.
- 2) In the case of illustrations or tabular material, we require that the copyright line © [Year of original publication] IEEE appear prominently with each reprinted figure and/or table.
- 3) If a substantial portion of the original paper is to be used, and if you are not the senior author, also obtain the senior author's approval.

Below this, it says "Requirements to be followed when using an entire IEEE copyrighted paper in a thesis:"

- 1) The following IEEE copyright/ credit notice should be placed prominently in the references: © [year of original publication] IEEE. Reprinted, with permission, from [author names, paper title, IEEE publication title, and month/year of publication]
- 2) Only the accepted version of an IEEE copyrighted paper can be used when posting the paper or your thesis on-line.
- 3) In placing the thesis on the author's university website, please display the following message in a prominent place on the website: In reference to IEEE copyrighted material which is used with permission in this thesis, the IEEE does not endorse any of [university/educational entity's name goes here]'s products or services. Internal or personal use of this material is permitted. If interested in reprinting/republishing IEEE copyrighted material for advertising or promotional purposes or for creating new collective works for resale or redistribution, please go to http://www.ieee.org/publications_standards/publications/rights/rights_link.html to learn how to obtain a License from RightsLink.

At the bottom, it says "If applicable, University Microfilms and/or ProQuest Library, or the Archives of Canada may supply single copies of the dissertation." There are two buttons at the bottom: "BACK" and "CLOSE WINDOW".

Figure C.1 IEEE permission for copying a paper as Chapter 4 in this dissertation

Chapter 4 of this dissertation © 2017 IEEE. Copied with permission. Citation: H. S. Samkari and B. K. Johnson, "Multi-Agent Protection Scheme for Resilient Microgrid Systems with Aggregated Electronically Coupled Distributed Energy Resources," *IECON 2018 - 44th Annual Conference of the IEEE Industrial Electronics Society*, 2018, pp. 752-757, doi: 10.1109/IECON.2018.8591848 [13].

Chapter 5 of this dissertation presented at the 74th Annual Georgia Tech Protective Relaying Conference and available at the conference proceedings. Citation: H. S. Samkari and B. K. Johnson, "Impact of Inverter Based Resources on Superimposed Quantities-Based Protection," *PRC 2021 - 74th Annual Georgia Tech Protective Relaying Conference*, 2021 [14].

Chapter 6 of this dissertation is accepted at the 2021 IEEE Power Energy Society General Meeting and will be available at the IEEE library. Citation: H. S. Samkari and B. K. Johnson,

"Impact of Distributed Inverter-Based Resources on Incremental Quantities-Based Protection," 2021 *IEEE Power Energy Society General Meeting*, to be published [15].

Chapter 7 of this dissertation is submitted to the IEEE Transactions on Smart Grid and will be available at the IEEE library. Citation: H. S. Samkari and B. K. Johnson, "Time-Domain Protection Scheme for Microgrids with Aggregated Inverter-Based Distributed Energy Resources," *IEEE Transactions on Smart Grid*, submitted for publication [16].